



**STRUCTURAL ANALYSIS AND DESIGN OF COLD FORMED STEEL SIGMA  
PURLINS**

by

**QIANG LIU**

A thesis submitted to the  
University of Birmingham  
for the degree of  
**DOCTOR OF PHILOSOPHY**

School of Civil Engineering  
College of Engineering and Physical Sciences  
University of Birmingham  
May 2012

UNIVERSITY OF  
BIRMINGHAM

**University of Birmingham Research Archive**

**e-theses repository**

This unpublished thesis/dissertation is copyright of the author and/or third parties. The intellectual property rights of the author or third parties in respect of this work are as defined by The Copyright Designs and Patents Act 1988 or as modified by any successor legislation.

Any use made of information contained in this thesis/dissertation must be in accordance with that legislation and must be properly acknowledged. Further distribution or reproduction in any format is prohibited without the permission of the copyright holder.

## **ABSTRACT**

Cold formed steel (CFS) sigma sections are commonly used as purlins in the construction of modern industrial and residential buildings due to their excellent strength-to-weight ratio. The strength design of CFS sections usually relies upon two empirical methods, i.e. the Effective Width Method (EWM) and the Direct Strength Method (DSM), both of which are developed primarily using CFS Z and C sections as a basis. Directly employing these methods for sigma sections needs to be examined in greater detail to validate their applicability. An additional issue is that both methods are elastic design methods. Therefore inevitable conservative outcomes will be obtained when they are used to design continuous beams. A more economical design approach, the pseudo-plastic design method, has been proposed to allow for the development of moment redistribution in the CFS purlin system. One key aspect to this design method is to determine the pseudo-plastic moment resistance (PPMR) at internal supports. In modern roof structures, sleeve connection is often favoured for CFS sigma purlins due to their ease of installation and the limited restriction on the length of the connected purlins. The characteristics of this type of connection will directly influence the stiffness and ultimate load of the purlin system. As a result, determining these characteristics is imperative for implementing sleeved purlin designs. Typically, in modern roof constructions, metal roof sheets are usually attached to purlins with mechanical fasteners. The interactive behaviour between purlins and roof sheeting is another important aspect to be considered in the design practice. Although extensive studies have been performed on this aspect, the structural behaviour of sigma purlins fastened to sheeting with large screw spacing, e.g. 400mm, has not yet been assessed in any detail.

This thesis reports on a series of investigations on the structural behaviour of CFS sigma purlins in three different parts of modern roof systems. In the first investigation, the pre-buckling, buckling, post-buckling and post-failure behaviour of continuous CFS sigma purlins near internal supports was studied by experimental and numerical methods. The results of ultimate moment resistance obtained were compared with the theoretical predictions from the EWM and DSM. From a comparison of the differences found, suggestions for improvement in using the EWM and DSM were made. Based on both the experimental and numerical results, the PPMR for each specimen was derived and a semi-empirical approach has also been proposed to determine the PPMR of CFS sigma sections at internal supports. In the second investigation, the moment-rotation response as well as the moment resistance of the sleeve connection of sigma purlins was studied by laboratory tests. Engineering models were developed to predict the behaviour of this connection and a good correlation was observed with the experimental data. The experimental results reported provide a well-documented first-hand data set for future reference of sleeve connections for CFS sigma sections in terms of the moment resistance, rotational stiffness and typical failure modes. The proposed analytical models also provide rational engineering methods that can be used in the design practice. In the third investigation, the flexural behaviour of CFS sigma purlins fastened to roof sheeting with large screw spacing was studied experimentally. The purlin-sheeting assemblies were subjected to both downward and uplift loadings, from which different behavioural aspects such as flexural stiffness, failure modes and ultimate load were examined. To the author's best knowledge, this investigation is the first one that studies the high strength sheeted sigma purlin subjected to both downward and uplift loads, with large screw

spacing. Test results are utilized to develop design proposals for sigma purlins that codes or standards have not yet covered.

**KEY WORDS:** cold-formed steel sections; thin-walled structures; sigma purlins; buckling; post-buckling; post-failure; pseudo-plastic design; collapse; moment resistance; continuous purlins; sleeve connections; moment rotation characteristics; semi-rigid connections; numerical modelling; roof sheeting; purling-sheeting interaction; flexural behaviour; downward load; uplift load; flexural stiffness

## **DEDICATION**

I wish to dedicate this thesis to my family, especially to my parents, for your continued support, encouragement and love.

## **ACKNOWLEDGEMENTS**

I would like to express my deepest gratitude to my supervisor, Dr. Jian Yang, for all he has done to assist me throughout the study of my PhD. It would not have been possible to complete this thesis without his solid supervision. He has provided expert guidance, valuable suggestions and persistent support in that period. To me, he is more than a supervisor, providing friendship and encouragement in my career.

I also would like to express my sincere thanks to Dr. Long Yuan Li, who gave me valuable academic advice at various stages of my study, and Professor Andrew Chan, who gave me constructive criticism and helpful advice in annual reviews of my study.

I am indebted to the School of Civil Engineering, University of Birmingham, for providing a Postgraduate Teaching Assistant Scholarship to conduct this research project, Albion Sections Ltd., for providing financial support and materials for experiments.

Thanks are due to my friend, Dr. Daniel Brown, for his enlightened help with my academic writing.

My ultimate thanks go to my father, Shi Zhong Liu, my mother, Qing Lian Lv, my sisters, Yan Ying Liu and Ke Liu, and my wife, Si Yuan Gao, who never doubted this thesis would be finished some day.

## PUBLICATIONS

### Journal papers:

1. Liu, Q. Yang, J. Chan, A. H. and Li, L.Y. (2011) **Pseudo-plastic moment resistance of continuous beams with cold-formed sigma sections at internal supports: A numerical study.** Thin-Walled Structures, 49, 1592-1604.
2. Liu, Q. Yang, J. and Li, L.Y. (2011) **Pseudo-plastic moment resistance of continuous beams with cold-formed sigma sections at internal supports: An experimental study.** Engineering Structures, 33, 947-957.
3. Yang, J and Liu, Q. (2012) **Sleeve connections of cold-formed steel sigma purlins.** Engineering Structures, Accepted.
4. Liu, Q. and Yang, J. (2012) **Numerical simulation of sleeve connections for cold formed steel sigma sections.** Journal of Constructional Steel Research, under review.
5. Yang, J and Liu, Q. (2012) **An experimental study into flexural behaviour of sigma purlins attached with roof sheets.** Engineering Structures, under review.

### Conference papers:

1. Yang, J. Liu, Q. and Chan, A. H. C. (2012) **Flexural behaviour of purlin-roof sheeting assemblies.** In: Proceedings of the 7<sup>th</sup> International Conference on Advances in Steel Structures, Nanjing, China.
2. Yang, J. and Liu, Q. (2011) **An experimental study of cold-formed steel sigma sections with sleeve connections.** In: Proceedings of the 6<sup>th</sup> International Conference on Thin Walled Structures, pp.649-656, Timisoara, Romania.
3. Yang, J. and Liu, Q. (2011) **Pseudo-plastic design of continuous beams with cold-formed sigma sections.** In: Proceedings of Advances in Steel and Aluminium Structures, pp.165-171, Sarawak, Malaysia.
4. Liu, Q. Yang, J. and Li, L.Y. (2010) **Numerical analysis of cold-formed Sigma Steel Beams.** In: Proceedings of Discrete Element Methods, Simulations of Discontinua: Theory and Application. pp.199-204, London, UK.
5. Liu, Q. Yang, J. and Li, L.Y. (2009) **Experimental study on post-buckling and post-failure behaviours of cold-formed sigma continuous steel beams at internal supports.** In: Proceedings of the 6<sup>th</sup> International Conference on Advances in Steel Structures, pp.450-459, Hong Kong, China.



## TABLE OF CONTENTS

<b>ABSTRACT .....</b>	<b>i</b>
<b>TABLE OF CONTENTS .....</b>	<b>vii</b>
<b>LIST OF FIGURES.....</b>	<b>xiii</b>
<b>LIST OF TABLES.....</b>	<b>xvii</b>
<b>LIST OF DEFINITIONS .....</b>	<b>xviii</b>
<b>CHAPTER 1 INTRODUCTION.....</b>	<b>1</b>
1.1 BACKGROUND OF COLD FORMED STEEL SECTIONS .....	1
1.2 RESEARCH NEEDS OF CFS SIGMA SECTIONS .....	4
1.3 AIMS AND OBJECTIVES.....	8
1.4 RESEARCH METHODOLOGY AND THE LAYOUT OF THIS THESIS .....	9
<b>CHAPTER 2 LITERATURE REVIEW .....</b>	<b>12</b>
2.1 GENERAL.....	12
2.2 ELASTIC CRITICAL BUCKLING OF CFS FLEXURAL MEMBERS .....	12
2.2.1 Local buckling.....	12
2.2.2 Distortional buckling .....	15
2.2.3 Lateral torsional buckling.....	20
2.2.4 Localised buckling due to in-plane concentrated load .....	23
2.3 POST-BUCKLING STRENGTH.....	24
2.4 ULTIMATE STRENGTHS OF CFS FLEXURAL MEMBERS .....	26

2.5 ELASTIC DESIGN METHODS .....	31
2.6 PLASTIC DESIGN METHODS.....	34
2.6.1 Conventional plastic design method for hot-rolled steel structures .....	35
2.6.2 Pseudo plastic design method.....	38
2.6.3 Yield line method .....	42
2.7 NUMERICAL METHODS IN THE RESEARCH OF CFS STRUCTURES .....	43
2.7.1 Finite Strip Method (FSM).....	44
2.7.2 Generalised Beam Theory (GBT) .....	45
2.7.3 Finite Element Method (FEM) .....	45
2.8 BOLTED CONNECTIONS IN CFS STRUCTURES .....	50
2.9 CFS PURLIN-SHEETING INTERACTIONS .....	57
2.10 SUMMARY .....	64
<b>CHAPTER 3 CONTINUOUS SIGMA PURLINS AT INTERNAL SUPPORTS.....</b>	<b>67</b>
3.1 INTRODUCTION .....	67
3.2 TEST PROGRAMME .....	67
3.3 TEST SPECIMENS .....	69
3.4 TEST APPARATUS AND SET-UP .....	71
3.5 TEST PROCEDURES AND INSTRUMENTATION.....	73
3.6 TEST RESULTS.....	74
3.7 DISCUSSION OF TEST RESULTS .....	78
3.8 FINITE ELEMENT MODELLING OF CONTINUOUS SIGMA PURLINS AT INTERNAL SUPPORTS.....	80

3.8.1 Modelling development.....	81
3.8.1.1 <i>Element type and meshing</i> .....	81
3.8.1.2 <i>Loading and boundary conditions</i> .....	83
3.8.1.3 <i>Material property</i> .....	84
3.8.1.4 <i>Geometric imperfections</i> .....	85
3.8.1.5 <i>Solution scheme</i> .....	87
3.8.2 Numerical results and comparison with experimental data.....	87
3.8.3 Parametric study .....	94
3.9 COMPARISON OF THE PREDICTED MOMENT RESISTANCE WITH CURRENT CODES OF PRACTICE .....	97
3.10 DESIGN PROPOSALS FOR THE IMPROVEMENT OF THE EWM AND THE DSM	103
3.11 MOMENT VERSUS PSEUDO-PLASTIC ROTATION CURVES.....	109
3.12 A SEMI-EMPIRICAL METHOD TO DETERMINE THE PPMR AND A DESIGN EXAMPLE BY USING THE PSEUDO-PLASTIC DESIGN METHOD .....	111
3.13 SUMMARY.....	119
<b>CHAPTER 4 SLEEVED SIGMA PURLINS AT INTERNAL SUPPORTS .....</b>	<b>121</b>
4.1 GENERAL.....	121
4.2 TEST PROGRAMME .....	121
4.3 TEST SPECIMENS .....	123
4.4 TEST SET-UP AND APPARATUSES .....	126
4.5 TEST PROCEDURE AND INSTRUMENTATION .....	127
4.6 TEST RESULTS.....	127

4.7 DISCUSSION OF THE TEST RESULTS .....	131
4.7.1 Moment-rotation relationship .....	131
4.7.2 Failure modes .....	138
4.7.3 Moment resistance .....	140
4.8 FINITE ELEMENT MODELLING OF SLEEVED SIGMA PURLINS AT INTERNAL SUPPORTS .....	148
4.8.1 Finite element idealisation .....	148
4.8.2 Validation of FE modelling .....	151
4.9 SUMMARY .....	155
<b>CHAPTER 5 SIMPLE SPAN SIGMA PURLINS WITH ROOF SHEETS .....</b>	<b>157</b>
5.1 GENERAL .....	157
5.2 TEST PROGRAMME .....	157
5.3 TEST SPECIMENS .....	159
5.4 SET-UP OF TEST APPARATUSES AND TEST PROCEDURE .....	161
5.5 TEST INSTRUMENTATION .....	164
5.6 TEST RESULTS .....	166
5.7 DISCUSSION OF THE TEST RESULTS AND OBSERVATIONS .....	171
5.7.1 Results compared with the prediction by the theoretical linear beam theory .....	171
5.7.2 Failure modes .....	174
5.7.2.1 Downward loading tests .....	174
5.7.2.2 Uplift loading tests .....	177
5.7.2.3 Discussion of the failure modes .....	178

5.7.3 Flexural resistance .....	179
5.7.3.1 Predictions of the flexural resistance from different design codes .....	179
5.7.3.2 Discussion of the codified methods for purlins under a downward loading .....	183
5.7.3.3 Discussion of the codified methods for purlins under an uplift loading .....	187
5.8 SUMMARY .....	188
<b>CHAPTER 6 CONCLUSIONS .....</b>	<b>191</b>
6.1 GENERAL .....	191
6.2 INVESTIGATION INTO STRUCTURAL BEHAVIOUR OF CONTINUOUS SIGMA PURLINS AT INTERNAL SUPPORTS .....	192
6.3 INVESTIGATION INTO STRUCTURAL BEHAVIOUR OF SLEEVED SIGMA PURLINS AT INTERNAL SUPPORTS .....	193
6.4 INVESTIGATION INTO FLEXURAL BEHAVIOUR OF SHEETED CFS SIGMA PURLINS .....	194
6.5 LIMITATIONS AND FUTURE WORK .....	196
Appendix I Procedures for calculating load resistance of CFS members by using BSI (2006a) ..	199
Appendix II Procedures of DSM for calculating load resistance of CFS members by using Standards Australia (2006) or AISI (2007) .....	203
Appendix III Derivation of the theoretical moment-rotation capacity curve used in the pseudo plastic design method .....	205
Appendix IV: Material strength tests .....	208
Appendix V: Comparison of FE predictions using different imperfection magnitudes .....	214

Appendix VI: Determination of the PPMR and PPR for each specimen .....	218
Appendix VII: Derivation of the relationship between rotation angle at support end and rotational stiffness provided by the sleeve connection .....	228
Appendix VIII: Derivation of the end rotation attributed to mid-span point loading for the sleeved beams in the sleeved internal support tests.....	230
Appendix IX: Derivation of the joint rotation due to bolt hole elongation in a four-bolt moment connection, after Bryan (1993).....	232
Appendix X: Comparison of moment vs. rotation graphs between the tests and the FE analysis	234
Appendix XI: Derivation of the theoretical moment vs. deflection curve .....	238
Appendix XII: Calculation of the lateral spring stiffness $K$ by following BSI (2006a).....	240
Appendix XIII: Calculation of the equivalent lateral load, $q_{h,Ed}$ , the lateral bending moment, $M_{fz,Ed}$ , and the buckling reduction factor, $\chi_{LT}$ , for purlins attached to sheeting by following BSI (2006a).....	245
REFERENCES .....	250

## LIST OF FIGURES

Figure 1-1 Cold forming methods .....	1
Figure 1-2 Typical forms of CFS sections, after BSI (2006a).....	2
Figure 1-3 Typical stress-strain curves of hot-rolled and cold worked steel, after Yu (2000).....	3
Figure 1-4 Definition of flexural and membrane residual stress, after Schafer and Peköz (1998) .	3
Figure 1-5 Typical CFS Z, C and sigma sections.....	4
Figure 1-6 Sleeved sigma purlin systems .....	6
Figure 1-7 Illustration of a purlin-sheeting system .....	7
Figure 2-1 Local buckling of CFS Z, C and sigma sections .....	13
Figure 2-2 Distortional buckling of CFS Z, C and sigma sections.....	16
Figure 2-3 Analytical models for determining distortional buckling stress of CFS purlins.....	19
Figure 2-4 Lateral torsional buckling of CFS Z, C and sigma purlins .....	20
Figure 2-5 Plates subjected to in-plane concentrated loads.....	23
Figure 2-6 Schematic diagram of post-buckling action, after Yu (2000).....	24
Figure 2-7 Stress distribution in an edge stiffened compression plate, after von Karman et al. (1932) .....	25
Figure 2-8 Rationale of EWM, after Yu (2000) .....	33
Figure 2-9 Plastification of a cross section.....	35
Figure 2-10 Moment-curvature relationship of a cross section.....	36
Figure 2-11 Schematic diagram of moment-rotation curve of a single-span CFS beam .....	39
Figure 2-12 Determination of the pseudo-plastic moment resistance $M_{pp}$ .....	41

Figure 2-13 The analytical model considering restraint effect by sheeting on purlins, after BSI (2006a).....	62
Figure 3-1 Two-span continuous beam .....	68
Figure 3-2 Test set-up.....	72
Figure 3-3 Calculation for the rotation of expected plastic zone .....	76
Figure 3-4 Moment-rotation curves.....	77
Figure 3-5 Typical localised collapse patterns .....	78
Figure 3-6 Post-buckling deformation.....	80
Figure 3-7 Finite element meshing.....	82
Figure 3-8 Modelling of loading and support conditions .....	83
Figure 3-9 Typical stress-strain curve of beam material .....	85
Figure 3-10 Basic imperfection modes.....	86
Figure 3-11 Comparison of moment-rotation curves between the experimental and FE results ..	90
Figure 3-12 Failure modes.....	93
Figure 3-13 Moment-rotation curves from FE analysis .....	97
Figure 3-14 Ratio of cross-sectional resistance between the numerical and theoretical results considering the interaction of bending and shear .....	100
Figure 3-15 Distribution of failure mode in relation to ratios of various buckling moments .....	106
Figure 3-16 Comparison of unimproved and improved methods .....	108
Figure 3-17 Moment vs. rotation capacity curves .....	111
Figure 3-18 PPMR against slenderness curve .....	112
Figure 3-19 Illustration of the bending moment redistribution using the proposed pseudo-plastic design method.....	115



Figure 3-20 Analytically and numerically predicted load-deflection curves for the double span purlin.....	117
Figure 3-21 von Mises stress distributions .....	118
Figure 4-1 Typical sleeve connection for CFS sigma purlins .....	122
Figure 4-2 Test set-up.....	127
Figure 4-3 Moment vs. rotation curves for both sleeve and continuous connections .....	129
Figure 4-4 Representative model of moment-rotation relation .....	132
Figure 4-5 Rotation components in the sleeve connection.....	134
Figure 4-6 Comparison between the test and predicted moment-rotation curves .....	137
Figure 4-7 Failure modes.....	139
Figure 4-8 Bending moment diagram of the sleeved purlin.....	139
Figure 4-9 Bearing forces induced in the purlin section .....	143
Figure 4-10 Numerical study for the localised load resistance of sigma sections.....	146
Figure 4-11 Interaction between bending moment and local bearing force .....	147
Figure 4-12 Finite element meshing.....	149
Figure 4-13 Tri-linear stiffness model for the springs.....	150
Figure 4-14 Comparison of the moment-rotation response.....	152
Figure 4-15 Deformation of the sleeved purlin .....	154
Figure 4-16 Stress distribution of the sleeved beam (von Mises stress, in $\text{N/mm}^2$ ).....	155
Figure 5-1 Overall view of test assemblies .....	158
Figure 5-2 Dimensions of the roof sheeting (in mm) .....	161
Figure 5-3 Screws connecting roof sheeting to sigma purlins .....	161
Figure 5-4 Schematic illustration of test set-up.....	163

Figure 5-5 Timber blocks used at loading points .....	164
Figure 5-6 Test instrumentation .....	165
Figure 5-7 Bending moment diagram of the tested sigma purlins .....	166
Figure 5-8 Load versus deflection curves for the downward loading test.....	169
Figure 5-9 Load versus deflection curves for the uplift loading test.....	170
Figure 5-10 Different screw spacings for specimens SD60-30025-1 and SD60-30025-2 .....	172
Figure 5-11 Typical deformation of sheeted purlin with unrestrained compression flange.....	173
Figure 5-12 Load versus deflection curves.....	174
Figure 5-13 Type I failure for downward loading tests.....	175
Figure 5-14 Type II failure for downward loading tests .....	176
Figure 5-15 Failure types for the uplift loading tests .....	178
Figure 5-16 Superposition of stresses, after BSI (2006a).....	181
Figure 5-17 Comparison of downward test results with analytical results .....	186
Figure 5-18 Standards Australia (2006) and AISI (2007) predictions for the uplift load tests ...	188

## LIST OF TABLES

Table 2-1 Local buckling coefficient for a long rectangular plate, after Timoshenko and Gere (1961) .....	15
Table 2-2 $\alpha_m$ in various loading cases, after Trahair (1993) .....	22
Table 3-1 Cross-sectional dimensions.....	70
Table 3-2 Test results of continuous purlins at internal support .....	75
Table 3-3 Failure mode, moment resistance and the PPMR from FE analysis .....	91
Table 3-4 Comparison of moment resistance and PPMR between the experimental and the FE results.....	94
Table 3-5 Predicted ultimate moment and shear resistance based on the EWM and the DSM ....	98
Table 3-6 Calculated elastic critical buckling moment by considering real loading conditions.	104
Table 4-1 Geometric and mechanical properties of test specimens .....	125
Table 4-2 Test results of sleeved purlins at internal support.....	130
Table 4-3 Comparisons of moment resistance between sleeved and continuous internal support tests and between the calculated and experimental results.....	142
Table 4-4 Comparison of moment resistance .....	152
Table 5-1 Tested purlin specimens.....	160
Table 5-2 Test results of sheeted purlins.....	167
Table 5-3 Predicted results of flexural moment resistance.....	183

## LIST OF DEFINITIONS

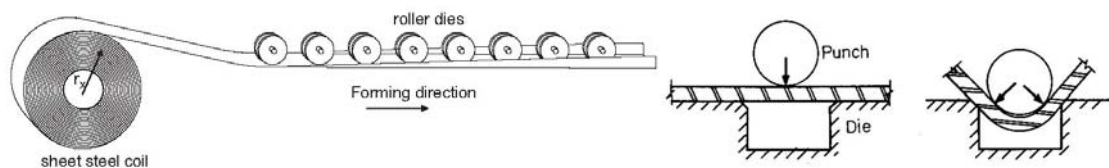
AISI	American Iron and Steel Institute
BSI	British Standards Institution
CFS	cold formed steel
DB	distortional buckling
DSM	direct strength method
$E$	Young's modulus
EWM	effective width method
FE	finite element
FEM	finite element method
FSM	finite strip method
GBT	generalised beam theory
$f_y$	yield stress or 0.2% proof stress
$I_{\text{eff}}$	effective second moment of area at the yield stress level
LB	local buckling
LTB	lateral torsional buckling
LVDT	linear variable displacement transducer
$\nu$	Poisson's ratio
$M_{\text{cr}}$	elastic critical buckling moment of a flexural member
$M_{\text{c,Rd}}$	cross-sectional moment resistance
$M_{\text{p}}$	plastic moment resistance of a cross section
$M_{\text{pp}}$	pseudo-plastic moment resistance of a cross section

$M_y$	first yield moment of a cross section
PMR	plastic moment resistance
PPMR	pseudo-plastic moment resistance
PPR	pseudo-plastic rotation
$\Theta$	rotation capacity of a pseudo-plastic hinge
UDL	uniformly distributed load
$W_{\text{eff}}$	effective section modulus at the yield stress level

# CHAPTER 1 INTRODUCTION

## 1.1 BACKGROUND OF COLD FORMED STEEL SECTIONS

Cold formed steel (CFS) sections are manufactured from steel sheets, strips or plates at room temperature. The thickness of the steel sheets, strips or plates used in cold formed steel sections is mostly in a range from 0.4mm to 6.4mm, and in exceptional cases, a steel plate with a thickness of up to 25mm can be cold formed into a section (Yu, 2000). Two cold forming methods are normally employed to manufacture the CFS sections, i.e. roll forming and press braking, as shown in Fig. 1-1. The roll forming involves a series of rollers which draw the steel strip or sheet through to form into the predesigned shape along the line of rollers. This method is usually suitable for sections with a thickness not exceeding 3mm and of a length up to 16m. The press braking method is normally used to manufacture sections from comparatively thicker steel plates and it is mainly practicable for sections with short lengths and simple shapes.



(a) Roll forming, after Moen et al. (2008)

(b) Press braking, after Yu (2000)

Figure 1-1 Cold forming methods

Typical forms of CFS sections are shown in figure 1-2. Thanks to their versatile structural shapes, CFS sections have many advantages compared to conventional hot-rolled steel sections, such as

the ease of fabrication, low cost in transportation, handling and storage, fast erection and installation, and excellent strength to weight ratio. As a result, in recent years CFS sections have been widely used as structural members in residential and industrial buildings.

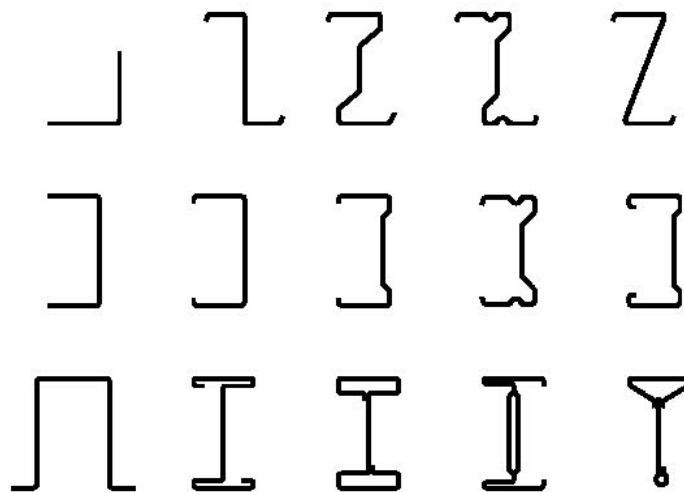


Figure 1-2 Typical forms of CFS sections, after BSI (2006a)

CFS sections possess several structural features quite different from those of hot-rolled steel sections. The plate elements forming CFS sections usually have greater width-to-thickness ratios, which result in CFS sections being susceptible to premature buckling. Having open and thin-walled sections, CFS members normally have low torsional rigidity as well as low flexural rigidity about their minor axes, rendering the sections prone to lateral torsional buckling. Because of the cold working forming process, the material properties, i.e. stress-strain relationship and residual stress distribution pattern, are also very different from those of hot-rolled sections. The stress-strain curve of hot rolled steel usually has an obvious horizontal yield plateau, which defines the yield point of the steel, as shown in Fig. 1-3 (a). In contrast, the stress-strain curve of

cold worked steel does not have an obvious yield point, as shown in Fig. 1-3 (b). In hot-rolled sections, residual stresses over the thickness of an element may be considered as the membrane type stresses; while in CFS sections, residual stress distribution through the thickness is generally of the flexural type (the definitions of membrane type and flexural type stresses are shown in Fig. 1-4). Because of these distinct structural features, the design approaches for CFS sections are therefore substantially different from that of hot-rolled sections.

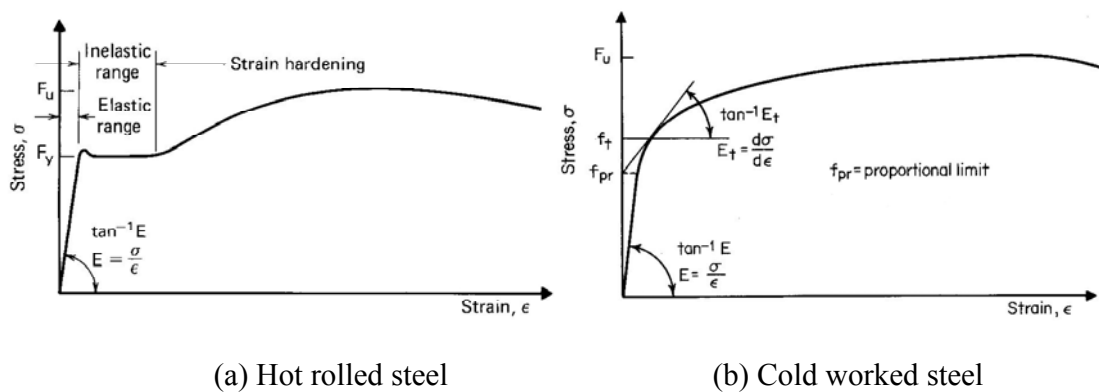


Figure 1-3 Typical stress-strain curves of hot-rolled and cold worked steel, after Yu (2000)

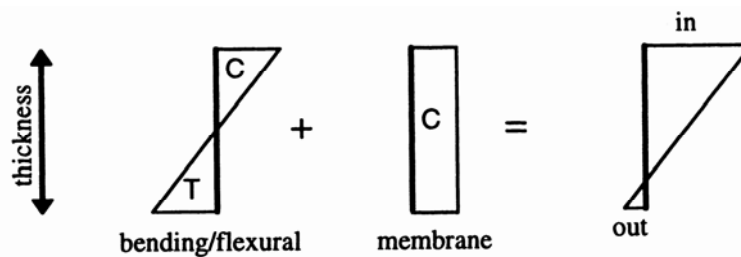


Figure 1-4 Definition of flexural and membrane residual stress, after Schafer and Peköz (1998)

The most commonly used CFS sections are Z, C and sigma sections, as shown in Fig. 1-5. Z sections are usually used in pitched roofs, where the principal major axis of the Z sections is nearly vertical when the sections are orientated in line with the pitch angle. This can effectively



avoid twisting movement induced by the gravity load. The emerging modern shallow roof construction created a need for other section shapes, e.g. C and sigma sections, whose major bending plane is in parallel to the applied load. This thesis concentrates on sigma sections formed by cold roll forming.

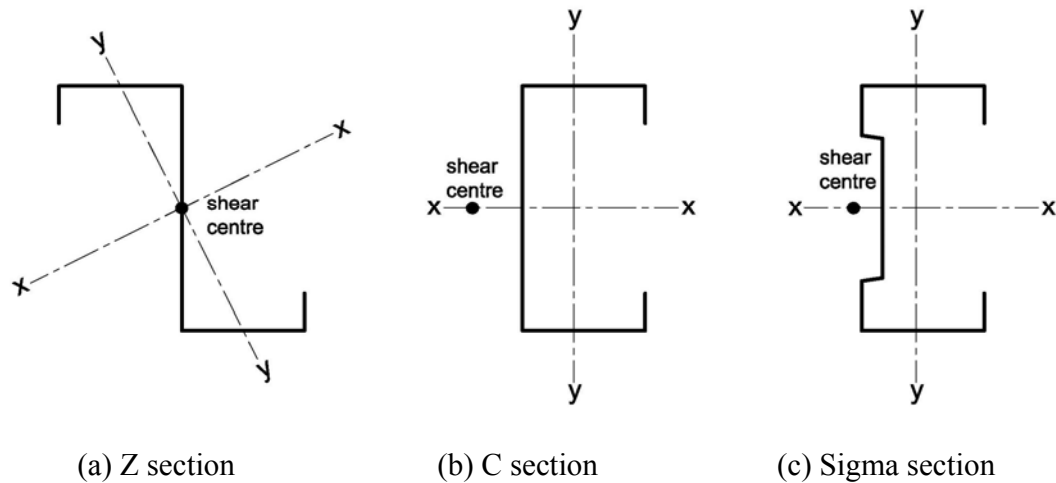


Figure 1-5 Typical CFS Z, C and sigma sections

## 1.2 RESEARCH NEEDS OF CFS SIGMA SECTIONS

CFS sigma sections have evolved from the conventional C sections by adding two insets in the web as stiffeners. The presence of stiffeners in the web brings the shear centre of the section closer to the web and hence reduces torsion introduced by applied load. Compared to their counterparts such as Z and C sections, sigma sections offer several advantages, such as higher load-carrying capacity, larger torsional rigidity and lightness (Yu, 2000). As a result, the use of sigma sections has been steadily growing over recent years, and they are now commonly used as purlins and side rails in modern industrial buildings and as floor joists in residential buildings.

Being considered as thin-walled structures, the conventional analysis and design of CFS beams is based on elastic theory. For instance, design methods from current codes of practice are mainly based on the elastic analysis, i.e. the Effective Width Method (EWM) (BSI, 2006a) or the Direct Strength Method (DSM) (Standards Australia, 2006; AISI, 2007). Both methods have been well established for Z and C sections subjected to uniform bending or axial loading. Directly employing these methods for sigma sections, however, is not appropriate due to the presence of web stiffeners. It is therefore imperative to examine these design models for sigma sections and hence to identify the limitation of their applicability. Such problems for sigma sections at internal supports can be worse in a multi-span beam system. Since the buckling behaviour near internal supports is rather complicated due to the coexisting occurrence of the concentrated load, bending moment and shear force, it requires special attention.

The reason for using the elastic design theory for thin-walled steel members is that there is concern about the premature failure associated with various modes of buckling. The elastic method ignores the moment redistribution effect that results from the occurrence of plastic hinges in high bending moment zones, and intrinsically yields an uneconomic result. To improve the design efficiency, a pseudo-plastic design method (Davis and Raven, 1986) has been proposed for statically indeterminate structures, such as multi-span beams and frames. This method does include the benefit of moment redistribution. It is acknowledged that the utilisation of moment redistribution relies on the beam having an adequate rotation capacity in the region of the plastic hinge. Traditional hot rolled compact sections are usually capable of providing adequate rotation capacity while retaining the full plastic moment resistance (PMR) until the system collapses. CFS

sections, however, exhibit moment softening characteristics because of the premature buckling experienced in constituent plate elements under compression of the cross section (Grundy, 1990). This results in a gradually reduced moment resistance near internal supports when the rotation develops. The reduced moment resistance is analogous to the PMR of a compact steel section and is referred to as the pseudo-plastic moment resistance (PPMR). Therefore, the key to implementing the pseudo-plastic design method for a multi-span beam system is to determine the PPMR near internal supports. Currently, the determination of the PPMR is purely based on experimental methods, which are expensive and time-consuming.

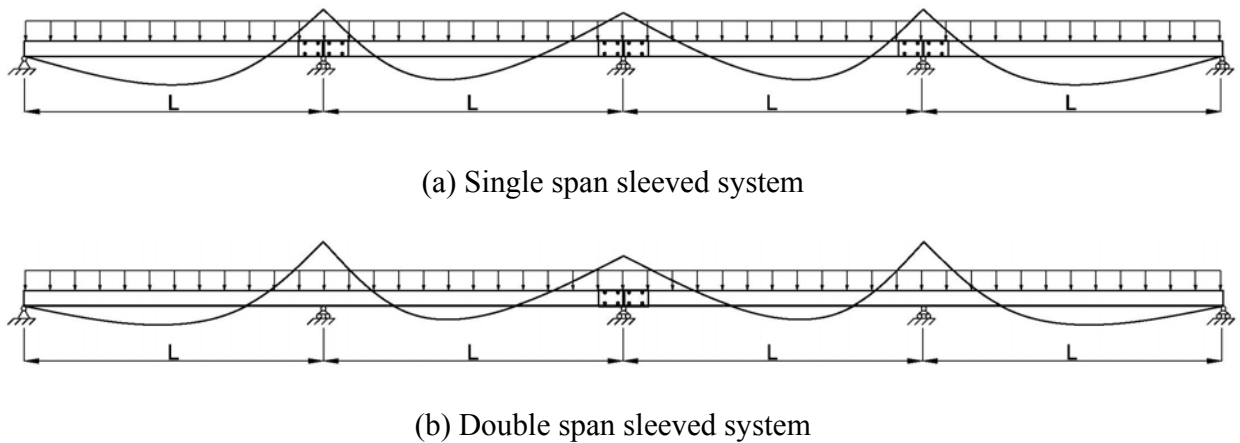


Figure 1-6 Sleeved sigma purlin systems

Four different forms of sigma purlin systems are commonly adopted in modern roof systems, i.e. single span butt, double span butt, single span sleeved and double span sleeved. As sleeve connections enable purlin systems to possess a higher level of continuity at rafts (which renders greater structural efficiency), they are usually preferable to simple connections. The general layouts of sigma purlin systems with sleeves are shown in Fig. 1-6. The bending moment

diagram of the system under uniformly distributed load (UDL) is also schematically presented in the same figure. The structural behaviour of sleeve connections influences moment distribution in the purlin systems. It is therefore crucial to the structural performance of the entire purlin systems and thus it is worth studying thoroughly. However, a lack of studies on sleeve connections has resulted in current design practice of sleeve purlin systems either resorting to expensive prototype tests or adopting simplifications. Such examples of simplifications include treating the sleeve connection as a simple type or assuming it to be a fully continuous one. To provide an economic and safe design of a sleeved sigma purlin system, investigations into the structural behaviour of sleeve connections are therefore needed.

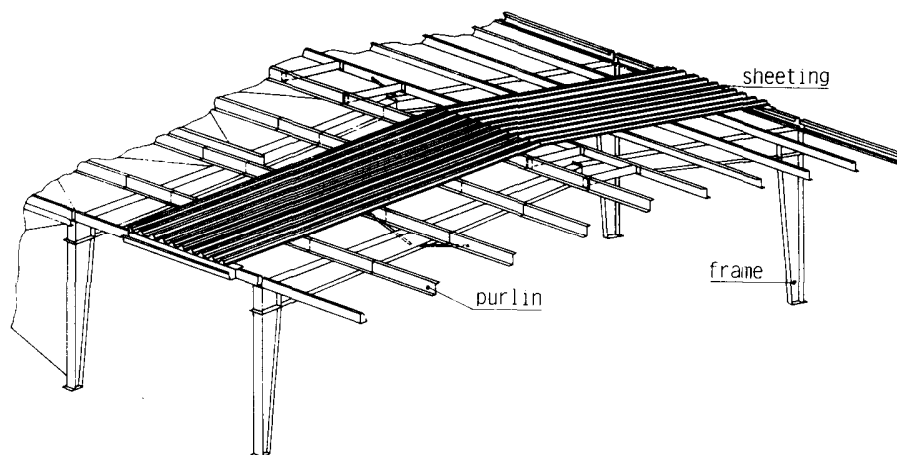


Figure 1-7 Illustration of a purlin-sheeting system, after Heinz (1994)

Fig. 1-7 schematically illustrates a typical purlin-sheeting system, where sheeting is attached to the top flange of purlins by screws. When the purlin-sheeting system is subjected to gravity load, compression flanges of the purlins in the sagging moment zone are restrained by sheeting. Therefore the moment resistance of the purlins is governed by their strength. On the other hand,

when the purlin-sheeting system is subjected to uplift load, the compression flanges of the purlins in the sagging moment zone are free. Therefore the moment resistance of the purlins is governed by their buckling resistance. The structural behaviour of a purlin-sheeting system has been the subject of extensive investigations for some time. However, due to the complexity of the system, knowledge regarding this subject is far from being well established. For example, the available investigations for purlin-sheeting systems were largely based on CFS C and Z sections, and only a small amount of research concerned sigma sections. This has resulted in the design of sheeted sigma purlins not being included in some current codes of practice, e.g. AISI (2007) and Standards Australia (2006). Moreover, in most of these investigations, the sheeting was assumed to be attached to the purlins by screws applied at every trough of the sheeting (the screw spacing is not greater than 300mm), and the influence of screw spacing on the structural behaviour of the purlin-sheeting system was not examined. It is thus necessary to assess the structural behaviour of sigma purlin-sheeting systems by taking into account the influence of screw spacing, e.g. 400mm, which is commonly used in practical applications.

### 1.3 AIMS AND OBJECTIVES

This thesis is primarily aimed at investigating the structural behaviour of double span sigma purlin systems with continuous or sleeved internal supports, and the structural behaviour of single span purlins restrained by sheeting on their top flange under both downward and uplift loads.

The main objectives of the project include:

- To study the post-buckling and post-failure behaviour of continuous CFS sigma purlins at internal supports.
- To examine the applicability of the design provisions of current codes of practice in predicting the load resistance of continuous CFS sigma purlins at internal supports.
- To develop a semi-empirical approach for calculating the PPMR of CFS sigma purlins at internal supports in order to facilitate the pseudo-plastic design method.
- To study the moment-rotation characteristics of sleeved CFS sigma purlins at internal supports.
- To develop an analytical model based on which the rotational stiffness of sleeve connections can be quantified.
- To establish a design model so that the moment resistance of sleeve connections can be assessed by calculation.
- To develop a FE model to carry out the parametric study for the structural behaviour of sleeved CFS sigma purlins at internal supports.
- To study the structural performance of simple span sheeted CFS sigma purlins under both gravity and uplift loads.
- To provide test data based on which the design coefficient quoted in AISI (2007) and Standards Australia (2006) may be calibrated for simple span sheeted CFS sigma purlins.
- To examine the applicability of the design rules given in BSI (2006a) for sheeted purlins.

#### 1.4 RESEARCH METHODOLOGY AND THE LAYOUT OF THIS THESIS

To achieve the above mentioned aims and objectives, an extensive literature review was carried out to understand the state of the art of this research field. Knowledge gaps have been identified, which will be addressed by the present study. A series of laboratory tests were then devised and carried out to provide first-hand datasets. For the study of the continuous CFS sigma purlins, numerical analysis by using FEM was carried out to extend the range of geometric dimension beyond the tested specimens. After being validated by the test results, the FEM will expand the dataset from the physical laboratory test results. For the study of sleeved sigma purlins, FE modelling was also carried out to reproduce the test results. Based on the test/numerical results, the appropriate analytical models and design recommendations were thus developed.

The layout of this thesis is as follows:

**Chapter 1** presents brief introduction including the background knowledge of CFS sections. It sets out the research scope, defines the aims and objectives, describes the research methodology and outlines the structure of this thesis.

**Chapter 2** presents a state-of-the-art literature review to document the existing research in cold-formed steel sections, with particular reference to flexural members and connections. This chapter summarizes the main findings from existing published research and identifies knowledge gaps that lead to the subject of this thesis.

**Chapter 3** presents the experimental and numerical investigations into the structural behaviour of continuous CFS sigma purlins at internal supports. It reports the details of test and numerical

modelling procedures. The test and numerical results are discussed and compared with current codes of practice. Design approaches are proposed to predict the moment resistance and the PPMR of the CFS sigma purlins at internal supports.

**Chapter 4** presents an experimental investigation into the structural behaviour of sleeved CFS sigma purlins at internal supports. Based on the test results, an analytical model is proposed to quantify the moment-rotation characteristics of the sleeved connections. Design models are established to predict the moment resistance of the sleeved connections. A FE-based model is also developed to simulate the structural behaviour of the sleeved purlins.

**Chapter 5** presents an experimental investigation into the structural behaviour of simple span sheeted CFS sigma purlins under both gravity and uplift loads. Details of the test procedure are described and the test results are presented and discussed. Design proposals are provided for the calculation of the moment resistance of sheeted purlins by following current codes of practice AISI (2007) and Standards Australia (2006). The test results are compared with the design rules in BSI (2006a). Design recommendations are also provided for the calculation of the moment resistance of sheeted purlins by following BSI (2006a).

**Chapter 6** presents a summary of the key findings from this project and the recommendations for future work.



## **CHAPTER 2 LITERATURE REVIEW**

### **2.1 GENERAL**

The increasing applications of CFS sections in both residential and industrial buildings have attracted much research into their structural behaviour and design methods. This chapter will present a state-of-the-art review of published research work in the structural aspect of CFS flexural members. The reviewed literature will be presented in eight sections, namely, the elastic buckling research in Section 2.2, post-buckling strength in Section 2.3, ultimate strength in Section 2.4, elastic design method in Section 2.5, plastic design method in Section 2.6, numerical approaches commonly used in CFS research in Section 2.7, bolted connections for CFS flexural members presented in Section 2.8, and CFS member-sheeting interaction in Section 2.9.

### **2.2 ELASTIC CRITICAL BUCKLING OF CFS FLEXURAL MEMBERS**

#### **2.2.1 Local buckling**

Local buckling is a common buckling mode occurring in the constituent plate elements of the CFS flexural members. The key characteristic of this buckling mode is that the compression flange and web plates will buckle and the web plate will often develop a deflection shape in a double curvature (Hancock, 2003). The half-wavelength of the buckling deflection curve is of the order of the flange width or partial web depth, and the corner junctions remain straight, as illustrated in Fig.2-1.

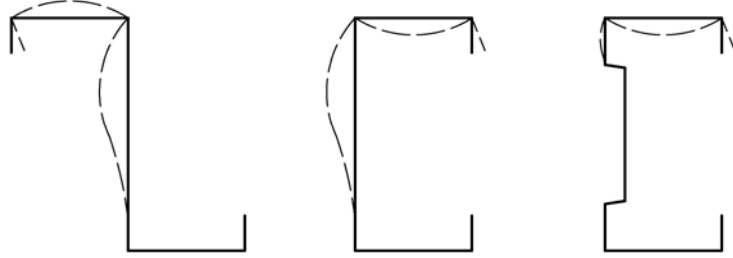


Figure 2-1 Local buckling of CFS Z, C and sigma sections

The occurrence of local buckling in a CFS section is primarily attributed to the high width-to-thickness ratios of individual plate components forming the CFS section. When these slender plate components are subjected to in-plane compression or shear force, local buckling is likely to occur before the material in the cross-section reaches the yield stress.

Early to the 19<sup>th</sup> century, Bryan (1891) established the differential governing equation in determining the critical buckling stress of a plate based on the small deflection theory. By solving the equation, the elastic critical local buckling stress of a rectangular plate subjected to compression, shear, or bending can be derived and is now well known as:

$$f_{cr} = \frac{k\pi^2 E}{12(1-\nu^2)(w/t)^2} \quad (2-1)$$

where  $E$ ,  $\nu$ ,  $w$ , and  $t$  are elastic modulus, Poisson's ratio, width, and thickness of the plate, respectively.  $k$  is called the plate local buckling coefficient and is associated with the aspect ratio, restraint condition, and stress distribution of the plate. Gerard and Becker (1957) demonstrated that under a given loading and restraint condition,  $k$  value tends to converge to a constant as the aspect ratio of a plate increases. Timoshenko and Gere (1961) systematically analysed the elastic

local buckling of a rectangular plate subjected to compression and shear, respectively, with various boundary conditions. The derived theoretical  $k$  values are summarized in Table 2-1. Bulson (1970) examined the effects of stress gradient on the local buckling of a rectangular plate and developed the  $k$  values as a function of stress gradient. As a result of intensive and constant research efforts in the past century, the elastic critical local buckling stress of rectangular plates with idealized boundary conditions (free, simply supported, or fully fixed), and with common stress distributions (uniformly and non-uniformly distributed in-plane stress, shear stress or combined stresses) can be easily calculated nowadays by well established engineering handbooks (e.g. Young and Budynas, 2002).

Where a cross section consists of several individual plate elements, seeking closed-form solutions to the local buckling stress becomes difficult, if not impossible. This is mainly due to the interaction effect amongst those constituent plate elements (Murray, 1986). With the advance of modern computational technology, numerical tools can usually be effectively used to overcome the problem. For example, Lee et al. (1996) studied the local buckling of 'I' sections with web stiffeners under shear by using numerical methods. They found that the effect of elastic constraint at the web-flange junction lines on the web buckling stress was influenced by the flange to web thickness ratio. Alinia and Moosavi (2008) performed a series of numerical studies on the local buckling behaviour of stiffened steel plates under in-plane bending, and identified the optimum locations and dimensions of stiffeners to resist the local buckling failure.

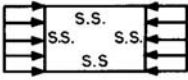
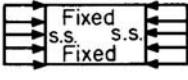
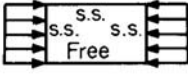
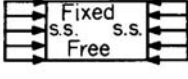
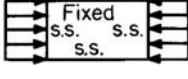
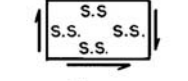

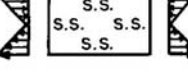
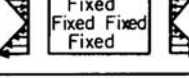
Case	Boundary condition	Type of stress	Value of k for long plate
(a)		Compression	4.0
(b)		Compression	6.97
(c)		Compression	0.425
(d)		Compression	1.277
(e)		Compression	5.42
(f)		Shear	5.34
(g)		Shear	8.98
(h)		Bending	23.9
(i)		Bending	41.8

Table 2-1 Local buckling coefficient for a long rectangular plate, after Timoshenko and Gere  
(1961)

### 2.2.2 Distortional buckling

Distortional buckling is another commonly observed buckling mode in CFS flexural members. The key characteristic of this buckling mode is that the compression flange and lip rotate together about the compression web-flange junction line, and the web will deflect in a double curvature (Hancock, 1997), as illustrated in Fig. 2-2. The buckling half-wavelength is longer than that of

local buckling but shorter than the member length. The compression web-flange junction may either translate in the direction normal to the web or remain straight, which depends on the flange width to web depth ratio (Lau and Hancock, 1987).

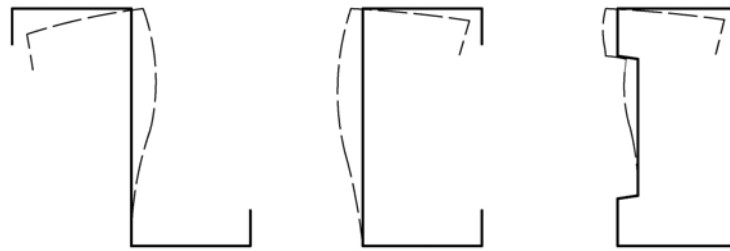


Figure 2-2 Distortional buckling of CFS Z, C and sigma sections

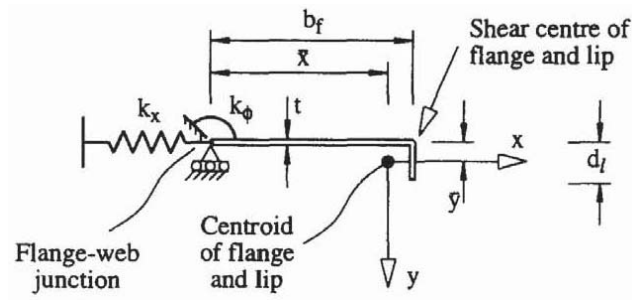
Like local buckling, studies on distortional buckling have also been well documented. Hancock (1985) started to use the term ‘distortional buckling’ in analysing CFS sections and discussed the distortional buckling behaviour of CFS columns by using a numerical method. Lau and Hancock (1987) subsequently developed a computational model for determining distortional buckling stress of CFS columns. Hancock (1997) later extended the model to determine the distortional buckling stress of CFS beams. Teng et al. (2003) employed the model for determining the distortional buckling stress of CFS beam-columns. This popular computational model is shown in Fig.2-3 (a), where a compression flange and lip section is torsionally and translationally restrained at the flange-web junction by one rotational spring (with the stiffness  $k_{\phi}$ ) and one translational spring (with the stiffness  $k_x$ ), respectively. The flange-lip section is assumed to be non-deformable. The two springs represent the restraining effects of the web on the flange. In doing so, distortional buckling of a CFS beam is transformed to flexural buckling of a column

resting on an elastic foundation represented by a series of springs. Since the problem of flexural buckling of columns resting on an elastic foundation has been well studied (Timoshenko and Gere, 1961), the distortional buckling of the flange-lip section can be analysed accordingly as long as the elastic spring stiffness can be determined. The restraining effect of the web plate, i.e. both spring constants, can be analysed by treating the entire cross-section as a generalised plane strain structure. In doing so, a roller support is introduced at the compression end of the web and a fixed support at the tension end is assumed (see Fig. 2-3 a). By assuming that  $k_{\phi}$  is the rotational stiffness from the web plate, Hancock (1997) proposed a formula to calculate  $k_{\phi}$ . It allowed for a reduction in  $k_{\phi}$  due to the in-plane stress in the web but assumed that the compression flange is rigid. They found that the translational stiffness provided by the web had little influence on the distortional buckling stress and thus suggested that it can be considered to be rigid.

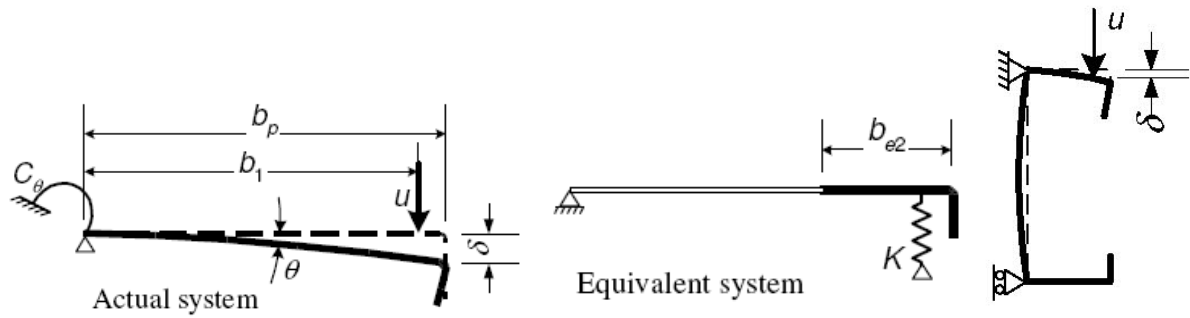
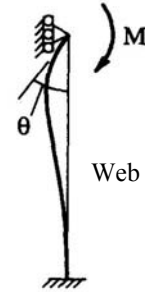
BSI (2006a) presented a different computational model, as shown in Fig. 2-3(b), to determine the distortional buckling stress of CFS beams. This model also considers the flange-lip section. The rotational restraining effect by the web is considered by a fictitious elastic spring placed at the centroid of the section. A generalised plane strain model is adopted for the cross section to determine the spring stiffness  $K$ . The calculation procedure is as follows: firstly, place a pin and roller supports at the junction lines between the web and compression and tension flanges respectively (see Fig. 2-3 b); secondly, apply a unit load  $u$  at the centroid of the compression/lip section and then calculate the induced deflection  $\delta$  at the load application point; lastly, determine the  $K$  value by  $u / \delta$ . Once the  $K$  value is calculated, the distortional buckling stress of the beam

on the elastic spring support can be calculated in a similar way to Hancock (1997)'s approach. The  $K$  value in BSI (2006a)'s model ignores the stiffness reduction due to the in-plane stress in the web but allows for the flexural stiffness of both the web and compression flanges. Another feature in the BSI (2006a)'s model is that it can easily allow for the interaction effect between local and distortional buckling.

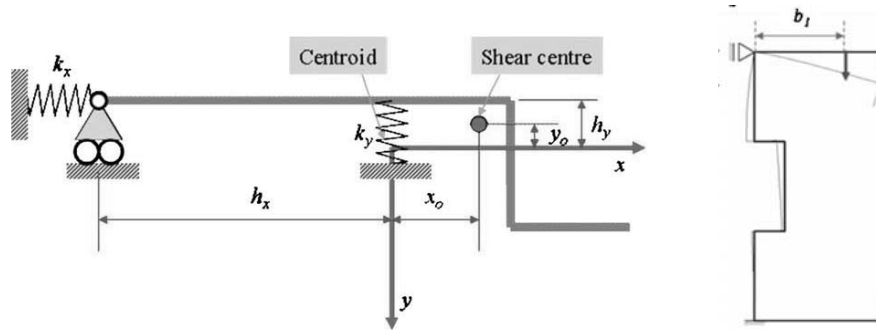
On the basis of the previous two models, Li and Chen (2008) proposed an improved computational model for determining distortional buckling stress of CFS beams. The improved model is similar to Hancock (1997)'s but follows the BSI model by treating the rotational spring as an equivalent lateral spring support at the centroid, as shown in Fig. 2-3(c). Li and Chen derived a formula for the spring stiffness allowing for not only the flexural stiffness of both the web and compression flanges but also the stiffness reduction due to the in-plane stress in the web. By comparing with the prediction from numerical methods, they reported that Hancock's model can produce unsafe predictions, whereas BSI's model can produce conservative predictions. It was claimed that their new model can produce predictions with better accuracy. The same paper also suggested using a roller support at the compression web-flange junction and a fixed support at the tensile web-flange junction in determining the elastic stiffness for sigma sections (see Fig. 2-3 c).



(a) Hancock (1997)'s model



(b) BSI (2006a)'s model



(c) Li and Chen (2008)'s model

Figure 2-3 Analytical models for determining distortional buckling stress of CFS purlins

The above mentioned research is applicable for a beam under uniform bending. For determining the distortional buckling stress of a beam under other loading conditions, numerical methods are usually adopted. For instance, Chu et al. (2005, 2006) numerically studied the elastic local



buckling and distortional buckling behaviour of CFS C and Z beams under uniformly distributed loads. It was found that for C and Z beams of commonly used sections, the presence of moment gradient has insignificant influence on their critical local buckling stress but has appreciable beneficial influence on their critical distortional buckling stress. Yu and Schafer (2007) performed a numerical analysis on the elastic distortional buckling behaviour of CFS C and Z sections under moment gradient. Similar conclusions were obtained. It is noted that unlike the simplified model used in analytical methods, the analysis by numerical methods can be performed on the basis of the whole cross section.

### 2.2.3 Lateral torsional buckling

In the absence of sufficient lateral bracing, CFS flexural members bent in their major planes are susceptible to lateral torsional buckling (LTB). The occurrence of LTB is primarily due to the relatively low lateral flexural stiffness and torsional stiffness of CFS sections. The LTB behaviour of CFS flexural members (Yu, 2000) involves lateral deflection and simultaneous rotation of the cross section, as illustrated in Fig. 2-4, with the buckling half-wavelength in the order of the length between effective supports.

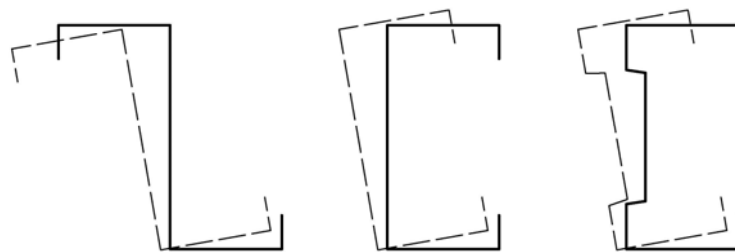


Figure 2-4 Lateral torsional buckling of CFS Z, C and sigma purlins

The critical LTB moment of a beam is influenced by a variety of parameters, e.g. cross-sectional properties, moment gradient and boundary conditions of the beam (Trahair, 1994). Based on differential equilibrium equations, Timoshenko and Gere (1961) analytically derived the critical LTB moment of double symmetric sections in uniform bending. The theoretical solution is known as:

$$M_{cr} = \sqrt{\frac{\pi^2 EI_z}{l^2} (GJ + \frac{\pi^2 EI_w}{l^2})} \quad (2-2)$$

In Eq. (2-2),  $E$ ,  $G$ ,  $I_z$ ,  $J$ ,  $I_w$ , and  $l$  are elastic modulus, shear modulus, second moment of area about minor axis, torsion constant, warping constant, and length of the beam, respectively. It is noted (Hancock, 2008) that Eq. (2-2) is also applicable for mono-symmetric sections, e.g. C and sigma sections, uniformly bent about their symmetric axis. Based on differential equilibrium equations and the energy method, respectively, Trahair (1993) analytically demonstrated the critical LTB moment of mono-symmetric sections uniformly bent in their symmetric planes. The theoretical formula is given by

$$M = M_{cr} \sqrt{[1 + (\frac{\pi^2 \beta_x EI_z}{2l^2 M_{cr}})^2] + \frac{\pi^2 \beta_x EI_z}{2l^2 M_{cr}}} \quad (2-3)$$

where  $\beta_x$  is a mono-symmetry property of the cross section; the rest of the symbols have the same denotation as those in Eq. (2-2). Trahair suggested that Eq. (2-3) is also applicable for asymmetric sections uniformly bent in their major planes. When moment gradient is present, closed form solutions for critical LTB moment can become very complicated, and thus they are not viable for practical applications. Based on extensive numerical analysis, Trahair (1993) provided the approximate expression for critical LTB moment of sections allowing for the effect of moment gradient. The expression is as shown below:

$$M_m = \alpha_m M_{cr} \quad (2-4)$$

where  $\alpha_m$  is an equivalent uniform moment distribution factor and  $M_{cr}$  is calculated by using (2-2). The numerically determined  $\alpha_m$  values for a number of practical loading cases are summarized in Table 2-2. By introducing this factor, the calculation for the critical LTB moment allowing for moment gradient is greatly facilitated.


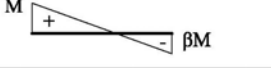
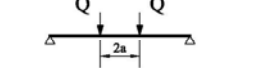
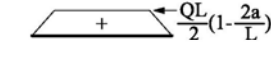
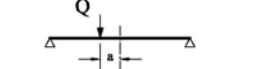

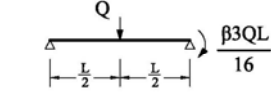
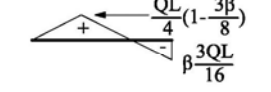
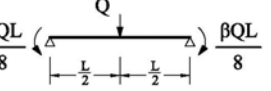
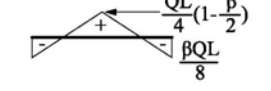
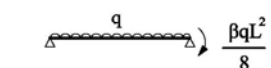

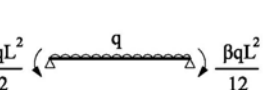
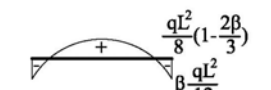
Beam Segment	Moment Distribution	$\alpha_m$	Range
		$1.75+1.05\beta+0.3\beta^2 \geq 2.5$	$-1<\beta<1$
		$1.0+0.35(1.0-2a/L)^2$	$0<2a/L<1$
		$1.35+0.4(2a/L)^2$	$0<2a/L<1$
		$1.35+0.15\beta$ $-1.2+3.0\beta$	$0<\beta<0.89$ $0.89<\beta<1$
		$1.35+0.36\beta$	$0<\beta<1$
		$1.13+0.10\beta$ $-1.25+3.5\beta$	$0<\beta<0.7$ $0.7<\beta<1$
		$1.13+0.12\beta$ $-2.38+4.8\beta$	$0<\beta<0.75$ $0.75<\beta<1$

Table 2-2  $\alpha_m$  in various loading cases, after Trahair (1993)

However, the values of  $\alpha_m$  in Table 2-2 were all derived on the basis of doubly symmetric sections. Therefore theoretically, they are not applicable for mono-symmetric CFS sections. To obtain both accurate and computational-friendly results, finite element method is normally adopted for the critical LTB moment of mono-symmetric CFS sections with account of moment

gradient. Kurniawan and Mahendran (2009) provided a good worked example which demonstrated this point.

#### 2.2.4 Localised buckling due to in-plane concentrated load

Thin plates are susceptible to localized buckling when they are subjected to in-plane concentrated loads. The typical concentrated loads to which plates may be subjected include the following three applications (BSI, 2006b):

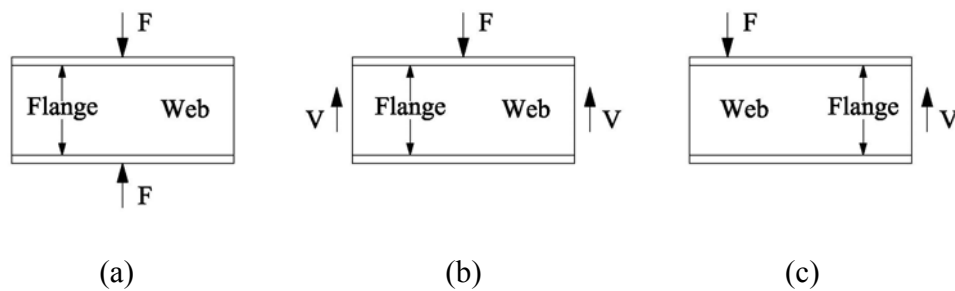


Figure 2-5 Plates subjected to in-plane concentrated loads

In Fig. 2-5 (a), a pair of equal and opposite concentrated loads act on both edges of a web plate. Fig. 2-5 (b) and (c) show a single concentrated force applied on one edge of the web plate and is balanced by the shear force along sections away from the load application point. Research has been documented for determining the critical localized buckling load of plates loaded in the above three scenarios. For example, based on the energy method, Timoshenko and Gere (1961) studied the critical buckling load of rectangular plates loaded for the case shown in Fig. 2-5(a). By using numerical methods, Rockey and Bagchi (1970) and White and Cottingham (1962) studied the critical buckling load of rectangular plates loaded as in the cases shown in Figs. 2-5(b

& c), respectively. BSI (2006b) has provided a calculation method for the critical buckling load of web panels with or without web stiffeners.

## 2.3 POST-BUCKLING STRENGTH

The occurrence of local buckling can reduce the stiffness of a plate (Bulson, 1970), but it does not normally lead to an immediate failure of the plate. Following the initial buckling, the plate is able to continue to carry more loads. This additional strength following the initial buckling is known as the post-buckling strength. The principal mechanism (Yu, 2000) of post-buckling strength is that once the plate starts to buckle, transverse fibres in the plate will develop a membrane action to reduce the out-of-plane deflections of longitudinal fibres, as shown in Fig. 2-6.

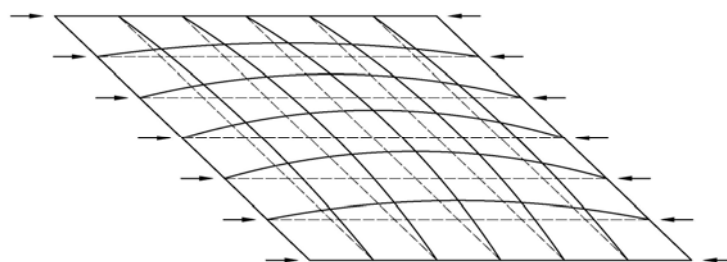


Figure 2-6 Schematic diagram of post-buckling action, after Yu (2000)

One effect of the post-buckling behaviour is that the stress induced in the plate will be redistributed, i.e. the high stress zone will be shifted from the centre to supporting edges. Plate components forming CFS sections can be categorized as two-edge supported plates (internal

plates) or one-edge supported plates (outstand plates), e.g. flanges and lips shown in Fig. 2-1, respectively. The post-buckling strength of an internal plate was analysed by von Karman et al. (1932). It was discovered that for a compression plate, a uniformly distributed stress in the pre-buckling stage will be redistributed into a non-uniformly distributed stress in post-buckling stage, as illustrated in Fig. 2-7. Based on this observation, von Karman et al. referred to the width of the high stress zone as the “effective width”. Following the work by von Karman et al., Peköz (1987) studied the post-buckling behaviour of internal plates under in-plane bending. Kalyanaraman et al. (1977) and Bambach (2006) studied the post-buckling behaviour of outstand plates under compression and in-plane bending, respectively. It was found that the plates in these load cases all exhibited appreciable post-buckling strength and the stress redistribution patterns are similar to those shown by von Karman et al. (see in Fig. 2-7), i.e. a shift toward the supporting edge region.

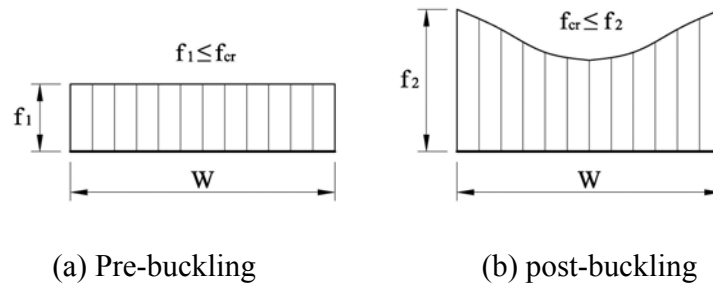


Figure 2-7 Stress distribution in an edge stiffened compression plate, after von Karman et al.

(1932)

More recently, research on post-buckling behaviour of CFS beams has been extended from the constituent plate level to the member level. Prola and Camotim (2002) and Dinis and Camotim

(2010) reported a series of numerical studies on distortional post-buckling behaviour of CFS C beams. Both papers state that although distortional buckling mode has relatively less post-buckling strength than that of local buckling, it is still worth considering. In contrast, it has been well acknowledged (Yu, 2000) that little post-buckling strength can be developed in the case of LTB.

## 2.4 ULTIMATE STRENGTHS OF CFS FLEXURAL MEMBERS

Because of the above mentioned premature buckling, the strengths of CFS flexural members will usually be lower than their elastic moment resistance. Failure of these members can be a result of an individual buckling mode as discussed previously or a mixture of buckling modes. Due to the complexity involved, studies for the flexural strength of CFS members are normally carried out by using experimental and numerical methods.

The flexural failure of CFS members predominantly caused by local buckling has been extensively investigated by many researchers, whose research covers various types of load cases and cross sections. Winter (1947) and Peköz (1987) experimentally studied the local buckling resistance of the compression flange of a hollow section, under uniform compression and a stress gradient. Kalyanaraman et al. (1977) and Bambach and Rasmussen (2004a) studied the local buckling resistance of the compression flange of an unlipped channel section, also under uniform compression and stress gradient. Desmond et al. (1981a) and Yu and Schafer (2003) carried out a series of four-point bending tests to study the local buckling resistance of CFS sections with lipped flanges. Desmond et al. specifically investigated the effect of lip length on the local

buckling resistance, while the study of Yu and Schafer was focused on the performance of the web in the compression zone. Desmond et al. (1981b) and Papazian (1994) experimentally studied the local buckling resistance of CFS sections with one or multiple intermediate stiffeners in the compression flange. Yu and Schafer (2006a) studied the influence of moment gradient on the local buckling resistance of CFS sections. It was found that the moment gradient has an insignificant influence on the ultimate strength because of the short half-wavelength of the local buckling mode. The above mentioned studies have all observed a significant post-buckling strength in local buckling mode.

The research work with regards to the distortional buckling resistance of CFS flexural members is mostly focused on C and Z sections. Moreyra and Peköz (1993), Roger (1995) and Hancock (1996) respectively reported experimental studies for the distortional buckling behaviour of laterally restrained C and Z sections in uniform bending. Yu and Schafer (2006b) experimentally studied the distortional buckling resistance of laterally unrestrained C and Z sections in uniform bending. Yu and Schafer (2007) numerically studied the distortional buckling resistance of laterally unrestrained C and Z sections subjected to varying bending moment. Schafer and Peköz (1999) numerically studied the distortional buckling resistance of laterally restrained sections with lipped flanges in a uniform bending. The study was focused on the behaviour of flange-lip sections. From these studies, it has been found that the distortional buckling resistance of CFS flexural members can be positively influenced by the presence of lateral movement restraints and the moment gradient. The post-buckling strength in distortional buckling mode is of less importance compared with that in local buckling mode.



A small amount of research has been carried out to experimentally study the lateral torsional buckling resistance of unbraced and intermediately braced CFS flexural members. Djugash and Kalyanaraman (1990) experimentally studied the LTB resistance of unbraced sigma and Z sections under uniform bending. Ellifritt and Haynes (1992) experimentally studied the LTB resistance of intermediately braced C and Z sections under uniform bending. Put et al. (1999a, 1999b) experimentally studied the LTB resistance of unbraced C and Z sections under mid-span point loading. The existing research reveals that the LTB performance of CFS sections differs from that of hot-rolled sections because of their different cross-sectional shapes and dimensions and manufacture methods. Furthermore, it was demonstrated that little post-buckling strength can be gained in LTB mode. From the literature survey, it is noted that there is no reported study regarding the LTB resistance of intermediately braced sigma sections under the mid-span point loading.

For those CFS members whose elastic critical loads of the three basic buckling modes are close, the failure of the members can be as a result of the interaction of various buckling modes (Schafer, 2002). It is known (Schafer, 2008) that the interaction effects can reduce the resistance of the members from that governed by a single buckling mode. A number of studies pertinent to the influence of the interaction effects on the resistance of CFS compression members have been performed (Yang and Hancock, 2004; Dinis et al., 2007). In contrast, the studies for that of CFS flexural members are relatively scarce. Furthermore, these limited studies are mostly focused on local and lateral torsional buckling interaction (Lindner and Aschinger, 1994; Batista, 2010). Very recently, Dinis and Camotim (2010) performed a numerical analysis to study the strength of uniformly bent CFS C sections which failed in local and distortional buckling interaction. It is

worth noting that a study for the resistance of CFS sigma beams failing in buckling mode interactions has yet to be reported.

Under concentrated loads as shown in Fig. 2-5 (a), (b) and (c), CFS sections may fail due to web crippling at the loading points. A number of investigations have been carried out to study the web crippling resistance of CFS sections. This research includes: Hetrakul and Yu (1978) and Rhodes and Nash (1998) who studied the web crippling resistance of CFS sections with unstiffened webs (such as C, Z and hat sections) by using experimental methods and numerical methods, Young and Hancock (2001) who experimentally studied the web crippling resistance of unlippped C sections and Graciano and Edlund (2003) who reported an experimental study on the web crippling resistance of plate girders with a longitudinal web stiffener. However, the literature survey reveals that research regarding the web crippling resistance of CFS sigma sections has not yet been publicly reported.

Although much research (Yoo and Lee, 2006) has been reported for hot-rolled flexural members, the shear buckling resistance of CFS flexural members, however, has been reported less frequently. One possible reason is that shear buckling rarely governs the strength of a CFS flexural member in engineering practice. LaBoube and Yu (1978a) experimentally studied the structural behaviour of short CFS sections subjected to shear force. The post-buckling strength of web under shear buckling was qualitatively discussed. Stein (1985) numerically studied the post-buckling strength of rectangular plates under shear buckling and found that in-plane restraints of the plates can highly influence the level of post-buckling strength. Based on the results from the

previous studies, Hancock (2001) stated that the web sections may not develop significant post-shear-buckling strength due to insufficient restraint provided by the flanges.

For continuous beams, high bending moment and shear act simultaneously at internal supports. The combined bending and shear action can lead to a further reduction in the flexural resistance of the section at any internal support. The reduced resistance of hot-rolled sections under bending and shear interaction has been well studied (Yu, 2000). On the other hand, similar research on CFS sections is rather limited. Three decades ago, LaBoube and Yu (1978b) reported an experimental study for the loading resistance of CFS sections (C sections) under bending and shear interaction. Since then little research has been reported until very recently, when Pham and Hancock (2010a, 2010b) experimentally and numerically studied the loading resistance of C sections made of high yield stress steel ( $550\text{N/mm}^2$ ) under bending and shear interaction, based on similar testing as used by LaBoube and Yu (1978b). The results were used to compare with the predictions suggested by codes of practice. Recommendations were proposed for the design method of C sections under combined bending and shear actions.

When bending moment and concentrated load occur simultaneously at the same location, the joint action can also lead to a reduced loading resistance of the section at this critical location. Studies for the influence of this joint effect on the flexural resistance of CFS members are mainly concentrated on the development of design rules based on regression analysis from experimental and numerical results (Hancock, 2001). The examples of these studies include Hetrakul and Yu (1978), Young and Hancock (2002) and Ren et al. (2006). Because of their empirical nature, the developed design methods are only valid for those studied specimens under the specified loading

conditions. Like the web crippling resistance of CFS sigma sections, research into the resistance of CFS sigma sections under a combined bending and concentrated load is also not currently available.

## 2.5 ELASTIC DESIGN METHODS

The strength calculations of flexural CFS members are usually based on one of two elastic design methods, i.e. Effective Width Method (EWM) or Direct Strength Method (DSM). The former is widely accepted and adopted in current codes of practice including Eurocodes (BSI, 2006a), North American specification (AISI, 2007) and Australian and New Zealand standard (Standards Australia, 2006). The latter is recommended as an alternative method in AISI (2007) and Standards Australia (2006).

EWM was initially introduced by von Karman et al. (1932) to consider the post-buckling stress redistribution of stiffened plates (see section 2.3). Assuming that the plate will reach its ultimate strength when the stress at the edge reaches the yield stress, as shown in Fig. 2-8 (a), von Karman et al. assumed that the failure load is carried by an effective width,  $b$  under uniformly distributed stress equal to the yield stress of the steel (see Fig. 2-8 (b)). The assumption can be written mathematically as:

$$t \int_0^w f dx = t b f_y \quad (2-5)$$

where  $f$  is the real direct stress distribution with respect to the distance from the edge of the plate and  $t$  is the thickness of the plate. Therefore for a long stiffened plate, the theoretical value of  $b$  can be determined from Eq. (2-1) as:

$$b = \frac{\pi t}{\sqrt{3(1-\nu^2)}} \sqrt{\frac{E}{f_y}} \quad (2-6)$$

Based on Eq. (2-1) and (2-6), the relationship between the effective width  $b$  and full width  $w$  of the plate thus can be established as:

$$\frac{b}{w} = \sqrt{\frac{f_{cr}}{f_y}} \quad (2-7)$$

After extensive experimental investigations conducted by Winter et al. in 1947, the design formula for the effective width of stiffened plates under uniform compression taking account of imperfections has been well developed and codified in most standards adopting the EWM, which is:

$$\frac{b}{w} = \sqrt{\frac{f_{cr}}{f_y}} (1 - 0.25 \sqrt{\frac{f_{cr}}{f_y}}) \quad (2-8)$$

For the sake of convenience, Eq. (2-8) is usually written in the form of

$$b = \rho w \quad (2-9)$$

where  $\rho$  is the reduction factor of the full width of the plate. Based on the same theory and experimental investigations by many other researchers (Peköz, Desmond, Bambach and Rasmussen) the reduction factors for the effective width of plates, stiffened or unstiffened, subject to uniform compression or stress gradient, with one or multiple intermediate stiffeners, have also been developed and codified.

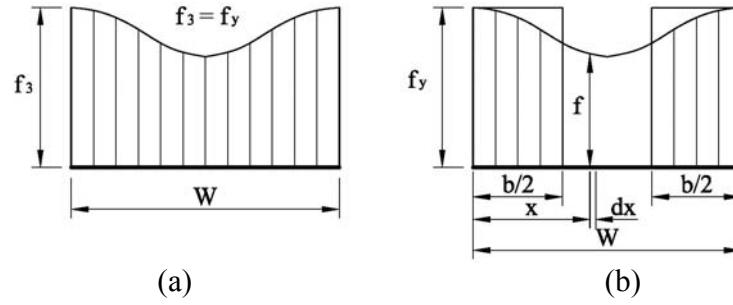


Figure 2-8 Rationale of EWM, after Yu (2000)

It can be seen that EWM is an elemental method, i.e. treating plate components of CFS sections individually. Therefore, EWM can become laborious in designing complex sections, e.g. sections with intermediate stiffeners. To overcome this shortcoming, DSM was developed by Schafer and Peköz (1998a). DSM was developed on the basis of gross cross section. The fundamental assumption behind DSM is that the strength of a CFS member can be directly determined by calculating the elastic buckling and first yield moment for the gross cross section (Schafer, 2008). This assumption can be mathematically expressed as following:

$$M_{Rd} = f(M_{cr,l}, M_{cr,d}, M_{cr,LTB}, M_y) \quad (2-10)$$

where  $M_{Rd}$  is the moment resistance of a member;  $M_{cr,l}$ ,  $M_{cr,d}$ , and  $M_{cr,LTB}$  are, respectively, elastic critical local buckling moment, elastic critical distortional buckling moment and elastic critical lateral torsional buckling moment for the gross cross section;  $M_y$  is the first yield moment of the gross cross section. The calculations of these basic variables can be accomplished by numerical methods (Schafer and Ádány, 2006). Subsequently, the member resistance can be directly obtained by applying simple empirically determined formulae. The effort required in performing effective width calculations for plate components can thus be avoided.

A representative design code in the application of EWM for CFS members is BSI (2006a), which was specifically developed to consider not only local buckling but also distortional buckling and interaction effect between two buckling modes. Currently DSM is only formally adopted by AISI (2007) and Standards Australia (2006) to design CFS members. The design procedures of DSM in these two codes are effectively identical. The design procedures of the EWM in BSI (2006a) and the DSM in AISI (2007)/Standards Australia (2006) are detailed in Appendix I and II, respectively. It is worth noting that the design equations in the DSM are all empirically determined. As a result, the applicable sections are listed in AISI (2007)/Standards Australia (2006). Unfortunately, sigma sections are not included in these sections. To apply DSM to design CFS Sigma sections, experimental validation is therefore needed.

## 2.6 PLASTIC DESIGN METHODS

In contrast to elastic design methods, plastic design methods allow for the use of strength reserve of structures beyond their elastic stage, which can provide a more economic design. It is worth distinguishing between the design based on the plastic cross-sectional strength and the plastic analysis method. The former takes into account the cross-sectional plastification of individual members but ignores the presence and the effect of plastic hinges; while the latter considers the moment redistribution as a result of emerging plastic hinges, which is only applicable to statically indeterminate structures. Plastic design methods based on plastic analysis can be classified into conventional plastic method (e.g. for hot-rolled steel structures), pseudo plastic method (e.g. for thin-walled steel structures), and yield line method for plate/shell structures.

### 2.6.1 Conventional plastic design method for hot-rolled steel structures

For a hot-rolled steel section consisting of stocky plate elements, a plastification process of the cross section under increasing bending moment is known (Timoshenko, 1956), as shown in Fig. 2-9. At a low bending moment, the maximum stress  $f$  and strain  $\varepsilon$  in the cross section are smaller than the yield stress  $f_y$  and yield strain  $\varepsilon_y$ . The cross section performs in an elastic stage. When the bending moment increases to first yield moment  $M_y$ , the extreme fibres of the cross section yield and the cross section commences plastification. As bending moment further increases, the plastic zone continues to grow until reaching the neutral axis. The stress in the plastic zone remains as the yield stress  $f_y$ . When the bending moment increases to plastic moment  $M_p$ , the whole cross section yields and thus is in a fully plastic stage. This plastification process can also be represented by the moment-curvature relationship of a cross section, as shown in Fig. 2-10, where points A, B, C and D correspond to a random point in the elastic region, first yield, partial plastic region and the onset of being fully plastic, respectively.

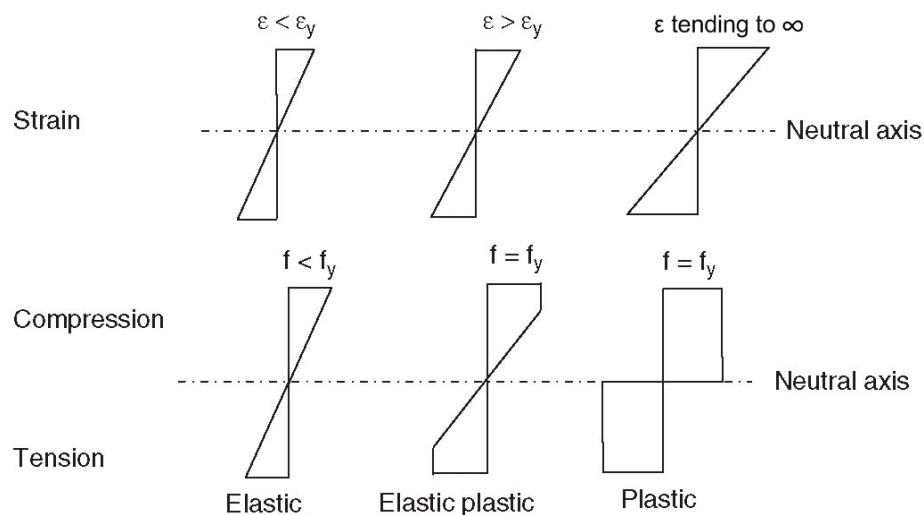


Figure 2-9 Plastification of a cross section



According to the moment–curvature relationship shown in Fig. 2-10, the full plastic cross section (beyond point D) experiences large plastic rotation at a constant bending moment  $M_p$ . This behaviour provides a mechanism to develop plastic hinges. In conventional plastic design, a structure can carry loads until the formation of a sufficient number of plastic hinges creates a collapse mechanism. To develop collapse mechanisms, plastic hinges are therefore required to undergo significant plastic rotation to allow for the redistribution of moments. As a result, plastic moment  $M_p$ , plastic hinge and plastic rotation capacity of the hinge become the key elements in conventional plastic design. Plastic hinges are assumed to be developed over an infinitesimal length and the rotation capacity of plastic hinges is usually evaluated in terms of curvature. The utilisation of the moment redistribution facilitated by the plastic hinges can only be allowed when the cross section has a sufficiently large plastic curvature capacity (Timoshenko, 1956).

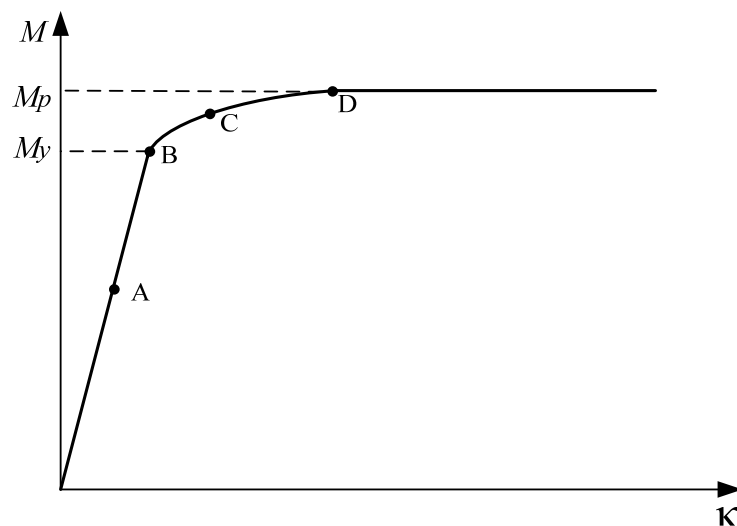


Figure 2-10 Moment-curvature relationship of a cross section

The number of plastic hinges required to form a collapse mechanism is related to the degrees of indeterminacy of the structure. The locations of the plastic hinges are related to the moment distribution and can be determined by elastic analysis or any rational engineering judgement. Provided that plastic hinges have adequate plastic rotational capacity, conventional plastic design can be carried out by an elastoplastic approach or rigid plastic approach in determining the collapse load of the structure. The procedures for obtaining plastic hinges, plastic moment, and performing elastoplastic approach and rigid plastic approach can be readily found in textbooks, e.g. Wong (2009), and so they are not detailed further in this thesis.

It is worth mentioning that unless using an advanced nonlinear method, the effect of lateral torsional buckling of the structure is not considered in plastic design (Davies and Brown, 1996). Therefore steel flexural members designed using the plastic design method should be provided with adequate lateral and rotational restraints to prevent lateral torsional buckling. Furthermore, the steel material should be ductile enough to undergo plastic deformation without fracture. In design practice, the beneficial effect of strain hardening of the steel material is normally ignored when the plastic design method is used, the nonlinearity in section BD of the moment-curvature relationship shown in Fig. 2-10 is usually ignored, and the bending moment is assumed to increase linearly from  $M_y$  to  $M_p$ .

Although the conventional plastic method provides more economic results than the elastic methods, it has a limitation. For instance, as plastic hinges must be able to sustain a constant plastic moment  $M_p$ , the conventional plastic method is only applicable to compact cross sections (or class 1 and class 2 cross sections in BSI, 2005a). As practical CFS sections are usually non-

compact (e.g. class 3 and class 4 cross sections defined by BSI, 2005a), the conventional plastic method cannot be directly employed to design CFS sections.

In studying the cross-sectional moment resistance, some CFS sections with relatively small slenderness ratios have been noticed to have a partial plastic capacity, which exceeds the first yield moment value but is below the plastic moment value (Reck et al., 1975). According to the cross section classification rules in BSI (2005a), this type of section should be classified as class 3. As the conventional plastic method was not applicable, Yener and Pekoz (1983) proposed an alternative method to employ the inelastic reserve strength. By carrying out experiments, they developed an empirical ultimate compressive strain criterion for the sections with compression flanges stiffened by stocky webs. Using this criterion, the partial plastic moment and rotation capacity of the sections can be semi-empirically derived. Subsequently the inelastic load resistance of beams made of these sections can be analytically determined (Yener and Pekoz, 1985a, 1985b). Bambach and Rasmussen (2004a) extended this maximum strain method to the sections with unstiffened elements of a similar nature. Very recently, based on the maximum strain method, Shifferaw and Schafer (2008) proposed design formulae to evaluate the partial plastic strength of class 3 C and Z sections. BSI (2006a), AISI (2007) and Standards Australia (2006) also provide design equations to calculate the partial plastic strength of class 3 CFS sections.

#### 2.6.2 Pseudo plastic design method

Most CFS sections are class 4 sections, with moment resistance lower than their first yield moment due to premature buckling. A typical moment-rotation relationship of a single-span CFS

beam (Kotelko, 2004) can be schematically represented by the curve in Fig. 2-11. Three distinct stages can be identified from this curve, i.e. the linear elastic, the nonlinear stable post-buckling and the softening unstable post-failure stages. In the first stage, the cross section is fully effective, and as such the beam exhibits a linear elastic behaviour. On the initiation of any buckling mode, the cross section gradually loses stiffness and therefore the moment-rotation curve starts to become nonlinear. In this stage, the section can still carry increasing loads due to the post-buckling strength. As large buckling deflection develops, material starts to yield and once sufficient material yields within a cross section, it ceases to carry any more loads and reaches the ultimate failure point. Beyond this point, the section develops a localised collapse mechanism and gradually loses moment resistance.

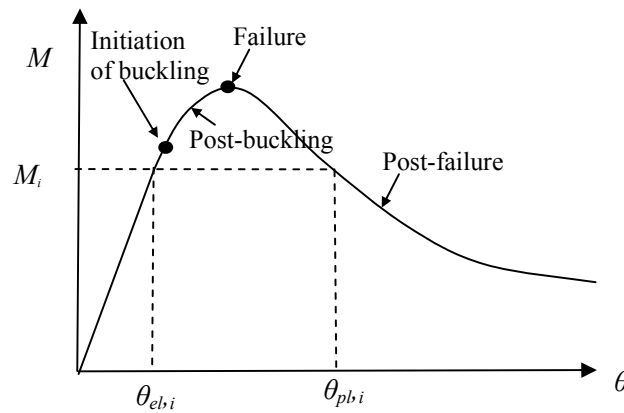


Figure 2-11 Schematic diagram of moment-rotation curve of a single-span CFS beam

In continuous CFS beams, thanks to the possession of post-failure strength of cross sections, sections over the failed zone near the internal supports can continue to develop rotation at a reduced moment level. This structural behaviour makes the moment redistribution possible and as

a result, the beams are capable of carrying additional loads following the sections near internal supports reaching their ultimate level. Moore and Sims (1988) observed this inelastic resistance of continuous CFS beams in a series of full scale tests on class 4 C, Z and sigma sections. It was found that due to the moment redistribution, the ultimate load of the continuous CFS beams was about 2.2 times their working load, which was much higher than that expected by using the elastic method. Davis and Raven (1986) proposed a pseudo-plastic method to make use of the strength reserve in CFS sections. As mentioned above, the advantage of the pseudo-plastic method is to allow the continuous beam to develop a pseudo-plastic hinge near the internal support so that the cross section in the sagging zone can reach the full moment resistance. To this end, adequate rotation capacity of the pseudo-plastic hinge is required. The rotation capacity  $\Theta_i$ , to sustain the reduced bending moment,  $M_i$ , can be derived as  $\Theta_i = \theta_{pl,i} - \theta_{el,i}$ , as indicated in the moment-rotation curve in Fig. 2-11. Hence the moment against available rotation capacity ( $M-\Theta$ ) can be plotted as the solid line curve in Fig. 2-12. The formed pseudo-plastic hinge subsequently allows the system to develop moment redistribution. Assuming the continuous beam will lose load resistance when the cross section in the sagging zone reaches its elastic moment resistance  $M_{c,Rd}$ , another  $M-\Theta$  curve for the required rotation from the pseudo-plastic hinge can be plotted as the dotted curve in Fig. 2-12. The interception point of two curves then yields the value of pseudo-plastic moment resistance (PPMR),  $M_{pp}$ . The corresponding  $\Theta$  value is defined as pseudo-plastic rotation (PPR)  $\Theta_{pp}$ . Provided that PPMR and PPR are obtained, the inelastic load resistance of the continuous beam can be quantified by general elastic analysis.

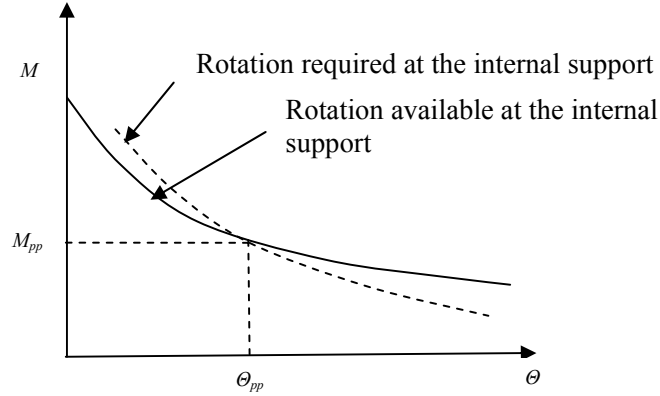


Figure 2-12 Determination of the pseudo-plastic moment resistance  $M_{pp}$

From Fig. 2-12 it can be seen that the required and available rotation curves at the internal support are crucial in obtaining PPMR and PPR. The former can be approximately estimated by elastic beam analysis (Davis and Raven, 1986). For a double span continuous beam under uniformly distributed load, the required rotation curve can be calculated by the following equation:

$$\Theta = \left( 2 + 2 \sqrt{1 + \frac{M}{M_{c,Rd}}} - \frac{3M}{M_{c,Rd}} \right) \frac{LM_{c,Rd}}{6EI_{eff}} \quad (2-11)$$

where  $L$  is the span length;  $I_{eff}$  is the effective second moment of area at the yield stress level;  $M_{c,Rd}$  is the cross-sectional moment resistance. The derivation of Eq. (2-11) is presented in Appendix III. The determination of the latter, however, has to be accomplished by experiment. The test programme in determining the available rotation curve is provided in BSI (2006a) to facilitate the pseudo-plastic design method. This test programme was used by Davis and Raven (1986) to demonstrate the validity of the pseudo-plastic method. In the study by Davis and Raven, the moment-rotation relationship of a sigma beam near an internal support was presented, and the moment level with a  $3^\circ$  rotation capacity was chosen as the PPMR. Using the same test

programme, Laine and Tuomala (1999) investigated the moment-rotation relationship of C, Z, Zeta and Hat shaped beams at internal supports.

As with the conventional plastic method, the pseudo-plastic method requires the members to be properly restrained against failure by LTB, and the steel material having sufficient ductility to develop local plastic mechanisms without any fracture. Additionally, it is worth mentioning that unlike the conventional plastic method which assumes that plastic hinges occur over an infinitesimal length, the pseudo-plastic method assumes that any plastic hinge takes place in a plastic zone over a finite length, and the moment-rotation relationship should be examined instead of the moment-curvature relationship. The reason for doing so is that the former assumption can lead to the violation of deformation compatibility when non-compact sections are considered, as suggested by Grundy (1990).

### 2.6.3 Yield line method

The yield line method is another tool used to analyse the plastic behaviour of plated structural members made of elastic-plastic material. This method was originally developed by Johansen (1962) for the limit design of reinforced concrete slabs. Later Murray and Khoo (1981) used it in analysing collapse behaviour of CFS sections. More recently, Ungureanu and Dubina (2004) adopted it in a study to determine the collapse load of CFS sections. The yield line method assumes that a plastic collapse mechanism of a section is composed of rigid plate segments connected by zero-width yield lines; and work done by the bending moment along yield lines is equal to the work done by forces in regions bounded by these yield lines by following kinematic rules. As the method is based on the kinematic theorem of the plastic theory of structures, it

produces an upper bound prediction for the collapse load. The accuracy of a prediction is therefore highly influenced by the selected collapse mechanism in the prediction. The prediction is also associated with the accuracy of the assumed plastic moment capacity of a yield line. At present, the application of the yield line method in predicting collapse loads for CFS sections has not yet been as well established as that for reinforced concrete slabs (Hiriyur and Schafer, 2005). In CFS sections, local plastic collapse mechanisms will develop. These mechanisms largely depend on the shape of the cross-section (Kotelko, 2004). Because CFS sections have a variety of cross-sectional shapes, sufficient experiments are required to identify the characteristic local plastic collapse mechanisms for each typical cross section. Moreover, the local plastic collapse mechanisms of CFS sections always have a spatial feature, where a second-order effect is present and results in a complex stress state in yield lines (Zhao and Hancock, 1993). The determination of the plastic moment capacity of the yield line thus becomes challenging. A number of investigations on the local plastic mechanisms have been carried out since Murray and Khoo (1981). Ungureanu et al. (2010) summarised these investigation results as a database of local plastic mechanisms for CFS sections. The investigated sections cover C section, rectangular box section, trapezoidal box section, triangular section and circular hollow section. It is noted that research into local plastic mechanisms for CFS sigma sections has not been made available.

## 2.7 NUMERICAL METHODS IN THE RESEARCH OF CFS STRUCTURES

With the advance of computational mechanics and computer hardware, numerical methods have become increasingly popular in research into the behaviour of CFS structures, as they offer advantages in parametric studies and in solving complex problems over experimental and



analytical methods. In general, there are three numerical methods commonly used in research into CFS structures, namely finite strip method (FSM), generalised beam theory (GBT) and finite element method (FEM) (Macdonald et al., 2008). FSM and GBT are mostly applied in studies for elastic buckling/post-buckling behaviour, while FEM is popular in ultimate strength analysis, post-failure analysis, and of course elastic buckling/post-buckling analysis.

#### 2.7.1 Finite Strip Method (FSM)

FSM was originally developed by Cheung (1976) to analyse elastic buckling/post-buckling behaviour of prismatic structural members. In this method, members are discretised into a number of longitudinal strips along the entire length of the member. The displacement functions of a strip are approximated by interpolation polynomials in the transverse direction and Fourier series functions in the longitudinal direction. The compatibility between adjacent strips is ensured by the coefficients in the polynomials. The selected Fourier series function is specified to satisfy the corresponding boundary conditions. The original FSM was not particularly suited to the analysis of members undergoing in-span loads or supported other than under simple conditions. Fan and Cheung (1983) overcame this disadvantage by replacing the Fourier series functions with spline functions to account for non-periodic deformations. FSM is mostly used (Camotim et al., 2005) in the research into elastic buckling/post-buckling behaviour of CFS members. This research includes Pham and Hancock (2009a) and Chu et al. (2005, 2006) which have been mentioned in the preceding sections. Based on the original FSM, Schafer (2006) developed a computer programme, namely CUFSM, to calculate elastic local buckling and distortional buckling loads of CFS sections. This programme is free to access and facilitates the determination of elastic buckling loads based on gross cross sections. However, as with the

limitations of the original FSM, CUFSM is limited to simply supported members in pure compression, pure bending or combined.

### 2.7.2 Generalised Beam Theory (GBT)

GBT was first proposed by Schardt (1983) to analyse elastic buckling/post-buckling behaviour of prismatic structural members. This method decomposes the cross-sectional displacement of the member into a series of independent deformation modes, i.e. rigid-body motions and various buckling modes. In contrast, the longitudinal displacement of the member is assumed to be Fourier series functions or spline functions similar to that adopted in FSM. Each displacement mode in GBT can be expressed by a governing differential equation that satisfies the equilibrium conditions. The unknown coefficients in the solutions to the differential equation represent generalised cross-sectional properties and are normally determined by computer analysis. The equation can then be solved by numerical techniques, such as finite differences, to obtain the desired results. Davies and Leach (1994) and Davies et al. (1994) provided the detailed procedures for the employment of GBT in geometrically linear or nonlinear analysis of CFS structures. Using GBT, Silvestre and Camotim (2004a, 2004b) performed a series of studies for the elastic distortional buckling behaviour of CFS C and Z sections.

### 2.7.3 Finite Element Method (FEM)

FEM emerged from the need to solve complex structural problems in engineering disciplines. It is difficult to define the exact origin of FEM but it is acknowledged that the method has served as a standard tool for modelling and analysing complex structural problems since Clough (1960). The standard procedure of a finite element analysis (FEA) can be separated into three consecutive

modules (Zienkiewicz and Taylor, 2000), i.e. pre-processing, solution and post-processing. In the first module, the structure to be analysed is represented by an equivalent geometric model, attributed with suitable element types and material properties. This model is then discretised into finite elements connected to each other at their nodes. After that, boundary conditions are applied to the finite element model in the form of loads and restraints. In the second module, the displacement field of each element is approximated by a linear combination of shape functions. Governing equations for the structure are then established according to the type of analysis (e.g. static or dynamic), selected element types, material properties, compatibility and boundary conditions etc. The equations are subsequently solved by numerical techniques. In the third module, the obtained solutions need to be checked to confirm their validity. Once the results are verified, the FEA is completed. Otherwise, the finite element model needs to be revised, following any noted error sources and iterated from the first module until satisfactory results are obtained.

Because of its versatility, such as being adept at incorporating geometric and material nonlinearities, and simulating structures under complex load and boundary conditions, nowadays FEM is being extensively adopted in CFS research. Using FEM, Lee et al. (1996), Alinia (2005), Alinia and Moosavi (2008), Yu and Schafer (2007), Trahair (1993), Kurniawan and Mahendran (2009) and Rockey and Bagchi (1970) studied elastic buckling/post-buckling behaviour of CFS structures. Yu and Schafer (2007), Kurniawan and Mahendran (2009), Schafer and Peköz (1999), Dinis and Camotim (2010), Rhodes and Nash (1998), Ren et al. (2006) and Pham and Hancock (2010b) studied ultimate strengths of CFS structures. Shifferaw and Schafer (2008) studied inelastic moment resistance of class 3 C and Z sections and Hiriyur and Schafer (2005) studied

the collapse behaviour of a CFS plate in compression. In addition to that, this research has also provided very good information regarding element selection, mesh density, geometric and material nonlinear simulation techniques, and solution scheme in the FEA of CFS members. In the past decade, there have been many other published papers offering important guidance on the application of FEM in the structural analysis of CFS members. Sarawit et al. (2003) presented several examples to specifically demonstrate the use of FEM to analyse thin-walled members. In the paper, they discussed the commonly used element types (shell elements, beam elements, contact elements and spring elements), material models (linear elastic, elastic-plastic and Ramberg-Osgood), and initial conditions (geometric imperfections and residual stresses) considered in the FEA of thin-walled structures. Bakker and Peköz (2003) gave an overview of possible errors during the processes of the FEA of thin-walled members. These errors include element type selection error and insufficient mesh density error in the pre-processing, convergence error in the solution, and interpretation error in the post-processing. Suggestions were made on how to check and prevent these errors. Schafer et al. (2006) carried out FEM based research on the elastic buckling and ultimate failure behaviour of the compression flange of laterally braced CFS profiles with complex edge stiffeners. Results suggested that nonlinear FEA was more versatile than closed-form solutions. Yang and Hancock (2006) used FE modelling to predict the ultimate resistance of high-strength CFS box columns. The selection of assumed initial imperfection and element size was discussed. The model has been proven to be capable of analysing both short and long columns of high strength. Recently, Pastor and Roure (2009) developed a FE model to study the collapse behaviour of U and  $\Omega$  sections under uniform bending moment. The model has been demonstrated to be able to reproduce test results and replicate the development of local plastic mechanism in post-failure stage observed during tests.

Schafer et al. (2010) reviewed the influence of input parameters, e.g. geometric and material imperfections and boundary conditions, on the accuracy of nonlinear collapse in modelling CFS members by using FEA. Sensitivity analysis of these input variables in modelling collapse behaviour of thin-walled structures was also performed and presented in the same paper.

Geometric nonlinearity and material nonlinearity play an important role in FEA for ultimate strength and post-failure behaviour of CFS structures. The former is usually associated with geometric imperfections, and the latter is generally caused by nonlinear stress-strain relationship and residual stress of the materials.

Geometric imperfections refer to the deviation of a practical member from a perfect geometry. According to their characteristics, they can be divided into three categories (Dubina and Ungureanu, 2002): local type, distortional type and global type (bending, twisting and warping). Ideally, the precise distribution and magnitude of the geometric imperfections may be determined by laboratory measurement. However, the measurement procedure is considered to be tedious and often become unrealistic when the number of the specimens is high in number. The geometric imperfections may also be randomly generated by following a stochastic pattern. However, a large number of laboratory measurements are also required to establish a reasonable stochastic model. Another approach to introduce geometric imperfections is to simulate them by applying additional loads with appropriate forms. This approach works well for global type of imperfections but is not suitable for local type and distortional type of imperfections. As a result, these three approaches are rarely used in FEA of CFS structures. The literature survey reveals that in FEA of CFS structures, the distribution of the geometric imperfections is commonly

represented by superimposing relevant local, distortional and global buckling modes from eigen-buckling analysis. In the meanwhile the magnitude of the geometric imperfections is normally determined by rules of thumb or probabilistic treatment (Schafer and Peköz, 1998b).

In most of the FE based research for ultimate strength and post-failure behaviour of CFS structures, the nonlinear stress-strain relationship of a CFS member is commonly determined by material tensile coupon tests. As large strain behaviour can be involved, the test-obtained engineering stress and strain need to be converted into true stress and strain as follows:

$$\sigma_{true} = \sigma_{eng} (1 + \varepsilon_{eng}) \quad (2-12)$$

$$\varepsilon_{true} = \ln(1 + \varepsilon_{eng}) \quad (2-13)$$

The true stress-strain curve is then approximated in a multi-linear way and is supplied into the finite element model. The multi-linear material model typically adopts von Mises yield criterion with isotropic hardening.

CFS members are typically made from hot-rolled steel sheets. Each sheet is cold worked, annealed and wound into a coil. Later the coil is unwound and fed into a production line to cold form the final shape of a structural member. This manufacturing process together with the shipping and storage process introduce residual stresses into CFS members. It is usually assumed that the residual stresses before coiling have been removed in the annealing furnace and those due to shipping and storage are thought to be so small as to be negligible. Therefore, the residual stresses in CFS members generally arise from two sources, i.e. the coiling-uncoiling process and the cold forming process (Moen et al., 2008). The residual stress distribution through the

thickness of CFS members was found to dominantly exhibit a flexural feature, i.e. tension in the outer surface with compression in the inner surface, as opposed to membrane residual stress normally found in hot-rolled members (Yu, 2000). Due to the lack of systematic data, and also the fact that flexural residual stresses have a less detrimental influence on the ultimate strength than the membrane stresses (Dubina and Ungureanu, 2002), the residual stresses are often not explicitly included in finite element analysis for CFS members. Schafer et al. (2010) further suggested that because residual stresses and yield strength increases are induced simultaneously during the cold work process, their effects should be assumed to cancel each other out and subsequently can be ignored in FEA.

## 2.8 BOLTED CONNECTIONS IN CFS STRUCTURES

Connections of CFS structural members are often provided by mechanical fasteners, such as bolts, screws and rivets. Tomà et al. (1993) systematically introduced the mechanical properties of these fasteners and indicated their respective applications in engineering fields. The derivation of the design expressions recommended in BSI (2006a) for these fasteners was briefly illustrated in their paper. In this section, the literature survey is mainly focused on the research concerning the bolted connections, which are the most commonly used method to connect two CFS structural members in construction engineering.

Bolted connections can be designed to undertake shear force (axial force), bending moment, or more commonly a combined shear force and bending moment.

Bryan (1993) experimentally studied the flexibilities and bearing strengths of single bolted CFS-sheet lap joints. The investigated variables included sheet thickness, sheet yield strength, bolt and washer diameter, and edge distance. From the test results, two design expressions were established to determine the flexibilities and bearing strengths of single bolted lap joints. Based on these expressions, the stiffness and moment resistance of two-bolted moment connections, three-bolted moment connections and four-bolted moment connections were analytically developed. Rogers and Hancock (2000) studied the failure modes of bolted CFS-sheet connections in shear. The discussed failure modes included bearing, end tear out, net-section fracture, localized tearing and block shear. The explicit definition for each failure mode was provided. The paper highlighted that due to misidentification of failure modes and misuse of test data, the design standards, e.g. Standards Australia (1996) and AISI (1997), may be inaccurate in evaluating the strengths of bolted CFS-sheet shear connections. Chung and Ip (2000, 2001) experimentally and numerically investigated the structural behaviour of bolted shear connections between CFS sheets and hot rolled steel plates. The structural components in the numerical model, i.e. CFS sheets, hot rolled steel plates, bolts and washers, were all simulated with solid elements. The relationships between the components were established via contact pairs. The key parameters, such as material properties, contact stiffness, and frictional coefficients, were empirically determined. The model was validated by tests. It was then used to study the failure patterns and loading resistance of the connections. The numerical results were compared with codified design rules and similar conclusions were obtained to those by Rogers and Hancock (2000). Casafont et al. (2006) experimentally studied the structural behaviour of bolted CFS-sheet shear connections under monotonic/cyclic loading. Casafont et al. identified two types of failure modes, i.e. (i) bolt tilting, bearing and tearing of the sheets and (ii) bolt tilting, bearing and net-section failure. The



ductility and strength of both modes were compared and discussed. Design recommendations were provided for the bolted CFS connections to be applied in seismic design. Zaharia and Dubina (2006) investigated a bolted connection, designed to withstand both axial force and bending moment, used in CFS trusses. The bolted connection was constructed in such a way that the flanges of single C sections (web members) were connected to the webs of double C sections (chord members) by 4 or 6 bolts (2 or 3 bolts each side). A number of T-joint tests and single lap joint tests were carried out to determine the stiffness of the connection. Calibrated by the test results, the equations used to calculate the rotational stiffness and axial stiffness of the connection were provided. The effect of these two types of stiffness on the structural behaviour of the trusses was also qualitatively studied by carrying out a full scale test and numerical analysis. It was shown that the rotational stiffness of the connection plays a more important role in the structural strength, whereas the axial stiffness of the connection is more important to the structural stiffness of the trusses. Kim et al. (2007) specifically investigated the finite element simulation of bolted connections. They compared four kinds of finite element models: (i) the bolt and nut were both simulated with solid elements; (ii) the bolt was simulated with solid elements, whereas the nut was replaced by nodal coupling between the bolt and steel plates; (iii) the bolt and nut were both simulated with beam elements; (iv) the bolt and nut were represented by a group of gripping forces. The connected steel plates were simulated with solid elements in each model. Contact elements were defined where necessary. It was found that the first model produced the best predictions, whilst the second model was most effective in terms of computational cost and accuracy.

CFS sections have recently been employed as primary structural members in portal frames and residential multi-storey steel frames. The structural behaviour of the bolted connections used in these types of structures was investigated by a number of researchers.

Lim and Nethercot (2003, 2004a, 2004b) reported a series of experimental and numerical studies on the rotational stiffness and moment resistance of a bolted connection used at eaves and apexes in CFS portal frames. In this type of connection, CFS back to back lipped C sections were connected to CFS brackets through a group of bolts. It was found that the concentrated forces transferred from the bolts can lead to web buckling of the connected sections and result in premature failure in the connections. It was demonstrated that the moment resistance of the connections correlated with the parameters including bolt pitches, number of bolts and thickness of connected sections. In the FE modelling, the structural members, i.e. CFS back to back lipped C sections and CFS brackets, were simulated with shell elements, and the bolts were simulated with beam elements. The interaction between bolts and bolt holes was idealised with spring elements. In order to determine the spring stiffness, the authors also developed a solid FE model to analyse the elongation stiffness of the bolt holes. Chung and Lau (1999) experimentally investigated the structural behaviour of a bolted moment connection, which was achieved by means of a gusset plate bolted onto the webs of connected sections. The connection was proposed to be used in portal frames, and the connected sections were CFS back to back lipped C sections. It was noticed that the connection was unable to be fully effective in carrying moment because of the discontinuity of the flanges in the connected sections. However, it was shown that with proper configurations the connection enabled the CFS portal frames to perform safely and economically. Wong and Chung (2002) carried out experiments to study the structural behaviour of a bolted

moment connection used at column bases or beam-column joints in residential multi-storey steel frames. The connection had a similar form to that studied by Chung and Lau (1999), i.e. CFS back to back lipped C sections bolted to a gusset plate. The failure modes of the connection were identified and discussed. Design recommendations were offered to allow for the connection to develop over 75% of the moment resistance of the connected members. Yu et al. (2005) studied the test data presented in Wong and Chung (2002) and proposed an analytical model to predict the strength of the bolted connection. Based on this analytical model, the internal forces in the bolted connection can be assessed and thus the critical cross section can be readily determined and checked. After normalizing the recorded moments and rotations from the tests, Yu et al. established the characteristic moment-rotation relationship of the connection, and developed a semi-empirical equation to calculate the stiffness of the connection. Yu et al. also developed a beam idealised finite element model to evaluate the structural performance of CFS structures with the connection. This FE model however, was not able to automatically compute the rotational stiffness of the connection, which was required to be input as a parameter, determined by the semi-empirical equation proposed.

Two types of bolted connections are most commonly used in practice to connect CFS flexural members. One type is lap connection, and the other type is sleeve connection. Since these two connections are normally applied at internal supports in a multi-span beam system, they are usually required to possess sufficient continuity to transfer bending moment and at the same time, to have adequate capacity to resist the moment, transverse load and shear force existing at the internal supports.

The moment-rotation behaviour of lap connections has attracted some research attention. Ghosn and Sinno (1995) experimentally investigated the failure modes and stress distributions of CFS Z purlins with lap connections. It was suggested that the failure modes were correlated with the lap length to span ratios, and that the failures were governed by bending stresses. Ho and Chung (2004, 2006a) carried out a series of tests to study the moment resistance and rotational stiffness of CFS Z sections with lap connections. The influences of the lap length to section depth ratios, and the lap length to span ratios on the structural behaviour were specifically examined. It was found that the cross section at the end of the lap was usually the critical section and suggested that the failure was due to the combined bending and shear. Based on this argument, an analytical method to design the strengths of CFS Z sections with lap connections was proposed by Chung and Ho (2005). Zhang and Tong (2008) experimentally studied the structural behaviour of lapped Z connections and the effect of using extra self-drilling screws and slotted bolt holes. Dubina and Ungureanu (2010) examined the test results presented by Ho and Chung (2004) and Zhang and Tong (2008) and suggested that the failure of lapped Z connections was primarily as a result of combined bending and web crippling, rather than of combined bending and shear as indicated by Ho and Chung, and Zhang and Tong.

In contrast to lap connections, research on the moment-rotation behaviour of sleeve connections is limited. Two decades ago, Moore (1990) reported an experimental study on the moment-rotation response of three types of CFS sections (Z, Zeta and sigma) with sleeve connections. It stated that the sleeve connection exhibited a highly non-linear rotational behaviour. In recognizing the fact that they are difficult to quantify precisely, the paper proposed simplified methods to determine the secant value of rotational stiffness and the moment resistance of sleeve

connection based on a limited number of test results. The proposed method employed an ideal elastic-plastic moment-rotation model to reproduce the results observed from tests. In that model, the rotation at the onset of yielding was chosen as 0.05 radians. Nevertheless, with only three testing specimens, results were not sufficient to establish any design formula to calculate the rotational stiffness or the moment resistance for sleeve connections. Since then, little research on the moment-rotation behaviour of sleeve connections has been done until very recently. Gutierrez et al. (2011) reported an experimental and numerical study on the moment-rotation behaviour of CFS Z sections with sleeve connections. The moment-rotation characteristic and the moment resistance of the sleeved Z sections were discussed on the basis of the test results. It was found that the sleeved Z sections were semi-rigid in flexural stiffness and exhibited partial strength in resistance. A FE model was proposed to simulate the moment-rotation behaviour with explicit dynamic analysis. However, because the investigated specimens also were limited in number (only two tests were conducted, in each of which a pair of nominally identical specimens were investigated), Gutierrez et al. did not develop any formulae enabling practical designers to design CFS Z sections with sleeve connections by calculation.

Bolt holes normally have clearance of 2mm to facilitate installation. Due to this clearance, the bolts can slip in the bolt holes when loads are applied to the bolted connections. The phenomenon of bolt slip has been confirmed by many researchers, such as the aforementioned Bryan (1993), Casafont et al. (2006) and Zaharia and Dubina (2006). The effect of bolt slip on global structural behaviour was specifically studied by Kitipornchai et al. (1994). Two idealized bolt slip models were used in Kitipornchai et al.'s study. One model assumed that the slip occurred at a specified load level and the other assumed that the slip developed gradually from the start of loading. Both

models showed that the slip of bolts had significant influence on the stiffness of the structures. At the same time, its effect on the ultimate strength of the structures was found to be insignificant. Similar conclusions were also demonstrated by Zaharia and Dubina (2006).

Due to the thin-walled nature of CFS sections, the bolt holes in the bolted connections can undergo appreciable deformation under bearing against the bolts. As with bolt slip, this localised deformation due to bearing can also significantly influence the stiffness of the structures. With the aid of FE analysis, Lim and Nethercot (2004a) revealed that the overall deflection of portal frames made of CFS sections was the result of four components, i.e. bolt-hole elongation, member flexure, bolt slip and shear deformation. Among these four components, it was found that the deflection due to bolt-hole elongation accounted for approximately 54% of the overall deflection, whilst the deflections due to member flexure and bolt slip shared approximately 38% of the overall deflection, and shear deformation contributed less than 8% of the total deflection. Ho and Chung (2006b) studied the stiffness of CFS Z sections with lap connections and assessed the percentage of deflection caused by various components. It was demonstrated that the deflections due to bolt-hole elongation, member flexure and shear deformation, respectively, accounted for approximately 66%, 25% and 9% of the overall deflection. It should be noted that in Ho and Chung's research, any deflection resulting from bolt slip was considered to be negligible by taking appropriate measures in their test programme.

## 2.9 CFS PURLIN-SHEETING INTERACTIONS

In industrial buildings, CFS purlins are often used with metal sheeting in a way that the top flange of the beam is connected to the sheeting by screws. Because of the lateral and rotational restraints provided by the sheeting, the structural behaviour of the sheeted purlin can differ greatly from that of the purlin without sheeting. Since Zetlin and Winter first reported an experimental study in the 1950's, extensive research (Yu, 2000) has been performed on the structural behaviour of the sheeted beam in subsequent decades. The literature survey included in this section is primarily focused on the representative research published from the 1980's to the present.

Depending on their aims, the research concerning the structural behaviour of sheeted purlins may be generally categorised into three groups, namely, (i) pre-buckling stress distribution and elastic buckling behaviour, (ii) lateral and rotational restraints provided by the sheeting, and (iii) load resistance performance.

The study of pre-buckling stress distribution and elastic buckling behaviour of sheeted purlins was largely included in the following research. Ings and Trahair (1984) developed a computational model to analyse the lateral torsional buckling behaviour of sheeted CFS C and Z purlins. In the model, the top flange of the purlin was assumed to be fully braced by sheeting in the lateral direction but free to twist about the restraining points. The same restraint conditions were applied at the supports and intermediate bridge points except for additional full rotational restraints. The model also assumed that the cross section of the purlin is non-deformable, and before lateral torsional buckling occurs the purlin deflects vertically without twisting. Through this analytical model and using finite element methods, Ings and Trahair worked out the elastic

buckling load and buckling resistance of the sheeted purlin subjected to uniformly distributed uplift/gravity loads. Ye et al. (2002, 2004) numerically analysed the influences of partial lateral and rotational restraints provided by sheeting on the pre-buckling stress distribution and elastic buckling loads of CFS Z sections subjected to uniformly distributed uplift loads. Li (2004) analytically studied the lateral torsional buckling of CFS Z sections, partial laterally restrained by sheeting and anti-sag bars, with various boundary conditions, under uniformly distributed uplift or gravity loads. The critical buckling loads were determined using energy methods. Based on the same methodology, Chu et al. (2004) extended Li's study to CFS C sections. Vieira et al. (2010) numerically studied the cross section longitudinal stress distribution of CFS C sections, accounting for fully lateral restraint and partial rotational restraint supplied by sheeting under uplift loads. An empirical method was developed to calculate the stress distribution.

As the lateral and rotational restraints provided by the sheeting play an important role in the structural behaviour of the sheeted beam, much research has been conducted on this subject. Vransky (2006) addressed the notion that the rotational stiffness provided by sheeting attached to the CFS purlin may vary with external loading because of the asymmetrical cross-sectional shapes of the CFS purlins and the distribution of contact forces between purlins and sheeting. An analytical model and a design formula were proposed to quantify the effects of loading on the rotational stiffness. A FE model was developed to verify the analytical model. Chung and St Quinton (1996) experimentally investigated the influences of complex roofing sheets, where thermal insulation was present, on the load resistance of Z and sigma beams. It was found that the presence of thick thermal insulation can impair the constraint action provided by the sheets and thus reduce the load resistance of the purlins. Katnam et al. (2007a, 2007b) developed two non-



linear finite element models used to estimate the rotational stiffness provided by single skin sheeting and complex sheeting, respectively, when attached to a CFS purlin. The models included the effects resulting from the deformations of sheeting and fasteners (screws with neoprene washers), but omitted the negligible effect contributed by the deformation of the CFS purlin. The relationship between the sheeting and the purlin was idealised by line contact. The proposed models were applicable to sheeting fixed to the CFS purlin through either trough or crest, under both uplift and gravity loadings. Very recently Gao and Moen (2011) reported an analytical method for the calculation of the rotational restraint stiffness provided by sheeting to CFS purlins. The method was demonstrated to be applicable for CFS C and Z sections screw-fastened to single skin sheeting. BSI (2006a) presented both analytical and experimental methods in the determination of the lateral and rotational restraints stiffness provided by single skin sheeting to CFS C, Z and sigma sections.

The load resistance performance of the sheeted purlin has attracted much research attention. Before the early 1990's, the research on this subject was mainly through the use of full scale tests. Moore and Sims (1988) carried out a series of full scale tests aimed at investigating the structural performance of typical CFS sigma, Z, and Zeta purlin-sheeting systems under both uniformly and variably distributed gravity loads, up to serviceability limit state and ultimate limit state, respectively. This experimental research found that the standard sleeve connection used in practice was only partially continuous over internal supports. In addition, from the tests, noticeable plastic behaviour was observed for these purlin-sheeting systems. Further research on moment-rotation characteristics of both continuous and sleeve connections at the internal supports were suggested by Moore and Sims. The test results also demonstrated that the sheeting

and intermediate bridges improved the structural performance of the purlins through restraining their lateral movement. Willis and Wallace (1990) tested the load resistance of sheeted CFS C sections and Z sections under gravity loads. The sheeted sections were subjected to uniformly distributed load and their tension flanges were laterally unbraced. The influences of the location of sheet fasteners, and the flange width to lip width ratio on the load resistance were particularly studied. With the advance of computational technology in the late 1990's, Lucas et al. (1997a, 1997b) developed a full FE model and a simplified FE model, respectively, which were used to evaluate the structural performance of purlin-sheeting systems under uniformly distributed loads. The former was a sophisticated model where the purlins and sheeting were modelled explicitly and the connections between them were idealised by using nodal constraint equations. The later included only the purlins with the sheeting's lateral and rotational restraint effects being accounted for by using linear elastic springs located at the purlin-sheeting connections. Both models took account of the cross-sectional deformations of the purlins and were able to predict the load resistance at which the the systems failed due to yielding or local buckling of the purlins. The predicted results were reported within 5% for the full model and 10% for the simplified model compared with the experimental results. Unfortunately, not all the modelling information was presented in detail in the paper and therefore, some of the parameters and processes, e.g. material property, meshing and the treatment of boundary conditions at support ends, can only be assumed if the modelling is to be re-implemented. It was also found that neither material nor geometric imperfection was included in the modelling.

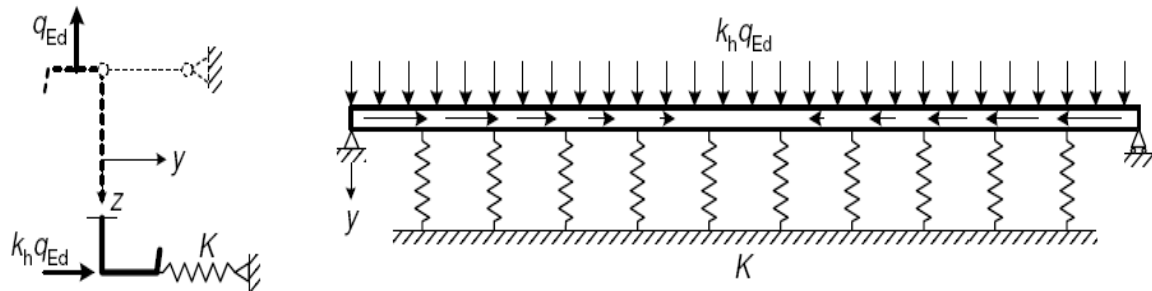


Figure 2-13 The analytical model considering restraint effect by sheeting on purlins, after BSI (2006a)

In order to determine the load resistance of the sheeted purlin by calculation, Peköz and Soroushian (1982) innovatively developed an analytical model, as shown in Fig. 2-13. In the figure, a CFS Z section with sheeting fastened on its top flange is subjected to uniformly distributed uplift load  $q_{Ed}$ . The sheeting is considered to be able to provide fully lateral restraint but partially rotational restraint to the purlin. To account for the effect of the partial rotational restraint, Peköz and Soroushian proposed to apply a translation spring with stiffness  $K$  at the free flange of the section. As the uplift load  $q_{Ed}$  is acting off the shear centre of the section, the stresses in the free flange result from both bending and torsion. Peköz and Soroushian suggested applying an equivalent lateral load  $k_h q_{Ed}$  to allow for the effect of torsion. The direction of the load  $k_h q_{Ed}$  is dependent on the direction of the load  $q_{Ed}$  (uplift or gravity). The calculation of the load resistance of the section is therefore equalised to the calculation of the load resistance of a beam-column on an elastic foundation. This analytical model was later officially adopted by BSI (2006a) to calculate the load resistance of sheeted purlins. Tomà and Wittemann (1994) illustrated the calculation model used in BSI (2006a) for CFS purlins restrained by sheeting. The calculation procedure in the code was demonstrated and the analytical results were compared

with the test results. It was found that BSI (2006a) yielded uneconomical predictions for the load resistance of the sheeted purlins under either gravity or uplift loadings. On the basis of the same calculation model, Sokol (1996) proposed a semi-analytical method to design CFS purlins restrained by sheeting. The proposed method incorporated the effects of anti-sag bars and moment gradients on the lateral torsional buckling resistance of the purlins. Rousch and Hancock (1997) carried out a series of laboratory tests for simple span CFS C and Z sections with screw-fastened sheeting under uniformly distributed uplift loads. The lateral displacements and stress distribution across purlin spans were specifically studied, and the test results were used to verify a simplified numerical model on the basis of Peköz and Soroushian's analytical model.

It is interesting to note that although Peköz is on an AISI committee on Specifications for the Design of Cold-Formed Steel Structural Members (AISI, 2007), the above mentioned model has not been adopted by AISI (2007). Instead, AISI (2007) uses a completely different approach called the *R*-factor method to calculate the load resistance of sheeted purlins. The employment of the *R*-factor method is straightforward; as it directly applies a reduction factor (*R* factor) to the cross-sectional load resistance of the purlin and then gives the load resistance of the purlin sheeted. The reduction factor given in AISI (2007) falls between 0.4 and 0.7, which is dependent on section types and sizes. It is worth noting that AISI (2007) does not provide a reduction factor applicable for sigma sections. Therefore, theoretically AISI (2007) is not suitable for use in the design of sheeted sigma purlins. Johnston and Hancock (1994) calibrated the reduction factor given in AISI (2007) by using the results of a series of simple span and continuous sheeted CFS C and Z purlin tests performed at the University of Sydney. Subsequently, the calibrated reduction factor was adopted by Standards Australia (2006).

Literature survey reveals that most existing studies on structural design of sheeted purlins rarely cover the sigma section. Furthermore, the existing studies on the purlin-sheeting systems concerns with low screw spacing (not greater than 300mm), e.g. at every corrugation trough of roof sheeting. In engineering practice, the application of screws is often recommended at every other trough to save installation time. Questions of whether and how this large screw spacing will affect the behaviour of sigma purlins under both downward and uplift loads are yet to be answered.

## 2.10 SUMMARY

An extensive literature review of the state-of-the-art research on the structural behaviour of CFS flexural members has been presented in this chapter. The review has been limited in scope relevant to the research subject and has addressed the following eight topics: elastic critical buckling, post-buckling strength, ultimate strength, elastic strength design method, plastic strength design method, numerical methods, bolted connections, and CFS flexural member-sheeting interaction. The major findings from the literature review are summarised as follows:

- Elastic critical buckling behaviour of CFS flexural members have been investigated extensively. Analytical formulae are available to calculate the elastic critical buckling loads of CFS flexural members in various buckling modes. However, these analytical formulae are only applicable for members in ideal loading and restraint conditions, such as pure bending/pure shear, fully simply supported/fully fixed. To attain the elastic critical

buckling load in general loading and restraint conditions, numerical methods are generally more efficient.

- Thin-walled plates have been demonstrated to possess significant local post-buckling strength. Non-negligible distortional post-buckling strength was observed in CFS C sections. LTB has little post-buckling strength.
- A large amount of research was available for load resistance of CFS purlins under various buckling models: web crippling, combined bending and shear, and combined bending and web crippling. By using experimental or numerical methods, semi-empirical/empirical design recommendations have been established for the relevant study cases. However, it was found that the investigated specimens were mostly based on CFS C and Z sections. The test or numerical data for CFS sigma sections are generally absent.
- Two codified design methods are available to design CFS purlins elastically. They are the Effective Width Method and the Direct Strength Method. Both provide semi-empirical/empirical design rules based on CFS C and Z sections. Their applicability to sigma sections is worth investigating, especially for continuous sigma purlins at internal supports, where high levels of bending moment, concentrated forces and shear forces coexist.
- Three types of plastic methods are available to make use of the plastic nature of a structure made of ductile materials. They are conventional plastic design method, pseudo-plastic design method and yield line method. The first method is well established and mostly suitable for steel structures made of Class 1 and 2 sections. The second method is suitable for steel structures made of Class 4 sections. To perform the pseudo-plastic

design method, currently the key parameter, PPMR, has to be determined by tests. The third method is suitable for structures having well defined yield mechanism and plastic moment in each yield line.

- Three types of numerical methods are most commonly used in the research of CFS structures, namely FSM, GBT and FEM. The first two are mostly applied in studies for elastic buckling/post-buckling behaviour of prismatic members, while the last one has the versatility to help study almost every aspect of the structural behaviour of CFS structures.
- A number of studies have been conducted into bolted connections used in CFS structures. It was revealed that the structural characteristic of the practical bolted connection is substantially influenced by two factors, i.e. bolt hole elongation due to bearing, and bolt slip within bolt-hole due to clearance. Lap connections and sleeve connections are normally employed to connect two beams in CFS structures. The structural behaviour of lap connections has been included in a number of studies, while research into sleeve connections is still very limited. Investigation is therefore needed to quantify the stiffness and resistance of sleeve connections.
- Extensive research has been carried out to study the structural behaviour of CFS purlins with sheeting attached on their top flange. This research includes pre-buckling stress distribution and elastic buckling behaviour, lateral and rotational restraints provided by the sheeting, and load resistance performance of the sheeted beams. It was found that due to the lack of test data, AISI (2007)/Standards Australia (2006) do not supply any design rules for sheeted sigma beams. BSI (2006a) provided calculation expressions that are mostly developed on the basis of fixing screws applied at every trough of the sheeting.

## **CHAPTER 3 CONTINUOUS SIGMA PURLINS AT INTERNAL SUPPORTS**

### **3.1 INTRODUCTION**

This chapter reports an experimental and nonlinear finite element study on the post-buckling and the post-failure behaviour of double span continuous CFS sigma purlins near internal supports. A simply supported purlin subjected to a central point load was constructed to represent the hogging moment region near an internal support. The length was taken between two inflexion points of the double span purlin near the internal support, and the central point load was used to represent the reaction at the internal support. Firstly, ten simple purlins were investigated by laboratory tests. Each purlin had two nominally identical specimens. Therefore, a total of twenty tests were carried out. Secondly, each simple purlin was analysed by FE modelling. Validated by the experimental data, the FE model was then employed to perform a parametric study. The ultimate loads of the sigma purlins were obtained from the FE analysis, and they were discussed and compared with the predictions from codified methods, i.e. the Effective Width Method and the Direct Strength Method. Using the moment-rotation relationship obtained from the FE analysis, the PPMRs for the CFS sigma purlins were determined. Finally, a semi-empirical approach was proposed to calculate the PPMRs for double span CFS sigma purlins at internal supports.

### **3.2 TEST PROGRAMME**



Consider a double span continuous purlin of span length,  $L$ , subjected to a uniformly distributed load (UDL). The elastic bending moment diagram is illustrated in Fig. 3-1 (a). The study was focused on the hogging zone, where the internal support was located. From the bending moment diagram, it is rational to suggest that the hogging zone can be approximately represented by a simply supported beam of length  $0.4L$  subjected to a central point load, as shown in Fig. 3-1 (b). In this study, the moment-rotation relationship of the sigma section at the internal support was investigated by carrying out a three point bending test for this representative beam (referred to hereafter as the *continuous internal support test*), as recommended in BSI (2006a).

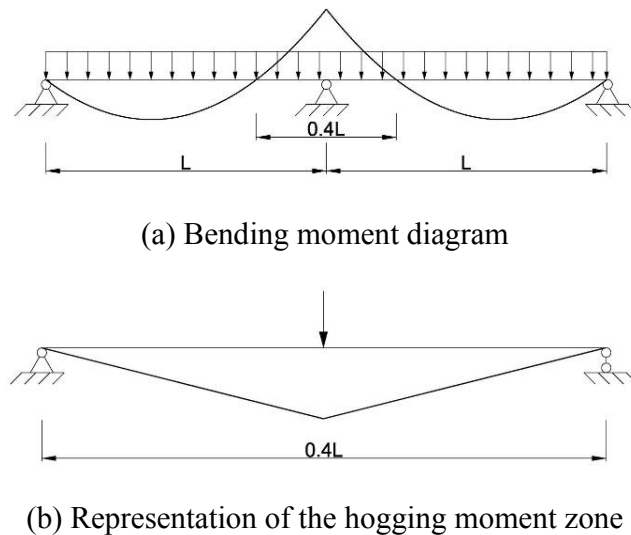


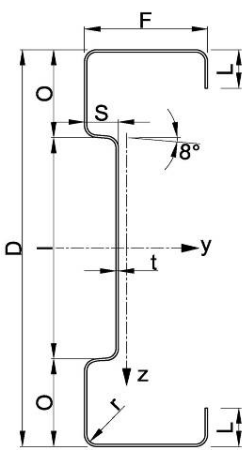
Figure 3-1 Two-span continuous beam

Ten sigma purlins with various depth, thickness and length were experimentally studied. Each one had two nominally identical specimens. A total of twenty tests were performed. In this test programme, each test was assigned a three-part unique ID symbol, e.g. 24-20012-c1 indicating

the beam span (2.4m), the section (200mm deep), the nominal thickness (1.2mm), the type of connection (c indicates continuous connection) and the number of the duplicated test specimen.

### 3.3 TEST SPECIMENS

A series of selected test specimens covering a wide spread of geometric dimensions was chosen for the continuous internal support tests. The nominal cross-sectional dimensions and the measured thicknesses of the test specimens were summarised in Table 3-1. The rolling of the specimens was numerically controlled, and hence the tolerance of the cross-sectional dimensions has been kept to a minimum. The cross-sectional thicknesses were measured by a 0-150 mm Digital Vernier Caliper. The measuring points were located on the inner web, top flange and bottom flange of the specimens, respectively. The nominal yield stress of the test specimens was 450 N/mm<sup>2</sup>. The true stress-strain relationship was obtained from material coupon tests. Each coupon was cut from the coil before the corresponding section was rolled. The procedures and the results of these coupon tests are detailed in Appendix IV. The effective second moment of area,  $I_{\text{eff}}$ , and the effective section modulus,  $W_{\text{eff}}$ , both calculated by following the EWM stipulated in BSI (2006a), are also presented in Table 3-1.

Specimen	$D$ (mm)	$F$ (mm)	$L$ (mm)	$O$ (mm)	$I$ (mm)	$S$ (mm)	$r$ (mm)	$t^*$ (mm)	$I_{eff}$ (cm <sup>4</sup> )	$W_{eff}$ (cm <sup>3</sup> )	
24-20012-c1	200	62.5	20	45	110	16	4	1.21	220	16.4	
24-20012-c2								1.25	231	17.4	
24-20016-c1	200	62.5	20	45	110	16	4	1.59	327	26.4	
24-20016-c2								1.59	327	26.4	
24-20025-c1	200	62.5	20	45	110	16	4	2.44	534	45.1	
24-20025-c2								2.46	538	45.5	
40-20025-c1	200	62.5	20	45	110	16	4	2.46	538	45.5	
40-20025-c2								2.47	540	45.7	
24-24015-c1	240	62.5	20	50	140	16	4	1.49	447	27.4	
24-24015-c2								1.49	447	27.4	
24-24023-c1	240	62.5	20	50	140	16	4	2.24	748	49.8	
24-24023-c2								2.24	748	49.8	
40-24030-c1	240	62.5	20	50	140	16	4	2.99	1019	69.7	
40-24030-c2								3.01	1026	70.2	
24-30018-c1	300	75	20	60	180	16	4	1.79	1001	47.6	
24-30018-c2								1.78	994	47.2	
24-30025-c1	300	75	20	60	180	16	4	2.43	1458	73.8	
24-30025-c2								2.45	1473	74.6	
40-30030-c1	300	75	20	60	180	16	4	2.93	1817	94.6	
40-30030-c2								2.91	1804	93.8	

\* Measured thickness

Table 3-1 Cross-sectional dimensions

Two different span lengths, i.e. 2.4m span and 4.0m span, were investigated in the continuous internal support tests. The horizontal distance between bolt holes is shown in Fig. 3-2. The vertical distance,  $a$ , between two rows of bolt holes varied with the depth of the section, i.e. 154 mm for 200 series sections, 190 mm for 240 series sections and 240 mm for 300 series sections.

### 3.4 TEST APPARATUS AND SET-UP

The following apparatus was employed in this test programme:

- 1× loading jack in a 60T Mand testing machine;
- 5× linear variable displacement transducer (LVDT) with  $\pm 0.01$ mm accuracy;
- 1× Grant data logger to acquire the measured displacement and send the data to a PC;
- 2× Inclinometer with  $\pm 10^\circ$  measuring range and  $\pm 0.01'$  accuracy;

The set-up for the continuous internal support test is schematically shown in Fig. 3-2. The central point load was applied by a strain controlled loading jack in the 60T Mand testing machine. The load was applied to the beam via a rigid universal beam section (UBS) and a stiffened loading cleat. The UBS section was rigidly fixed to the loading jack on its top flange and connected to the loading cleat on its bottom flange. The loading cleat was bolted to the sigma purlin using four bolts. Because the loading jack was sufficiently rigid, the sigma purlin was laterally and rotationally restrained at the load application point. Therefore, the loading condition was equivalent to the load being applied through the shear centre of the sigma purlin. At each end, the sigma purlin was connected onto a stiffened supporting cleat using two bolts. In this test programme, all bolt holes where the sigma purlin was connected to the cleats had a standard

clearance, i.e. 2mm. This clearance allowed some horizontal movement between the two bolts at each support end and therefore the two bolts did not provide any significant rotational fixity at the support. The supporting cleats were fixed to square hollow sections (SHS), which were clamped by separate loading jacks to prevent toppling or moving. Grade 8.8 M12 bolt sets (bolt, nut and washers) were used for the 200 and 240 series sections, and Grade 8.8 M16 bolt sets were used for the 300 series sections. Three linear variable differential transformers (LVDTs) were placed at the two quarter and middle span points, respectively, to measure the vertical deflections, and two additional LVDTs were placed at both quarter points to measure the lateral movements. Two inclinometers were glued at the central line of the top flange at the support ends to measure the end rotation angles.

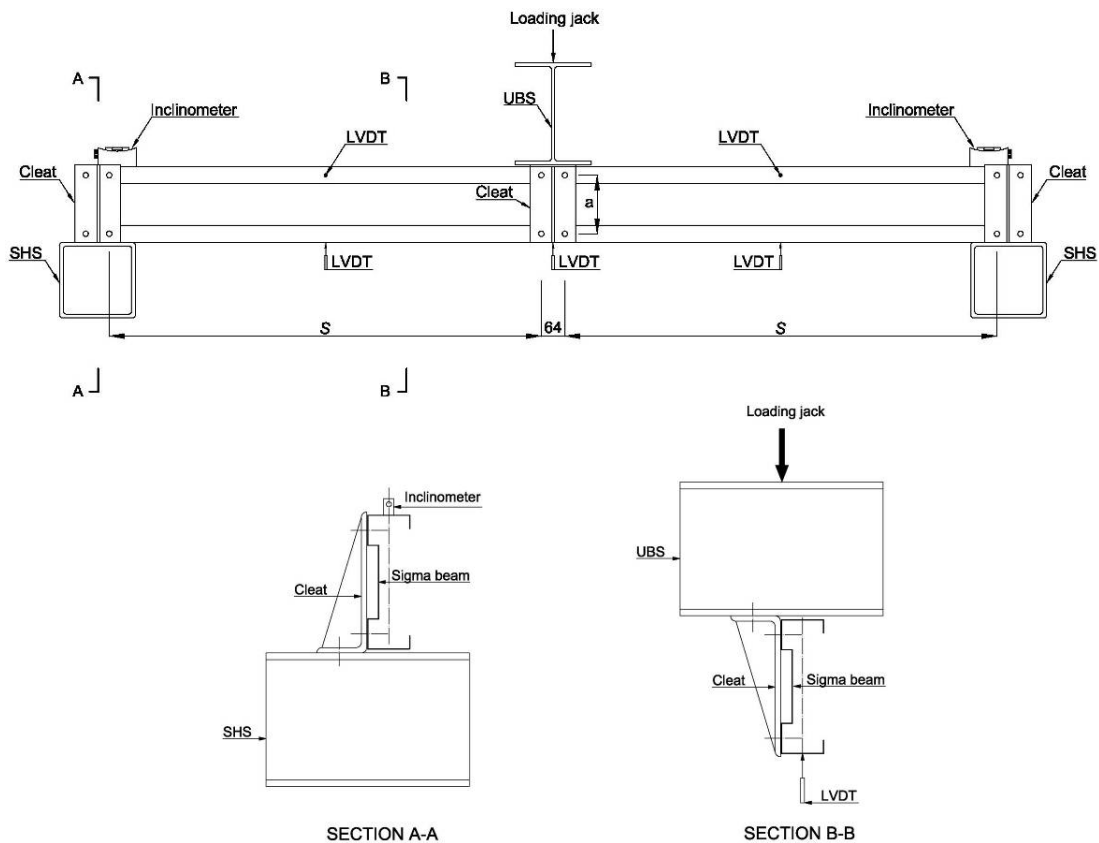


Figure 3-2 Test set-up

### 3.5 TEST PROCEDURES AND INSTRUMENTATION

The tests were performed using the 60T Mand testing machine. An incrementally increased load was first applied to the specimens. The load increment was set as 2kN. This loading procedure was maintained until the linearly ascending stage of load-deflection relationship of the specimens had ended. The loading procedure was then switched to the displacement control mode. The load induced by the monotonically applied displacement can be simultaneously displayed on the screen of the Mand testing machine. Within each displacement step, a 2kN load was generated and applied to the specimens. This process was repeated until the ultimate load was about to be reached. The displacement increment was then changed to 1mm until the ultimate load was obtained. Beyond the ultimate load, the displacement was continually applied with an increment of 5mm until the deflection had roughly reached a value of six times the maximum elastic displacement.

Three LVDTs were placed on the bottom flange of the test specimens at the mid-span and the quarter spans, to measure vertical deflections. Two additional LVDTs were placed on the outer web of the specimens at the quarter spans to measure horizontal deflections. The measured deflections were collected by the Grant data logger and sent to a PC. Two inclinometers were placed on the top flange of the specimens at both support ends to measure the end rotations in the major bending plane. The data from the inclinometers and the LVDTs were recorded manually at the end of each load/displacement step. The interval between the load/displacement steps for the

data readings was largely kept to no more than 30 seconds. This test procedure was repeated for each specimen.

### 3.6 TEST RESULTS

Twenty continuous internal support tests were carried out. Presented in Table 3-2 are the Young's modulus and the 0.2% proof stress measured from material coupon samples, the shear span,  $s$  (see Fig. 3-2), the recorded failure load,  $P_t$ , the corresponding failure moment  $M_t$  and shear force  $V_t$ , the observed initial buckling mode and the localised collapse pattern for each test. By using the method mentioned in Chapter 2.5.2, the PPMR and the PPR were also calculated, and they are presented in the same table except for those specimens experiencing Lateral Torsional Buckling (LTB) as the critical buckling mode. According to the initial buckling mode, specimens were grouped into three categories: local buckling-initiated specimens, distortional buckling-initiated specimens and LTB-initiated specimens.

Test sample	E (kN/mm <sup>2</sup> )	$f_{0.2}$ (N/mm <sup>2</sup> )	s (mm)	$P_t$ (kN)	$M_t = \frac{P_t \times s}{2}$ (kNm)	$V_t = \frac{P_t}{2}$ (kN)	Buckling mode*	Localised collapse pattern (Fig. 3-5)	PPMR (kNm)	PPR (degree)
24-20012-c1	206	471	1139	13.3	7.6	6.7	LF	Type I	5.5	2.4
24-20012-c2			1139	13.8	7.9	6.9	LF	Type I	5.2	2.5
24-20016-c1	214	433	1139	19.8	11.3	9.9	LF	Type I	8.9	2.2
24-20016-c2			1139	20.2	11.5	10.1	LF	Type I	9.0	2.2
24-20025-c1	207	447	1139	39.2	22.3	19.6	DB	Type III	21.2	1.9
24-20025-c2			1139	39.5	22.5	19.8	DB	Type III	21.8	1.8
40-20025-c1	207	447	1939	22.2	21.5	11.1	LTB	Type IV	N/A	N/A
40-20025-c2			1939	22.0	21.3	11.0	LTB	Type IV	N/A	N/A
24-24015-c1	208	507	1139	23.8	13.6	11.9	LF	Type II	10.4	2.1
24-24015-c2			1139	24.8	14.1	12.4	LF	Type II	10.8	2.0
24-24023-c1	205	456	1139	44.8	25.5	22.4	DB	Type III	22.5	1.6
24-24023-c2			1139	44.4	25.3	22.2	DB	Type III	21.7	1.7
40-24030-c1	217	453	1939	37.8	36.6	18.9	LTB	Type IV	N/A	N/A
40-24030-c2			1939	37.8	36.6	18.9	LTB	Type IV	N/A	N/A
24-30018-c1	207	455	1139	41.8	23.8	20.9	LF	Type II	19.9	1.2
24-30018-c2			1139	39.8	22.7	19.9	LF	Type II	17.0	1.4
24-30025-c1	207	447	1139	67.0	38.2	33.5	DB	Type III	29.8	1.3
24-30025-c2			1139	65.8	37.5	32.9	DB	Type III	30.7	1.2
40-30030-c1	208	417	1939	51.3	49.7	25.7	LTB	Type III + IV	N/A	N/A
40-30030-c2			1939	50.0	48.5	25.0	LTB	Type IV	N/A	N/A

\*LF-local buckling in flange; DB-distortional buckling; LTB-lateral torsional buckling

Table 3-2 Test results of continuous purlins at internal support



The length of the plastic zone is assumed to be 20% of the span length, which has been proven to be long enough to cover all the locally deformed zones near the internal support (Grundy, 1990). Therefore, the rotation angle of the expected plastic zone was estimated based on the differential deflections between the mid and quarter-span points on both sides of the load application point i.e.  $\theta = (2 \cdot \delta_2 - \delta_1 - \delta_3) / L$ , as illustrated in Fig. 3-3. The curves of moment at internal supports against the corresponding rotation were plotted, and they are presented in Fig. 3-4. They are grouped into five graphs based on three variables, namely section thickness (a) – (c), section depth (d) and beam span (e).

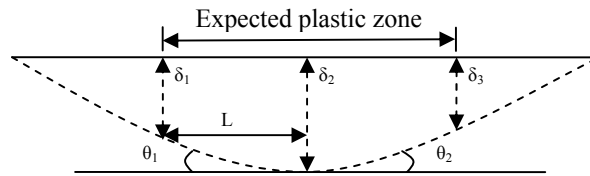
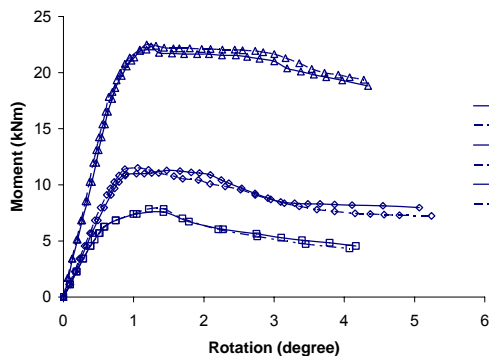
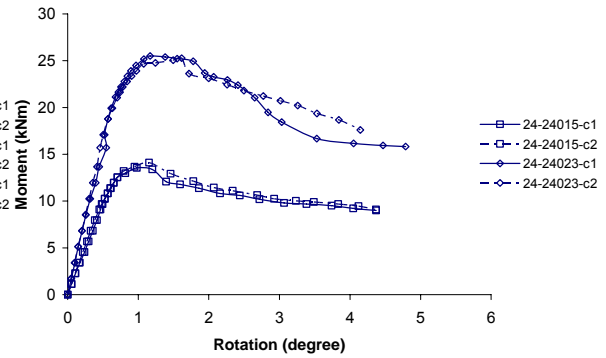


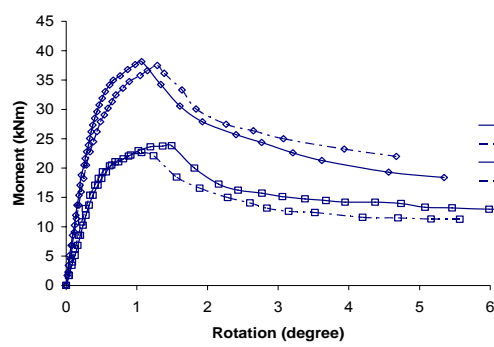
Figure 3-3 Calculation for the rotation of expected plastic zone



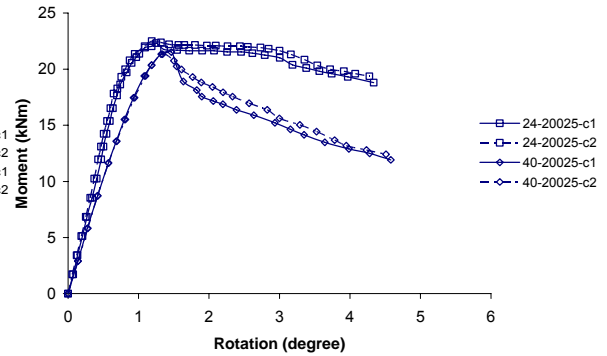
(a) 24-200 series with various thicknesses



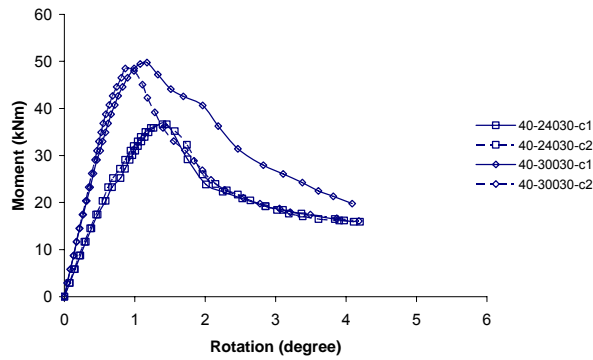
(b) 24-240 series with various thicknesses



(c) 24-300 series with various thicknesses



(d) 20025 series with various lengths



(e) 4m specimen with various depths

Figure 3-4 Moment-rotation curves

Four different types of localised plastic collapse patterns were identified and are summarised in Table 3-2. The characteristic of each type is illustrated in Fig. 3-5. These localised plastic collapse patterns may be useful in the determination of cross-sectional load carrying capacity by using yield line theory.



Type I



Type II



Type III



Type IV

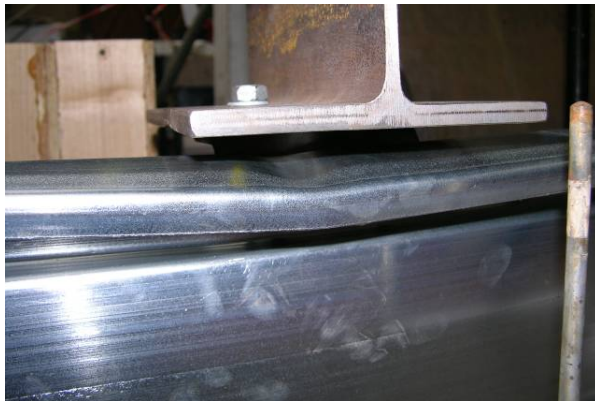
Figure 3-5 Typical localised collapse patterns

### 3.7 DISCUSSION OF TEST RESULTS

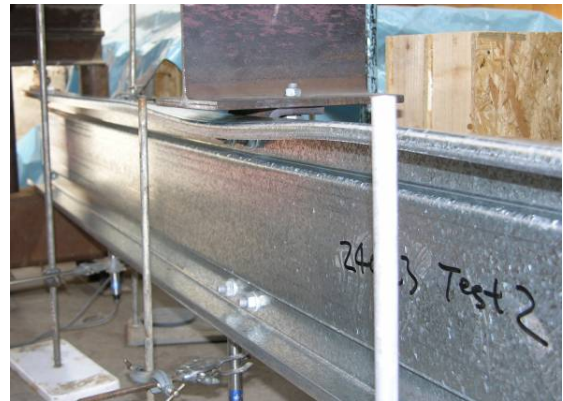
As shown in Fig. 3-4, all moment-rotation curves exhibit three distinct stages, i.e. linearly ascending stage (pre-buckling), nonlinear ascending stage (post-buckling) and softening stage (post-failure). Appreciable post-buckling strength for both local buckling and distortional buckling modes was observed during the tests. Table 3-2 shows that no specimen exhibited local buckling initially in the web due to the presence of two stiffeners.

It was observed in specimens 24-20012-c, 24-20016-c, 24-24015-c and 24-30018-c that local buckling was initiated in the compression flange panels (LF mode) near the mid-span. Distortional buckling (DB mode) was also triggered prior to the occurrence of failure. At the failure point, the specimens experienced a coupled local and distortional buckling failure mode, as shown in Fig. 3-6 (a). For specimens 24-20025-c, 24-24023-c and 24-30025-c, the buckling was initially triggered by DB at the mid-span. No LF was observed prior to failure and the failure showed a DB only mode, as shown in Fig. 3-6 (b). For specimens 40-20025-c, 40-24030-c and 40-30030-c, LTB was initiated at a critical cross section that was approximately 500mm away from the mid-span. For specimens 40-20025-c and 40-24030-c, neither LF nor DB was observed when failure occurred and the failure showed a LTB only mode, as shown in Fig. 3-6 (c); while for specimens 40-30030-c, DB was also involved when failure occurred and the failure showed a combined DB and LTB mode, as shown in Fig. 3-6 (d).

Fig. 3-4 shows that the post-failure curves of two nominally identical specimens were in very good agreement for 200 and 240 series sections, but were somewhat different from the 300 series sections. Since all the sections were manufactured, delivered, installed and tested in the same fashion, such a variation may indicate that post-failure behaviour of the 300 series sections were more sensitive to inherent imperfections of testing specimens. However, as far as the peak moment was concerned, the influence of imperfections was not significant. Comparing the peak moment of the duplicated test specimens, it can be found that the maximum variation was only 5%, arising from specimen 24-30018-c.



(a) LB and DB interaction



(b) DB



(c) LTB



(d) DB and LTB interaction

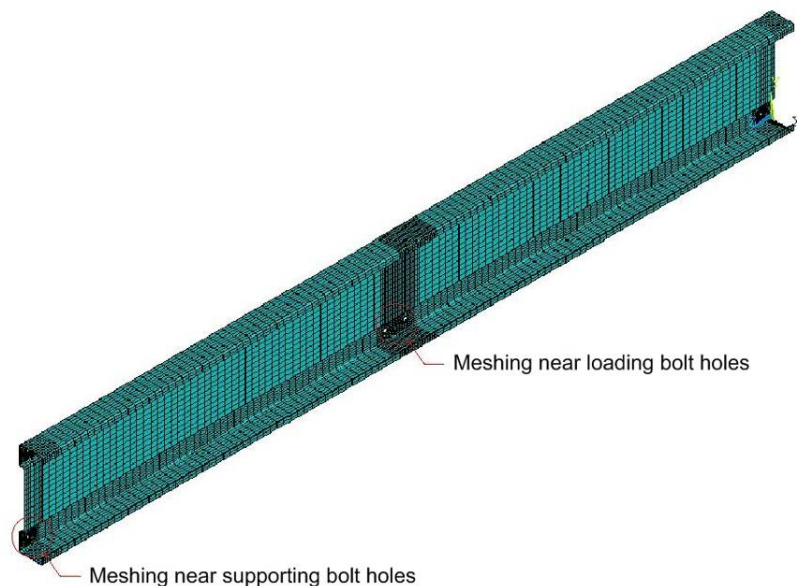
Figure 3-6 Post-buckling deformation

### 3.8 FINITE ELEMENT MODELLING OF CONTINUOUS SIGMA PURLINS AT INTERNAL SUPPORTS

### 3.8.1 Modelling development

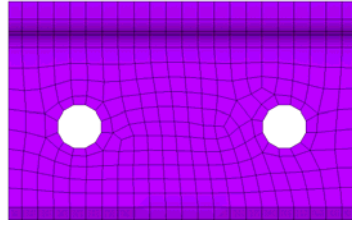
#### 3.8.1.1 Element type and meshing

The general purpose FEA programme, ANSYS, was used for the numerical modelling (ANSYS, 2007). A shell element, i.e. SHELL181, was chosen to model the elements of the sigma purlin. This type of finite strain shell element is capable of analysing thin-walled structures and allows for both material and geometric nonlinearity. The element is defined by 4 nodes. Each node has 6 degrees of freedom. The nodes of the shell elements were located at the mid-plane of the wall thickness of the sigma purlin. Reduced integration with hourglass control was selected for the element which can significantly reduce the computational time and still maintain adequate accuracy. The chosen element has 5 integration points in the thickness direction. The bolts that were used to connect the sigma sections and supporting cleats were modelled with 4-node elastic shell element, i.e. SHELL63.

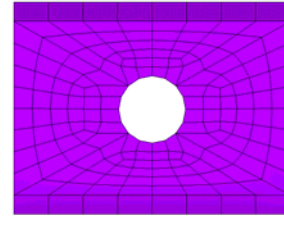


(a) Overall view





(b) Meshing near loading bolt holes



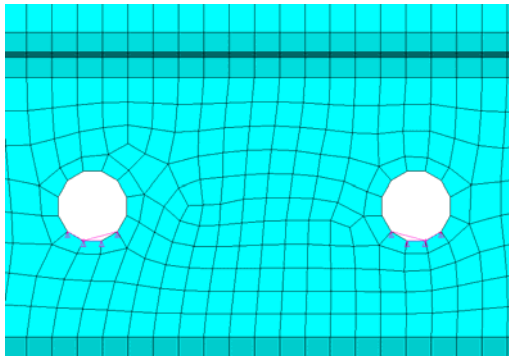
(c) Meshing near supporting bolt holes

Figure 3-7 Finite element meshing

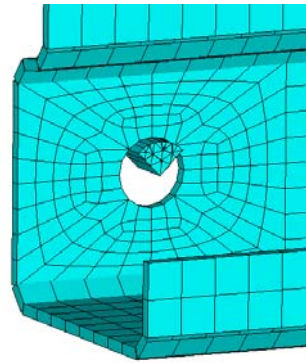
As the nature of meshing can directly influence the convergence rate and the degree of accuracy of FEA results, the selection of the shape and size of the element in the present FE modelling was determined through extensive trial and improvement process. It was found that the most satisfactory result was achieved through the following discretisation pattern for most sections: 2 elements in the lip, 8 elements in the flange, 8 elements in the outer-web, 8-12 elements in the inner-web and 1 element in the rounded corners. The aspect ratio of the elements near the middle span and two ends, where a high stress gradient was present, was kept between 1 and 2. The aspect ratio of the remaining elements was kept between 1 and 3. The meshing pattern of the sigma purlin is illustrated in Fig. 3-7 (a). Areas near bolt holes at both load application and support points were specifically considered as indicated by the modelling shown in Fig. 3-7 (b) and (c). It was found that if the meshing near the loading and support zones was too fine, excessive localised distortion of elements could occur when the load reached the post-failure stage. These overly distorted elements can result in a convergence difficulty and fail to produce a full load-deflection curve. Therefore, elements with approximate size 1.8 to 2.5 mm around bolt holes were used, which can effectively resolve the convergence problem while maintaining sufficient accuracy.

### 3.8.1.2 Loading and boundary conditions

Loads were directly applied at the edge of four bolt holes near the middle span point. The circular edge of each hole was predefined by 4 arcs. Loads were applied onto the lower quarter of the circular edge (see Fig. 3-8 (a)), which reflects the real bearing detail between the bolt and the corresponding bolt hole.



(a) Modelling of loading



(b) Modelling of bolts at supports

Figure 3-8 Modelling of loading and support conditions

At supports, bolts were simulated with 10mm thick quarter circular plates (see Fig.3-8(b)). The radius of the plate was equal to that of the bolt. The central node on the plate was vertically restrained. The nodes on the upper quarter of the bolt hole and the external circular surface of the plate were coupled together. This was done to avoid any additional rotational restraints about the major bending axis while minimising the adverse effect caused by unwanted stress concentration and excessive local distortion near the bolt-beam interface.



All cleats were treated as rigid bodies because their stiffness was significantly greater than that of the cold-formed sections. Full lateral restraints were imposed on the sigma purlin at mid-span and both ends. In the mid-span cross-sectional plane of the sigma purlin, the longitudinal movement was restrained at two nodes located in the upper and the lower outer webs. This was to prevent global movement of the purlin during the course of loading.

#### *3.8.1.3 Material property*

The material property of the purlin was modelled by using a multi-linear stress-strain model with von-Mises yield criterion and the isotropic hardening rule. The isotropic hardening option was chosen to accommodate the large-strain behaviour in the post-failure stage. The nonlinear material model was defined by the true stress-strain curve, which was derived from the tension coupon tests (see Appendix IV). As illustrated in Fig. 3-9, the curve starts from the origin and has an initial slope equal to the Young's modulus,  $E$  of steel. Denser data points were included in the curve where large curvature was present. The slope of the stress-strain curve reduces gradually until the ultimate stress,  $f_u$ , is reached. The slope beyond the ultimate stress was assumed to be zero. The Poisson's ratio,  $\nu$ , of the elements was assumed to be 0.3.

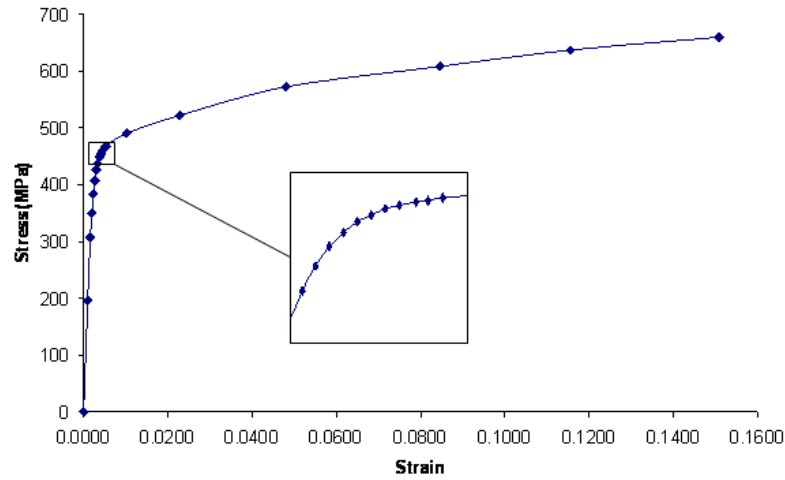
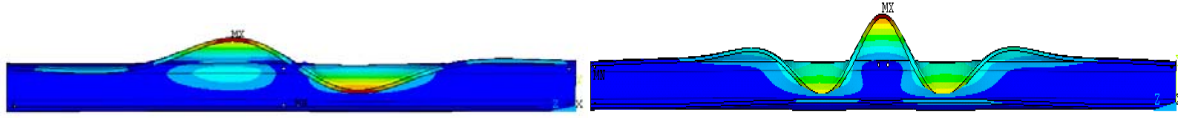


Figure 3-9 Typical stress-strain curve of beam material

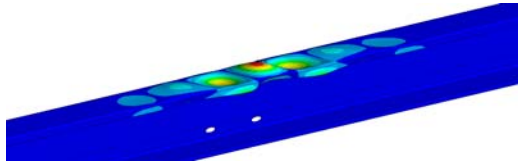
Elastic materials for bolts were modelled by using  $E = 210\text{kN/mm}^2$  and  $\nu = 0.3$ . Residual stress and strain hardening effects in the section resulting from the cold forming process were not included in this FE model due to the counteractive effect between these two factors (Schafer et. al., 2010; Dubina and Ungureanu, 2002).

#### 3.8.1.4 Geometric imperfections

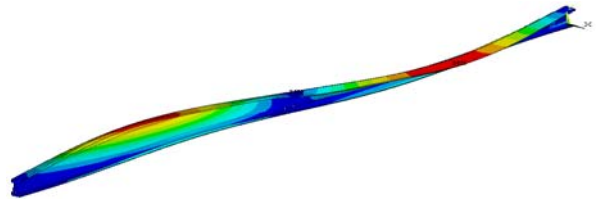
It is acknowledged that initial geometric imperfections play an important role in nonlinear behaviour of CFS members. In this research, they were introduced into the present FE modelling by the superposition of selected basic linear buckling modes (Sarawit et. al., 2003; Schafer et. al., 2006; Yang and Hancock, 2006; Kurniawan and Mahendran, 2009). Three types of basic imperfection shapes determined from linear buckling analysis are presented in Fig. 3-10, i.e. the local, distortional and lateral torsional buckling shapes.



(a). Distortional buckling mode: antisymmetric and symmetric



(b). Local buckling mode



(c). Lateral torsional buckling mode

Figure 3-10 Basic imperfection modes

Since the first buckling mode from elastic buckling analysis is usually critical on structural behaviour, the corresponding buckling shape was selected as one of the imperfection components for each specimen. Other modes were included only if the ratio of the respective buckling loads to the critical one was within 1.6. The amplitudes of local- and distortional-type imperfection shapes adopted in the model were determined by a trial and comparison process. Three different amplitudes were used for each buckling mode, i.e.  $0.14t$ ,  $0.66t$  and  $0.5t$  for local buckling type imperfection mode and  $0.64t$ ,  $1.55t$  and  $t$  for distortional buckling type imperfection mode, where  $t$  is the corresponding cross-sectional thickness. These chosen amplitudes were based on a statistical study by Schafer and Pekoz (1998). They represent the lower quartile (25%), the upper quartile (75%) and middle values of the measured imperfection sizes, respectively. The moment-rotation curves produced by the FE modelling using three different imperfection amplitudes are presented in Appendix V. By comparing with test results from Section 3.6,  $0.5t$  for the local buckling type imperfection mode and  $t$  for the distortional buckling-type imperfection mode were finally selected in this FE study as they produced the most satisfactory predictions. The amplitude

of the lateral torsional type imperfection mode was initially selected as the value suggested by BSI (2006a), i.e. the unrestrained span length divided by 1000. However, from the trial analysis, it was found that this value resulted in an overly conservative prediction. Hence, 1/1500 of the unrestrained span length was assumed in this study.

#### *3.8.1.5 Solution scheme*

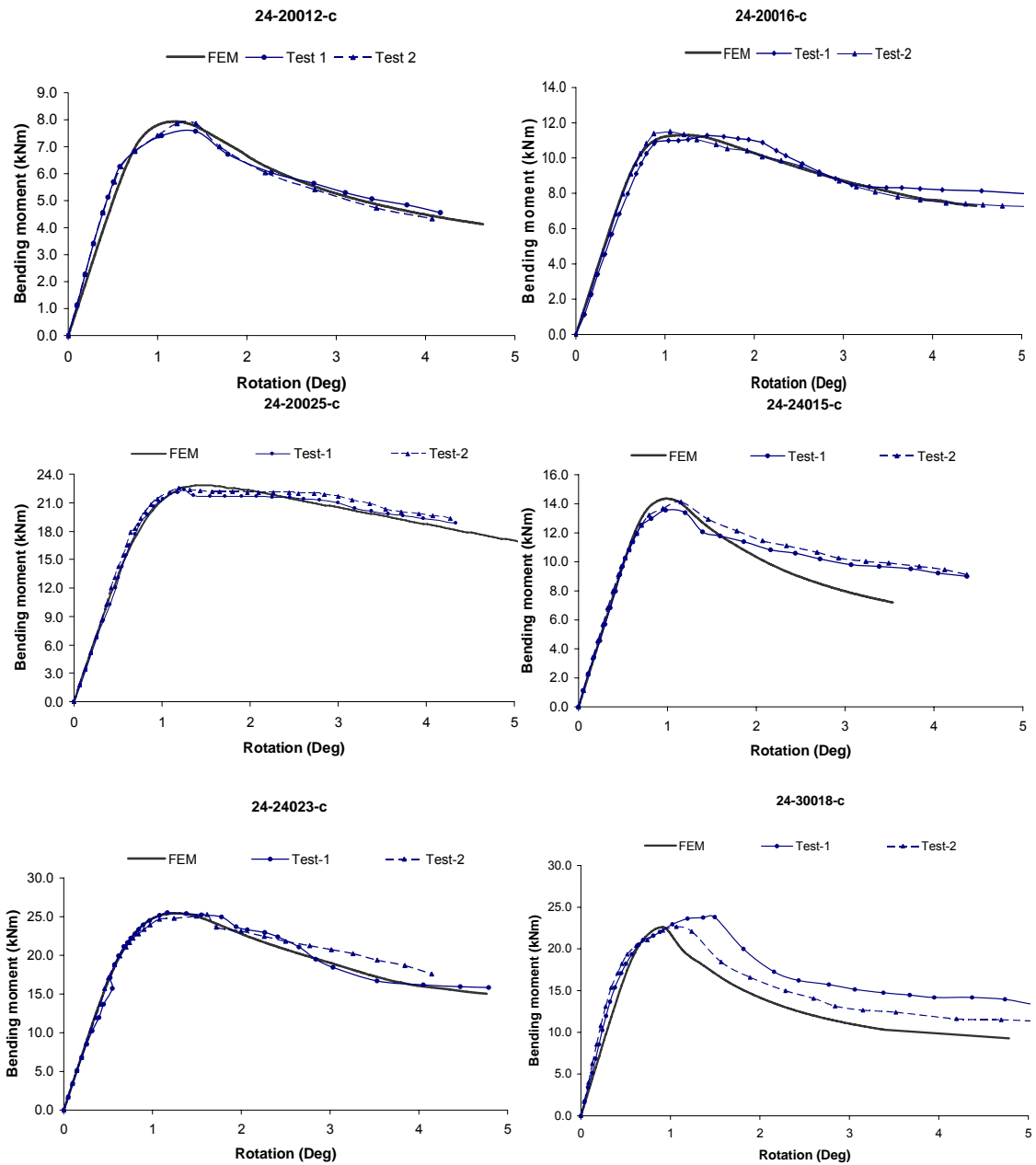
The arc-length method was used to obtain the full range of load-deflection responses in the FE modelling. The initial value of arc-length radius was set as the first buckling load divided by the selected increment value. In this modelling, the value was normally taken as 200-250, which was large enough to reach softening stage. The multiplier for the arc-length radius was set in a range between 1/1000 and 5. The arc-length radius was updated based on the number of iterations required in the previous load increment, and varies accordingly within the range of the specified limit. The solution ends when it fails to converge with the minimum arc-length radius.

#### *3.8.2 Numerical results and comparison with experimental data*

Twenty specimens were physically tested in ten different cases in the laboratory. These ten cases were modelled independently. Moment-rotation response curves obtained from the tests and FE simulations are presented in Fig. 3-11, in which the rotation was calculated by using the differential deflections between the mid- and quarter- span points.

As revealed in Fig. 3-11, all moment-rotation curves exhibit three noticeable stages, i.e. linear ascending, nonlinear ascending and nonlinear descending. They are respectively associated with the pre-buckling, post-buckling and post-failure behaviour of purlins. It can be seen that the

comparison of the pre-buckling curve between experimental and numerical results consistently agrees well. In the post buckling stage, FEA results show a marginally stiffer trend as demonstrated in 24-20012-c, 24-24015-c, 40-24030-c and 40-30030-c. A marked difference between the numerical and experimental results was observed for 24-30018-c and 40-30030-c in the post-failure stage. A similar difference was also noticed in the test results for the two duplicated 300 series specimens. This disparity may indicate that the nonlinear behaviour of the 300 series sections was more sensitive to imperfections. It can be seen in Table 3-3, however, that the observed disparity in post-failure behaviour only has a small influence on the ultimate moment resistance and the PPMR. It is worth noting that in the FE model, the boundary condition at both ends, as described in the preceding section, was effectively modelled to be simply supported. The excellent agreement of pre-buckling stiffness between the numerical and experimental results indicates that the partial fixity provided by two bolts at the supports was negligible in practice.



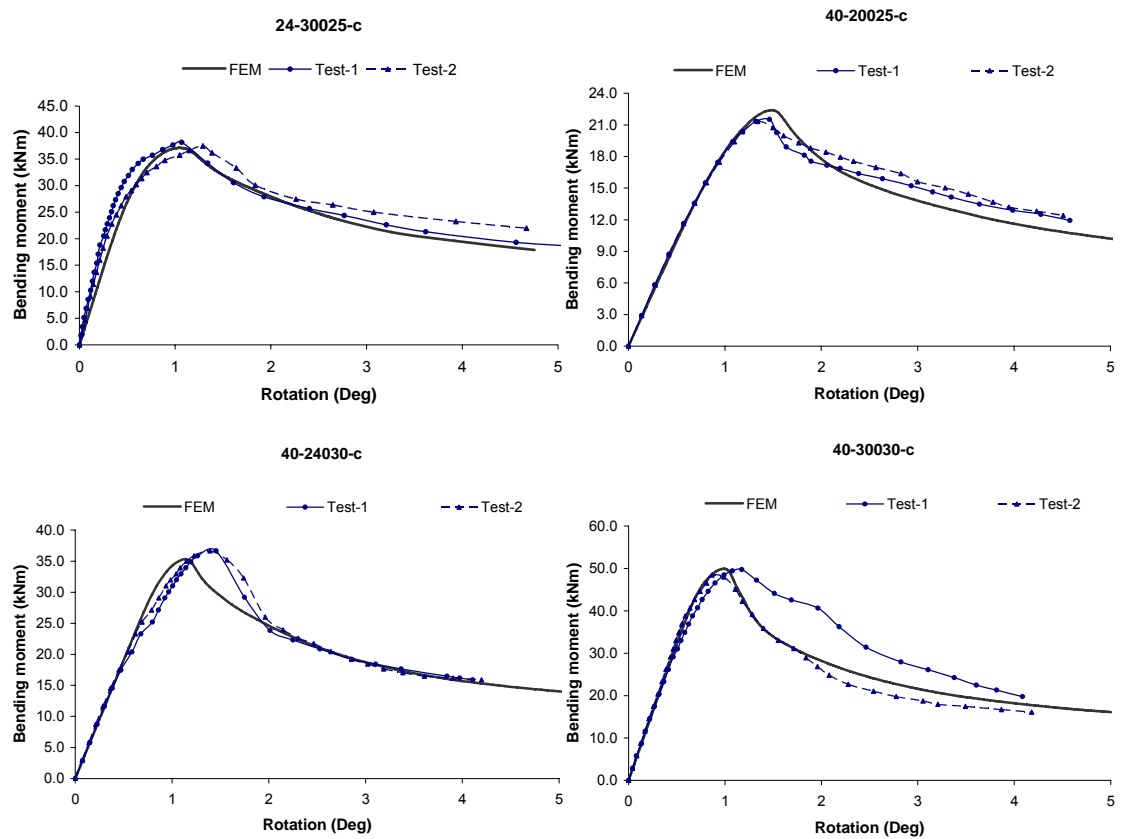


Figure 3-11 Comparison of moment-rotation curves between the experimental and FE results

Table 3-3 presents the failure modes, ultimate moment resistance and the PPMR obtained from the FEM results for the tested ten specimens. The moment resistance was taken as the peak values in the FE moment-rotation curves in Fig. 3-11. The determination of the PPMR was based on the method described in Chapter 2.6.2 and is demonstrated in Appendix VI. In the same table, similar results are also presented for the other seventeen specimens, for which there are no test results.

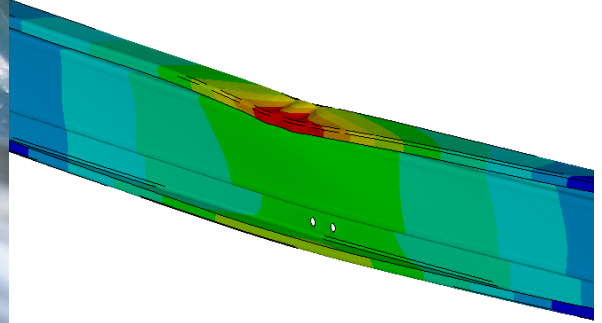
Specimen	Failure mode	Ultimate moment resistance $M_R$ (kNm)	PPMR $M_{PP}$ (kNm)
24-20012-c <sup>1</sup>	LB+DB	7.9	5.3
24-20016-c <sup>1</sup>	LB+DB	11.3	9.1
24-20025-c <sup>1</sup>	DB	22.8	20.8
40-20025-c <sup>1</sup>	LTB	22.4	9.4 <sup>2</sup>
24-24015-c <sup>1</sup>	LB+DB	14.4	8.4
24-24023-c <sup>1</sup>	DB	25.4	21.1
40-24030-c <sup>1</sup>	LTB	35.3	14.7 <sup>2</sup>
24-30018-c <sup>1</sup>	LB+DB	22.6	14.2
24-30025-c <sup>1</sup>	DB	37.1	28.3
40-30030-c <sup>1</sup>	DB+LTB	49.9	20.8 <sup>2</sup>
24-24030-c	DB	35.9	34.2
24-30030-c	DB	46.5	37.3
32-20012-c	LB+DB	8.2	4.6
32-20016-c	LB+DB	11.6	8.8
32-20025-c	DB	21.9	18.1
32-24015-c	LB+DB+LTB	14.7	7.6 <sup>2</sup>
32-24023-c	DB+LTB	26.6	12.1 <sup>2</sup>
32-24030-c	DB+LTB	36.8	18.5 <sup>2</sup>
32-30018-c	DB	24.1	13.9
32-30025-c	DB	40.4	27.6
32-30030-c	DB	49.8	36.4
40-20012-c	LB+DB+LTB	8.4	3.7 <sup>2</sup>
40-20016-c	LB+DB+LTB	11.9	7.1 <sup>2</sup>
40-24015-c	LB+DB+LTB	15.5	6.3 <sup>2</sup>
40-24023-c	LTB	24.9	10.0 <sup>2</sup>
40-30018-c	LB+DB+LTB	24.8	12.0 <sup>2</sup>
40-30025-c	DB+LTB	38.6	17.4 <sup>2</sup>

<sup>1</sup> Tested specimens; <sup>2</sup> LTB occurred

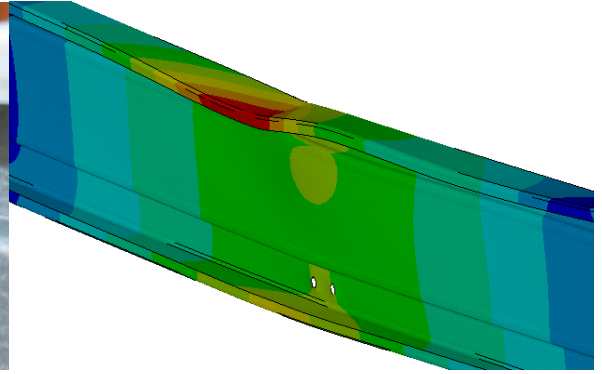
Table 3-3 Failure mode, moment resistance and the PPMR from FE analysis

The failure modes cited in Table 3-3 are presented in Fig. 3-12 by using photos taken from laboratory tests and pictures from the FE modelling results.

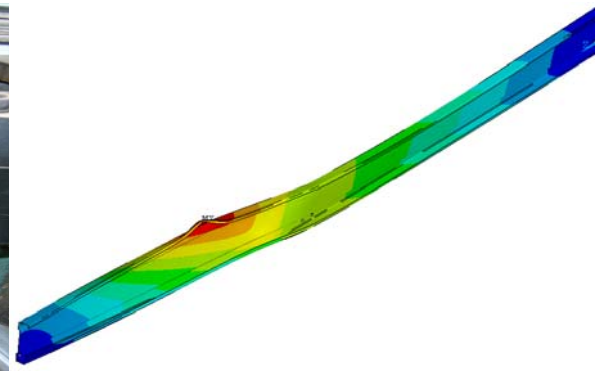




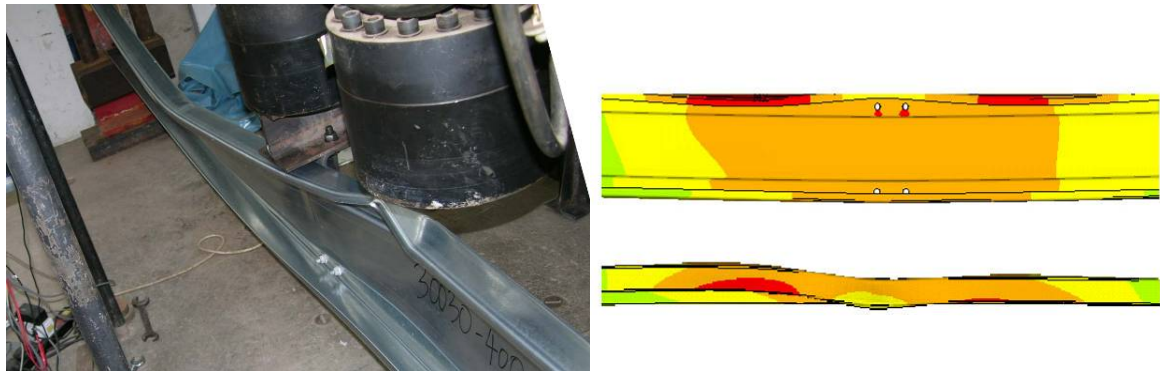
(a) LB+DB



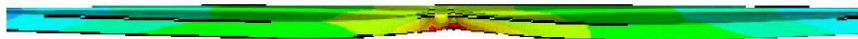
(b) DB



(c) LTB



(d) DB+LTB



(e) LB+DB+LTB

Figure 3-12 Failure modes

Table 3-4 presents the comparison between test results and predictions from the FE modelling. It reveals that the FE modelling was able to provide good predictions of the failure mode, ultimate moment resistance and the PPMR. The predicted values of ultimate moment resistance are in very good agreement with the experimental results; the difference of PPMR predictions was in a range of  $-2\%$  and  $7\%$  except for two specimens, i.e. 24-24015-c and 24-30018-c. However, predictions for these two specimens were on the safe side, and therefore, the results can still be deemed as being acceptable from a practical point of view.

Configuration	Coincidence of failure modes	Ultimate moment resistance $M_{\text{test}}(\text{mean}) / M_{\text{FEM}}$	PPMR $M_{\text{test}}(\text{mean}) / M_{\text{FEM}}$
24-20012-c	Yes	0.98	1.01
24-20016-c	Yes	1.01	0.98
24-20025-c	Yes	0.98	1.03
40-20025-c	Yes	0.96	NA*
24-24015-c	Yes	0.96	1.26
24-24023-c	Yes	1.00	1.05
40-24030-c	Yes	1.04	NA*
24-30018-c	Yes	1.03	1.30
24-30025-c	Yes	1.02	1.07
40-30030-c	Yes	0.98	NA*
Average		<b>1.00</b>	<b>1.10</b>
Standard deviation		<b>0.03</b>	<b>0.12</b>

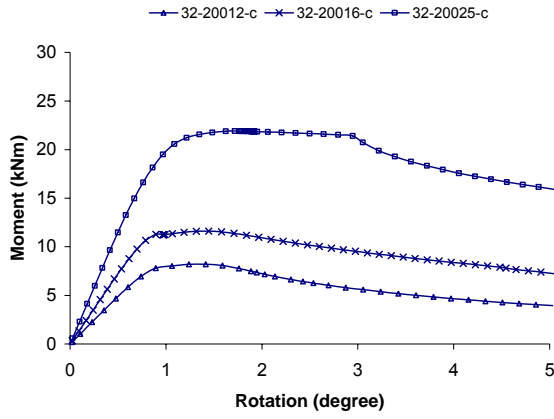
\*As the specimen failed due to LTB, the PPMR was not available from the test

Table 3-4 Comparison of moment resistance and PPMR between the experimental and the FE results

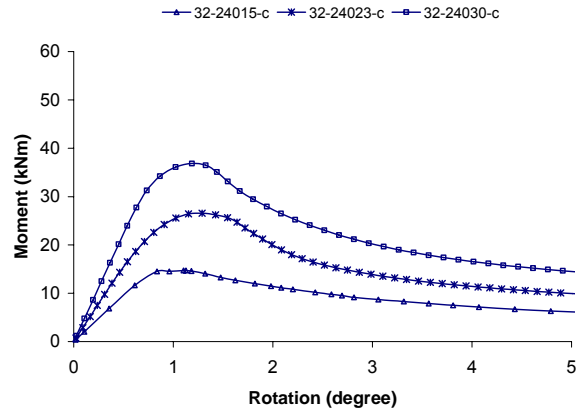
### 3.8.3 Parametric study

Following the successful verification of the numerical modelling, the established FE model was used to carry out a parametric study. The influence of geometric dimensions (the cross-sectional thickness, the depth, and the shear span) on the failure mode, the ultimate moment resistance and the PPMR of CFS sigma purlins at internal supports was studied. Three span lengths, i.e. 2.4 m, 3.2 m and 4.0 m, were selected for each section. These lengths approximately represent the length

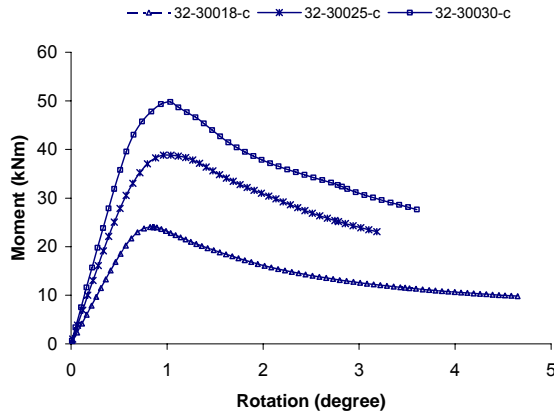
of hogging moment zone ( $0.4L$ ) of double span continuous beams with span length 6.0 m, 8.0 m and 10.0 m, respectively (BSI, 2006a). The study thus has covered the range of geometric dimensions that is most frequently used in practice. They were analysed by utilising the developed FE model. In this parametric study, the measured stress-strain data of the cross sections for the tested specimens were used for those untested specimens with the same nominal cross sections. Results of the analysis are summarised in Table 3-3. Curves of the moment-rotation response are plotted in Fig. 3-13, in which they are grouped into seven graphs based on three parameters, i.e. cross-sectional thickness (a-c), cross-sectional depth (d), and beam span (e-g). Table 3-3 and Fig. 3-13 (a-d) show that varying the thickness or depth will only, as expected, change the stiffness and the ultimate moment resistance, but will not alter the shape of the moment-rotation curve significantly. The thickness will affect the failure mode in a way that thin walled sections (e.g. 32-20012-c and 32-24015-c) will experience LB mode in addition to the other modes experienced by the thick counterpart. Table 3-3 and Fig. 3-13 (e-g) show that for a given section, the length has a modest effect on the moment-rotation curve unless the LTB mode becomes the dominant component in the failure mode as in specimens 32-24023-c, 40-24023-c and 40-30025-c. If this is case, the descending part of the curve will be steeper.



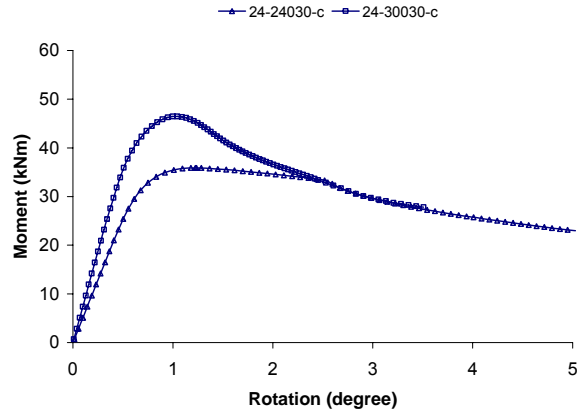
(a) 32-200 series with various thicknesses



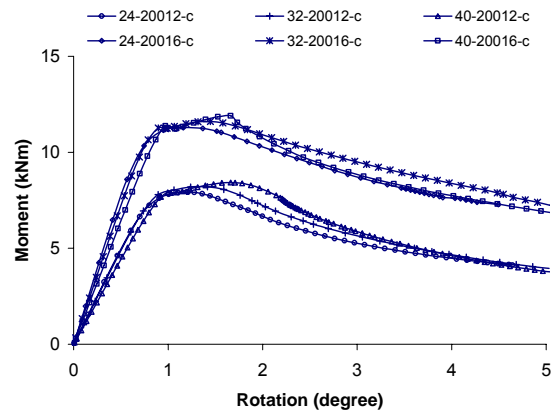
(b) 32-240 series with various thicknesses



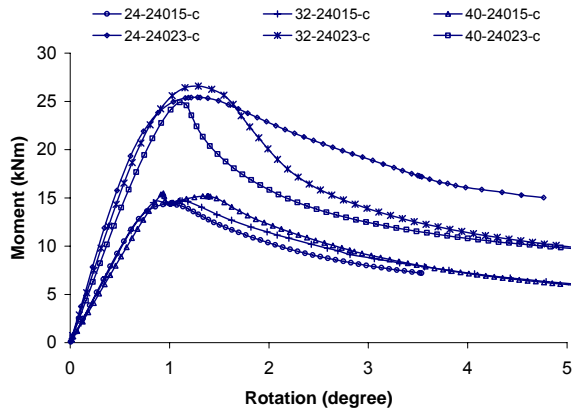
(c) 32-300 series with various thicknesses



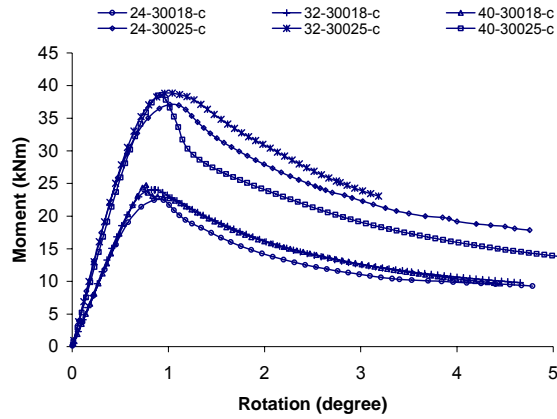
(d) 2.4m specimens with various depth



(e) 200 series with various lengths



(f) 240 series with various lengths



(g) 300 series with various lengths

Figure 3-13 Moment-rotation curves from FE analysis

### 3.9 COMPARISON OF THE PREDICTED MOMENT RESISTANCE WITH CURRENT CODES OF PRACTICE

In order to determine the PPMR, which is usually presented as a fraction of the ultimate moment resistance (UMR), it is worth first examining the theoretical UMR predictions obtained by codified methods (BSI, 2006a; AISI, 2007; Standards Australia, 2006).

It is noted that, apart from high bending moment near internal supports, shear force is also presented concurrently. Both BSI (2006a) and AISI (2007)/Standards Australia (2006) provide methods to consider the interaction effect of bending moment and shear force. Table 3-5 presents the results of the calculated ultimate moment resistance  $M_E$  and  $M_D$ , and shear resistance  $V_E$  and  $V_D$ , by using the EWM in BSI (2006a) and the DSM in AISI (2007)/Standards Australia (2006). Subscripts E and D represent the prediction method, i.e. the EWM and the DSM, respectively, by which the theoretical results were obtained. For instance,  $M_E$  represents the calculated result of

ultimate moment resistance by following the EWM. For the tested specimens, the calculations were all based on the measured Young's modulus, 0.2% proof stress and thickness. While for the untested specimens, the calculations were all based on the measured Young's modulus and 0.2% proof stress of the identical cross sections used in the test specimens but the nominal cross-sectional thickness. Taking one untested specimen 24-24030-c for instance, the calculation was based on the measured Young's modulus and 0.2% proof stress of the cross section 24030 used in the specimen 40-24030-c1 (which is tested), but the nominal cross-sectional thickness, i.e. 3.0mm. The material properties used in the calculations therefore all agree with those used in FE analysis.

Specimen <sup>1</sup>	$M_E$ (kNm)	$V_E$ (kN)	$M_D$ (kNm)	$V_D$ (kN)	Specimen	$M_E$ (kNm)	$V_E$ (kN)	$M_D$ (kNm)	$V_D$ (kN)
24-20012-c1	7.7	27.8	8.6	33.8	24-24030-c	31.5	147.5	35.9	201.6
24-20012-c2	8.2	29.4	9.1	37.2	24-30030-c	40.5	137.7	45.7	190.1
24-20016-c1	11.4	44.4	12.0	65.3	32-20012-c	7.4	27.4	8.6	32.9
24-20016-c2	11.4	44.4	12.0	65.3	32-20016-c	11.1	44.9	12.2	66.1
24-20025-c1	20.1	98.3	21.4	136.4	32-20025-c	19.4	102.8	22.1	143.0
24-20025-c2	20.3	99.8	21.6	138.6	32-24015-c	13.3	42.5	15.3	48.3
40-20025-c1	17.3	99.8	20.9	138.6	32-24023-c	21.5	87.7	25.3	124.8
40-20025-c2	17.4	100.5	21.0	139.7	32-24030-c	29.6	147.5	35.4	201.6
24-24015-c1	13.9	42.0	15.1	47.3	32-30018-c	21.8	56.0	24.5	60.8
24-24015-c2	13.9	42.0	15.1	47.3	32-30025-c	33.7	101.2	37.7	150.1
24-24023-c1	22.7	83.4	24.4	118.3	32-30030-c	39.8	137.7	45.7	190.1
24-24023-c2	22.7	83.4	24.4	118.3	40-20012-c	7.0	27.4	8.6	32.9
40-24030-c1	26.8	146.6	32.6	200.2	40-20016-c	10.3	44.9	12.2	66.1
40-24030-c2	27.0	148.5	32.8	202.9	40-24015-c	11.9	42.5	15.3	48.3
24-30018-c1	21.7	55.5	24.3	59.8	40-24023-c	20.2	87.7	25.3	124.8
24-30018-c2	21.6	54.9	24.1	58.8	40-30018-c	20.8	56.0	24.5	60.8
24-30025-c1	33.0	95.9	36.3	137.8	40-30025-c	31.8	101.2	37.7	150.1
24-30025-c2	33.4	97.4	36.7	141.2					
40-30030-c1	36.9	131.8	44.4	181.4					
40-30030-c2	36.6	130.1	44.0	178.9					

<sup>1</sup> Tested specimens

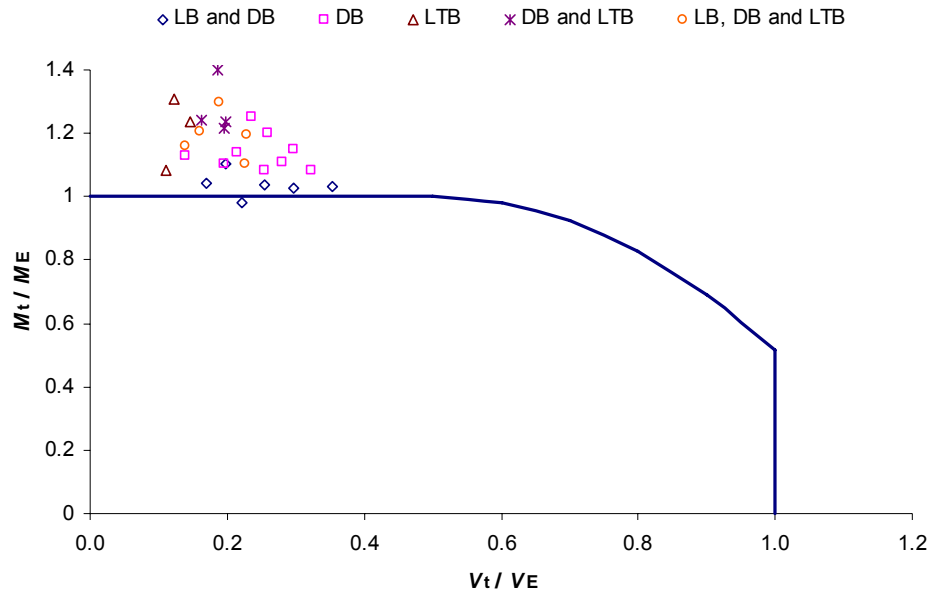
Table 3-5 Predicted ultimate moment and shear resistance based on the EWM and the DSM

It is worth mentioning that in the determination of  $M_E$  for sigma sections, BSI (2006a) does not provide a specific clause accounting for the favourable effect of the web stiffeners on the distortional buckling behaviour. The analytical model proposed by Li and Chen (2008) was employed to allow for this favourable effect.

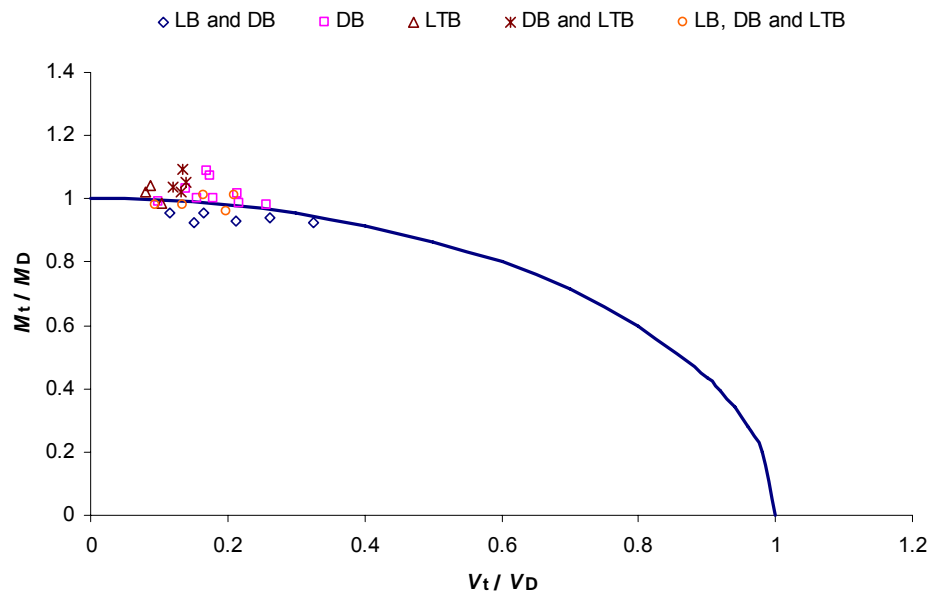
Dimensionless failure envelope curves considering the interaction between the bending moment and shear force are shown in Fig. 3-14. The curve in Fig. 3-14 (a) was based on the interaction design equation suggested by BSI (2006a), in which the shear action only affected the failure load when the shear force was greater than half of the shear resistance.  $M_E$  and  $V_E$  shown in Fig. 3-14 (a) are the resistance of the member under sole bending or shear action, respectively, and their values were calculated by using the EWM in BSI (2006a) and are presented in Table 3-5. In Fig. 3-14 (b), the elliptical curve was plotted on the basis of the design equation in AISI (2007)/Standard Australia (2006).  $M_D$  and  $V_D$  shown in Fig. 3-14 (b) are also the resistance of the member under sole bending or shear action, respectively, but their values were calculated by using the DSM in AISI (2007)/Standard Australia (2006). The values of  $M_D$  and  $V_D$  are also presented in Table 3-5. In Fig. 3-14,  $M_t$  and  $V_t$  represent the bending moment and the shear force of the member at the ultimate load state. The ultimate loads from the FE analysis were used to find the moment ( $M_t$ ) and shear force ( $V_t$ ). Ratios of  $V_t$  to  $V_E$  were plotted against ratios of  $M_t$  to  $M_E$  in Fig. 3-14 (a), and ratios of  $V_t$  to  $V_D$  were plotted against ratios of  $M_t$  to  $M_D$  in Fig. 3-14 (b). According to their failure modes observed from numerical modelling, the studied specimens were categorised into five groups, i.e. combined local and distortional buckling mode (LB and DB), distortional buckling mode (DB), lateral torsional buckling mode (LTB), combined distortional



and lateral torsional buckling mode (DB and LTB), and combined local, distortional and lateral torsional buckling mode (LB, DB and LTB), as shown in Fig. 3-14.



(a) Interaction curve based on BSI (2006a)



(b) Interaction curve based on AISI (2007)/Standard Australia (2006)

Figure 3-14 Ratio of cross-sectional resistance between the numerical and theoretical results considering the interaction of bending and shear

It can be seen from Fig. 3-14, that the EWM provided good predictions for the combined LB and DB specimens, moderately conservative predictions for the DB specimens, and overly conservative predictions for the LTB related specimens. In contrast, the DSM provided good predictions for the LTB related specimens, slightly conservative predictions for the DB specimens, and unsafe predictions for the combined LB and DB specimens.

In the EWM suggested in BSI (2006a), it was assumed that the compression flange experienced local buckling first, and that next the compression flange and the lip underwent distortional buckling. An iteration process was undertaken to consider the interaction of these two buckling modes until a converged effective area was attained. This process corresponded well with the buckling behaviour of the combined LB and DB specimens observed from the tests or FE analysis. Therefore it explains why the EWM produced good predictions for those specimens. In the DSM suggested in AISI (2007)/Standards Australia (2006), however, the local buckling and distortional buckling were considered independently. Test or FE analysis observations revealed that the LB-initiated specimens had experienced a noticeable coupled local-distortional buckling mode in the post-buckling stage (see Fig. 3-12 (a)), and therefore neglecting this interaction leads to the unsafe predictions, as indicated by the results in Fig. 3-14 (b).

For the DB specimens, it was observed that failure was primarily associated with distortional buckling, and no strong evidence of local buckling was observed (see Fig. 3-12 (b)). This phenomenon can be well represented by the prediction process by using the DSM. The EWM, however, has automatically included the interaction effect between the local and distortional buckling by the iteration process. Therefore, predictions by the DSM were closer to the test or FE

results for this group of specimens than those by the EWM. Additionally, since neither the EWM nor the DSM has included the beneficial effect (Yu and Schafer, 2007) of moment gradient on the distortional buckling strength, somewhat conservativeness may also be introduced in the predictions by both methods.

The LTB related specimens have three subcategories, i.e. LTB only specimens, combined DB and LTB specimens, and combined LB, DB and LTB specimens. It is found that the DSM is able to produce good predictions for the LTB only and the combined LB, DB and LTB specimens, and slightly conservative predictions for the combined DB and LTB specimens. On the other hand, the EWM produced overly conservative predictions for all of the LTB related specimens. The underestimation is primarily attributed to two factors. Firstly, for LTB susceptible members, BSI (2006a) recommends using buckling curve *b* to calculate LTB resistance for cold-formed sections. However, since these curves were mainly derived from hot rolled or welded steel sections, their applicability to CFS sections is unproven. According to the observation from Fig. 3-14 (a), the adoption of curve *b* appears to result in conservative predictions for all LTB related specimens. Secondly, for LTB susceptible specimens, a rapid failure was usually observed after LTB occurred. This suggests that LB or DB cannot be substantially developed prior to failure if LTB had already started in these specimens. This can be shown by Fig. 3-12 (c), in which neither LB nor DB was developed near the critical section caused by the LTB, i.e. the quarter-span section. Therefore the inclusion of the reduction effect associated with local/distortional buckling in the EWM inherently can lead to a conservative prediction. Unlike the EWM, in the DSM, the interaction between LB and LTB was only considered if the square root of the nominal LTB moment resistance to critical LB moment ratio was greater than 0.776. This assumption agrees

well with the test observations. Therefore, for LTB related specimens, the DSM provides more accurate predictions than the EWM.

### 3.10 DESIGN PROPOSALS FOR THE IMPROVEMENT OF THE EWM AND THE DSM

The elastic critical buckling moments of each specimen by considering real loading conditions, i.e. three-point bending with mid-span point fully restrained, are presented in Table 3-6, where  $M_{cr, LB}$ ,  $M_{cr, DB}$  and  $M_{cr, LTB}$  represent the critical buckling moment for LB, DB and LTB, respectively. These values were obtained by running eigen-buckling analysis via the developed FE model. The initial buckling mode of each specimen can be identified by the lowest critical buckling moment, and the results are also presented in Table 3-6. By comparing the predicted buckling modes with the recorded test results in Table 3-2, it can be found that they are in almost perfect agreement except for specimens 24-30018-c1 and 24-30018-c2. The occurrence of these two anomalies was because the critical LB and DB moments were so close to each other that either LB or DB could take place first in the physical test. From the comparison of the initial buckling mode in Tables 3-2 and 3-6, it is suggested that the initial buckling mode can be predicted by running an eigen-buckling analysis for the beam considering the real loading conditions. Since the initial buckling mode of a CFS beam is highly associated with the failure mode of the member, the critical buckling moments of the member may be further extended to identify the failure mode of the member, as follows.

Specimen <sup>1</sup>	$M_{cr, LB}$ (kNm)	$M_{cr, DB}$ (kNm)	$M_{cr, LTB}$ (kNm)	Initial buckling mode	Specimen	$M_{cr, LB}$ (kNm)	$M_{cr, DB}$ (kNm)	$M_{cr, LTB}$ (kNm)	Initial buckling mode
24-20012-c1	10.6	15.1	51.6	LB	24-24030-c	197.8	105.1	152.0	DB
24-20012-c2	11.6	15.6	53.2	LB	24-30030-c	196.5	112.9	285.9	DB
24-20016-c1	24.3	26.0	68.9	LB	32-20012-c	10.4	13.1	28.1	LB
24-20016-c2	24.3	26.0	68.9	LB	32-20016-c	24.9	23.6	38.1	DB
24-20025-c1	82.3	56.7	98.1	DB	32-20025-c	88.5	54.9	60.3	DB
24-20025-c2	84.3	57.6	98.8	DB	32-24015-c	25.1	24.3	41.2	DB
24-24015-c1	24.5	26.4	78.3	LB	32-24023-c	86.9	55.7	55.0	LTB
24-24015-c2	24.5	26.4	78.3	LB	32-24030-c	198.7	98.3	83.5	LTB
24-24023-c1	80.0	56.8	111.6	DB	32-30018-c	43.5	38.8	99.0	DB
24-24023-c2	80.0	56.8	111.6	DB	32-30025-c	115.6	73.5	133.8	DB
24-30018-c1	42.5	41.5	188.4	DB	32-30030-c	197.5	105.5	157.5	DB
24-30018-c2	41.9	41.0	187.4	DB	40-20012-c	10.4	12.2	17.8	LB
24-30025-c1	105.7	75.4	249.1	DB	40-20016-c	24.9	22.5	23.6	DB
24-30025-c2	108.2	76.5	250.9	DB	40-24015-c	25.3	23.1	24.0	DB
40-20025-c1	85.4	51.0	34.9	LTB	40-24023-c	87.2	53.2	41.7	LTB
40-20025-c2	86.4	51.4	35.0	LTB	40-30018-c	43.8	36.6	62.5	DB
40-24030-c1	198.4	94.4	53.7	LTB	40-30025-c	116.2	70.1	84.7	DB
40-24030-c2	202.5	95.6	54.0	LTB					
40-30030-c1	186.7	96.7	92.1	LTB					
40-30030-c2	183.0	95.4	91.0	LTB					

<sup>1</sup>Tested specimens

Table 3-6 Calculated elastic critical buckling moment by considering real loading conditions

Ratios of  $M_{cr,DB}$  to  $M_{cr,LB}$  are plotted against ratios of  $M_{cr,LTB}$  to  $M_{cr,LB}$  in Fig. 3-15. It can be seen from Fig. 3-15 that the specimens fall into four distinct regions. One solid demarcation line and one dashed demarcation line are plotted in the same figure. It can be found that on or above the solid line specimens do not suffer from LTB, while below the solid line they are susceptible to LTB. On the left side of the dashed line most of the specimens do not undergo LB, while on the right side of the dashed line the specimens are all affected by LB. The solid demarcation line can be described by the following equations:

The first linear part ranging from 0 to 0.53 on the horizontal axis separates DB region and LTB region, and can be analytically expressed as follows:

$$M_{cr,LTB}/M_{cr,LB} = 0.77 \quad \text{when} \quad 0 \leq M_{cr,DB}/M_{cr,LB} \leq 0.53 \quad (3-1a)$$

The second nonlinear part ranging from 0.53 to 1.43 on the horizontal axis distinguishes the LB and DB failure modes from the LTB related failure modes, and the equation is:

$$M_{cr,LTB}/M_{cr,LB} = 2.57 \left( M_{cr,DB}/M_{cr,LB} \right)^2 - 0.43 \left( M_{cr,DB}/M_{cr,LB} \right) + 0.27$$

$$\text{when } 0.53 \leq M_{cr,DB}/M_{cr,LB} \leq 1.43 \quad (3-1b)$$

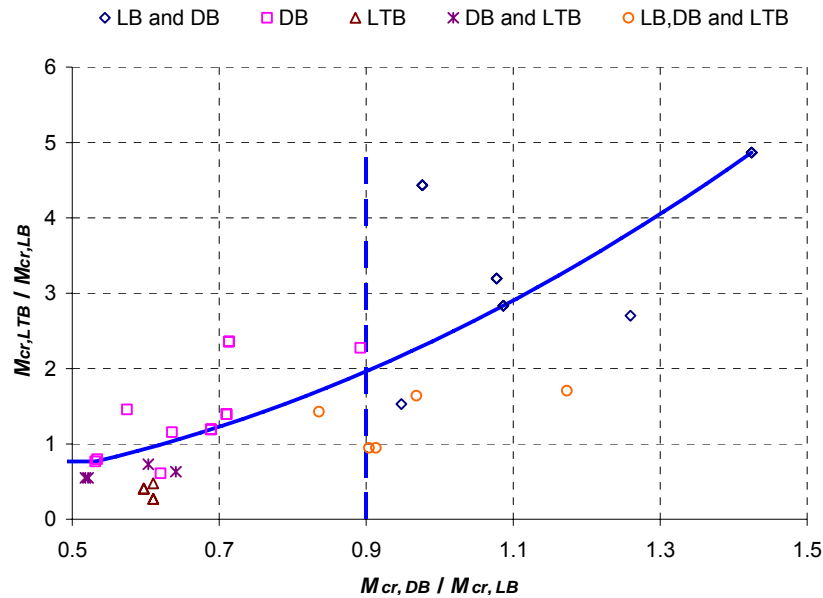


Figure 3-15 Distribution of failure mode in relation to ratios of various buckling moments

It is worth noting that this approach to identify the potential failure mode is only applicable for CFS sigma purlins with thin-walled cross sections. For beams with compact cross sections, buckling failure may no longer be the governing mode and therefore the above approach will not be applicable.

Once the potential failure mode of the beam is identified, the prediction of moment resistance by using the EWM and the DSM can be improved as follows.

As discussed above, the EWM were overly conservative for all LTB related beams. If BSI (2006a) is used to calculate the buckling resistance for a LTB susceptible beam at internal support (the identification of this type of beam can be implemented with reference to the solid demarcation line in Fig. 3-15), buckling curve *a* in BSI (2005a) is suggested instead of the currently suggested

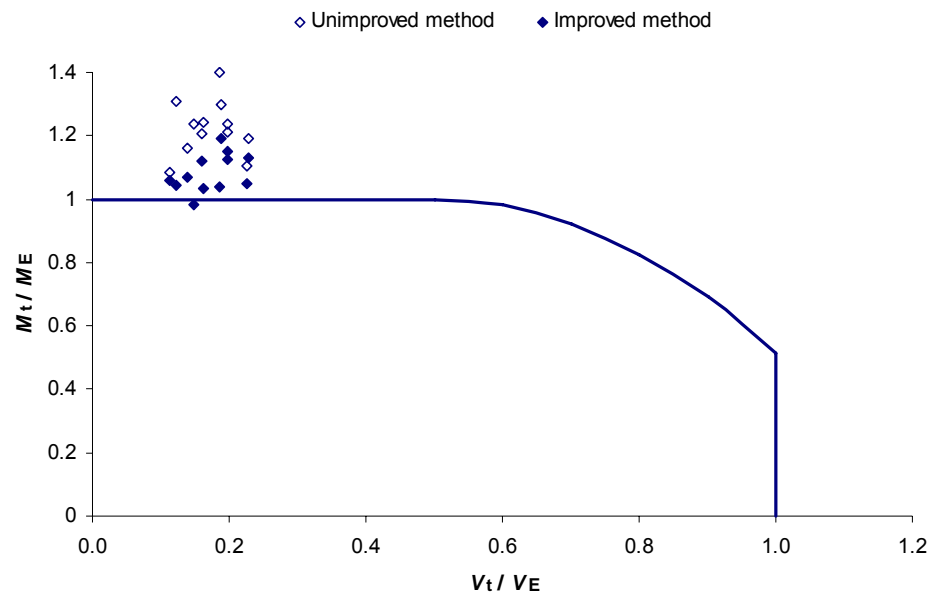
curve *b*. In addition, for LTB-initiated beams, i.e. beams having the LTB initial buckling mode predicted by the above-mentioned eigen-buckling analysis, the design method can be further improved as follows. As stated in the preceding section, LTB-initiated members will only have a limited level of post-buckling strength, and as such, unless the critical LB moment is sufficiently close to the LTB moment, the likelihood of developing an LB mode in the post-buckling stage is low. Therefore, for this type of member, a gross cross-section should be considered in predicting the LTB moment. A proposal has been made in AISI (2007)/Standards Australia (2006) that when the square root of the nominal LTB to the critical LB moment ratio is not greater than 0.776, the interaction effect can be neglected. The same proposal can be utilised here to improve the EWM prediction: for an LTB-initiated member, if the square root of the critical LTB to the critical LB moment ratio is not greater than 0.776, i.e.  $\sqrt{M_{cr,LTB} / M_{cr,LB}} \leq 0.776$ , then the gross cross section should be chosen in calculating the ultimate moment resistance,  $M_E$ . Otherwise, the effective cross-section should be used. As the critical LTB moment of a member will not be less than the nominal LTB moment quoted in AISI (2007)/Standards Australia (2006), this proposed range by using the former is a more cautious approach.

If AISI (2007)/Standards Australia (2006) are used to design a LB initiated member, the unsafe predictions from the DSM can be improved by introducing a simple correction factor of 0.92, when the member meets the criteria of  $0.70 \leq M_{cr,LB}/M_{cr,DB} \leq 1.06$ . The corrected moment resistance will therefore be  $M_D \times 0.92$ , where  $M_D$  is the predicted ultimate moment resistance by using the existing DSM. This range is defined on the basis of the specimens used in this experimental and numerical study, and it may be extended when more data are available.

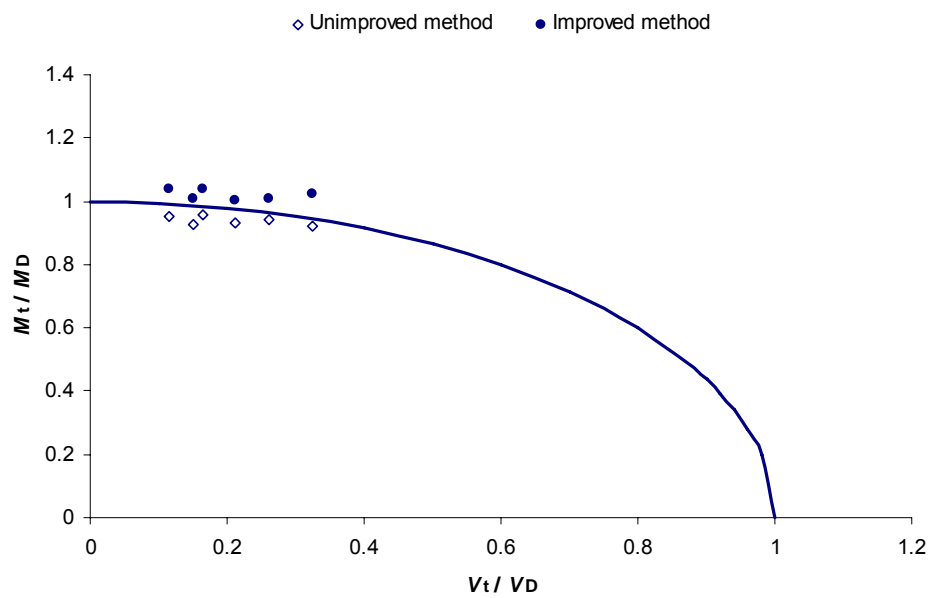


Fig. 3-16 presents the comparison of predictions by using the unimproved and improved methods.

It can be seen that the proposed methods are able to provide predictions with better accuracy.



(a) BSI (2006a) method



(b) AISI (2007)/Standards Australia (2006) method

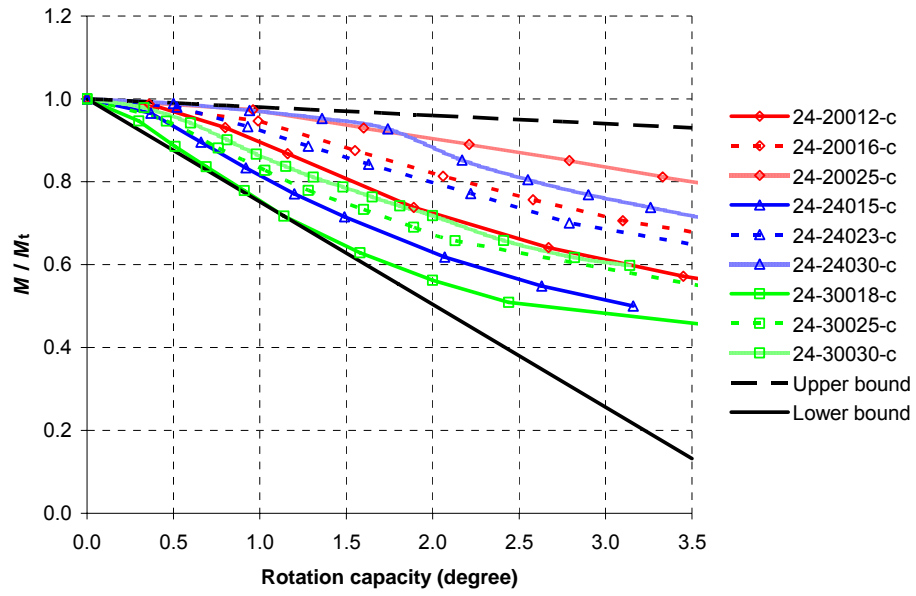
Figure 3-16 Comparison of unimproved and improved methods

### 3.11 MOMENT VERSUS PSEUDO-PLASTIC ROTATION CURVES

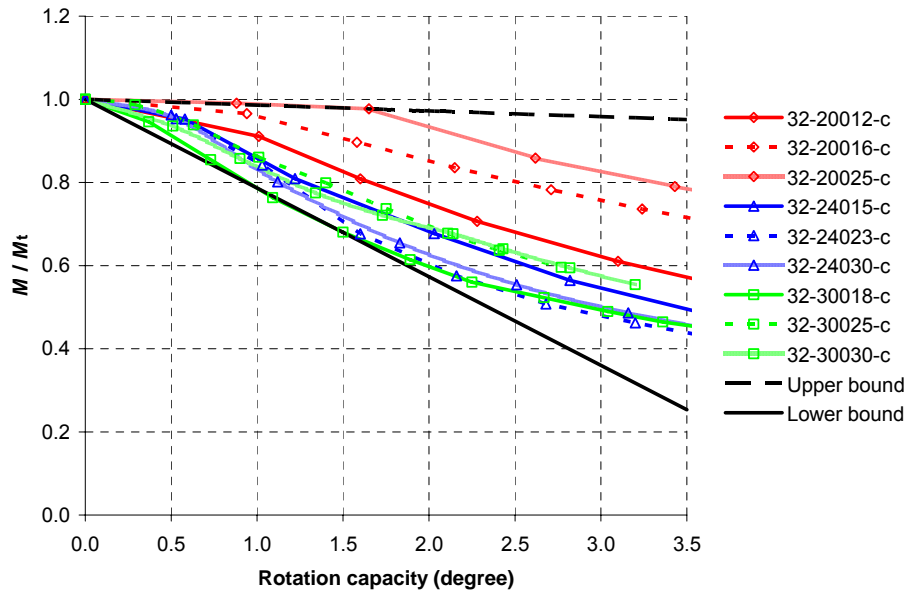
In the moment-rotation curves as presented in Fig. 3-13, if we draw a horizontal line at any moment level  $M$ , the difference of the two intersection points can be defined as the rotation capacity associated with  $M$ . It is apparent that at the peak moment level, the rotation capacity is zero. It will increase as the moment decreases. By extracting the data from the moment-rotation curves in Fig. 3-13, the moment vs. rotation capacity curves can be obtained, as demonstrated in Fig. 3-17. In this figure,  $M$  is normalised by  $M_t$ , which is the ultimate moment resistance from numerical analysis. Results are presented in three groups with respect to span length.

By comparing the moment-rotation capacity curves presented in Fig. 3-17, it is found that for the beams with a given span length, the softening rate of these curves was increased as either the section thickness was decreased or the section depth was increased, provided that the beams are resistant to LTB (these beams include all the 2.4m span beams, 32-20012-c, 32-20016-c, 32-20025-c, 32-30018-c, 32-30025-c and 32-30030-c). This observation reveals that a greater depth-to-thickness ratio of constituent plates leads to a more rapid loss in post-failure strength of the beams. It was also found that the span length appears to have marginal influence on the softening rate of the curves, provided that the beams are resistant to LTB. As demonstrated in Fig. 3-17 (a) and (b), the slope angles of the curves for 2.4m span beams are in a range from  $-1.1^\circ$  to  $-14.2^\circ$ , while those for 3.2m span beams are in a range from  $-0.8^\circ$  to  $-12.2^\circ$ . However, if the span length becomes so long that LTB is triggered, the softening rate can be significantly increased. This can

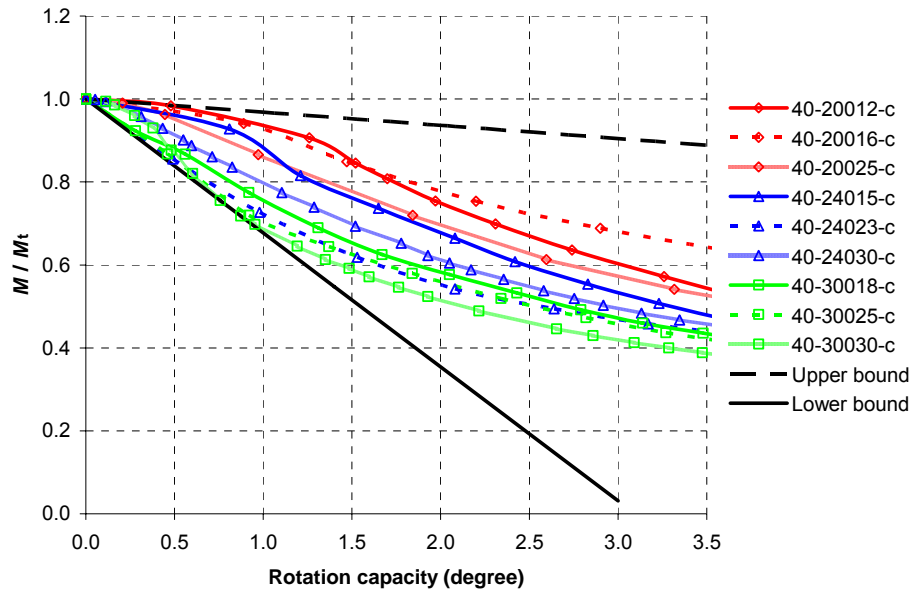
be shown by Fig. 3-17 (c), in which all of the 4.0m span beams experienced LTB and the slope angles of the curves are in a range from  $-1.8^\circ$  to  $-18.5^\circ$ .



(a) 2.4m span length



(b) 3.2m span length



(c) 4.0m span length

Figure 3-17 Moment vs. rotation capacity curves

### 3.12 A SEMI-EMPIRICAL METHOD TO DETERMINE THE PPMR AND A DESIGN EXAMPLE BY USING THE PSEUDO-PLASTIC DESIGN METHOD

Based on the discussions in the previous section, it is known that for a continuous CFS sigma purlin at internal support, provided that it is resistant to LTB, the decreasing rate of its moment-rotation capacity curve is closely related to the depth-to-thickness ratios of the constituent plates, i.e. the slenderness of the beam. The relationship is such that higher slenderness leads to a greater rate of descent. Since the calculation of the PPMR uses the moment-rotation capacity characteristic, it can be concluded that the PPMR is also greatly related to the slenderness of the beam. A relationship between the PPMR and the slenderness was consequently established, as demonstrated in Fig. 3-18. Fig. 3-18 presents a curve reflecting the correlation of the PPMR and

the slenderness, in which  $M_{PPMR}$  represents the PPMR listed in Table 3-3 which is normalised by the ultimate moment resistance  $M_E$  calculated based on BSI (2006a).  $M_y$  is the first yield moment of the gross cross section and  $M_{cr}$  is the critical elastic buckling moment of the specimen based on the gross cross section under central point load and laterally braced at the loading point and both supports. The curve is defined by the lower bound of all data points representing beams whose failure did not involve LTB. This curve is composed of two parts. The first part is a horizontal line  $M_{PPMR} / M_E = 1$  for the slenderness range between 0 and 0.627. The second part corresponds to higher slenderness values from 0.627 to 1.1. The PPMR can be obtained from the equation

$$M_{PPMR} / M_E = 1.9(M_y / M_{cr}) - 4.2\sqrt{M_y / M_{cr}} + 2.9 \quad (3-2)$$

It should be noted that Eq. (3-2) can only be applicable for beams resistant to LTB. With the aid of Fig. 3-15 (or Eq. (3-1a and 3-1b)), those relevant beams can be identified, i.e. beams on or above the solid curve in Fig. 3-15.

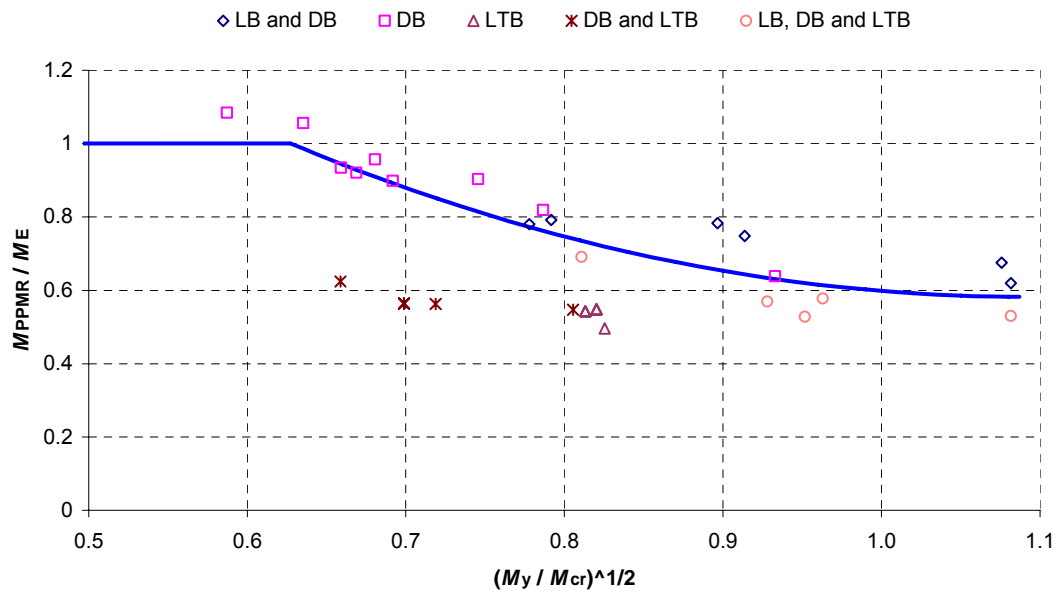


Figure 3-18 PPMR against slenderness curve

The procedure to determine the PPMR at internal support of two-span continuous sigma purlins comprises the following two steps: (1) only consider the hogging moment zone and treat it as a simply supported beam subjected to a central point load; determine whether the beam will experience LTB related failure modes by using Eq. 3-1a and 3-1b; (2) if the failure involves LTB, the pseudo-plastic design method is not recommended; otherwise, Eq. 3-2 can be used to find the PPMR.

Consider an example of a double beam with sigma 30018 section subjected to a uniformly distributed load, as illustrated in Fig. 3-19. The beam is laterally and torsionally restrained at the supports, and also laterally and torsionally restrained by sheeting on the top flange. The beam has a single span length of 6m, Young's modulus  $210\text{kN/mm}^2$ , yield stress  $450\text{N/mm}^2$  and a cross-sectional thickness of 1.8 mm. The pseudo-plastic design process is outlined as follows:

- 1) Calculate the ultimate moment resistance  $M_E$  by using the EWM suggested in BSI (2006a), which yields:

$$M_E = 21.8\text{kNm}$$

- 2) Calculate the first yield moment  $M_y$  of the gross cross section:

$M_y = 33.4\text{kNm}$ ; as  $M_E < M_y$ , it is known that sigma 30018 section is classed as a thin-walled section.

- 3) Calculate the critical buckling moments of LB, DB and LTB (by running an eigen-buckling analysis via any applicable FE programmes) for the beam in the hogging moment zone. This part of the beam is treated as a simply supported beam with a span

length of  $0.4L$  (i.e. 2.4m) subjected to a central point load (the load application point is restrained laterally and torsionally).

$$M_{cr, LB} = 43.8 \text{ kNm}; M_{cr, DB} = 42.5; M_{cr, LTB} = 189.8 \text{ kN}$$

with reference to Fig. 3-15, it is known that  $M_{cr, DB} / M_{cr, LB}$  against  $M_{cr, LTB} / M_{cr, LB}$  is above the solid demarcation line; therefore this beam is applicable to the pseudo-plastic design method

- 4) The critical elastic buckling moment of the beam is equal to the minimum value of

$$M_{cr, LB}, M_{cr, DB} \text{ and } M_{cr, LTB}$$

$$M_{cr} = 42.5 \text{ kNm}$$

- 5) Calculate the PPMR by using the author's Eq. (3-2)

$$M_{pp} = 14.6 \text{ kNm}$$

- 6) Calculate the load  $q_1$  that results in the ascertained PPMR at the internal support by elastic analysis:

$$q_1 = 8 \times M_{pp} / L^2 = 3.2 \text{ kN/m}$$

- 7) Calculate the excess load  $q_2$  that yields a total sagging moment equal to the ultimate moment resistance  $M_E$  after the plastic hinge zone is formed:

$$q_2 = M_E (4 - 6M_{pp} / M_E + 4\sqrt{1 + M_{pp} / M_E}) / L^2 = 3.1 \text{ kN/m}$$

- 8) The load resistance is then equal to  $q_1 + q_2$ , i.e. 6.3kN/m.

Compared to the result from the elastic design method, i.e.  $8 \times M_E / L^2 = 4.8 \text{ kN/m}$ , this method provides an increase of 31%. If required, the rotation capacity of the section can also be obtained by using Eq. (2-11), in which  $M = M_{pp} = 14.6 \text{ kNm}$ ,  $M_{c, Rd} = M_E = 21.8 \text{ kNm}$  and  $I_{eff} = 1013 \text{ cm}^4$ , so that  $\Theta_{pp} = 1.5^\circ$ .

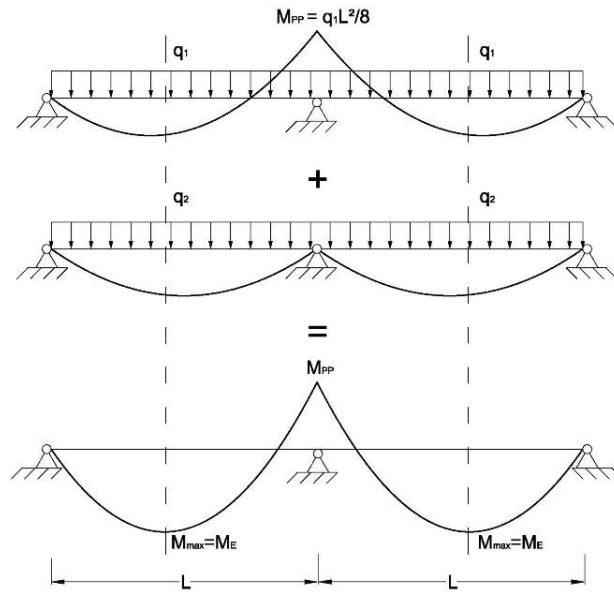


Figure 3-19 Illustration of the bending moment redistribution using the proposed pseudo-plastic design method

To demonstrate the validity of the proposed PPMR used in the pseudo-plastic design method, the ultimate load of a double span sigma 30018 purlin is numerically assessed by using the developed FE model. In practice, the top flange of the purlin is attached to sheeting, which provides lateral and torsional restraints to the purlin. The degree of the lateral restraint and the torsional restraint supplied are strongly affected by the shear and in-plane bending stiffness of the sheeting and the rotational stiffness at the sheeting/purlin screw connections. Since the sheeting normally has adequate shear stiffness, it is usually considered that the sheeting can provide fully effective lateral restraint to the purlin; whereas a partial torsional restraint is assumed, as suggested by other researchers (e.g. Ings and Trahair, 1984; Vieira et al., 2010). In this numerical assessment, two extreme cases of torsional restraint are considered. The first is that the top flange has full torsional restraint, and the second one is that the top flange of the beam has no torsional restraint.



Therefore, the numerically predicted load resistance from these two cases will represent the upper and lower bounds. Fig. 3-20 presents the comparison of the load-deflection curves between the analytical and numerical predictions. The mid-span deflections caused by loads  $q_1$  and  $q_2$  as defined above are calculated by using equations  $\Delta_1 = \frac{q_1 L^4}{192EI_{eff}}$  and  $\Delta_2 = \frac{5q_2 L^4}{384EI_{eff}}$ , respectively. It

is noted that for the beam with full lateral and torsional restraints, the numerical load-deflection curve does not have any descending part. This is because under the full lateral and torsional restraint condition, a catenary action will be developed so that the applied load continues growing as the displacement increases. In order to avoid any overestimation of the ultimate load for this case, the load level causing the first yield of the cross section in the sagging moment zone is chosen as the failure load of the beam. This choice of failure load agrees with the definition recommended in current codes of practice (BSI, 2006a; AISI, 2007; Standards Australia, 2006) for CFS sections. The upper bound and the lower bound predictions for the load resistance of the purlin hence are 7.6kN/m and 6.4kN/m, as shown in Fig. 3-20. By comparing these two values with the analytical value, i.e. 6.3kN/m, the safety of the proposed PPMR can therefore be proved.

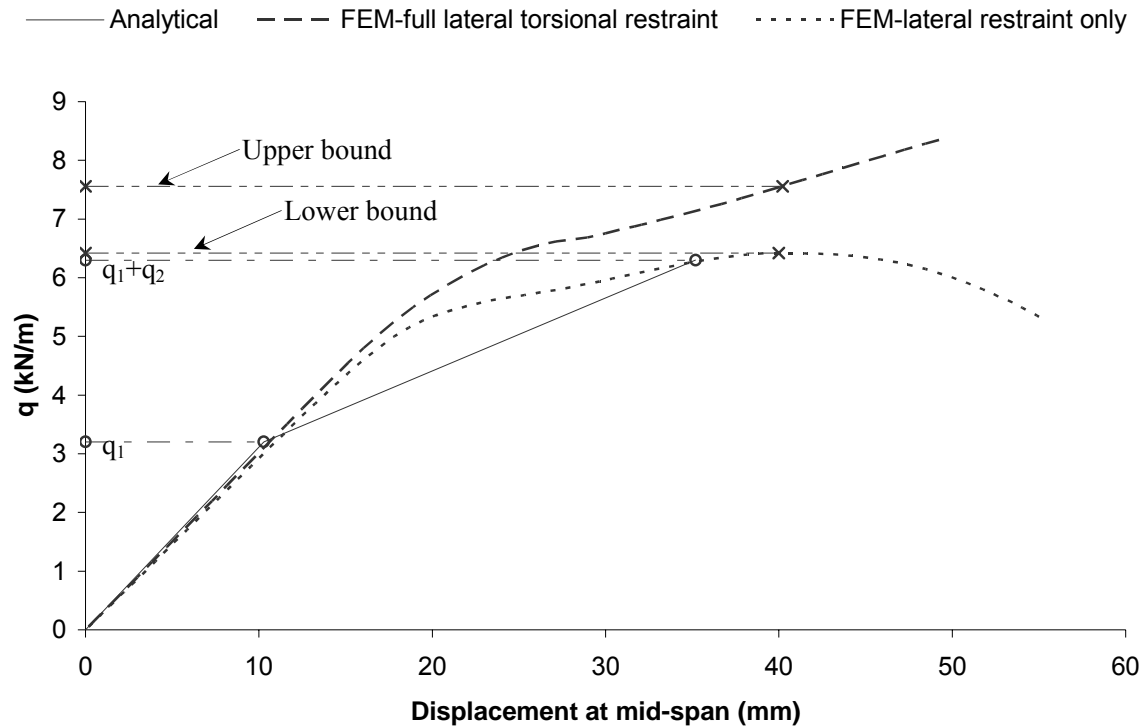
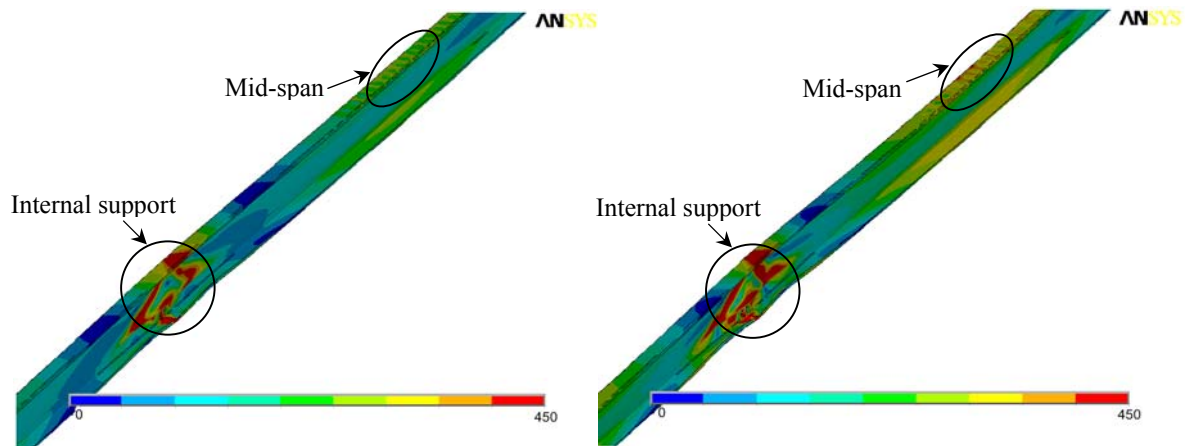


Figure 3-20 Analytically and numerically predicted load-deflection curves for the double span purlin

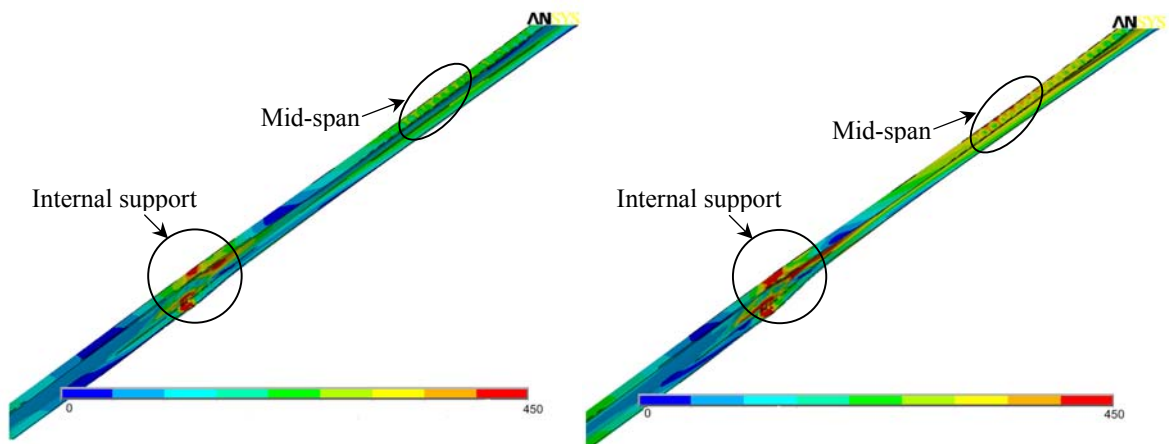
The numerical results presented in Fig. 3-20 also show that the structural behaviour of the double span CFS purlin under the entire loading process. In the elastic stage, the purlin behaves linearly and its stiffness agrees with the theoretical value. As load increases to a level where a knee starts to appear in the load-deflection curve, the beam begins to form a pseudo-plastic hinge at the internal support and moment redistribution initiates. As the load further increases beyond the knee point, the pseudo-plastic hinge is formed, as demonstrated by the stress distributions shown in Fig. 3-21 (a) and (c), and moment redistribution will take place during this stage. The purlin starts to carry load with a reduced stiffness. As the load continues to increase until the cross section at mid-span starts to yield, the failure of the purlin is triggered, as demonstrated by the

stress distributions shown in Fig. 3-21 (b) and (d). The structural behaviour of the double span beam during this loading process is in agreement with the theoretical assumption of the pseudo-plastic design method.



(a) at the onset of the first plastic hinge      (b) at ultimate failure

(I) Full lateral and torsional restraint



(c) at the onset of the first plastic hinge      (d) at ultimate failure

(II) Full lateral restraint but no torsional restraint

Figure 3-21 von Mises stress distributions, from 0 to 450N/mm<sup>2</sup>

### 3.13 SUMMARY

The post-buckling and the post-failure moment-rotation behaviour of double span continuous CFS sigma purlins at internal supports were both experimentally and numerically studied. This chapter presents the details and the results of the study. A wide range of sigma sections (nine different section dimensions) with two different spans (2.4m and 4.0m) were tested under a central point load to investigate the moment-rotation characteristics of continuous sigma purlins at internal supports. A total of twenty tests were carried out. The ultimate moment resistance and the pseudo-plastic moment resistance were established for each test specimen. The initial buckling modes and localised collapse patterns were also observed and defined. Four typical localised collapse patterns were established, which can be further used to perform post-failure analysis by using the yield-line method. The nonlinear structural behaviour of the sigma sections were then simulated by using FEA software, ANSYS. The selected element type, meshing pattern, material property, implementation of the boundary and loading conditions, the introduction of the initial imperfections, and the selection of solution scheme in the FE modelling process have been described in detail. The FE model was verified by experimental results and was then used in a parametric study of CFS sigma sections. The moment softening behaviour of the continuous beams at internal supports was numerically studied. The ultimate moment resistance obtained from the FE analysis was used to assess the predictions by the Effective Width Method and the Direct Strength method. The pseudo-plastic moment resistance of the continuous purlins was also established by the FE model.

A worked example has been presented to illustrate the use of the approach in the determination of the PPMR. Based on the attained PPMR, the pseudo-plastic design method was used to acquire the design failure load. The efficiency of the pseudo-plastic design method compared to the elastic design method has been demonstrated. The safety of the proposed PPMR that was used in the pseudo-plastic design method was also demonstrated by a FE analysis based on the developed FE model.

## **CHAPTER 4 SLEEVED SIGMA PURLINS AT INTERNAL SUPPORTS**

### **4.1 GENERAL**

This chapter reports an experimental study on the moment-rotation characteristic of sleeve connection for CFS sigma purlins at internal supports. The rotational stiffness, failure modes and moment resistance of the sleeve connection for a wide range of sigma profiles were particularly studied. The detailed discussion on these three structural aspects of the sleeve connection is presented. Based on the test results, an analytical model is proposed to predict the rotational characteristics of the sleeve connection to capture the different behaviour at various moment levels. Calculation methods are established to design the moment resistance of the sleeve connection. A FE model is developed to simulate the structural behaviour of the sleeve connection investigated in the tests.

### **4.2 TEST PROGRAMME**

The assembly of a typical sleeve connection is illustrated in Fig. 4-1, in which two sigma purlin members are sleeved together with a specially designed profile by using eight standard steel bolts. The sleeve profile has a similar sigma shape but without one of the flanges to facilitate practical installation.

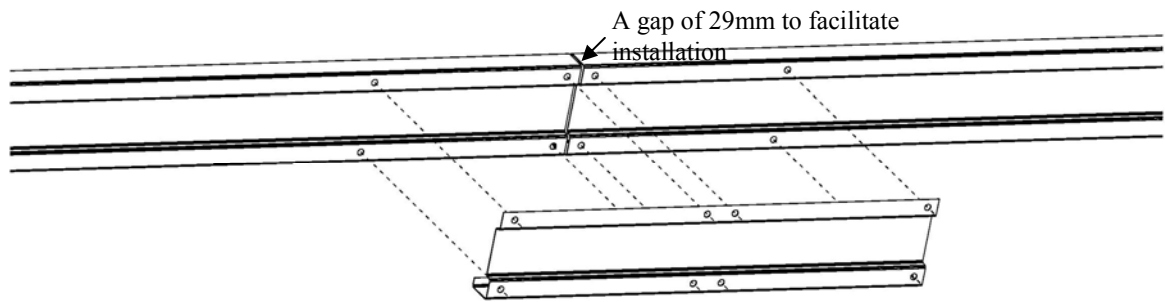


Figure 4-1 Typical sleeve connection for CFS sigma purlins

A laboratory testing programme has been constructed to study the characteristics of sleeve connection for CFS sigma purlins. In this programme, a series of specimens with matching sleeve connection were subjected to a three-point bending test. A concentrated load applied at the mid-span point represents the support reaction at the connection. The selected sample lengths and loading condition resemble the portion of multi-span purlins near an internal support where hogging moment is present, and it is called *sleeve internal support test* hereafter. Ten different purlin cross-sections were selected for testing, each with two duplicated specimens. A total of twenty sleeve internal support tests were carried out. The selected specimens have various depths, thicknesses and lengths. The dimensions of sleeve profiles vary accordingly in order to match the connected purlin members.

In this test programme, each test specimen has been assigned a three-part unique ID symbol. For instance, 24-20012-s1 indicates the beam span length (2.4m), the section depth and thickness (200mm deep and 1.2mm thick), the sleeve connection and the number of the duplicated test (s1).

#### 4.3 TEST SPECIMENS

Sigma sections of series 200, 240 and 300 were selected to perform the sleeve internal support tests. The nominal cross-sectional dimensions of these sections are as summarised in Table 3-1. The dimensions of corresponding sleeve profiles are presented in Table 4-1 (a). As can be seen from this table, the wall thickness of sleeve profiles for purlin specimens 20012, 20016 and 20025, is 2.0mm, 2.5mm and 3.0mm, respectively; for specimen 24015, is 2.5mm; and for purlin specimens 24023 and 24030 and section series 300, i.e. 30018, 30025 and 30030, is 3.0mm.

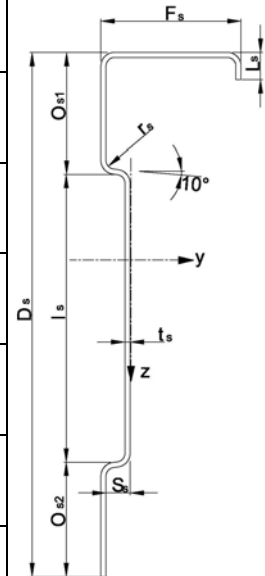
The thicknesses of all specimens were measured before the testing with a Digital Vernier Caliper. For the purlin sections, the measuring points were located at the inner web, top and bottom flanges, respectively; for the sleeve sections, they were located at the inner web, lower outer web and the flange, respectively. The measured wall thicknesses of both purlins and sleeves are presented in Table 4-1 (b). Based on the measured thicknesses, the second moment of area about the major principal axis for both purlin and sleeve sections were calculated and are summarised in Table 4-1 (b) as well.

Two span lengths, i.e. 2.4m and 4.0m, were examined in the sleeve internal support tests. The corresponding length of each purlin profile was 1.197m and 1.997m, respectively. All sleeves have only a single length, i.e. 1.0m. The horizontal bolt spacing is indicated in Fig. 4-2. The vertical spacing  $a$  varied with the depth of the section, i.e. 154 mm for section series 200, 190 mm for section series 240 and 240 mm for section series 300.



The purlin profiles used in this test programme were made from the same coils forming those corresponding purlin profiles used in continuous internal support tests. Therefore the measured yield stresses summarised in Table 3-2 are still valid. For convenience purposes, the yield stresses of the purlin profiles together with those of sleeves were presented in Table 4-1 (b). The details of the material coupon tests were described in Appendix IV.

Specimen	$D_s$ (mm)	$F_s$ (mm)	$L_s$ (mm)	$O_{s1} / O_{s2}$ (mm)	$I_s$ (mm)	$S_s$ (mm)	$r_s$ (mm)	$t_s$ (mm)	
24-20012-s1 24-20012-s2	203	80	18	60 / 50	93	16	4	2.0	
24-20016-s1 24-20016-s2	203	80	18	60 / 50	93	16	4	2.5	
24-20025-s1 24-20025-s2	203	80	18	60 / 50	93	16	4	3.0	
40-20025-s1 40-20025-s2	203	80	18	60 / 50	93	16	4	3.0	
24-24015-s1 24-24015-s2	243	80	18	70 / 60	113	16	4	2.5	
24-24023-s1 24-24023-s2	243	80	18	70 / 60	113	16	4	3.0	
40-24030-s1 40-24030-s2	243	80	18	70 / 60	113	16	4	3.0	
24-30018-s1 24-30018-s2	303	85	18	80 / 70	153	16	4	3.0	
24-30025-s1 24-30025-s2	303	85	18	80 / 70	153	16	4	3.0	
40-30030-s1 40-30030-s2	303	85	18	80 / 70	153	16	4	3.0	



(a)

Specimen	*Thickness (mm)		Second moment of area (cm <sup>4</sup> )		Length (mm)		0.2% proof stress (N/mm <sup>2</sup> )	
	Section	Sleeve	Section	Sleeve	Section	Sleeve	Section	Sleeve
24-20012-s1 24-20012-s2	1.24	1.98	264	271	1197	1000	471	518
24-20016-s1 24-20016-s2	1.61	2.48	340	337	1197	1000	433	447
24-20025-s1 24-20025-s2	2.46	2.87	509	388	1197	1000	447	453
40-20025-s1 40-20025-s2	2.48	2.91	513	394	1997	1000	447	453
24-24015-s1 24-24015-s2	1.53	2.47	501	541	1197	1000	507	447
24-24023-s1 24-24023-s2	2.24	2.93	721	640	1197	1000	456	453
40-24030-s1 40-24030-s2	3.07	2.98	968	651	1997	1000	452	453
24-30018-s1 24-30018-s2	1.79	3.00	1096	1206	1197	1000	458	417
24-30025-s1 24-30025-s2	2.43	3.00	1471	1208	1197	1000	447	417
40-30030-s1 40-30030-s2	2.90	2.98	1739	1198	1997	1000	417	417

\* Measured average thickness

(b)

Table 4-1 Geometric and mechanical properties of test specimens

#### 4.4 TEST SET-UP AND APPARATUSES

The detailed set-up for the test is shown in Fig. 4-2. The purlin-sleeve assembly consists of two notionally identical sigma purlins and one sleeve profile. A point load was applied to the assembly by a 60T loading jack. The load was applied through a rigid universal beam section (UBS) and a stiffened loading cleat. The UBS section was rigidly fixed to the loading jack in the top flange and connected to the cleat in the bottom one. The loading cleat was then connected to the purlin-sleeve assembly by using four bolts. Since the loading jack is sufficiently rigid, the assembly was laterally braced at the load application point. Hence, no torsional moment was introduced on the test specimen, namely, the load was applied through the shear centre of the cross section. At both ends, the specimens were bolted onto two stiffened supporting cleats. Grade 8.8 M12 bolt was used for section series 200 and 240, and Grade 8.8 M16 bolt was used for section series 300. All bolt holes had a standard clearance, i.e. 2mm. It is worth mentioning that when the sigma purlins and sleeve were bolted together, no attempt was made to centralise bolts in the bolt holes and no specially controlled pre-tension was applied to them either. All bolts were tightened by hand. This is to reflect the normal erection practice. The supporting cleats were then fixed onto two stabilized square hollow sections (SHS). Three LVDTs were placed at two quarter and the middle span points, respectively, to measure the vertical deflections. Other two LVDTs were placed at both quarter points to measure the lateral movements. Furthermore, two inclinometers were glued along the central line of the top flange at both ends to measure the end rotation angles.

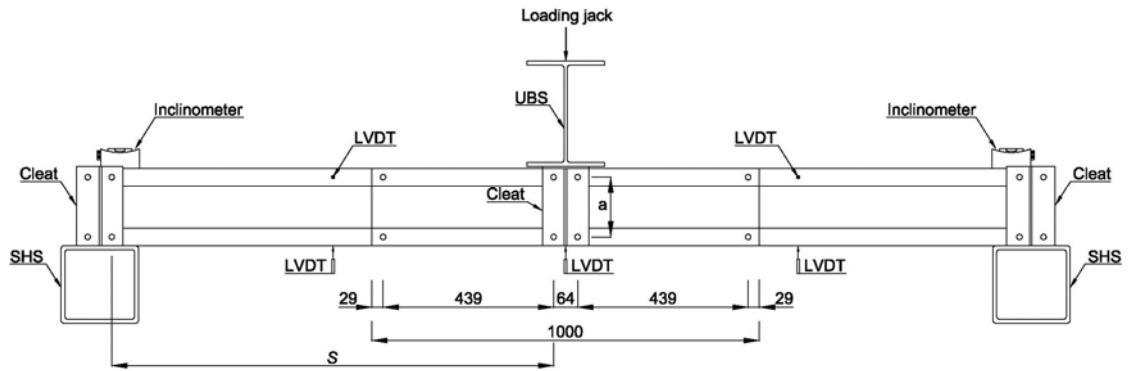


Figure 4-2 Test set-up

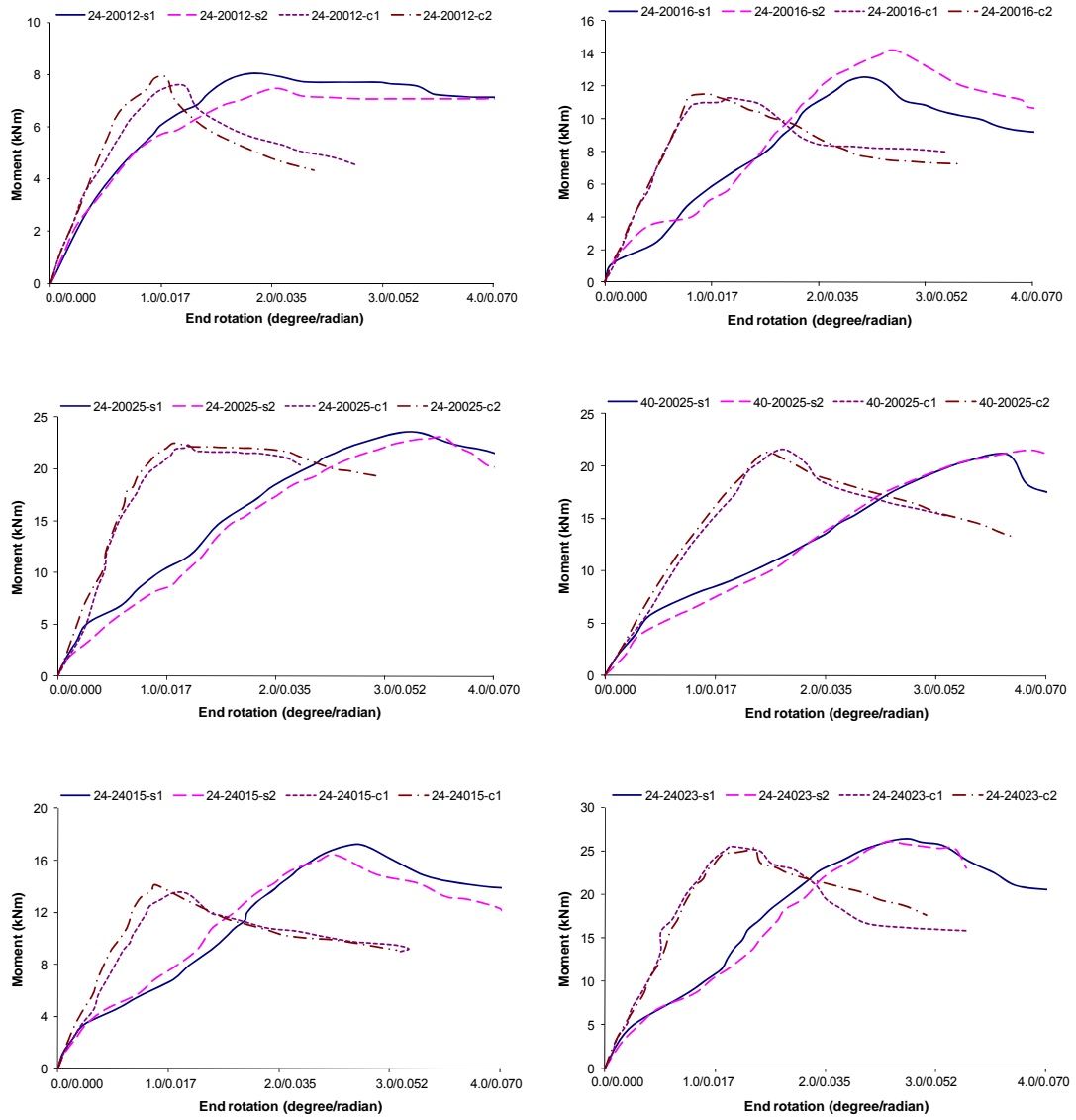
#### 4.5 TEST PROCEDURE AND INSTRUMENTATION

Prior to the application of any load, both the load display unit and LVDTs were zeroed. The loading was applied in a displacement controlled mode. Readings were initially taken at each 1mm increment. After passing the ultimate load, the displacement was continually applied but readings were taken at increments of 5mm until the displayed load had dropped more than 10% of the peak value. The same loading regime was repeated for each specimen. The interval between the displacement steps for the data readings was largely kept no more than 30 seconds. These test procedures were repeated for each specimen.

#### 4.6 TEST RESULTS

Due to symmetry of the test set-up, the measured two end rotation angles are similar to each other. Therefore an averaged value is used to plot the moment-rotation curve for each specimen and they are presented in Fig. 4-3. For comparison purposes, two duplicated tests are presented in one

graph. It can be seen that the two duplicated tests show good correlation in moment-rotation responses, especially in the pre-failure stage. In order to directly compare the stiffness and resistance between the sleeve and continuous connections, the moment-rotation curves for continuous purlins are also presented in the corresponding graphs. They are indicated as “c” in the ID symbols, to distinguish from sleeved purlins (as “s” in the ID symbols), as shown in Fig. 4-3. The detailed test procedure of continuous purlins can be found in Chapter 3.



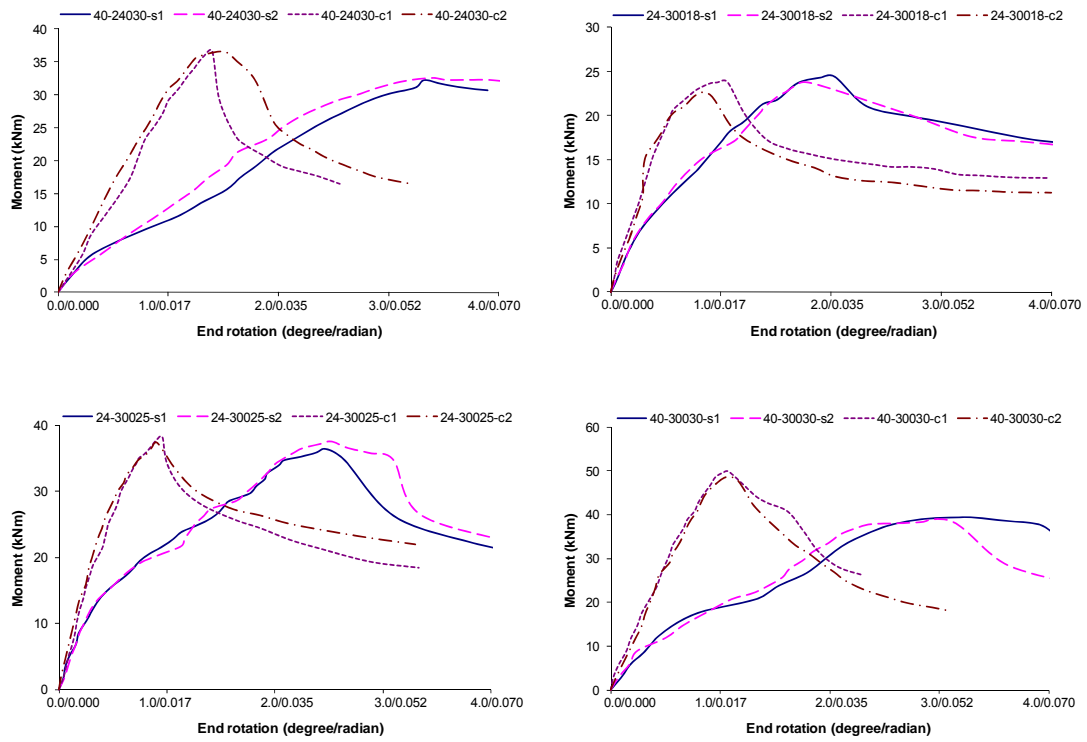


Figure 4-3 Moment vs. rotation curves for both sleeve and continuous connections

Table 4-2 presents the detailed results for each test including the shear span,  $s$  (see Fig. 4-2), the recorded ultimate load,  $P_t$ , the corresponding ultimate moment,  $M_t$ , and the observed failure modes.

Specimen	s (mm)	$P_t$ (kN)	$M_t = \frac{P_t \times s}{2}$ (kNm)	Failure pattern*	Rotational stiffness (kNmdeg <sup>-1</sup> / kNmrad <sup>-1</sup> )
24-20012-s1	1139	14.1	8.0	OB	3.0/172
24-20012-s2		13.1	7.5	OB	2.4/138
24-20016-s1	1139	21.4	12.5	OB	3.4/195
24-20016-s2		24.2	14.2	OB	3.4/195
24-20025-s1	1139	41.5	23.6	STF	4.7/269
24-20025-s2		40.5	23.1	STF	4.1/235
40-20025-s1	1939	21.8	21.1	STF	4.2/241
40-20025-s2		22.2	21.5	STF	3.9/223
24-24015-s1	1139	30.2	17.2	OB	3.9/223
24-24015-s2		28.8	16.4	OB	4.1/235
24-24023-s1	1139	46.3	26.4	OB	6.1/350
24-24023-s2		45.8	26.1	OB	6.6/378
40-24030-s1	1939	33.2	32.2	SCF	6.5/372
40-24030-s2		33.6	32.6	SCF	6.5/372
24-30018-s1	1139	42.8	24.4	OB	7.3/418
24-30018-s2		41.8	23.8	OB	8.4/481
24-30025-s1	1139	59.8	36.4	OB	8.8/504
24-30025-s2		65.8	37.5	OB	8.9/510
40-30030-s1	1939	40.0	38.8	SCF	7.4/424
40-30030-s2		39.4	38.2	SCF	8.4/481

\*OB- Local buckling purlin sections near outer bolts; SCF- Local buckling in the compression flange of sleeve sections; STF- tension fracture in sleeve sections.

Table 4-2 Test results of sleeved purlins at internal support

Also summarised in Table 4-2 are the rotational stiffness of the sleeve connection that is calculated by using the following equation:

$$k = \frac{1}{\frac{2\theta}{M_t} - \frac{l}{2EI}} \quad (4-1)$$

in which  $\theta$  is the rotation angle at the support end measured at the ultimate load level and  $l$  is the span length;  $E$  and  $I$  are, respectively, the elastic modulus and the second moment of area of the sigma purlin section. The derivation of Eq. (4-1) is presented in Appendix VII. The rotational stiffness can be used in global analysis for sleeved purlin system.

## 4.7 DISCUSSION OF THE TEST RESULTS

### 4.7.1 Moment-rotation relationship

The comparison of the sleeve and continuous systems in Fig. 4-3 reveals that the sleeve connection exhibits a semi-rigid type of characteristics that have high moment resistance but a low rotational stiffness. Moment-rotation curves for the sleeve connection show a strong non-linearity. Unlike the conventional semi-rigid joints for hot rolled steel sections, the initial stiffness of the sleeve connection is not clearly predictable. This is primarily attributed to the uncontrollable slips between the purlins and sleeve.

Drawn from the common trends revealed by the experimental results shown in Fig. 4-3, the pre-failure moment-rotation relationship of the sleeve connection features three distinct stages. In the first stage, the friction induced at the contact interfaces of the connection produce relatively



higher rotation stiffness, which has been reflected by a linear section with a steep slope at the beginning of the curve. As the applied moment increases, the moment resistance provided by the friction is gradually overcome and the connected members start to slip due to the clearance in the bolt holes. This type of rigid body movement leads to a profound decrease in the rotational stiffness that is indicated by a nearly levelled section in the moment-rotation curve. In the third stage, all bolts have been engaged with the edges of the bolt holes, which lead to another increase in the rotation stiffness as revealed in Fig. 4-3. The end rotation in this stage consists of two components, i.e. one caused by the bending of the composite purlin/sleeve system, and the other associated with the elongation of bolt holes due to the localised yielding at bearing points.

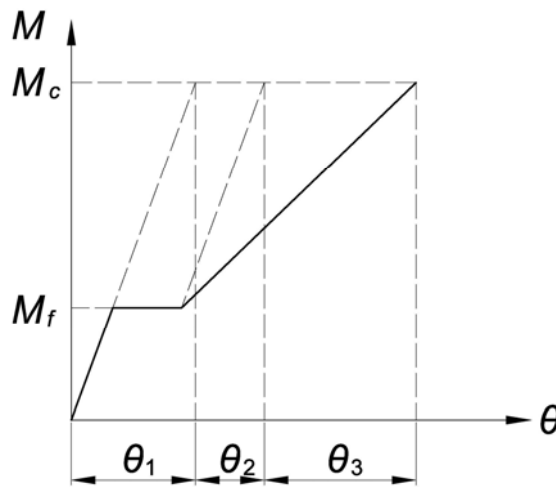
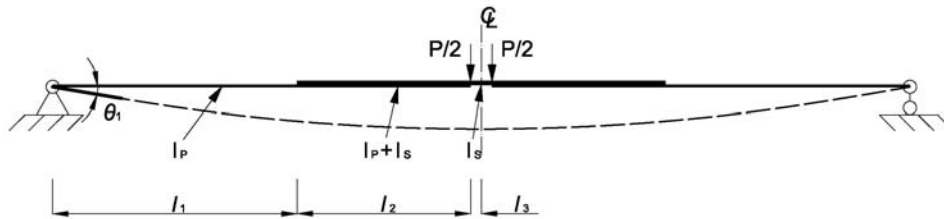


Figure 4-4 Representative model of moment-rotation relation

In line with the above analysis, a tri-linear model, as shown in Fig. 4-4, can be developed as the idealisation of the moment-rotation curve of a sleeve connection. In the first ascending part of the model, the friction generated between the purlin and sleeve is assumed to be sufficient to resist

the applied moment, and the end rotation angle is therefore attributed entirely to the bending of the composite purlin-sleeve system. The horizontal part of the curve produced in the second stage starts when the moment resistance due to friction  $M_f$  is reached. Considering the clearance between bolts and bolt holes, it is assumed that the sleeve connection rotates freely at this moment level. This rigid body movement results in more end rotation. The second ascending straight line of the curve developed in stage three begins when the bolts are in contact with the edges of bolt holes. As has been mentioned previously, the rotation in this stage is attributed to two parts, i.e. the flexure of the composite purlin/sleeve system and the elongation of bolt holes due to local bearing. In real term, the elongation of the bolt holes should have a nonlinear behaviour with the applied loads (Lim and Nethercot, 2004b). Furthermore, any occurrence of buckling in purlin or sleeve will also cause nonlinear moment-rotation behaviour. However, in order to simplify the model, it is assumed that in this stage, the system rotates in proportion to the applied moment until the moment resistance of the sleeve connection  $M_c$  is reached. By using the superposition principle, the resultant end rotation of sleeved purlins at a given moment level can be determined as shown in Fig. 4-4, in which the rotation angles attributed to the composite bending of the assembly, slips of bolts and the elongation of bolt holes are denoted as  $\theta_1$ ,  $\theta_2$  and  $\theta_3$ , respectively.



(a) Rotation due to the composite bending of the assembly

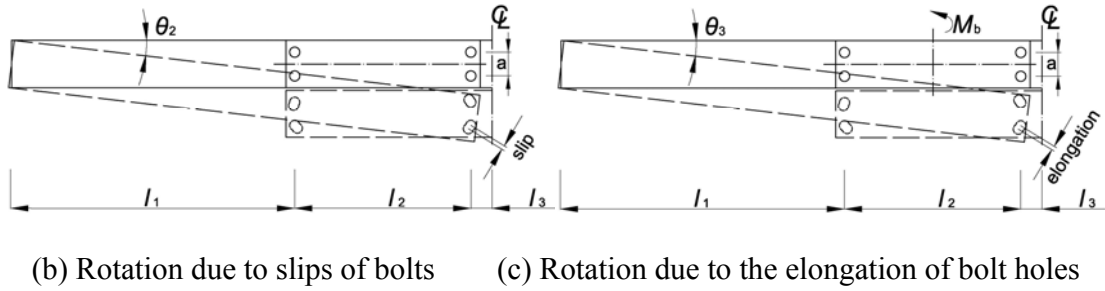


Figure 4-5 Rotation components in the sleeve connection

The flexural rotation  $\theta_1$  can be calculated by assuming that the purlins and sleeve work together. Therefore, the assembly can be treated as a simple beam with various cross-sections. Considering only the left-half of the beam, the beam can be divided into three regions (Fig. 4-5a), i.e. (1) from the beam end to the outer bolts constituting a length  $l_1$  that consists of only the purlin section with a second moment of area  $I_p$ ; (2) the overlap zone of a length  $l_2$  where the cross-section comprises both the purlin and sleeve sections with a second moment of area  $I_p + I_s$ ; (3) from the inner bolts to the center of the sleeve with a length  $l_3$  and having a second moment of area equal to that of the sleeve  $I_s$ . The end rotation  $\theta_1$  of the composite system under a mid-span point load  $P$  can be calculated and expressed in terms of the mid-span moment  $M$  as:

$$\theta_1 = \frac{Ml_1}{EI_p} \left[ \frac{l_1}{2(l_1 + l_2)} + \frac{l_2(2l_1 + l_2)}{2l_1(l_1 + l_2)} \frac{I_p}{I_p + I_s} + \frac{l_3}{l_1} \frac{I_p}{I_s} \right] \quad (4-2)$$

The derivation of Eq. (4-2) are detailed in Appendix VIII.

The rotation angle  $\theta_2$  due to slips (Fig. 4-5b) is a variable dependent on the bolt hole clearance  $e$ , the vertical bolt spacing  $a$  (the values of  $a$  for various test specimens are given in section 4.3), and the horizontal bolt spacing  $l_2$ . It can be calculated by

$$\theta_2 = 4e / \sqrt{a^2 + l_2^2} \quad (4-3)$$

The actual locations of bolts are dependent on the installation process and thus are highly unpredictable. For the design purpose, a conservative value is adopted in this study. For a bolt hole with a standard clearance 2mm, the maximum value of slip is assumed to be 2mm as well.

The rotation angle  $\theta_3$  (Fig. 4-5c) due to the elongation of bolt holes can be determined by using an equation suggested by Bryan (1993) for four-bolt moment connections, i.e.

$$\theta_3 = 2M_b c / (a^2 + l_2^2) \quad (4-4)$$

where  $M_b$  is the moment carried by the four-bolt connection at the centre of the bolt groups and  $c$  (mm/kN) is the elongation compliance and an empirical formula is given by Bryan (1993) as:

$$5n(10/t_1 + 10/t_2 - 2) \times 10^{-3} \quad (4-5)^*$$

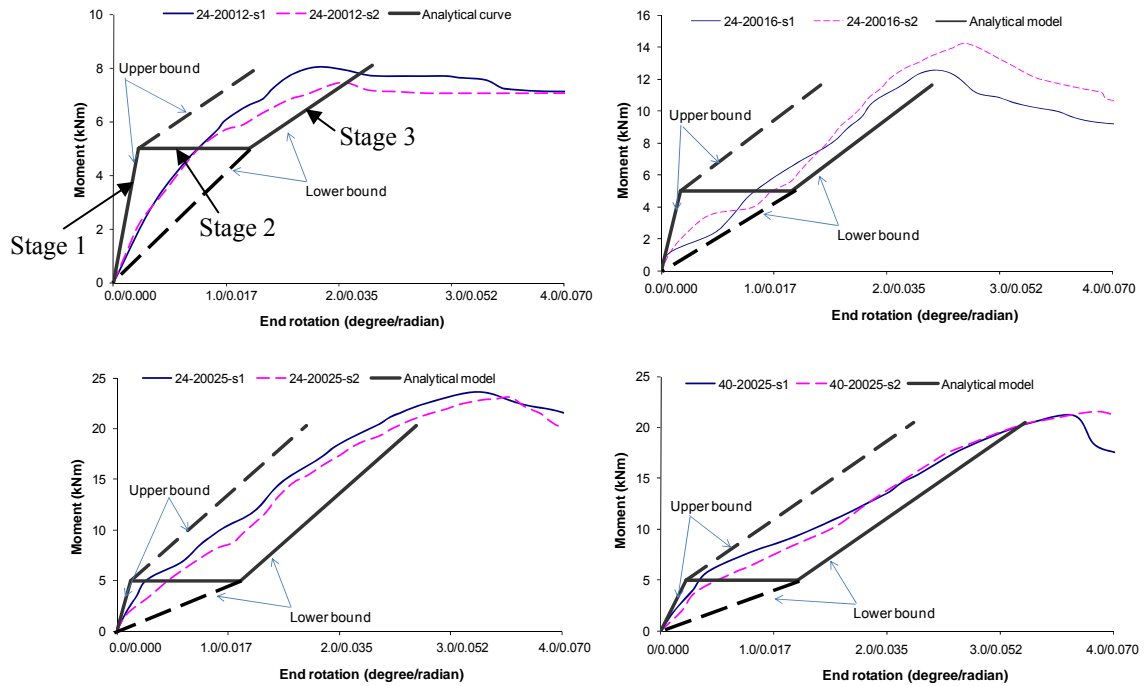
\* The dimensional consistency of this equation is not clear.

where  $t_1$  and  $t_2$  are the thicknesses of purlin and sleeve;  $n$  is an empirical factor dependent on the type of bolt and joint; and, in this case, it is conservatively chosen as 5. The derivation of Eq. (4-4) is illustrated in Appendix IX.

Another two unknown variables in this tri-linear moment-rotation model are the friction moment  $M_f$  and the moment resistance  $M_c$  of the connection. The value of  $M_f$  can be influenced by many factors, such as the size of bolts or washers, friction coefficient of the contact surface, bolt spacing and the installation process (e.g. the applied torque to bolts). It is difficult to precisely estimate the value of  $M_f$ . However, from the test results shown in Fig. 4-3, the value of  $M_f$  for connections with M12 bolts (section series 200 and 240) and M16 bolts (section series 300) may be approximately taken as 5kNm and 10kNm, respectively. The moment resistance  $M_c$  of the

connection can be taken as the lesser value of the moment resistance of the sleeve and purlin sections, as will be elaborated on in Section 4.7.3.

By using the proposed tri-linear model, the moment-rotation relationship of the sleeve connection in each test specimen is calculated and presented with strong solid lines in Fig. 4-6. Two dot lines are also constructed at the both ends of the horizontal line. One of them is the duplicated copy of the ascending line from stage 3 and the other one connecting the origin and the ending point of the horizontal line. By doing so, upper and lower bounds can be found for the moment-rotation response. The upper bound ignores slips in the connection, and the lower bound considers slips developing gradually throughout stages 1 and 2. The experimental moment-rotation response of each test specimen is also presented in the corresponding graph shown in Fig. 4-6. It can be seen that most experimental results lie between these two bounds.



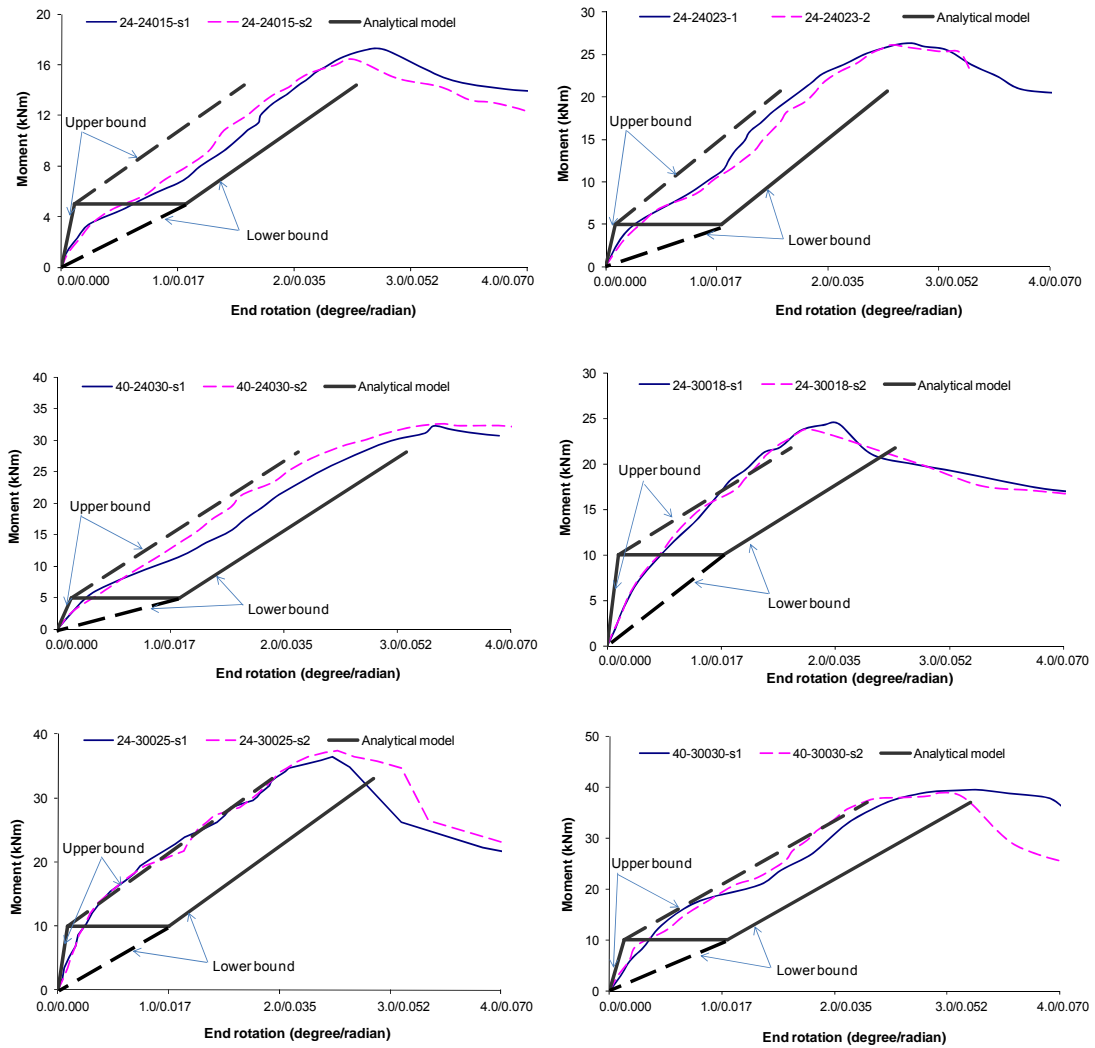


Figure 4-6 Comparison between the test and predicted moment-rotation curves

The comparison between the predicted and experimental results also indicates that the initial stiffness below the friction moment has been over-estimated by the proposed model but a conservative estimate for the rotation caused by slip has brought the prediction back to the conservative side. The common trend exhibited by test results has suggested that bolt slips have developed in a progressive fashion instead of with a sudden occurrence. The predicted results for

stage 3 show a close agreement with test results. In engineering practice, the lower bound can be used to calculate the moment-rotation response of sleeve connections.

#### 4.7.2 Failure modes

Three types of failure modes were observed from tests, i.e. (1) the local buckling of a purlin profile at the end of sleeve connection (Fig. 4-7 a); (2) the tension fracture of the sleeve at the mid-span point (Fig. 4-7 b) and (3) the local buckling in the compression flange of the sleeve at the mid-span point (Fig. 4-7 c). The failure mode for each test specimen was summarised in Table 4-2. Amongst these test specimens, 24-20025-s1, 24-20025-s2, 40-20025-s1 and 40-20025-s2 failed with the second mode; 40-24030-s1, 40-24030-s2, 40-30030-s1 and 40-30030-s2 failed with the third mode, and the remaining twelve test specimens were found to all fail with the first failure mode. In all test specimens, one common observation was the significant local deformation around bolt holes (Fig. 4-7 d). It is worth mentioning that unlike the continuous internal support tests, the sleeve internal tests did not have any specimen that failed due to the lateral torsional buckling.



(a) Local buckling in the outer web of purlin section (failure mode 1)



(b) Tension fracture failure in sleeve section (failure mode 2)



(c) Local buckling in the compression flange of sleeve section (failure mode 3)



(d) Elongation of bolt holes (common failure pattern)

Figure 4-7 Failure modes

The bending moment diagram of the sleeved purlin under the central point load is shown in Fig. 4-8. According to the diagram, the critical section can be either the purlin section at one end of the sleeve connection or the mid-span section of the sleeve. This agrees with the locations of failure observed in the test. However, due to the presence of local forces on these two critical sections, the moment resistance of the specimens may be influenced by the interaction between the bending and local bearing.

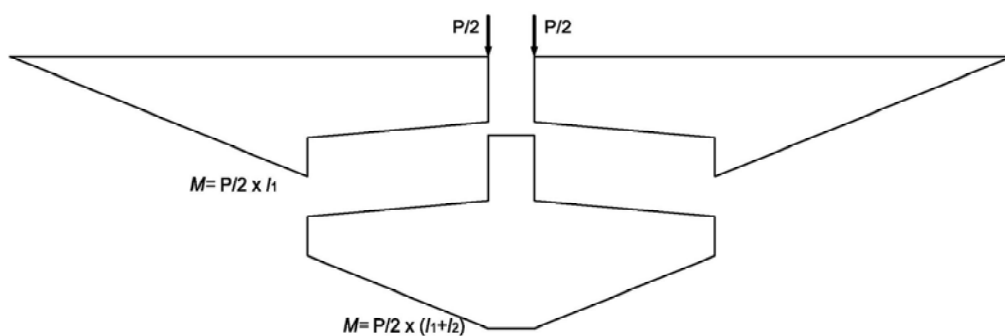


Figure 4-8 Bending moment diagram of the sleeved purlin



#### 4.7.3 Moment resistance

Table 4-3 lists the comparison of the experimental results of ultimate moment between sleeved ( $M_{t,s}$ ) and continuous purlins ( $M_{t,c}$ ). As can be seen that the range of the ratio of these two is from 0.78 to 1.21 and, by large, the sleeved purlins produce higher ultimate moment. A closer examination of these results suggests that, for those specimens failing in the first mode, the ultimate moment of sleeve connection is 0.98 to 1.21 times that of continuous purlins; for those failed in the second mode, the ratio has changed to 1.00 to 1.04; and for those specimens experiencing the third failure mode, the ratio has dropped to 0.78 to 0.89. In summary, specimens that failed in the first and second modes, the sleeve connection can provide a full moment resistance; and whereas for those that failed due to the local buckling in sleeve flanges, the sleeve connections can only provide a reduced moment resistance.

Table 4-3 also summarises the calculated cross-sectional moment resistance ( $M_c$ ) of the purlin and sleeve sections. The calculation is based on the measured thickness of specimen and following the effective width method in BSI (2006a). The comparison of the calculated results of moment resistance between the purlin and sleeve indicates that for the specimens of 24-20012-s, 24-20016-s, 24-20025-s, 40-20025-s, 24-24015-s, 24-24023-s, 24-30018-s and 24-30025-s, their resistance is governed by the purlin section; while for the remaining specimens, their resistance is governed by the sleeve section. This observation agrees well with the observed failure model for most specimens with only two exceptions, 24-20025-s and 40-20025-s. The occurrence of these two exceptions is likely due to the close values of moment resistance between the purlin and sleeve

sections. Taking specimen 40-20025-s for instance, the difference of moment resistance between these two sections is less than 2.5%, so the failure of the specimen can be triggered by either of them. It should be noted that due to the asymmetric cross-sectional shape of sleeve, the initial yielding of the sleeves is likely to take place at the tension side where the flange is not present. As the tension zone is not affected by a local buckling, a plastic zone should be allowed for in the calculation as suggested by BSI (2006a).

Based on the above discussion, a simplified method to determine the moment resistance of the sleeve connection can be developed as follows:

$$M_{Rd,1} = \min (M_{c,section}, M_{c,sleeve}) \quad (4-6)$$

where  $M_{Rd,1}$  is the moment resistance of the sleeve connection;  $M_{c,section}$  and  $M_{c,sleeve}$  are calculated moment resistance for purlin and sleeve sections, by using the effective width method in BSI (2006a). The moment resistance  $M_{Rd,1}$  calculated by this method and the ratios of the calculations to experimental results are summarised in Table 4-3. It can be seen that most of the predictions are safe, and on average, the safety margin is approximate 12%. Therefore the proposed method can be used to predict the moment resistance of the sleeve connection.

Specimen	$*M_{t,s} / *M_{t,c}$	$*M_c$ (kNm)		$M_{Rd,1}$ (kNm)	$*M_{t,s} / M_{Rd,1}$	$M_{Rd,2}$ (kNm)	$*M_{t,s} / M_{Rd,2}$
		Section	Sleeve				
24-20012-s1 24-20012-s2	1.00	8.1	14.4	8.1	0.96	7.9	0.98
24-20016-s1 24-20016-s2	1.17	11.6	17.1	11.6	1.16	11.3	1.18
24-20025-s1 24-20025-s2	1.04	20.3	20.7	20.3	1.15	20.0	1.17
40-20025-s1 40-20025-s2	1.00	20.5	21.0	20.5	1.04	17.9	1.19
24-24015-s1 24-24015-s2	1.21	14.4	22.2	14.4	1.17	13.0	1.29
24-24023-s1 24-24023-s2	1.03	20.7	27.6	20.7	1.27	21.7	1.21
40-24030-s1 40-24030-s2	0.89	32.4	28.1	28.1	1.15	28.1	1.15
24-30018-s1 24-30018-s2	1.04	21.7	37.2	21.7	1.11	18.9	1.28
24-30025-s1 24-30025-s2	0.98	33.0	37.2	33.0	1.12	29.2	1.27
40-30030-s1 40-30030-s2	0.78	39.0	36.9	36.9	1.04	36.9	1.04

\*Mean value

Table 4-3 Comparisons of moment resistance between sleeved and continuous internal support tests and between the calculated and experimental results

In the above proposed moment resistance design method, the interaction effect between bending and local bearing is not considered. For comparison purposes, an alternative method addressing the interaction effect will be present next and the predicted results are also presented in Table 4-3 with a denotation  $M_{Rd,2}$ .

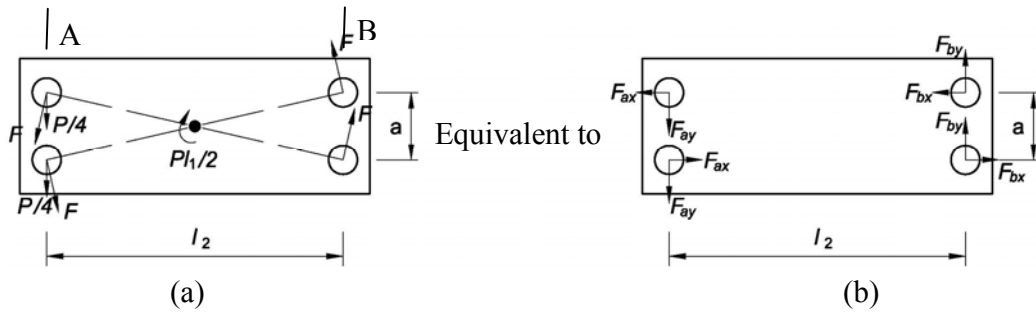


Figure 4-9 Bearing forces induced in the purlin section

The local bearing effect arises from the bolt bearing force in the connection. Fig. 4-9 shows a schematic diagram of the bolt bearing forces induced in the purlin section within the left half connection zone. The point load  $P$  applied at the centre through the loading bracket will be borne by the sleeve section initially and then transfer to the purlin section at the outer bolts, which produces a bearing force  $P/4$  at each of them. The moment transferred by the bolt group is  $Pl_1/2$  and that will induce a bearing force  $F$  at each bolt. The superposition of these two groups of force will lead to a bearing at each bolt hole in the purlin section (see Fig. 4-9 b), which can be calculated as follows:

$$F_{ax} = F_{bx} = \frac{Pal_1}{4(a^2 + l_2^2)} \quad (4-7a)$$

$$F_{ay} = \frac{P}{4} \left( 1 + \frac{l_1 l_2}{a^2 + l_2^2} \right) \quad (4-7b)$$

$$F_{by} = \frac{Pl_1 l_2}{4(a^2 + l_2^2)} \quad (4-7c)$$

where  $P$ ,  $l_1$ ,  $l_2$  and  $a$  can be found by referring to Fig. 4-5.

The critical bearing force in section A together with the corresponding bending moment in the same section can be used to check the moment resistance of connection by employing the following interaction design model in BSI (2006a):

$$M_{Ed} / M_{c,Rd} \leq 1.0, \quad F_{Ed} / F_{Rd} \leq 1.0$$

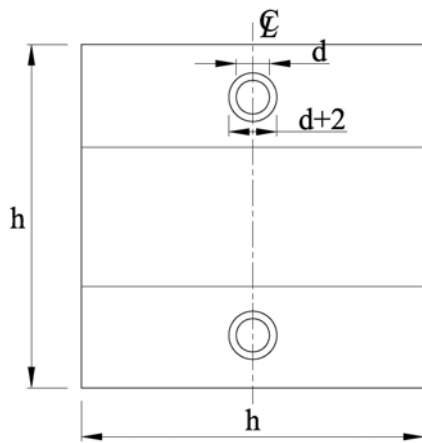
and

$$M_{Ed} / M_{c,Rd} + F_{Ed} / F_{Rd} \leq 1.25 \quad (4-8)$$

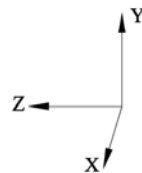
where  $M_{Ed}$  and  $F_{Ed}$  are the applied bending moment and local bearing force present in the critical cross-section,  $M_{c,Rd}$  and  $F_{Rd}$  are the moment resistance and local bearing resistance of the cross section. From the previous discussion, the critical cross section for the purlin section is at the end of the sleeve (section A shown in Fig. 4-9), where  $M_{Ed}$  is  $Pl_1/2$  and  $F_{Ed}$  can be taken as  $2 \times \sqrt{F_{ax}^2 + F_{ay}^2}$ .  $M_{c,Rd}$  has the same value as  $M_{c,section}$  shown in Table 4-3. Current codes of practice do not provide any provisions to assess the local bearing resistance of sigma section subjected to forces caused by bolts. Those methods for hot-rolled sections do not apply for cold-formed steel sections since the failure is mainly caused by localised buckling in front of the bearing surface rather than squashing. As a result, nonlinear FE analyses have been carried out to calculate  $F_{Rd}$ .

Fig. 4-10 (a) shows the specimen studied in the FE analysis. The modelled specimens were composed of only webs and bolts. Purlin flanges do not play a significant role in the local bearing failure, and hence were excluded in the analysis. The length of the modelled specimen was selected to be equal to the depth of the specimen, since the local bearing failure only took place within this zone. The bolt holes had a 2 mm standard clearance.

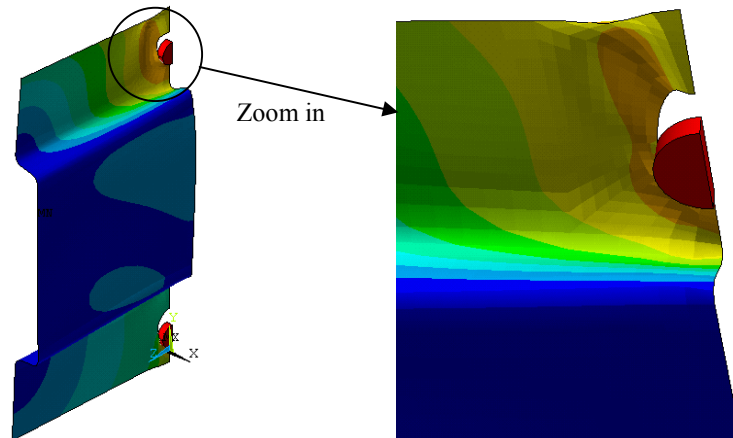
ANSYS package was used to perform the FE analysis. SHELL181 and SOLID45 were chosen as the elements of the web and bolts, respectively. The interaction between the web and the bolts was realised by setting contact pairs. TARGE170 and CONTA177 were assigned to the round surfaces of bolts and the edges of bolt holes. Due to the symmetric nature of the model, only half of the specimen was included, as shown in Fig. 4-10 (b). The selection of the shape and size of element was determined on the basis of the studies by (Chung and Ip, 2000, 2001). The numbers of element around the half edge of bolt hole and in the rounded corner of the web are 24 and 2, respectively. The meshing pattern in the remaining parts of the model is illustrated in Fig. 4-10 (b), where the aspect ratio of all elements is kept between 1 and 2. A bilinear stress-strain material model with the von-Mises yield criterion and the isotropic hardening rule was selected for the purlin. The yield stress, the elastic modulus  $E$  and the Poisson's ratio  $\nu$  of these elements were 450MPa, 210kN/mm<sup>2</sup> and 0.3 respectively. The slope of the second line in the stress-strain curve was set as 0.5%  $E$ . An elastic material model with  $E = 210 \text{ kN/mm}^2$  and  $\nu = 0.3$  was used for bolts.



(a) Specimen studied in FE analysis



(b) Meshing pattern of the FE model



(c) Typical failure pattern

Figure 4-10 Numerical study for the localised load resistance of sigma sections

Vertical incremental displacements were applied to both bolts simultaneously. Bolts and the two horizontal edges of web were restrained from moving in the X direction, and the left vertical edge of the web was restrained from moving in both X and Y directions (see the definition of coordinate system in Fig. 4-10a). Symmetry boundary conditions were applied on the symmetrical plane of the specimen. In addition, the outer webs on the symmetrical plane were also restrained from moving in the X direction to allow for the restraining effect from the sleeve. The FE model included initial imperfections. The shape of the imperfections was determined on the basis of the first linear buckling mode from a prior eigenvalue buckling analysis and the magnitude was chosen to be 10% of section thickness. Full Newton-Raphson procedure and sparse solver were employed as the solving engine. The results of the numerical modelling provided the local bearing resistance for all tested sections. Fig. 4-10 (c) presents a typical failure pattern for a sigma sections under bearing forces caused by bolts. The failure is always attributed to a local buckling of the outer web adjacent to the upper bolt.

By utilizing the results of  $F_{Rd}$  obtained from the numerical modelling, a graph of  $F_{Ed} / F_{Rd}$  versus  $M_{Ed} / M_{c,Rd}$  for all test specimens, was produced and is presented in Fig. 4-11. Also included in the figure is the interaction failure envelope between the bending moment and local bearing force based on Eq. 4-8. It can be seen that most data points lie outside the interaction failure envelope, which suggests a safe prediction by utilizing this model. Detailed data are also tabulated in Table 4-3 by using the denotation  $M_{Rd,2}$ .

Results reveal that the interaction method produces a safety margin around 19.9%, which is moderately (7.9%) higher than that from the simple method. Nevertheless, both methods can yield safe predictions and therefore, it is suggested that the interaction effect may be ignored when predicting the moment resistance of sleeve connection.

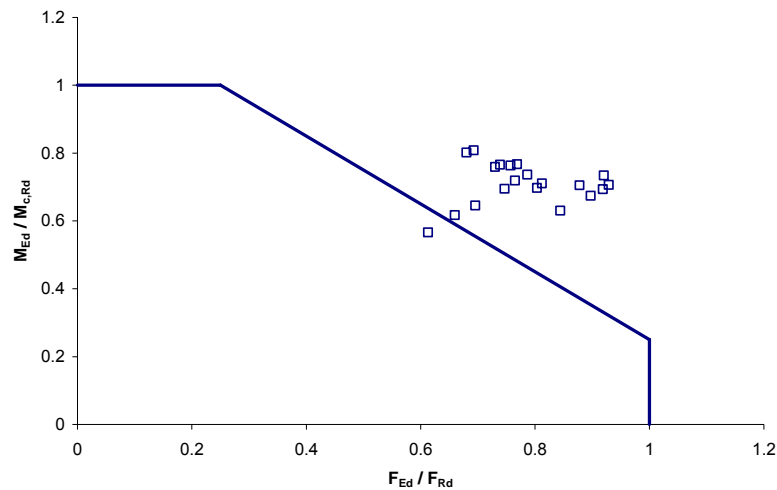


Figure 4-11 Interaction between bending moment and local bearing force



## 4.8 FINITE ELEMENT MODELLING OF SLEEVED SIGMA PURLINS AT INTERNAL SUPPORTS

In order to reproduce the test results of the sleeve internal support tests a FE based numerical modelling was developed by using ANSYS.

### 4.8.1 Finite element idealisation

The elements of the sigma sections and the sleeve were chosen as SHELL181. The bolts used to connect the sigma sections and supporting cleats (these bolts are called supporting bolts hereafter) were modelled with SHELL63; the bolts used to connect the purlin and the sleeve (these bolts are called connecting bolts hereafter) were modelled with SOLID45. The contact between the purlin and the sleeve was established by contact pairs, i.e. CONTA173, attached to the sigma sections, and TARGE170, attached to the sleeve. The contact between the bolt holes and the connecting bolts was realised by CONTA175 and TARGE170. The former was attached to the circumferential surface of the bolts and the latter was attached to the edges of the bolt holes. The discretization pattern for the supporting bolts and the flanges, the outer webs and the inner webs of the sigma section and the sleeve was similar to that adopted in the FE modelling for the continuous internal support tests, which was explained in Chapter 3. The connecting bolts were discretized by the sweep meshing method. The meshing pattern of the sleeved beam is illustrated in Fig. 4-12. Due to the symmetry, only half of the sleeved purlin was simulated in this FE modelling.

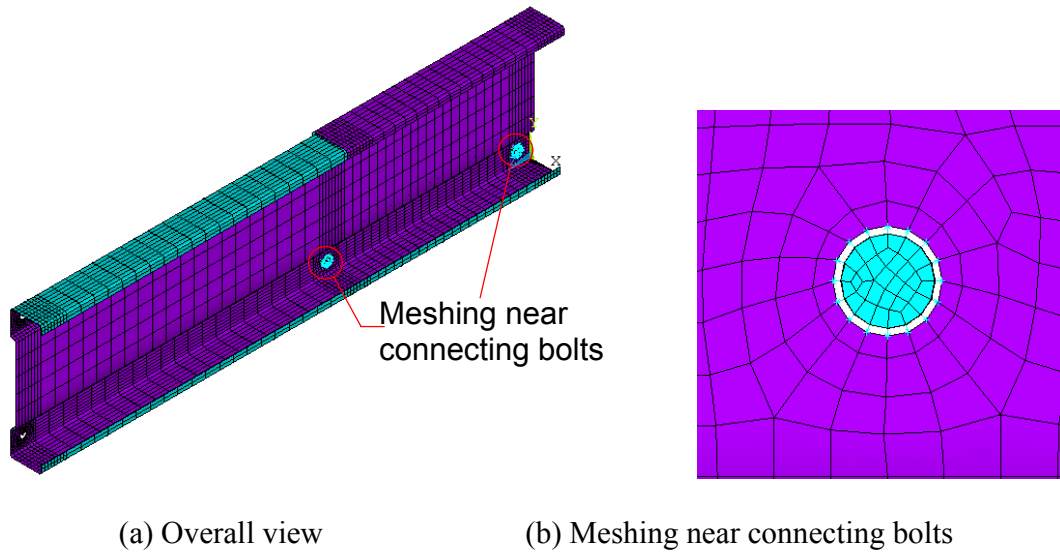


Figure 4-12 Finite element meshing

In this FE modelling, the connecting bolts were centralised to their respective bolt holes. The diameter of the bolts is 2mm less than the bolt holes. In order to avoid rigid body motion of these bolts, a number of weak springs were provided to link the bolts to the edges of the bolt holes, as shown in Fig. 4-12 (b). A tri-linear model, as shown in Fig. 4-13, was proposed for the stiffness of the springs. The stiffness of these springs is  $F_0$  (N/mm) or  $-F_0$  (N/mm) if their deformation (lengthen or shorten) is within 1.0 mm and -1.0 mm, otherwise the stiffness becomes zero. These springs can therefore prevent the rigid motion of the bolts before they are engaged in the bolt holes and in the meanwhile, have no influence on the structural performance of the sleeved purlin after the bolts are in contact with the bolt holes. In this research, 10 N/mm is selected for the value of  $F_0$ .

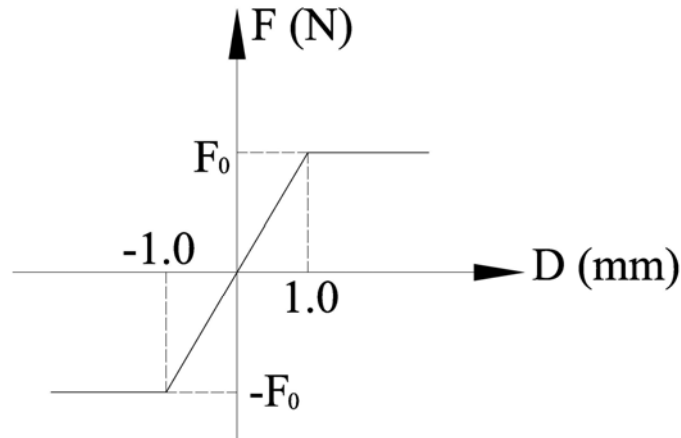


Figure 4-13 Tri-linear stiffness model for the springs

Two connecting bolts on the cross sections where the two outer bolts are located were coupled with the edges of the bolt holes in the normal direction of the web of the purlin. In the same direction, the other two connecting inner bolts on the inner bolted cross section, together with the edges of the bolt holes, were restrained from translation. Such a boundary condition was to allow for the constraint effect provided by the washers to the outer bolts and bolt holes, and to consider the lateral restraint effect on the inner bolts provided by the loading jack. Each connecting bolt was also constrained from rotation about its longitudinal axis by using the nodal coupling method. Symmetrical boundary conditions were applied on the cross section at the mid-span of the sleeve. The boundary conditions at two support ends were the same as those adopted in the FE modelling for the continuous internal support tests (the details of these support conditions were presented in Chapter 3).

Nonlinear material properties of the sigma sections and the sleeves were modelled with the true stress-strain curves obtained from the tension coupon tests. The stress-strain

curves input in this FE modelling are presented in Appendix IV. Elastic materials were used to model all the bolts. The Young's modulus  $E$  and Poisson's ratio  $\nu$  of the elastic materials were  $210\text{kN/mm}^2$  and 0.3, respectively.

Vertical displacement was applied incrementally onto the sleeved purlin via the two connecting bolts on the inner bolted cross section. The displacement increment was set to be 0.2 mm. The solution of the FE modelling was implemented by using full Newton-Raphson procedure and sparse solver.

#### 4.8.2 Validation of FE modelling

The structural behaviour predicted by the FE modelling was compared with 20 test results. Presented in Fig. 4-14 are the moment-rotation responses obtained from the FE analysis and the tests for specimens 24-20016 and 24-24023. The comparison of the moment-rotation responses for other specimens was presented in Appendix X. As has been explained previously, the moment-rotation characteristic of a sleeve connection is composed of three parts, i.e. rotations due to the flexural of purlin, the slip of bolts in bolt holes and elongation of bolt holes under local bearing action. Among these three parts, the rotation due to bolt slip is usually difficult to predict because the initial positions of the bolts in the bolt holes are normally difficult to control in the erection practice. In this FE modelling, the bolts are all ideally centralised to the bolt holes. This arrangement has lead to zero stiffness at the beginning of loading due to the slackness. After the slackness has been taken up, the rotational stiffness predicted by the FE modelling became almost constant. In the test, the bolts moved gradually within the bolt hole at the low loading

level until they were fully engaged. This stage has been characterised with a low rotational stiffness. The rotational stiffness exhibited by both the lab test and FEA model is in a good correlation. The horizontal gap between the FEM and test results is attributed to the free movement before the bolts are fully engaged.

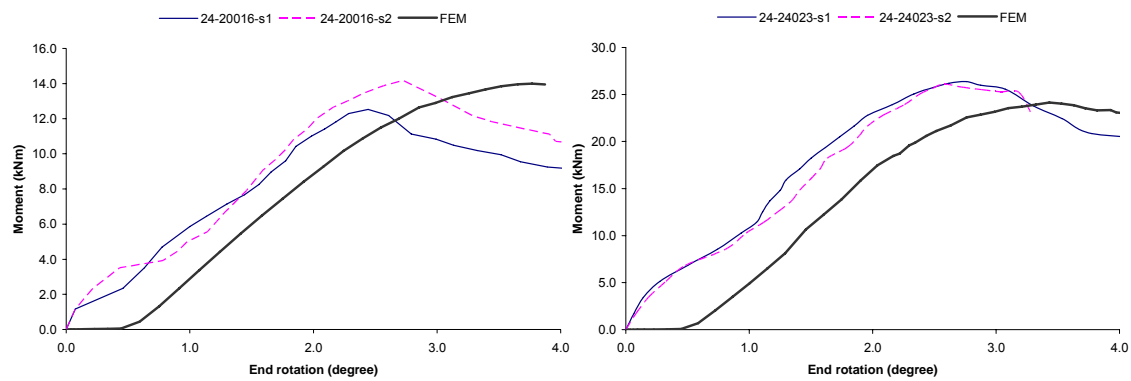


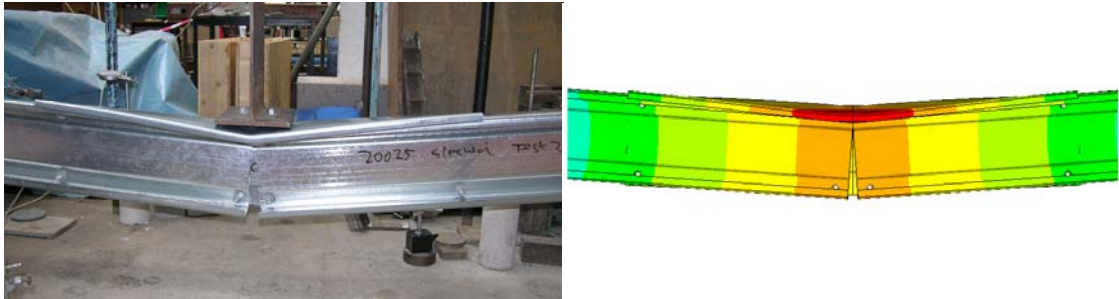
Figure 4-14 Comparison of the moment-rotation response

Table 4-4 presents the comparison of moment resistance between the FE results and the test results. The FE analysis shows good agreement with the test results. The ratio of FE analysis to test results ranges from 0.89 to 1.08, and has a mean of 0.96 with a standard deviation of 0.06.

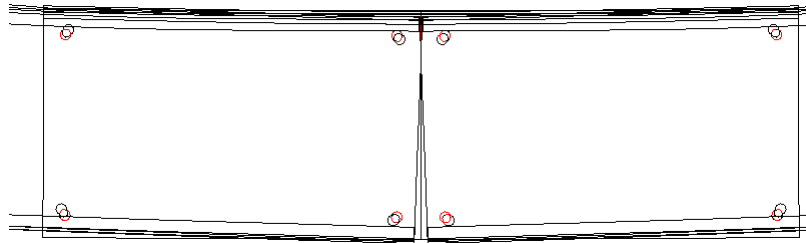
Specimen	Moment resistance, FEM (kNm)	Ratio (FEM / test)
24-20012-s	7.4	0.95
24-20016-s	14.0	1.05
24-20025-s	21.5	0.92
40-20025-s	21.5	1.01
24-24015-s	18.1	1.08
24-24023-s	24.1	0.92
40-24030-s	29.0	0.90
24-30018-s	24.2	1.00
24-30025-s	34.0	0.92
40-30030-s	34.3	0.89
Average		0.96
Standard deviation		0.06

Table 4-4 Comparison of moment resistance

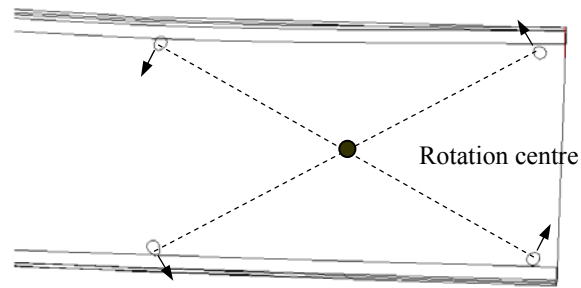
Fig. 4-15 (a) shows the deformation observed from the test FE analysis. High similarity between the test and the simulation can be found from the figure. It is normally difficult to observe the relative rotation between the sigma purlin and the sleeve from tests. While FE analysis results provide a clear observation as shown in Fig. 4-15 (b). Apart from this, Fig. 4-15 (c) presents the deformation in bolt holes of the sigma sections obtained from the FE analysis. On the basis of such deformation pattern, the direction of the moment produced in the bolt group and the corresponding rotation centre of the moment can be determined. By comparing Fig. 4-15 (c) with Fig. 4-5 (c) and Fig. 4-9, it can be seen that the assumption made in the proposed analytical methods, i.e. the rotation centre of the bolt group located at the geometric centre of the four-bolt connection, is rational.



(a) Overall deformation



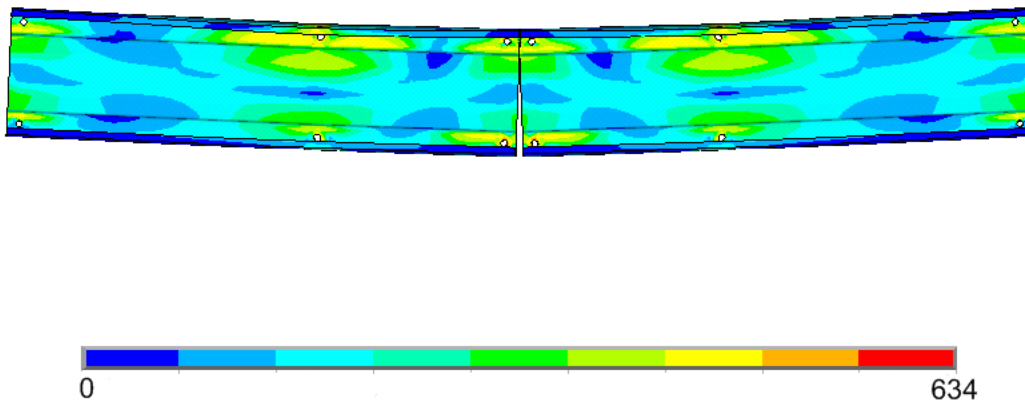
(b) Relative rotation between the sigma sections and the sleeve (the bolt holes in red colour are in the sleeve)



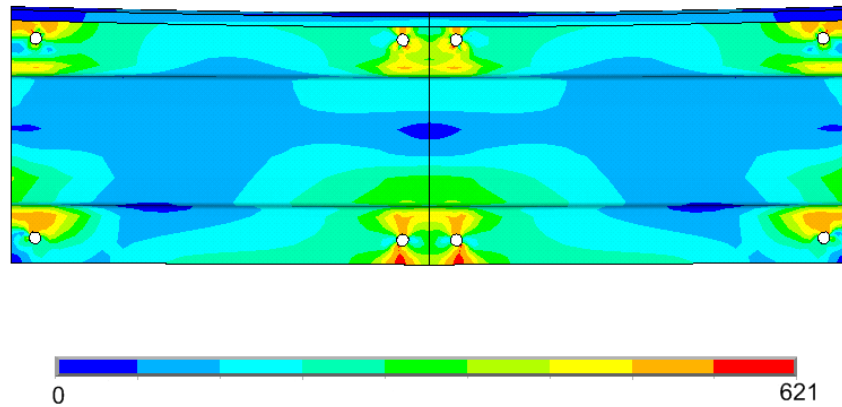
(c) Bolt hole deformation of sigma sections

Figure 4-15 Deformation of the sleeved purlin

Fig. 4-16 shows the stress distribution of the sleeved purlin at the ultimate load. From Fig. 4-16 (a), it can be seen that the critical part of the sigma purlin is around the cross section where outer bolts are located. Whilst from Fig. 4-16 (b) it can be seen that the critical section of the sleeve is around the cross section where inner bolts are located. This agrees with the locations of failure observed in the tests.



(a) Purlin sections



(b) Sleeve sections

Figure 4-16 von Mises stress ( $\text{N/mm}^2$ ) distribution of the sleeved purlin

#### 4.9 SUMMARY

The moment-rotation characteristics of sleeve connection for sigma purlins have been investigated in detail. The study was based on a total of twenty sleeve internal support tests, in which a wide range of sigma sections were covered. The moment-rotation response, moment resistance and typical failure modes were recorded and examined carefully for each test specimen. Based on the test results and observations, a three-stage moment-rotation model for sleeve connection was proposed. This model can capture the initial stiffness contributed by the friction, slips of bolts and the composite action of the purlin and sleeve following the engagement of bolts. It is the first engineering-oriented model for sleeve connections of this kind, and it produces both upper and lower bounds for different initial bolt locations that are practically unpredictable. The lower bounds can be safely used as an engineering design model. A simple engineering model to predict the moment resistance of sleeve connection was also developed. When compared with a



more rigorous model that considers the bending/local bearing interaction, the simple one is deemed to be adequately safe in predicting the moment resistance. Finally, a FE based numerical model was developed with the aim to analyse the structural behaviour of the sleeve connection numerically. Validated by the test results, the FE model demonstrated the rationality of the assumptions made in the three-stage moment-rotation model.

## **CHAPTER 5 SIMPLE SPAN SIGMA PURLINS WITH ROOF SHEETS**

### **5.1 GENERAL**

This chapter reports an experimental research on the flexural behaviour of a series of purlin-sheeting assemblies. Each assembly was composed of two single span cold formed steel (CFS) sigma purlins attached to trapezoidal profiled roof sheets. These sheets were fastened onto purlins by using self-drilling screws applied at predefined intervals. A total of 27 full scale assemblies were subjected to downward and uplift loadings, respectively. Test details and results are reported in this chapter together with the discussion of results and observations. Predicted results of moment resistance of the tested specimens by using the codified design specifications are also presented to compare with test results, from which suggestions of adaption are proposed for design models of sigma purlins attached with roof sheeting.

### **5.2 TEST PROGRAMME**

In this test programme, purlin-sheeting assemblies, as shown schematically in Figs. 5-1 (a) and (b), were subjected to both downward and uplift loadings representing the actions of positive and negative wind pressure applied on a roof system. They will be respectively referred to as downward and uplift loading tests hereafter. In each assembly, a pair of identical sigma purlins of 6m length were placed in parallel with opposing faces. The

purpose of such arrangement was to reduce the lateral movement of sheeting, through the opposing torsional movement from attached purlins, to fix the low in-plane shear stiffness problem due to the use of sheeting with a small width (0.66m). Both purlin members were covered by overlapping single layer roof sheets throughout their spans. A six-point loading system was applied through four spreader beams placed on each test assembly.

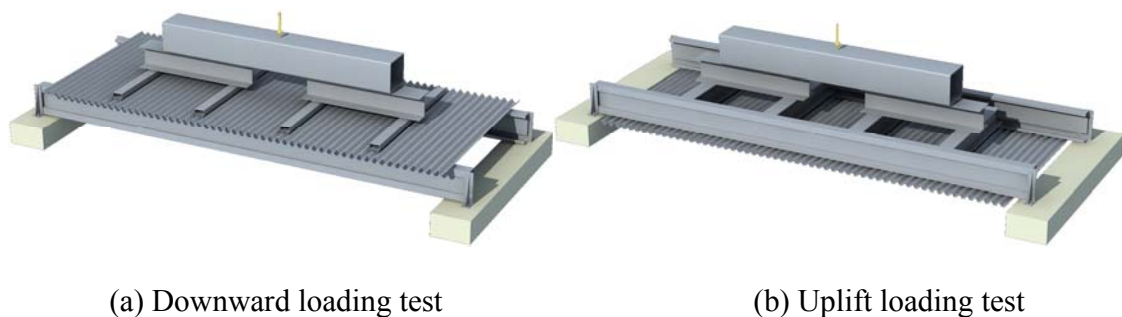
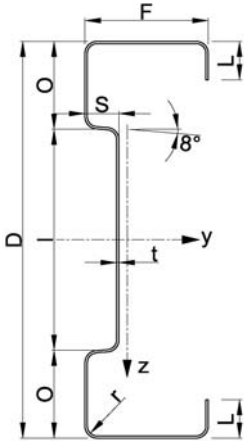


Figure 5-1 Overall view of test assemblies

Nine sigma purlin sections of different depths and thicknesses were chosen in this test programme. Two duplicated tests for each section were carried out for the downward loading test to demonstrate the repeatability of test results and only one test was for the uplift loading test. A three-part reference system is used to identify each test. For instance, if a test is referred as SD60-20012-1 or SU60-20012-1, the first part “SD60” or “SU60” indicates that the corresponding specimen is subjected to a single span downward or uplift loading test and has a 6m of specimen length; the second part “20012” refers to the section dimensions, i.e. 200mm of depth and 1.2mm of thickness; and the last part “1” is the number of the duplicated test.

### 5.3 TEST SPECIMENS

The sigma purlin sections chosen for tests include three depths, i.e. 200, 240 and 300 mm. The nominal cross-sectional dimensions of the sections are presented in Table 5-1 (a). The Young's Modulus, 0.2% proof stress, and the measured mean thickness of the sections are summarised in Table 5-1 (b). The material properties were obtained from material tensile coupon tests by following BSI (2001), and the thickness was measured with a Digital Vernier Caliper at points located in the inner web, top flange and bottom flange, respectively. Table 5-1 (b) also presents the second moment of area about the major axis of each section. A type of single layer trapezoidal steel roof sheeting system was used to cover these purlins. This type of sheeting is the most commonly used in industrial buildings that do not require thermal insulation. They were measured 0.69mm thick and were cut and delivered in 1m lengths. Other sheet dimensions are given in Fig. 5-2. Self drilling screws of 5.5mm diameter, with EPDM bonded washers, were used to connect the sheeting with purlin sections at their middle flange point. In this study, #12-14×25 HEX washer head self drilling screws (Fig. 5-3) were used.

Section	$D$ (mm)	$F$ (mm)	$L$ (mm)	$O$ (mm)	$I$ (mm)	$S$ (mm)	$r$ (mm)	$t$ (mm)	
20012	200	62.5	20	45	110	16	4	1.20	
20016	200	62.5	20	45	110	16	4	1.60	
20025	200	62.5	20	45	110	16	4	2.50	
24015	240	62.5	20	50	140	16	4	1.50	
24023	240	62.5	20	50	140	16	4	2.30	
24030	240	62.5	20	50	140	16	4	3.00	
30018	300	75	20	60	180	16	4	1.80	
30025	300	75	20	60	180	16	4	2.50	
30030	300	75	20	60	180	16	4	3.00	

(a) Nominal cross-sectional dimensions

Section	Young's Modulus (kN/mm <sup>2</sup> )	0.2% proof stress (N/mm <sup>2</sup> )	Thickness (mm)	Second moment of area (cm <sup>4</sup> )	Number used
20012	206	471	1.24	265	6
20016	214	433	1.60	339	6
20025	207	447	2.45	508	6
24015	208	507	1.49	489	6
24023	205	456	2.22	716	6
24030	217	453	3.02	956	6
30018	207	455	1.82	1117	6
30025	207	447	2.42	1468	6
30030	208	417	2.91	1747	6

(b) Geometrical and mechanical properties

Table 5-1 Tested purlin specimens

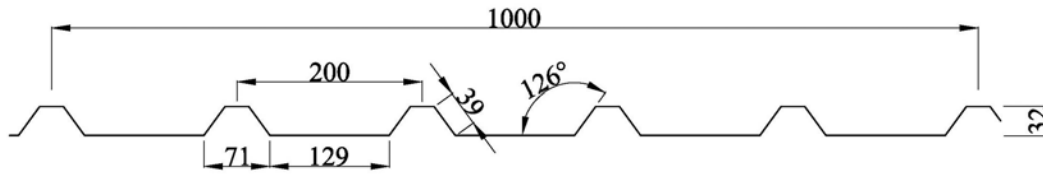


Figure 5-2 Dimensions of the roof sheeting (in mm)

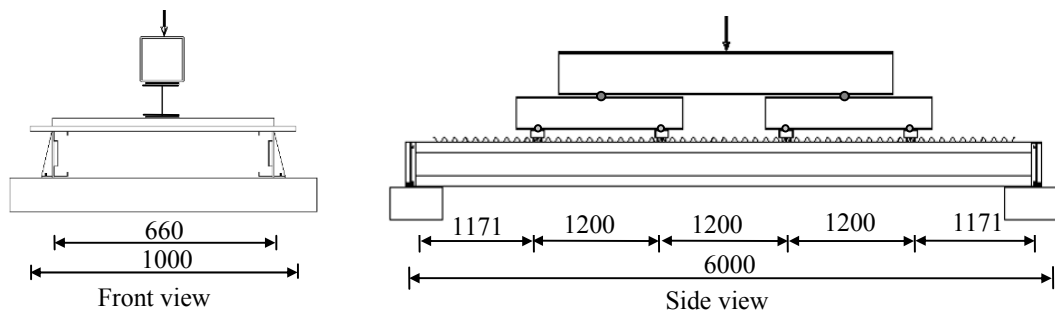
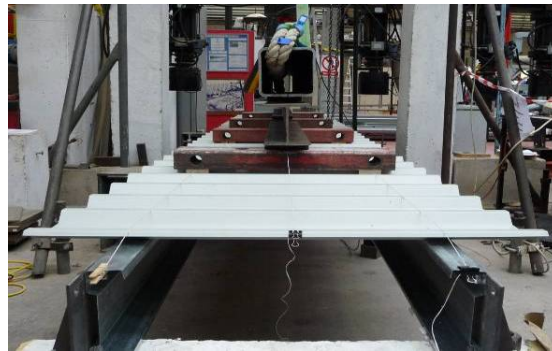


Figure 5-3 Screws connecting roof sheeting to sigma purlins

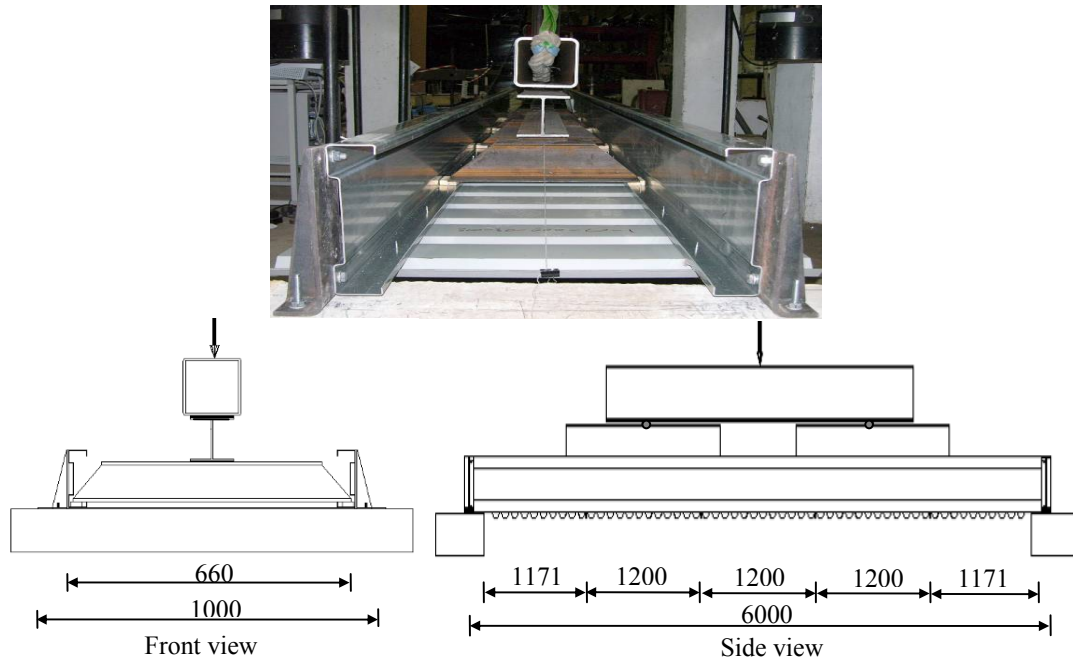
#### 5.4 SET-UP OF TEST APPARATUSES AND TEST PROCEDURE

The purlin/roofing assembly was supported by two massive concrete blocks that have been crane lifted onto pre-marked positions through stiffened angle cleats. The cleats were made of mild steel and pre-fixed onto the concrete blocks by using M16 expansion anchor bolts. The connections between cleats and purlins are through Grade 8.8 M12 bolts for section series 200 and 240 and M16 for section series 300. Standard clearance, i.e. 2mm, in bolt holes allowed a relative horizontal movement between two bolts and therefore did not provide any significant rotation fixity at supports. The horizontal distance between the outer webs of both purlins was 0.66m and the clear span length of all tested assemblies was 5.942m. Six pieces of 1m by 1m roof sheets were placed on the top flanges of purlins, with the corrugation profiles perpendicular to the longitudinal span.

Adjacent sheets were overlapped at one cap length of 71mm (see Fig. 5-2) producing a total covered length of 5.66m. For most specimens, the roof sheets were connected to purlins at every other corrugation trough (400mm) apart from the overlap joints where screws were applied at every trough (200mm). The only exception not following this connection arrangement was test SD60-30025-2, where screws were applied at each trough (200mm) throughout the sheeted length.



(a) Downward loading test



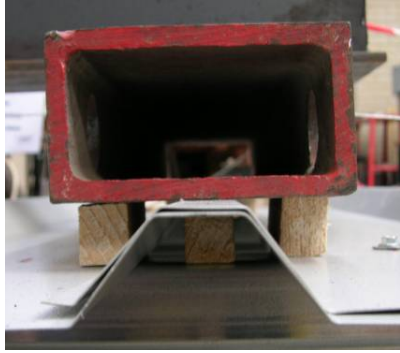
(b) Uplift loading test

Figure 5-4 Schematic illustration of test set-up

In the downward loading tests, as shown in Fig. 5-4 (a), four load spreader beams were used to divide the purlin/roof assembly into five nearly equal lengths. On the top of spreader beams, two UB sections were placed along the centreline of both purlins and supported with rollers. One stiff square hollow section (SHS) sat on the top of the two UB sections and was supported with two rollers located at their central points. In the uplift loading tests, the purlin-sheeting assemblies were placed with purlins on the top. Similar loading mechanisms to the downward loading test were employed except that the spreader beams were placed on the bottom flanges of purlins. The upper corners of spreader beams were cut off with a  $45^\circ$  angle to prevent them from touching purlins during testing. The set-up details for the uplift loading test is shown in Fig. 5-4 (b).



Timber blocks were used between the load spreader beams and the roof sheeting to create a more uniformly loaded surface (see Fig. 5-5).



(a) Downward loading tests



(b) Uplift loading tests

Figure 5-5 Timber blocks used at loading points

## 5.5 TEST INSTRUMENTATION

Continuously increasing displacements at a rate of 0.1mm per second were applied by a loading jack in the 60T Mand test machine to the SHS beam until the response passed the ultimate failure point. Between the loading jack and the SHS beam, a load cell was placed to record the value of applied load at a predefined data sampling frequency. Through the abovementioned loading mechanism, the total load was assumed to be equally split into four parts, and each was applied on a traverse spreader beam that subsequently applied equal loads on both purlins.



(a) Downward loading test



(b) Uplift loading test

Figure 5-6 Test instrumentation

In the downward loading tests, four LVDTs were applied for one sigma purlin. Three of them were placed at the mid-span and both quarter-span points on the free flange to measure vertical deflections. The remaining one was placed on the upper outer web in the mid-span cross section to measure the horizontal deflection. Two other LVDTs were applied to measure the vertical and horizontal deflections at the mid-span point of the second purlin. In the uplift loading tests, three LVDTs were applied on one purlin. They were placed under sheeting and at the mid-span and quarter-span points. Another LVDT

was applied to measure the vertical deflection at the mid-span point of the second purlin in a same manner. The test instrumentation is shown in Fig. 5-6. All LVDTs and the load cell were connected to a data logger. The data logger collected the synchronized data of deflections and forces instantaneously.

## 5.6 TEST RESULTS

The bending moment diagram of a single test purlin is illustrated in Fig. 5-7. The maximum bending moment at the mid-span point is:

$$M_{\max} = 3.542P / 4 \quad (5-1)$$

in which  $P$  is the total applied load on each purlin and is composed of the recorded load by the load cell and the self-weight of loading system.

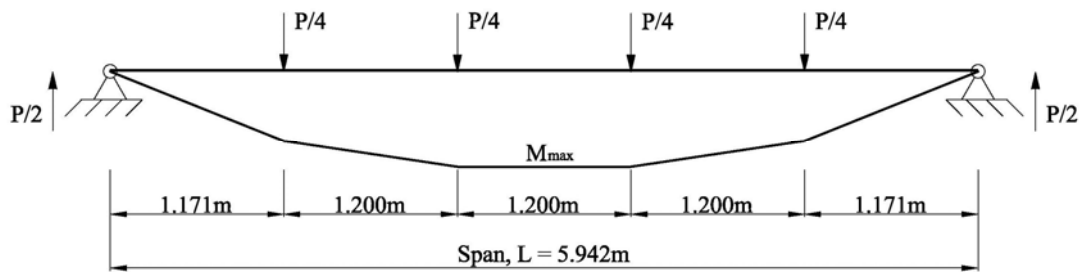


Figure 5-7 Bending moment diagram of the tested sigma purlins

Table 5-2 summarizes the recorded ultimate load  $P_{ult}$  and the corresponding bending moment in the mid-span point  $M_{Rd,t}$ . Also presented in Table 5-2 are the failure modes, i.e. the local and distortional buckling of purlin (Type I), the local failure of roof sheets together with the distortional buckling of purlin (Type II), the local and lateral torsional

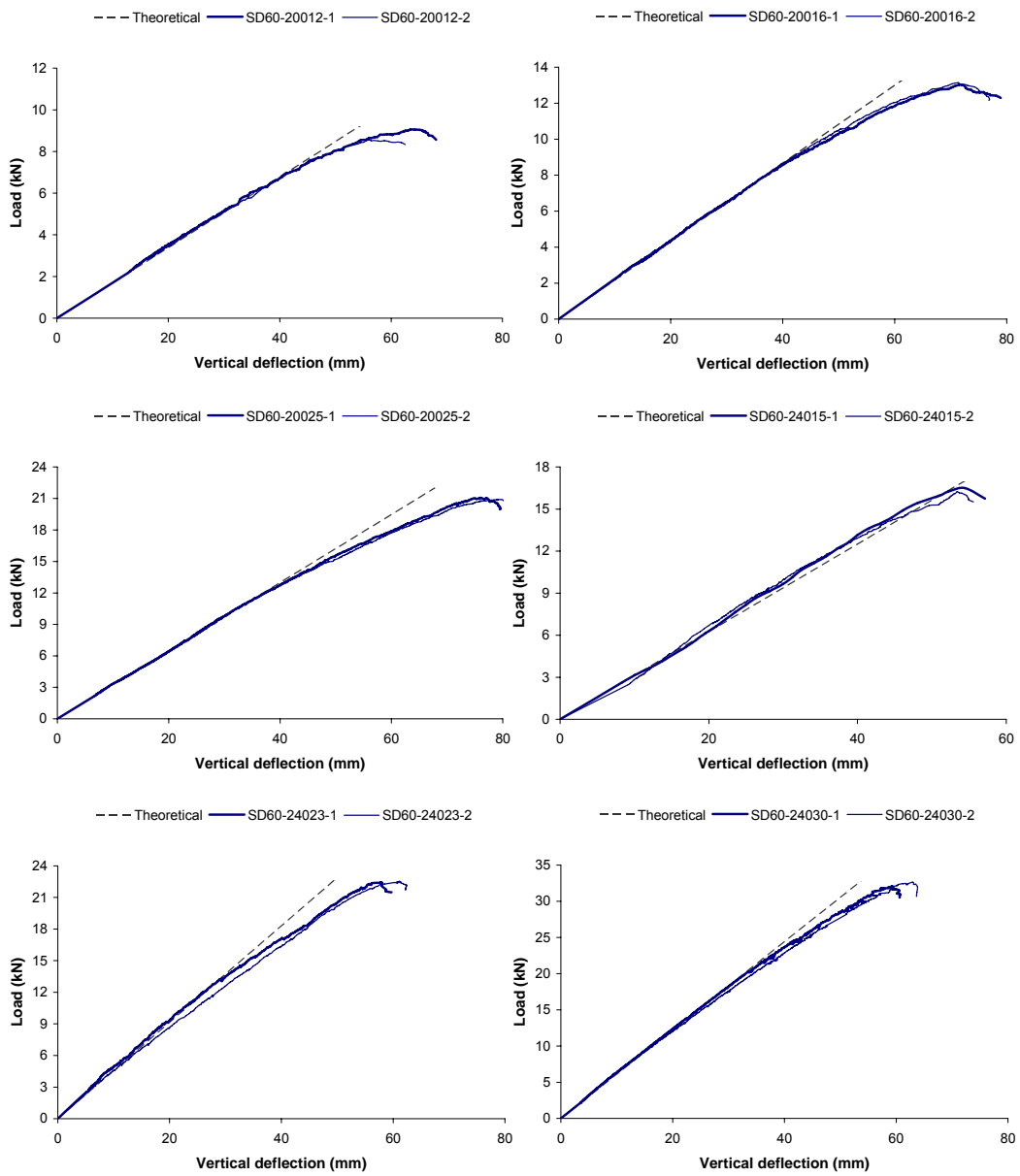
buckling of purlin (Type III), the lateral torsional buckling of purlin in a symmetric manner (Type IV) and the lateral torsional buckling of purlin in an asymmetric manner (Type V). The detailed information of these failure modes are provided in section 5.7.2.

Test ID	$P_{ult}$ (kN)	$M_{Rd,t}$ (kNm)	Failure mode	Test ID	$P_{ult}$ (kN)	$M_{Rd,t}$ (kNm)	Failure mode
SD60-20012-1	9.05	8.0	Type I	SU60-20012-1	6.12	5.4	Type III
SD60-20012-2	8.55	7.6	Type I				
SD60-20016-1	13.03	11.5	Type I	SU60-20016-1	8.31	7.4	Type III
SD60-20016-2	13.14	11.6	Type I				
SD60-20025-1	21.05	18.6	Type II	SU60-20025-1	13.67	12.1	Type V
SD60-20025-2	20.90	18.5	Type II				
SD60-24015-1	16.50	14.6	Type I	SU60-24015-1	8.50	7.5	Type V
SD60-24015-2	16.24	14.4	Type I				
SD60-24023-1	22.43	19.9	Type II	SU60-24023-1	14.33	12.7	Type IV
SD60-24023-2	22.56	20.0	Type II				
SD60-24030-1	32.09	28.4	Type II	SU60-24030-1	18.98	16.8	Type IV
SD60-24030-2	32.63	28.9	Type II				
SD60-30018-1	23.26	20.6	Type I	SU60-30018-1	14.66	13.0	Type III
SD60-30018-2	24.00	21.2	Type I				
SD60-30025-1	39.50	35.0	Type II	SU60-30025-1	19.00	16.8	Type IV
*SD60-30025-2	43.69	38.7	Type I				
SD60-30030-1	40.15	35.5	Type II	SU60-30030-1	49.14	21.8	Type IV
SD60-30030-2	41.83	37.0	Type II				

Note: \* Self-drilling screws were applied at every trough.

Table 5-2 Test results of sheeted purlins

Fig. 5-8 shows the load vs. mid-span deflection curves of tested specimens, in which the deflection is the average value of two parallel purlins. For comparison purposes, the corresponding theoretical results calculated based on the linear beam theory are also presented in the same graphs. The detailed derivation of the theoretical results is provided in Appendix XI.



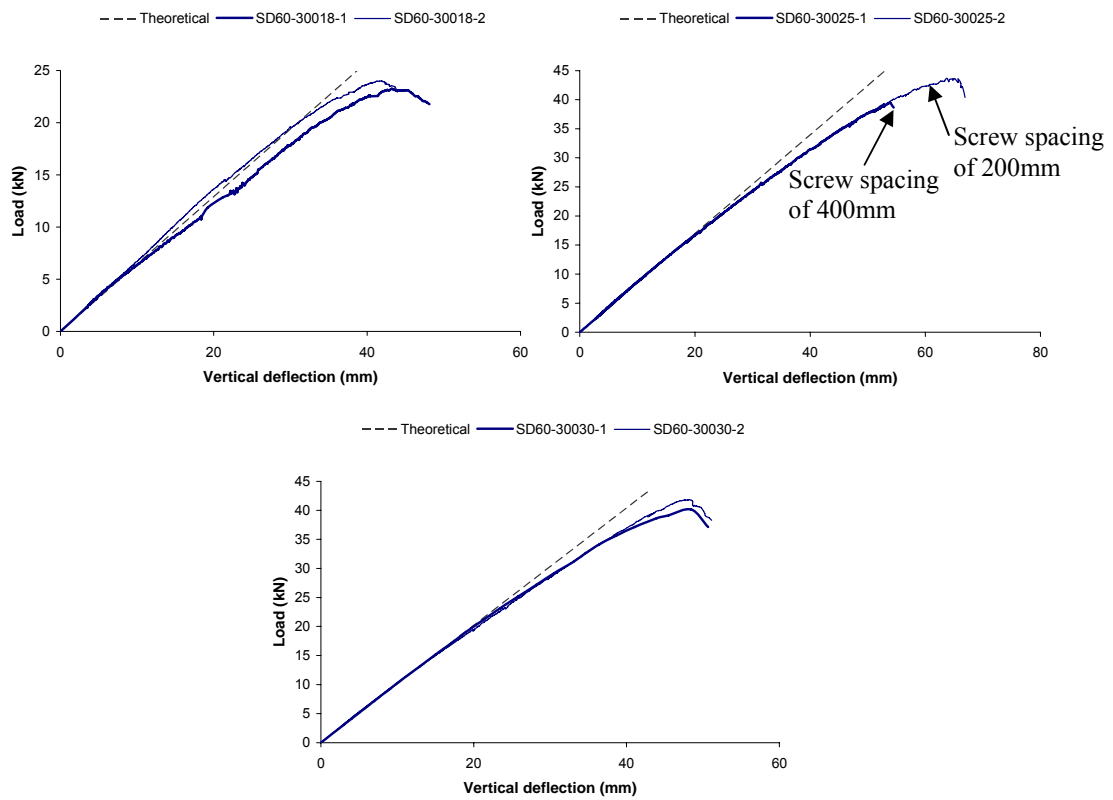
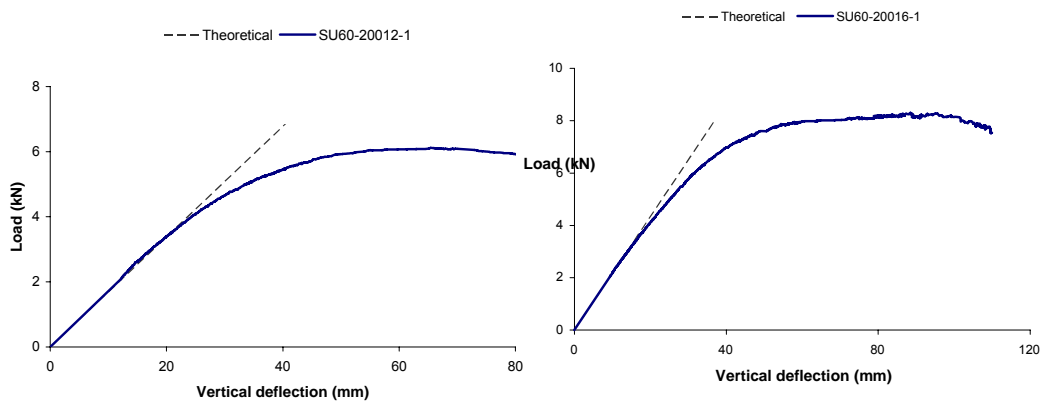


Figure 5-8 Load versus deflection curves for the downward loading test



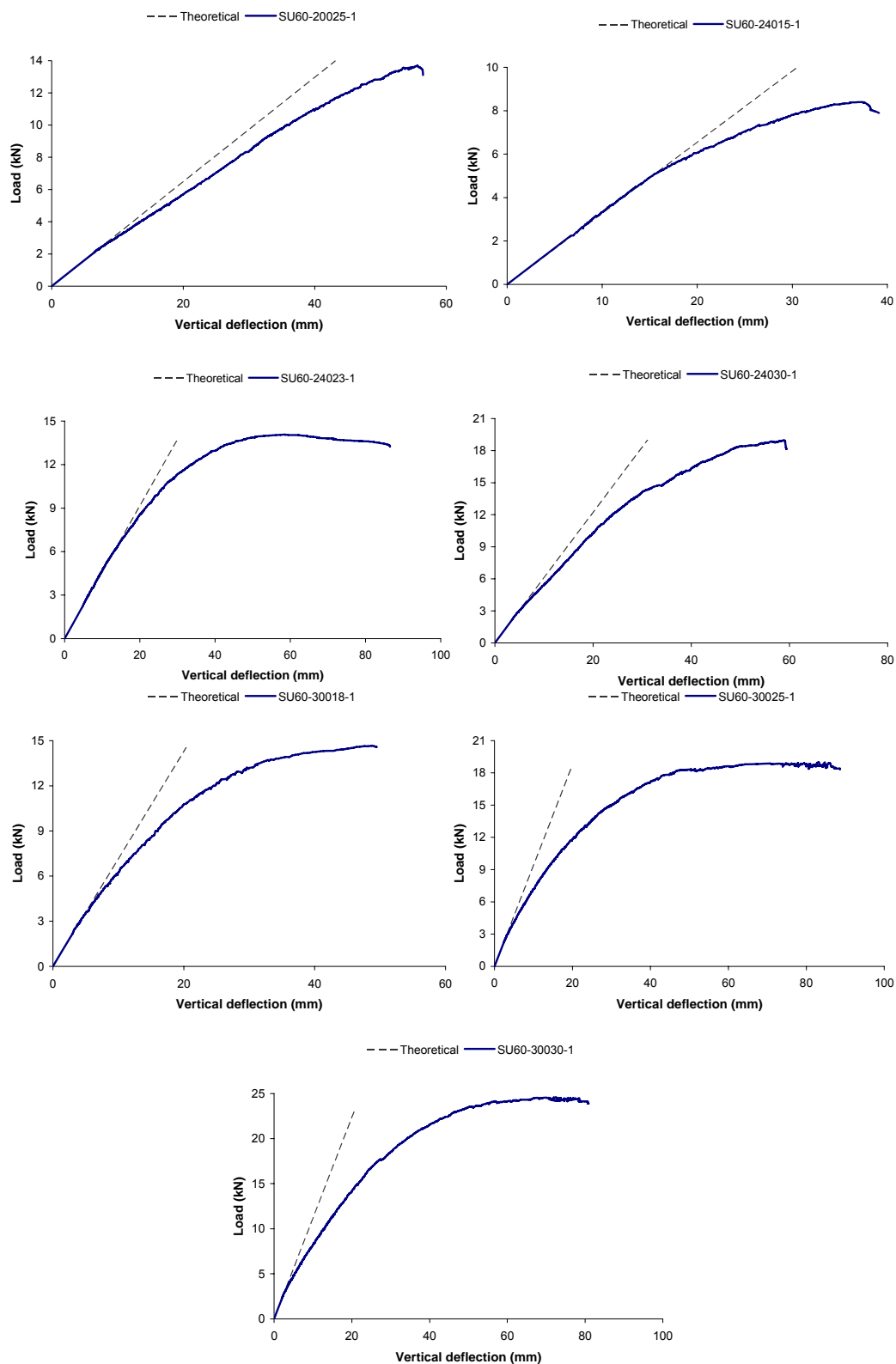


Figure 5-9 Load versus deflection curves for the uplift loading test

## 5.7 DISCUSSION OF THE TEST RESULTS AND OBSERVATIONS

### 5.7.1 Results compared with the prediction by the theoretical linear beam theory

Results from Fig. 5-8 show a good agreement between the theoretical predictions and experimental results for central deflection in the linear behaviour region. It is worth noting that the theoretical calculations only considered the bending effect. The torsional movement caused by the eccentric loads from the shear centre has been ignored. A constant full cross section was considered in the calculations for the entire loading region. This has rendered the discrepancy between the two sets of results in the high loading region, where purlins started to behave nonlinearly. Nevertheless, the close agreement in the linear region suggests the following four conclusions: (1) the support connections of purlin do not impose any fixity and should be deemed as a simple support condition; (2) the compression flange is fully restrained by roof sheeting so that any lateral movement of purlin cross-section will not take place; (3) the change in cross-section resulting from any local or distortional buckling is insignificant; and (4) the material is still elastic. The third conclusion can also be interpreted that the torsional effect from the applied load can be ignored in this stage. However, these findings only hold true for low loading levels. As applied loads increased, the load versus deflection curves gradually became nonlinear, which may be a combination of the above four factors becoming gradually invalid. Some specimens, such as SD60-30018, entered the nonlinear stage at a loading level less than 30% of the ultimate load. As a result, simple beam theory, with the full cross-section,



may lead to an unsafe determination of deflection when checking the serviceability limit load case.

As mentioned above, only in one specimen, (SD60-30025-2), had its roof sheet installed differently in terms of the spacing of the screw application (see Fig. 5-10). This arrangement was planned to demonstrate the effect of screw spacing on the behaviour of sheeted purlins. The comparison of the load vs. deflection curves between SD60-30025-1 and SD60-30025-2 in Fig. 5-8 shows that the variation of screw spacing influences the flexural ultimate load, but does not change the flexural stiffness. Halving the screw spacing will increase the ultimate load by around 11% in this particular case.



Figure 5-10 Different screw spacings for specimens SD60-30025-1 and SD60-30025-2

The load vs. deflection curves shown in Fig. 5-9 for the uplift loading tests suggest that linear beam theory considering only bending effect does not apply to purlins subjected to uplift loading except at a low loading level. The reasons for this finding are: (1) the way that the load was applied introduces a torsional moment in addition to the bending moment, and hence the purlin section was subjected to a combined action of bending and

torsion; (2) since the compression flange of the purlin was unrestrained, it will be susceptible to failure by lateral torsional buckling. These two observations are confirmed by the observed deformation of purlin. This is shown in Fig. 5-11.



Figure 5-11 Typical deformation of sheeted purlin with unrestrained compression flange

Current codes of practice, such as AISI (2007), BSI (2006a) and Standard Australia (2006), suggest that the serviceability check of the CFS members can be based on applying simple beam theory. BSI (2006a) further recommends that the effective cross-section at an actual stress level should be used, after allowing for the effect of local and distortional buckling. Two examples of tests in the download loading test were used to calculate the deflection by using this method and results are presented in Fig. 5-12. It can be seen that the BSI recommendation provides a safe and satisfactory prediction. However, as revealed by the present test results, all the current analytical methods are not applicable for the case of uplift loading.

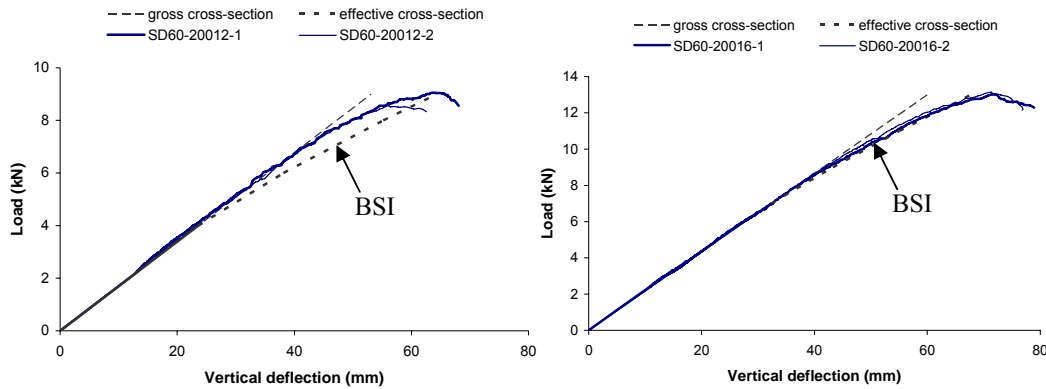


Figure 5-12 Load versus deflection curves

## 5.7.2 Failure modes

### 5.7.2.1 Downward loading tests

Failure modes observed in the downward loading tests can be categorized into two types. Fig. 5-13 shows failure mode I, where a local buckling in the outer web of the sigma purlin first appeared at one of the load application points next to the mid-span section (see Fig. 5-13 a). Due to the post-buckling strength of the local buckling mode, the specimen continued carrying more loading until distortional buckling occurred at the mid-span point, and the maximum load was reached (see Fig. 5-13 b). After loading tests were completed, the covering sheets were removed from the two purlins, to expose buckling deformation as seen in Fig. 5-13 (c).



(a)

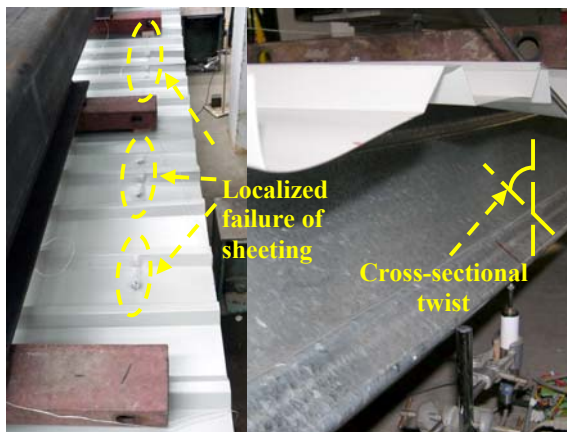


(b)



(c)

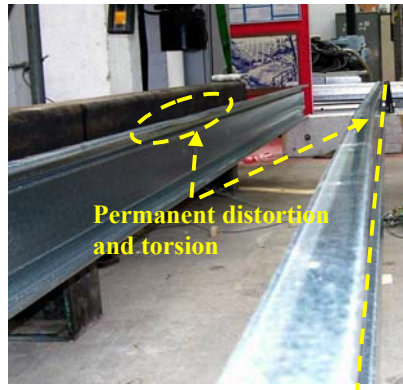
Figure 5-13 Type I failure for downward loading tests



(a)



(b)



(C)

Figure 5-14 Type II failure for downward loading tests

The second failure mode is shown in Fig. 5-14, where localized failure of sheeting occurred first around the screw connection points (see Fig. 5-14 a). This localized failure was due to local couples generated by a tensile force developed in the screw and a reaction along the contact line between the sheeting and one edge of the purlin flange when the purlin section tended to rotate. The localized failure of sheeting did not directly prompt a failure in the purlins. However, it reduced the restraining effect provided by the sheeting, therefore encouraged the torsional deformation of purlins, and subsequently precipitated the occurrence of the type II failure. As Fig. 5-14 (b) shows with type II failure, there is also significant distortional buckling in the high bending moment zone (see Fig. 5-14 b). After the covering sheets were removed, permanent distortion and twist deformations in the cross-section were observed (see Fig. 5-14 c).

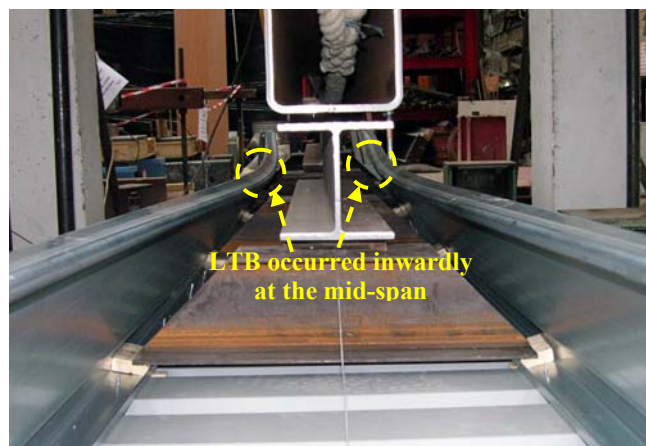
### 5.7.2.2 Uplift loading tests

In the uplift loading tests, failures were all caused by the lateral torsional buckling (LTB).

A closer examination discovered that the LTB induced failure can be further divided into three types, which are numbered III to V.



(a) Type III



(b) Type IV







(c) Type V

Figure 5-15 Failure types for the uplift loading tests

Fig. 5-15 shows the failure modes observed. In type III failure, one of the purlins experiences a local buckling at the mid-span, which rapidly prompted a LTB failure. It was found that the local buckling always located near the flange and outer web junction line, and the unrestrained compression flanges of both purlins moved inwardly when LTB failure occurred as shown in Fig. 5-15 (a). In type IV failure, purlins failed solely due to LTB, and as seen in Fig. 5-15 (b) the unrestrained compression flanges moved towards each other. In type V failure, like type IV, the sigma purlin failed purely in LTB, but one of the purlins rotated outward at failure (see Fig. 5-15 c). It was observed with this type that the maximal lateral displacement did not occur exactly at the mid-span section. Fig. 5-15 (c) shows it occurring approximately 200mm from the centre.

#### 5.7.2.3 Discussion of the failure modes

Failure modes of the test specimens are summarised in Table 5-2. It can be seen that for the downward loading tests, the specimens with relatively thin gauge (i.e. less than

2.0mm) all failed in type I mode. Most of the thick specimens ( $t > 2.0\text{mm}$ ) failed in type II mode. Duplicated tests show good repeatability in respect of the failure mode. Another interesting observation can be made from the comparison of tests SD60-30025-1 and SD60-30025-2, where different screw spacing was used. The results of these two tests indicated that decreasing screw spacing altered the failure mode from type II to type I. One of the reasons for this shift is that reduction of screw spacing will also reduce the couple developed at each screw point and consequently minimize the tendency of localised failure in the roof sheets.

The correlation of the failure mode and the cross-sectional wall thickness shows a similar trend between the uplift and downward loading tests. Most specimens with wall thickness less than 2.0 mm failed in type III mode, and those having greater wall thickness failed in type IV mode. The two exceptions were with specimens SU60-20025-1 and SU60-24015-1, whose failure mode was that of type V, which has a clear asymmetric nature. Since test assemblies were all set-up and tested with the same procedure, the likely cause of this anomaly may be attributed to the geometric imperfections experienced by the purlin sections. It is also observed that types III and IV failure modes led to a more ductile post-failure behaviour than type V.

### 5.7.3 Flexural resistance

#### *5.7.3.1 Predictions of the flexural resistance from different design codes*

Both Standards Australia (2006) and AISI (2007) recommend the same design equation to calculate the flexural resistance, and it is:



$$M_{Rd,m} = \gamma M_{Rd,s} \quad (5-2)$$

in which  $M_{Rd,m}$  is the flexural resistance of the purlin member;  $M_{Rd,s}$  is the cross-sectional moment resistance;  $\gamma$  is an empirical reduction factor associated with the section type. For Z or C purlins, Australia and AISI standards recommend four  $\gamma$  values based on the range of section depth, that is, 0.70 for section depths  $\leq 165\text{mm}$ ; 0.65 for the section depths between 165 and 216mm; 0.50 for Z sections and 0.40 for C sections, if their depths are between 216 and 292mm. However, there is no provision for  $\gamma$  when the section is of sigma shape. If the compression flange is screw-fastened to the sheeting, AISI suggests that, providing the maximum lateral displacement of the restrained flange relative to the supporting points does not exceed 1/360 of the span length, the full cross-sectional moment resistance can be used as the member flexural resistance.

BSI (2006a) recommends a completely different approach to calculate the flexural resistance of a purlin with one flange restrained by sheeting. Allowing for the restraining effect of sheeting, BSI suggests checking the maximum stress in the restrained and free flanges separately as follows:

for the restrained flange:

$$\sigma_{\max} = M_{y,Ed} / Z_e \leq f_y \quad (5-3)$$

for the free flange:

$$\sigma_{\max} = M_{y,Ed} / Z_e + M_{fz,Ed} / Z_{fz} \leq f_y \quad (5-4)$$

if the free flange is in compression, its maximum stress should also satisfy:

$$\sigma_{\max} = (M_{y,Ed} / Z_e) / \chi_{LT} + M_{fz,Ed} / Z_{fz} \leq f_y \quad (5-5)$$

in which  $M_{y,Ed}$  is the bending moment resulted from a vertical load  $q_{Ed}$  in the major bending plane;  $Z_e$  is the effective section modulus;  $f_y$  is the yield stress;  $M_{fz,Ed}$  is the bending moment in the free flange due to an equivalent lateral load  $k_h q_{Ed}$ , which allows for the effect of torsion and lateral bending;  $Z_{fz}$  is the gross elastic section modulus of the free flange plus the contributing part of the web, which is suggested to be 1/5 of the web height in the case of Z and C sections, and 1/6 of the web height for sigma sections;  $\chi_{LT}$  is the reduction factor for the lateral torsional buckling of the free compression flange. BSI recommends using buckling curve b ( $\alpha_{LT}=0.34$ ;  $\bar{\lambda}_{LT,0}=0.4$ ;  $\beta=0.75$ ) in calculating the reduction factor  $\chi_{LT}$ . The superposition of stresses by Eq. (5-4) is schematically illustrated in Fig. 5-16.

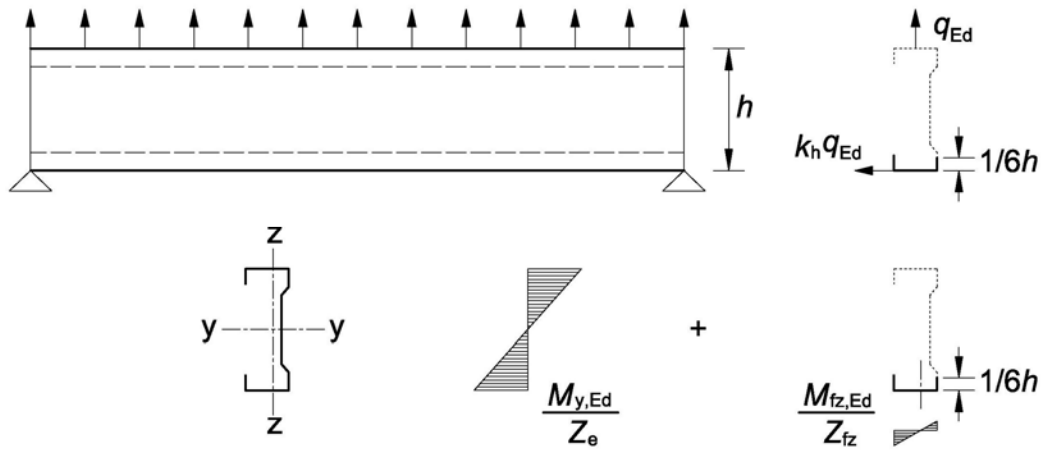


Figure 5-16 Superposition of stresses, after BSI (2006a)

For a sheeted purlin subjected to a downward load, the lesser result of ultimate moment calculated by Eqs. (5-3) and (5-4) should be taken as the moment resistance. This often leads to the free flange governing the moment resistance.

The moment resistance of each test specimen was calculated by the above codified methods and is presented in Table 5-3, in which  $M_{R,SA/AISI}$  and  $M_{R,BSI}$  stand for the moment resistance predicted by the Standards Australia (2006) and AISI (2007), and by the BSI (2006a) provisions.  $M_{R,SA/AISI}$  is not presented for the uplift loading case due to the lack of an appropriate  $\gamma$  value for sigma sections.  $M_{LTB,BSI}$  is the member moment resistance due to the LTB of the free compression flange in the uplift loading case. In BSI provisions, the rotational restraint stiffness ( $C_{D,A}$ ) provided by sheeting to the purlin is modelled as an equivalent lateral spring stiffness  $K$  acting at the free flange of the purlin. The detailed calculation procedures of  $C_{D,A}$  and  $K$ , and  $M_{R,BSI}$  and  $M_{LTB,BSI}$  are given in Appendix XII and XIII, respectively.

Test ID	$C_{D,A}$	$K$	$M_{R,SA/AISI}$	$M_{R,BSI}$	$M_{L,TB,BSI}$
	(Nm/m/rad)	(N/mm <sup>2</sup> )	(kNm)	(kNm)	(kNm)
SD60-20012-1 & 2	652	0.00635	8.9	8.1	NA
SD60-20016-1 & 2	652	0.00957	12.1	11.5	
SD60-20025-1 & 2	652	0.0136	21.5	20.7	
SD60-24015-1 & 2	652	0.00557	15.1	14.0	
SD60-24023-1 & 2	652	0.00860	23.9	23.4	
SD60-24030-1 & 2	652	0.0101	35.7	31.6	
SD60-30018-1 & 2	938	0.00521	24.7	21.9	
SD60-30025-1	938	0.00732	35.7	34.3	
SD60-30025-2	1454	0.00974	35.7	34.3	
SD60-30030-1 & 2	938	0.00838	43.9	40.5	
SU60-20012-1	308	0.00390	NA	6.4	3.0
SU60-20016-1	308	0.00536		8.7	4.6
SU60-20025-1	308	0.00685		14.6	7.3
SU60-24015-1	308	0.00330		10.4	4.4
SU60-24023-1	308	0.00450		15.9	7.3
SU60-24030-1	308	0.00500		20.1	9.3
SU60-30018-1	444	0.00308		14.2	7.0
SU60-30025-1	444	0.00393		20.4	10.6
SU60-30030-1	444	0.00430		22.9	12.4

Table 5-3 Predicted results of flexural moment resistance

#### 5.7.3.2 Discussion of the codified methods for purlins under a downward loading

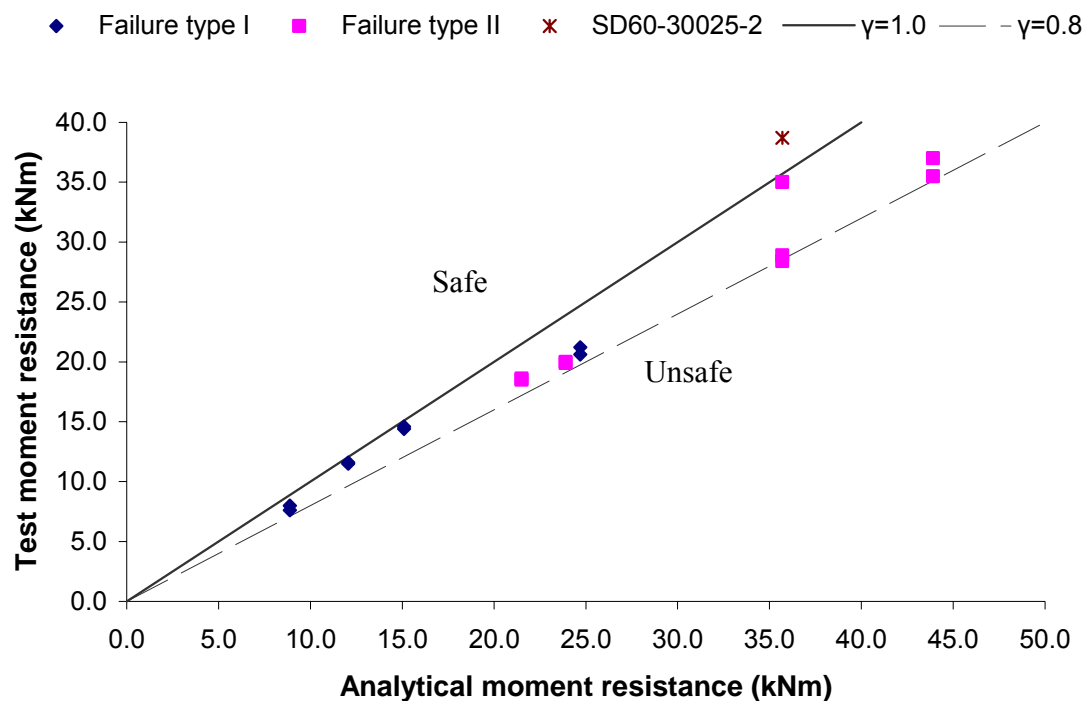
The experimental results of moment resistance  $M_{Rd,t}$  against the predicted results by using the codified methods of SA/AISI  $M_{R,SA/AISI}$  are plotted in Fig. 5-17 (a). It can be seen that except for test SD60-30025-2, the predicted results with  $\gamma$  equal to 1.0 are all unsafe. It

indicates that the assumption of a full restraining effect from sheeting to purlins is inappropriate for the test cases in which the connection screws were applied at every other corrugation trough. In other words, to achieve a full restraining effect from a single layer trapezoidal roof sheeting system, the connection screw should be applied in every trough. Nevertheless, if the reduction factor is changed from 1.0 to 0.8, new predictions will move to the safe region, as shown by the dashed line constructed in Fig. 5-17 (a).

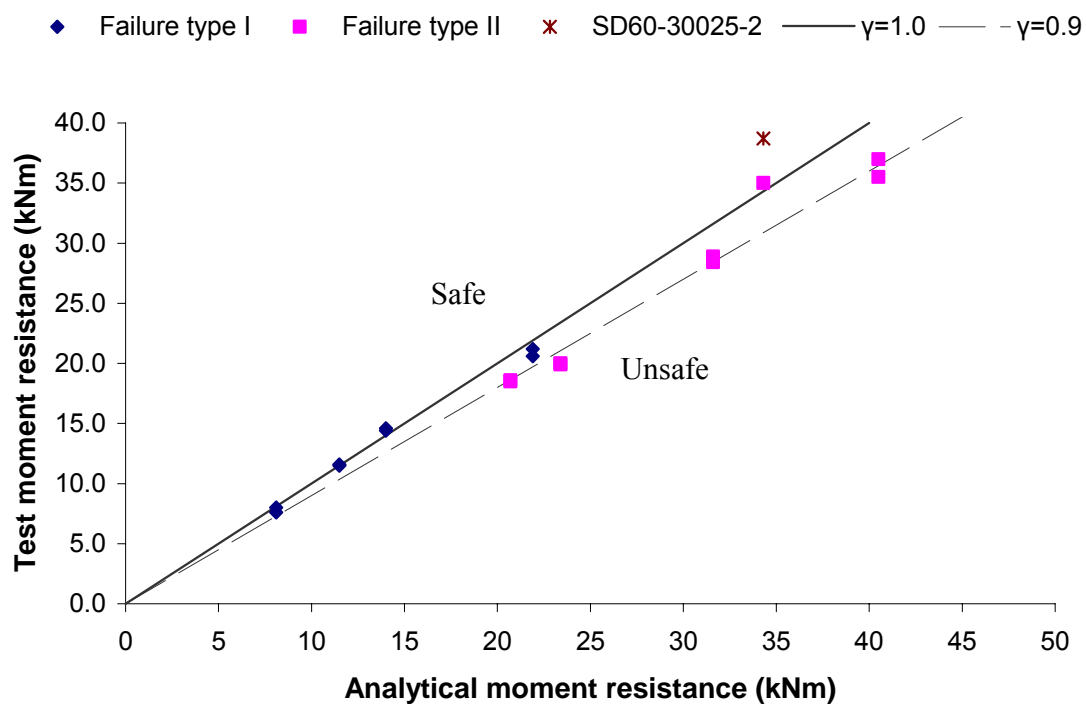
The experimental results  $M_{Rd,t}$  against the predicted ones based on the BSI provision  $M_{R,BSI}$  are plotted in Fig. 5-17 (b). For the specimens failed in type I mode (except SD60-30025-2), the ratio of  $M_{Rd,t} / M_{R,BSI}$  is between 0.94 and 1.04 with a mean value 0.99 and a standard deviation 0.04. According to the test observations described in the preceding section, the sigma purlins in these specimens experienced a local buckling at a concentrated load point before the failure occurred. Considering the point load always imposes an adverse effect on the moment resistance, the test results for ultimate load are expected to be lower than for the case of a uniform distributed wind load. Hence, the BSI predictions are deemed to be adequate. On the other hand, for the specimens failing with type II mode, the ratio  $M_{Rd,t} / M_{R,BSI}$  ranges from 0.85 to 1.02 with a mean value 0.90 and a standard deviation 0.05. This group of specimens experienced torsional deformation after the occurrence of a localised failure of sheeting around the fastening screws. This type of localised failure reduced the effectiveness of restraints on the purlins and consequently led to a lower value of moment resistance than a fully restrained member. BSI assumes that for the downward load situation, the sheeting is able to provide a full restraint and does not consider the effect of the reduction in the restraint due to the

localised failure. This weakness in the BSI method leads to the unsafe predictions for this group of specimens. It is evident that the resistance to the localised failure in roof sheeting near the screw points will be governed by the thickness of the sheeting, the screw spacing and the torsional rigidity of purlin members. The tested cases represent a rather adverse condition in terms of the restraining effect from the roof sheeting. In engineering practice, without further information, a worst case scenario option can be adopted. Therefore, to use the BSI method to predict the moment resistance for the purlins with the compression flange restrained by roof sheeting, a reduction factor 0.9 is recommended by the author to allow for the ineffective restraining effect of roof sheeting associated with the localised failure. The predicted results with and without this reduction factor are shown in Fig. 5-17 (b).

It is worth mentioning that from the result of the special case SD60-30025-2, we can see that the moment resistance has been increased by 11% compared with its counterpart SD60-30025-1. This increase has demonstrated that the screw spacing will affect the restraining effect and hence the moment resistance. The ratios of  $M_{Rd,t} / M_{R,SA/AISI}$  and  $M_{Rd,t} / M_{R,BSI}$  for SD60-30025-2 reveal that both  $M_{R,SA/AISI}$  and  $M_{R,BSI}$  are sufficiently safe to be taken as a member's moment resistance.



(a) Analytical results by Standards Australia (2006) or AISI (2007)



(b) Analytical results by BSI (2006a)

Figure 5-17 Comparison of downward test results with analytical results

#### 5.7.3.3 Discussion of the codified methods for purlins under an uplift loading

As mentioned in Section 5.7.3.2, both Standards Australia (2006) and AISI (2007) use Eq. (5-2) to calculate the member moment resistance of CFS purlins with the tension flange restrained by sheeting. A value for reduction factor  $\gamma$  in Eq. (5-2), however, is only available for Z or C sections. By comparing the test results of moment resistance of sigma sections with  $M_{Rd,s}$  (listed as  $M_{R,SA/AISI}$  in Table 5-3), it is found that  $\gamma = 0.5$  leads to a satisfactory prediction for member moment resistance, as shown in Fig. 5-18. The ratio of  $M_{Rd,t} / 0.5 M_{Rd,s}$  is in a range of 0.94 and 1.23 with a mean value of 1.06 and a standard deviation of 0.10.

BSI (2006a) method for the uplift load case includes a lateral flange moment applied to the free compression flange and also requires a check of the resistance for purlin failure by lateral torsional buckling. From the results presented in Table 5-3, the moment resistance of all the sheeted sigma purlins is governed by the lateral torsional buckling resistance. This agrees well with the observed failure modes from the uplift loading tests. However, the ratios of  $M_{Rd,t} / M_{LTB,BSI}$  indicate that the BSI method underestimates the moment resistance ( $M_{Rd,t}$ ) by 72%. BSI adopts a rather complex model to calculate the LTB resistance, which concerns the parameter of the buckling length of the free flange ( $l_{fz}$ ) and recommends using buckling curve  $b$  (see detailed information of  $l_{fz}$  and buckling curve  $b$  in Appendix XIII). The recommended empirical formula for  $l_{fz}$  is mainly applicable for Z and C sections, and buckling curve  $b$  is proposed mainly for hot rolled or welded steel sections. This may be the explanation for the conservatism in the predicted



results. A detailed study of the improvement of predictions on the moment resistant for LTB of sigma purlins can be a subject of future research work.

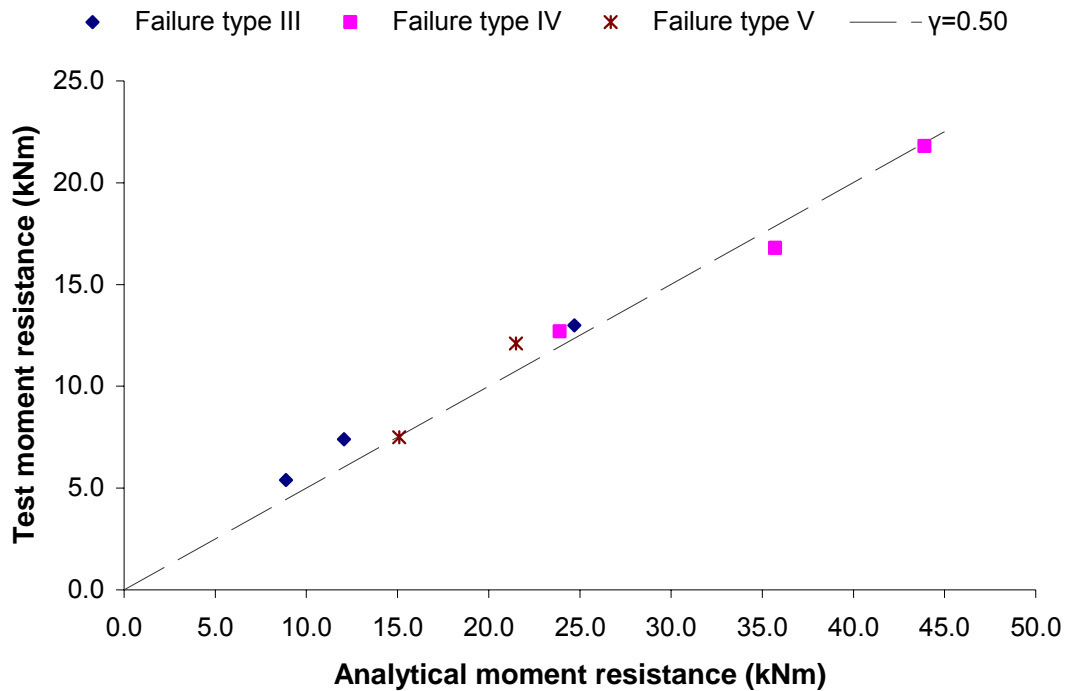


Figure 5-18 Standards Australia (2006) and AISI (2007) predictions for the uplift load tests

## 5.8 SUMMARY

This chapter presents an experimental study on the flexural behaviour of single span CFS sigma purlins screw-fastened with roof sheeting. A range of 27 purling-roofing assemblies were subject to either downward or uplift load cases. The test results were used to examine different flexural stiffness, failure modes and ultimate loads. It has been found that linear beam theory, based on a full cross-section only, produced satisfactory predictions for flexural stiffness with the downward load case in the low loading region.

Beyond that, purlins will behave in a nonlinear manner mainly because of the occurrence of local and distortional buckling. To address this nonlinearity in the stiffness calculation, varying effective cross-sectional properties with regard to the actual stress level should be employed, as suggested by BSI (2006a). For purlins under the uplift load case, the flexural stiffness characteristic was found to be more complex due to the combined action of flexural and torsion, as well as the occurrence of lateral torsional buckling. Therefore, a second-order nonlinear analysis considering the effect of roof sheeting should be performed to characterise response to uplift wind loading.

It was discovered that the failure modes of sheeted purlins under both loading conditions were highly related to the wall thickness of purlins. Test specimens subject to the downward load case exhibited two typical failure modes. In one of the failure modes, a localised failure of sheeting near the screw connections promoted distortional and lateral torsional buckling of purlins, and the restraining effects have been diminished. Methods of avoiding this type of failure are to reduce the screw spacing or to increase the local bending stiffness of sheeting. Three typical failure modes were observed for the uplift load case, all of which were related to purlins failing by lateral torsional buckling. It is believed that the eccentric load from the shear centre introduced a torsional moment and it accelerated the initiation of the lateral torsional buckling mode. Increasing the restraining effect of sheeting by reducing the screw spacing or increasing the thickness of sheeting will increase the flexural resistance.

Two sets of codified methods have been tested to predict the moment resistance of sheeted sigma purlins. It has been concluded that two  $\gamma$  factors should be used in the present test conditions when Standards Australia (2006) or AISI (2007) method is employed. It is 0.8 for the down load case and 0.5 for the uplift load case. BSI (2006a) offers a design method that can provide satisfactory resistance predictions for specimens experiencing type I failure mode, but is not safe for those experiencing type II (when the full restraining effect was unavailable). Now, a single reduction factor of 0.9 can be proposed to cover all specimens (with depth ranging from 200 to 300mm; with thickness ranging from 1.2 to 3.0mm) in the downward load case. When loading is for the uplift situation, failure is primarily governed by LTB. The BSI provision to predict sigma purlin resistance is shown to give rather conservative results. The author recommends that future work is required to develop further the BSI model so that it can adequately be used to determine resistance for uplift loads.

## CHAPTER 6 CONCLUSIONS

### 6.1 GENERAL

This thesis has reported a series of detailed investigations into the structural behaviour of CFS sigma purlins. The investigations included continuous/semi-continuous (sleeved) multi-span purlins along with simple span purlins with sheeting attached.

For continuous CFS sigma purlins, the investigation was primarily focused on their post-buckling and the post-failure moment-rotation behaviour at internal supports. A total of twenty laboratory tests and seventeen finite element analyses were carried out to study such behaviour. The initial buckling mode, ultimate moment resistance, localised collapse pattern, moment softening behaviour, and pseudo-plastic moment resistance were determined for each specimen. Based on both the experimental and numerical results, a semi-empirical approach was proposed to determine the PPMR of CFS sigma sections at internal supports.

For sleeved CFS sigma purlins, the investigation was focused on the moment-rotation characteristic of sleeve connections at internal supports. A total of twenty laboratory tests were performed. The moment-rotation response, ultimate moment resistance and failure mode of the sleeve connections were captured for each specimen. A model to predict the moment-rotation response was also proposed.

In the investigation of sheeted purlins, the flexural behaviour of simple span CFS sigma purlins attached with sheeting by screws were specifically studied for both downward and uplift loads. The study was based on a total of twenty-seven laboratory tests. The moment-deflection response, ultimate moment resistance and failure mode of the sheeted beams under two loading conditions were established for each specimen. Based on current codes of practice (BSI, 2006a; Standards Australia, 2006; AISI, 2007), design proposals were presented to predict the resistance of simple span CFS sigma purlins screw-fastened to sheeting with large screw spacing, under both downward and uplift loads.

## 6.2 INVESTIGATION INTO STRUCTURAL BEHAVIOUR OF CONTINUOUS SIGMA PURLINS AT INTERNAL SUPPORTS

From this part of the study, the following findings have been observed:

- The rotational fixity provided by two bolts with standard clearance through outer-webs of the sigma sections can be considered to be negligible in practical design.
- The initial buckling mode of a CFS sigma purlin at internal supports was highly related to its elastic critical buckling mode obtained by running an eigen-buckling analysis.
- The failure mode of a CFS sigma purlin at internal supports also had good correlation with its elastic critical buckling mode obtained by running an eigen-buckling analysis, provided that the purlin is made of Class 4 section.

- The Effective Width Method given in BSI (2006a) yielded overly conservative predictions for purlins whose failure involved LTB, while the Direct Strength Method in AISI (2007)/Standards Australia (2006) led to unsafe predictions for purlins experiencing LB and DB interaction. The respective causes were discussed and suggestions of improvement for both methods were proposed.
- Four typical localised collapse patterns for CFS sigma purlins were identified, which will be useful in future collapse analysis using the yield line method.
- The moment softening behaviour of a CFS sigma purlin was found to be highly dependent on the slenderness of the purlin, provided that the purlin does not experience any lateral torsional buckling.
- A semi-empirical approach to determine the pseudo-plastic moment resistance of a continuous sigma purlin at internal supports was developed, which can be used to facilitate the pseudo-plastic design method for cold-formed sigma purlins.

### 6.3 INVESTIGATION INTO STRUCTURAL BEHAVIOUR OF SLEEVED SIGMA PURLINS AT INTERNAL SUPPORTS

The following points summarise the most significant findings in this part of the study:

- The moment-rotation response of a sleeve connection has semi-rigid characteristics.
- The pre-failure moment-rotation behaviour features a three stage tendency. The effect of bolt slips plays a significant role on the rotation response at low loading levels and leads to a much larger rotation. An analytical model characterising the

moment-rotation response of sleeve connections was established, which can be used to assess the flexural stiffness of sleeved purlins.

- The critical section of the sleeve connection may occur either in the purlin near the outer columns of bolts or in the sleeve near the centre of the connection. The corresponding failure modes are the local buckling in purlin webs due to a combined bending and local bearing action, tension fracture failure in the tension flange of sleeves due to bending and the local buckling in the compression flange of sleeves also due to bending.
- Sleeve connections can survive higher ultimate moment values than their continuous counterparts except for those suffering failure due to local buckling in sleeve sections.
- The bearing forces between bolts and member plates in the sleeve connection may have an adverse effect on the moment resistance of purlins, but the effect is limited. Therefore, a simple method without considering the moment/local bearing interaction can be utilized to produce safe predictions of the moment resistance.
- A FE model used to simulate the structural behaviour of sleeve connection was developed. The model has been verified by the test results and thus can be used to carry out parametric studies for the sleeve connections in the future.

#### 6.4 INVESTIGATION INTO FLEXURAL BEHAVIOUR OF SHEETED CFS SIGMA PURLINS

Listed as follows are the principal findings from this part of the study:

- The elastic flexural stiffness of the sheeted CFS sigma purlins is different under downward and uplift loading conditions. Normally, the elastic flexural stiffness under downward loads is higher than that under uplift loads.
- The theoretical flexural stiffness recommended in current codes of practice (BSI, 2006a; AISI, 2007; Standards Australia, 2006) agrees well with the test results of elastic flexural stiffness under the downward load but is higher than the test results of elastic flexural stiffness under the uplift loads; this also suggests that the use of theoretical flexural stiffness is un-conservative for the uplift loads.
- Two types of failure modes were identified for the sheeted purlins under the downward loads and three types of failure modes are identified for the sheeted purlins under the uplift loads. It was found that the failure modes of the sheeted purlins under both loading conditions were highly related to the thickness of the purlins.
- For the sheeted purlins under the downward loads, the predictions using the Direct Strength Method given in AISI (2007)/Standards Australia (2006) are generally un-conservative, while the predictions using the Effect Width Method in BSI (2006a) are satisfactory provided that the cross-sectional thickness of the purlin is less than 2.0mm.
- For the sheeted purlins under the uplift loads, AISI (2007)/Standards Australia (2006) is not applicable, and the predictions using the Effect Width Method in BSI (2006a) are generally rather conservative.



- Design proposals are presented, which can be used to improve the predictions using BSI (2006a), AISI (2007)/Standards Australia (2006) for the moment resistance of the simple span sheeted CFS sigma purlins.

## 6.5 LIMITATIONS AND FUTURE WORK

The pseudo plastic design method has been demonstrated to be capable of exploiting the plastic reservation of CFS structures. The key step in employing the pseudo plastic design method is to determine the pseudo plastic moment resistance of the CFS members. The pseudo plastic moment resistance is related to the slenderness of the CFS members, as has been stated in this thesis. In addition to this, they may also be affected by other factors, such as material properties of the CFS members and moment gradient patterns at internal supports. This thesis only considers the CFS sigma sections having a nominal yield stress of  $450\text{N/mm}^2$  in double span purlin systems with equal span length, where moment gradient is symmetrical about the plane of the internal support. For the CFS sigma sections having a lower yield stress, the proposed semi-empirical design expression for the pseudo plastic moment resistance can be applicable because the steels with lower yield stress normally have higher ductility. On the other hand, for the CFS sigma sections having a higher yield stress, further study may be needed to calibrate the semi-empirical design expression proposed. A double span CFS beam with unequal span length is not uncommon in practice; therefore it is also worth assessing the influence of an unsymmetrical moment gradient about the internal support on the pseudo plastic moment resistance of such beams. The influence of material properties and moment

gradient pattern on the pseudo plastic moment resistance of CFS sigma sections may be numerically studied by using the FE model developed in this thesis together with a number of necessary material coupon tests. In addition to this, by using the same methodology described in this thesis, the pseudo plastic moment resistance of other commonly used CFS sections, such as C and Z sections, may also be investigated. It is hoped that a generalised method can be established in the future for determining the pseudo plastic moment resistance of commonly used CFS sections by theoretical calculation. Moreover, CFS members have been applied in portal frames and steel wall frames as built-up beam-columns. It is also worth investigating the pseudo plastic moment behaviour of such CFS beam-columns; so that the pseudo plastic design method can be extended to portal frames and steel wall frames made of CFS sections.

In the study of moment-rotation characteristic of sleeve connections, all of the sleeve sections were subjected to loading in a way that the flanged side of the section was in compression while the flange-free side of the section was in tension. This loading condition represents the sleeve system under a gravity load. However if the sleeved double span beam is under an uplift load, the flanged side of the sleeve section becomes in tension while the flange-free side of the sleeve section becomes in compression. Based on the FE model developed in this thesis for sleeve connections, the moment-rotation characteristic of sleeve connections under other loading conditions may be studied.

Purlin-sheeting interaction is a complicated subject, which concerns many parameters, such as the types of purlins, sheeting and screws, number and locations of screws. This

thesis has only studied the structural behaviour of CFS sigma sections fastened to single layer sheeting by screws applied at every second trough of the sheeting. In modern roofs, sandwich sheeting is often used to increase thermal performance of the roofs. Due to the presence of the thermal insulation, the restraints provided by the sandwich sheeting can be significantly different from that provided by the single layer sheeting. Therefore it is of value that future work investigates the structural behaviour of CFS purlins restrained by sandwich sheeting. It is also worth mentioning that due to the limitation of the laboratory equipment, in this thesis the structural behaviour of the sheeted sigma purlins are investigated by six-point bending tests. However, in practice, the sheeted purlins are normally subjected to uniformly distributed loading (UDL), which is different from the loading condition used in the tests portrayed. The presence of the concentrated loads in the tests more or less reduces the load resistance of the sheeted purlins. Therefore if possible, it is recommended to use a vacuum chamber or air bag to apply UDL on the sheeted purlins in the future test.

## Appendix I Procedures for calculating load resistance of CFS members by using BSI (2006a)

Taking a CFS sigma section for example, the calculation procedures for load resistance of CFS members by using BSI (2006a) are illustrated as follows:

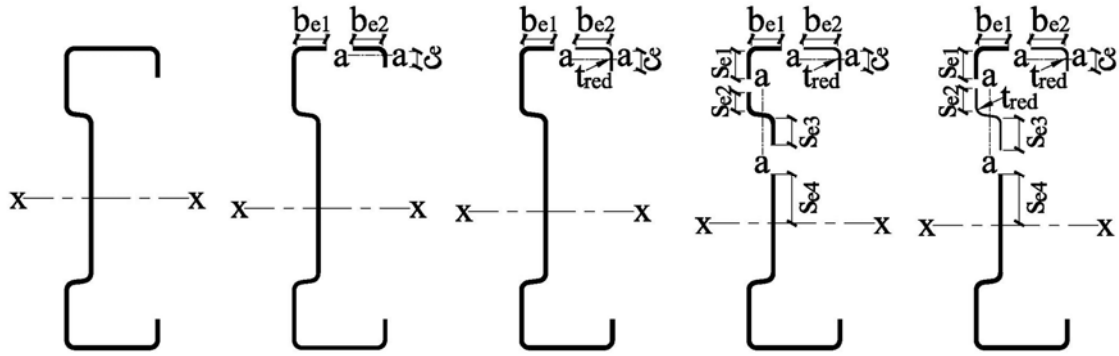


Figure I-1 Stages of determining effective cross section

**Step 1:** Calculate effective widths,  $b_{e1}$ ,  $b_{e2}$  and  $c_e$ , for the compression flange and edge stiffener by Eq. (2-9) to account for local buckling;

**Step 2:** Calculate a reduced thickness,  $t_{red}$ , for the effective area of the edge stiffener to account for distortional buckling; the reduction factor  $\chi_d$  of thickness is calculated as follows:

$$\chi_d = 1 \quad \text{if} \quad \overline{\lambda}_d \leq 0.65 \quad (\text{I-1a})$$

$$\chi_d = 1.47 - 0.723\overline{\lambda}_d \quad \text{if} \quad 0.65 < \overline{\lambda}_d < 1.38 \quad (\text{I-1b})$$

$$\chi_d = \frac{0.66}{\overline{\lambda}_d} \quad \text{if} \quad 1.38 \leq \overline{\lambda}_d \quad (\text{I-1c})$$

where  $\overline{\lambda}_d = \sqrt{f_y / \sigma_{cr,s}}$ ,  $f_y$  is the material yield stress,  $\sigma_{cr,s}$  is the elastic critical stress for the stiffener, and

$$\sigma_{cr,s} = \frac{2\sqrt{KEI_s}}{A_s} \quad (I-2)$$

where  $K$  is the spring stiffness provided by the web (see Fig. 2-3 (b)),  $I_s$  is the effective second moment of the effective area  $A_s$  of the stiffener about the centroidal axis a - a (see Fig. I-1);

**Step 3:** The reduction factor  $\chi_d$  may be refined by an iteration procedure repeating Step 1 and 2 to allow for local buckling and distortional buckling interaction;

**Step 4:** Calculate effective widths  $s_{e1}$ ,  $s_{e2}$ ,  $s_{e3}$  and  $s_{e4}$  for the web in compression zone to account for local buckling in the web by using Eq. (2-9);

**Step 5:** Calculate another reduced thickness for the effective area of the intermediate stiffener in the compression zone to account for distortional buckling of web stiffener; the reduction factor  $\chi_d$  can be determined as that described in Step 2 except calculating  $\sigma_{cr,s}$  with a different formula, which is:

$$\sigma_{cr,s} = \frac{1.05K_f E \sqrt{I_s t^3 s_1}}{A_s s_2 (s_1 - s_2)} \quad (I-3)$$

where  $K_f$  is the spring stiffness provided by the flange and normally taken as equal to 1.0 corresponding to a pin-jointed condition,  $s_1$  and  $s_2$  are determined by geometric parameters of the web and web stiffener;

**Step 6:** The reduction factor  $\chi_d$  may be refined iteratively by Step 4 and 5;

**Step 7:** Calculate effective section modulus  $W_{eff}$  based on the determined effective section;

**Step 8:** Calculate cross-sectional moment resistance  $M_{c,Rd}$ , which is

$$M_{c,Rd} = W_{eff} f_y \quad (I-4)$$

The shear resistance  $V_{c,Rd}$  of the section is determined from:

$$V_{c,Rd} = \frac{h_w t f_{bv}}{\sin \phi} \quad (I-5)$$

where  $h_w$  is the web height between the midlines of the flanges,  $\phi$  is the slope of the web relative to the flanges,  $f_{bv}$  is the shear strength considering buckling;

For cross sections subject to combined bending and shear, and the applied shear force is larger than half of the shear resistance, the following equation is used to account for bending and shear interaction:

$$\frac{M_{Ed}}{M_{c,Rd}} + \left(1 - \frac{M_{f,Rd}}{M_{pl,Rd}}\right) \left(\frac{2V_{Ed}}{V_{c,Rd}} - 1\right)^2 \leq 1.0 \quad (I-6)$$

where  $M_{f,Rd}$  is the moment of resistance of a cross-section consisting of the effective area of flanges only,  $M_{pl,Rd}$  is the plastic moment of resistance of the cross-section. If the applied shear force is no larger than half of the shear resistance, the resistance reduction due to bending and shear interaction can be neglected.

For a CFS member that is susceptible to lateral torsional buckling, BSI (2006a) adopts the design formulae in BSI (2005a) to determine the design lateral torsional buckling resistance moment of the member. The formulae are as follows:

$$M_{b,Rd} = \chi_{LT} W_{eff} f_y \quad (I-7)$$

where  $\chi_{LT}$  is the reduction factor for lateral torsional buckling and is calculated by:

$$\chi_{LT} = \frac{1}{\Phi_{LT} + \sqrt{\Phi_{LT}^2 - \bar{\lambda}_{LT}^2}} \quad \text{but} \quad \chi_{LT} \leq 1.0 \quad (\text{I-8})$$

$$\Phi_{LT} = 0.5[1 + \alpha_{LT}(\bar{\lambda}_{LT} - 0.2) + \bar{\lambda}_{LT}^2] \quad (\text{I-9})$$

$$\bar{\lambda}_{LT} = \sqrt{\frac{W_{eff} f_y}{M_{cr,LTB}}} \quad (\text{I-10})$$

$\alpha_{LT}$  is an imperfection factor related to cross-sectional shapes and manufacture methods.

BSI (2005a) provides four empirical values of  $\alpha_{LT}$ , i.e. 0.21, 0.34, 0.49 and 0.76, for commonly used hot rolled sections and welded sections. By applying these four values into Eq. (I-8),  $\chi_{LT}$  is graphed with respect to  $\bar{\lambda}_{LT}$  in BSI (2005a) in the form of four curves, i.e. buckling curves *a*, *b*, *c*, and *d* respectively. BSI (2006a) selects curve *b* for CFS sections, which corresponds to imperfection factor 0.34.

## Appendix II Procedures of DSM for calculating load resistance of CFS members by using Standards Australia (2006) or AISI (2007)

The procedures of DSM for calculating load resistance of CFS members by using Standards Australia (2006) or AISI (2007) are illustrated as follows:

**Step 1:** Calculate nominal lateral torsional buckling resistance moment  $M_{ne}$  of the member:

$$M_{ne} = M_{cr,LTB} \quad \text{if} \quad M_{cr,LTB} < 0.56M_y \quad (\text{II-1a})$$

$$M_{ne} = \frac{10}{9} M_y \left(1 - \frac{10M_y}{36M_{cr,LTB}}\right) \quad \text{if} \quad 2.78M_y \geq M_{cr,LTB} \geq 0.56M_y \quad (\text{II-1b})$$

$$M_{ne} = M_y \quad \text{if} \quad M_{cr,LTB} \geq 2.78M_y \quad (\text{II-1c})$$

**Step 2:** Calculate nominal local buckling resistance moment  $M_{nl}$  of the member:

$$M_{nl} = M_{ne} \quad \text{if} \quad \sqrt{M_{ne} / M_{cr,l}} \leq 0.776 \quad (\text{II-2a})$$

$$M_{nl} = \left[1 - 0.15\left(\frac{M_{cr,l}}{M_{ne}}\right)^{0.4}\right] \left(\frac{M_{cr,l}}{M_{ne}}\right)^{0.4} M_{ne} \quad \text{if} \quad \sqrt{M_{ne} / M_{cr,l}} > 0.776 \quad (\text{II-2b})$$

**Step 3:** Calculate nominal distortional buckling resistance moment  $M_{nd}$  of the member:

$$M_{nd} = M_y \quad \text{if} \quad \sqrt{M_y / M_{cr,d}} \leq 0.673 \quad (\text{II-3a})$$

$$M_{nd} = \left[1 - 0.22\left(\frac{M_{cr,d}}{M_y}\right)^{0.5}\right] \left(\frac{M_{cr,d}}{M_y}\right)^{0.5} M_y \quad \text{if} \quad \sqrt{M_y / M_{cr,d}} > 0.673 \quad (\text{II-3b})$$

**Step 4:** Calculate design moment resistance of the member:



$$M_{Rd,DSM} = \min(M_{ne}, M_{nl}, M_{nd}, M_y) \quad (II-4)$$

The shear resistance  $V_{Rd,DSM}$  of the section is determined by following:

$$V_{Rd,DSM} = V_y \quad \text{if} \quad \sqrt{V_y / V_{cr}} \leq 0.841 \quad (II-5a)$$

$$V_{Rd,DSM} = 0.841 \sqrt{V_{cr} V_y} \quad \text{if} \quad 0.841 < \sqrt{V_y / V_{cr}} \leq 1.191 \quad (II-5b)$$

$$V_{Rd,DSM} = V_{cr} \quad \text{if} \quad \sqrt{V_y / V_{cr}} > 1.191 \quad (II-5c)$$

where  $V_{cr}$  is elastic shear buckling force of web,  $V_y$  is yield shear force of web.

The combined bending and shear action is accounted for by the following equation:

$$\left( \frac{M_{Ed}}{M_{Rd,DSM}} \right)^2 + \left( \frac{V_{Ed}}{V_{Rd,DSM}} \right)^2 \leq 1.0 \quad (II-6)$$

## Appendix III Derivation of the theoretical moment-rotation capacity curve used in the pseudo plastic design method

The derivation of the theoretical moment-rotation capacity curve used in the pseudo plastic design method is detailed as follows.

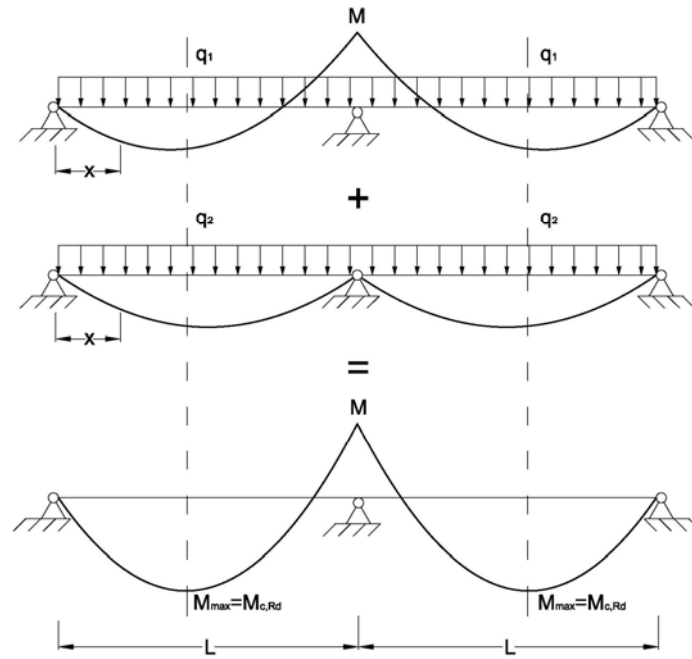


Figure III-1 illustration of the pseudo plastic design method

With reference to Fig. III-1, before a pseudo plastic hinge is formed at the internal support, the moment distribution with respect to  $x$  of a double span continuous CFS beam under UDL  $q_1$  is

$$M_1 = \frac{q_1 L x}{8} \left( 3 - \frac{4x}{L} \right) \quad (\text{III-1})$$

After the pseudo plastic hinge is formed, moment redistribution takes place and the moment distribution under additional load  $q_2$  is

$$M_2 = \frac{q_2 L x}{2} \left(1 - \frac{x}{L}\right) \quad (\text{III-2})$$

By using the principle of superposition, the moment distribution under  $q_1 + q_2$  therefore is

$$M(x) = M_1 + M_2 = -\frac{q_1 + q_2}{2} x^2 + \left(\frac{3}{8} q_1 L + \frac{q_2 L}{2}\right) x \quad (\text{III-3})$$

The first derivative of  $M(x)$  is

$$M'(x) = -(q_1 + q_2)x + \left(\frac{3}{8} q_1 L + \frac{q_2 L}{2}\right) \quad (\text{III-4})$$

By setting  $M'(x) = 0$ , it can be solved that

$$x = \frac{3q_1 L + 4q_2 L}{8(q_1 + q_2)} \quad (\text{III-5})$$

where the maximum sagging moment  $M_{\max}$  locates.

Hence

$$M_{\max} = \frac{(3q_1 + 4q_2)^2}{128(q_1 + q_2)} L^2 \quad (\text{III-6})$$

The pseudo plastic moment  $M$  at the internal support is equal to  $\frac{q_1 L^2}{8}$ . Let  $M_{\max}$  equal to

the cross-sectional moment resistance  $M_{c,Rd}$  of the beam. Replacing  $M_{\max}$  and  $q_1$  in Eq.

(III-6) with  $M_{c,Rd}$  and  $8M/L^2$ , it can be found that

$$q_2 = M_{c,Rd} \left(4 - \frac{6M}{M_{c,Rd}} + 4 \sqrt{1 + \frac{M}{M_{c,Rd}}}\right) / L^2 \quad (\text{III-7})$$

Hence, the rotation angle  $\varphi$  at the internal support can be calculated by

$$\varphi = \frac{q_2 L^3}{24EI_{eff}} \times 2 = (2 + 2\sqrt{1 + \frac{M}{M_{c,Rd}}} - \frac{3M}{M_{c,Rd}}) \frac{M_{c,Rd} L}{6EI_{eff}} \quad (\text{III-8})$$

in which  $I_{eff}$  is the second moment of area of the effective cross section.

## Appendix IV: Material strength tests

The Young's Modulus, tensile proof stress and ultimate stress of each steel coil sample were determined by following standard test method in BSI (2001).

One 300×20 mm sample was cut from each coil that was used to make sigma sections. The sample was gripped by the wedge-shaped jaws in a 50T Denison machine. The grip surface was roughen up so that the sample can be firmly gripped. The net length between the grips of the test machine is 100mm. An extensometer was attached to the sample with gauge length 50mm (see Fig. IV-1). The loading rate was initially set as 20MPa/s and after the material starts to yield strain rate was set as 0.002/s until the ultimate strength of the sample was obtained. During the test, the entire load-strain relation was recorded by the test machine. Based on the measured dimensions of the sample, the recorded load-strain relation was converted to true stress-strain relation by using the equations  $\sigma_{\text{true}} = (1 + \varepsilon_e)\sigma_e$  and  $\varepsilon_{\text{true}} = \ln(1 + \varepsilon_e)$ , where  $\sigma_e$  and  $\varepsilon_e$  are engineering stress and strain. From the true stress-strain curve, the Young's modulus, the 0.2% proof stress and the ultimate stress of the sample were obtained.



Figure IV-1 Set-up of material test

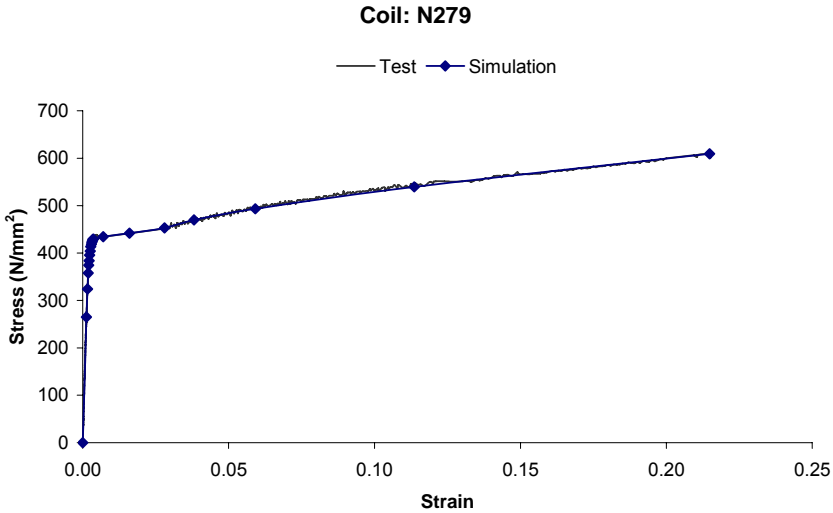
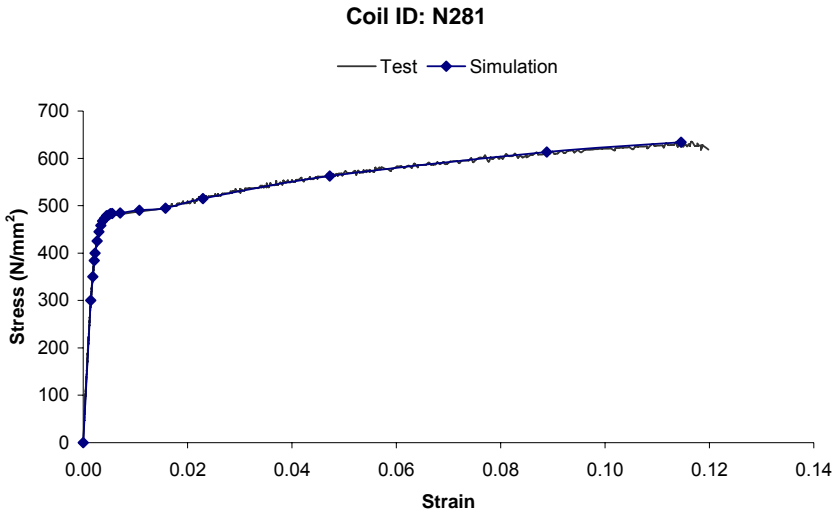
Table IV-1 summarises the test results for each sample.

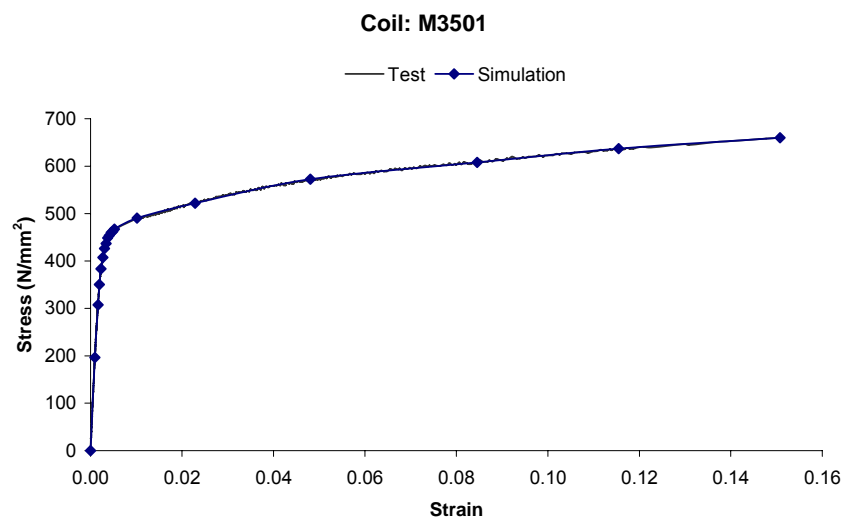
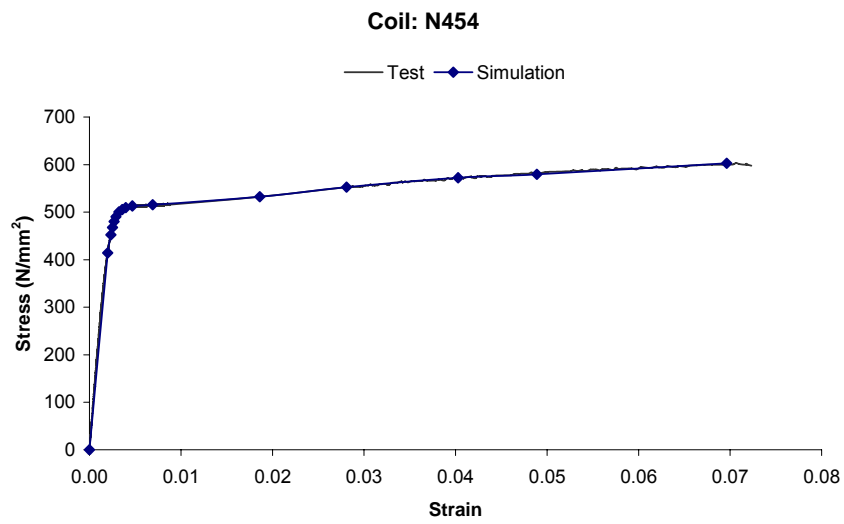
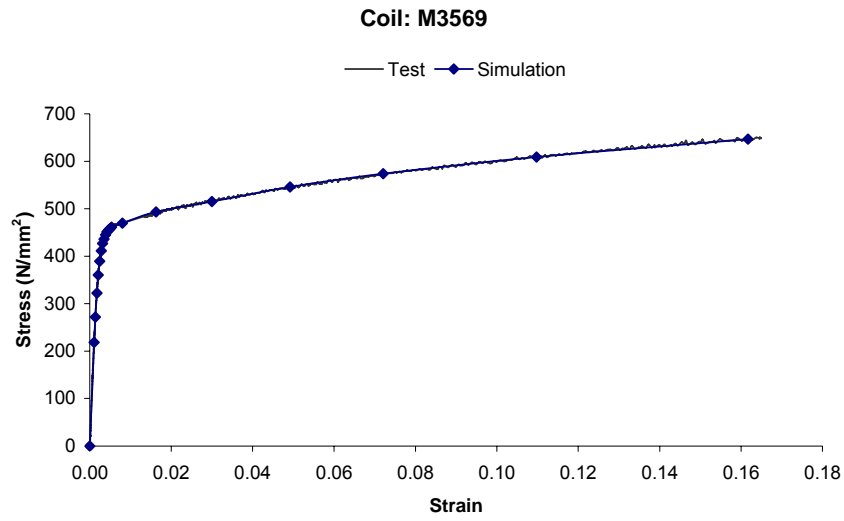
Coil ID	Measured width and thickness (mm)	Young's Modulus (kN/mm <sup>2</sup> )	0.2% proof stress (N/mm <sup>2</sup> )	Ultimate tensile stress (N/mm <sup>2</sup> )	Associated sections
N281	w:19.70, t:1.23	206	471	634	20012
N279	w:19.68, t:1.54	214	433	609	20016
M3569	w:20.94, t:2.44	207	447	646	20025 *20025 *24025 30025
N454	w:21.01, t:1.51	208	507	603	24015
M3501	w:20.88, t:2.28	205	456	660	24023
N070	w:21.07, t:3.07	217	453	575	*20030 *24030 24030
N452	w:19.45, t:1.80	207	455	666	30018
N456	w:20.75, t:3.05	208	417	516	30030 *30030
N465	w: 20.87, t: 2.03	224	518	655	*20020

\* sections used as sleeves in the sleeved internal support tests

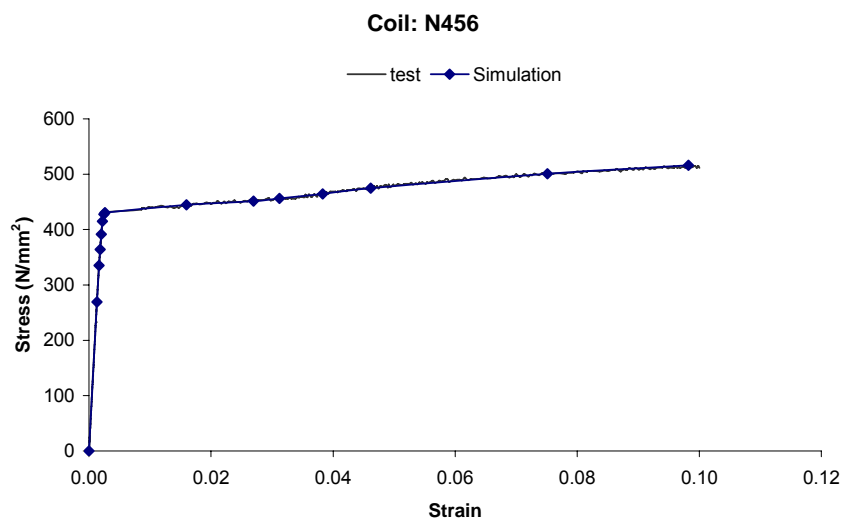
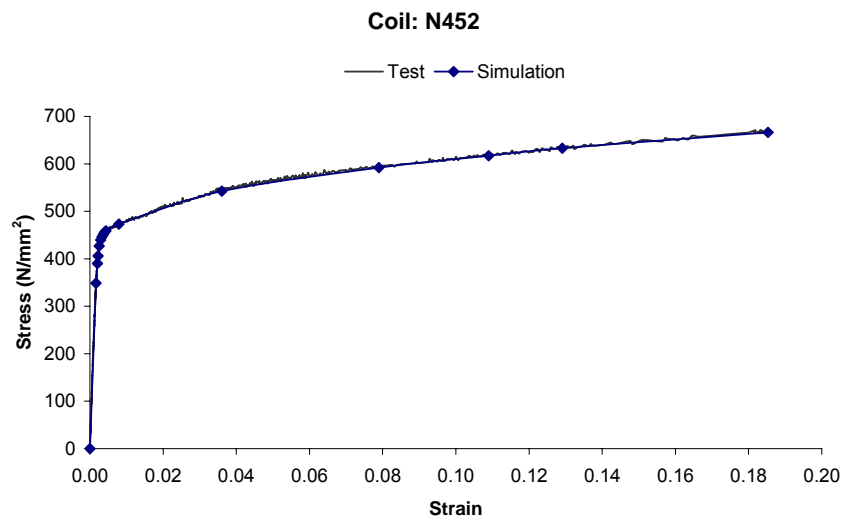
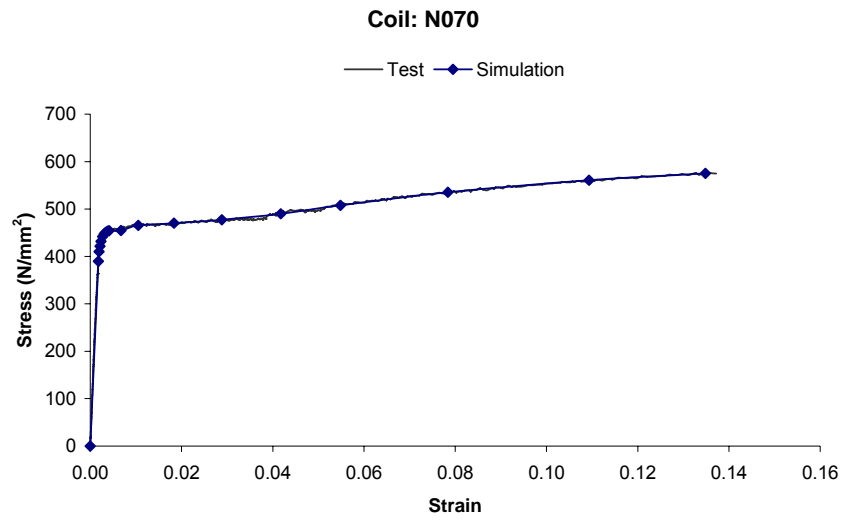
Table IV-1 Results of material strength tests

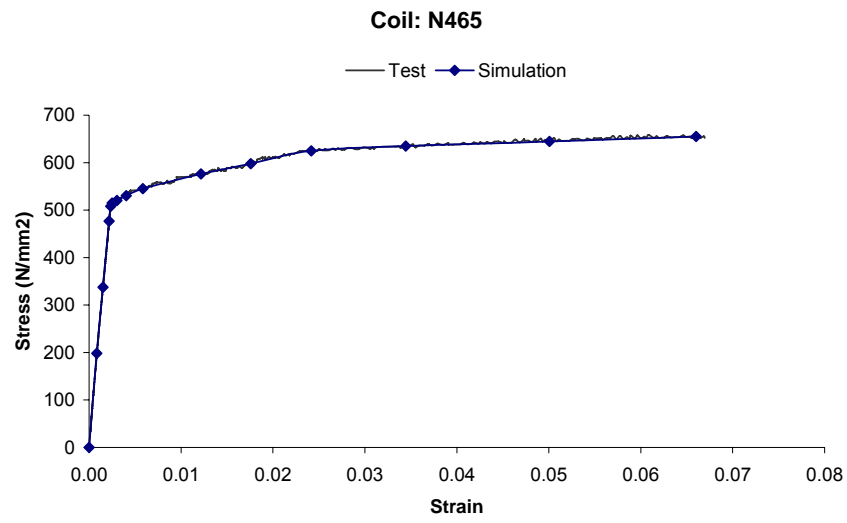
The true stress-strain curves obtained for each coupon sample are presented in the following graphs. The data points used for the simulation of the material property in the FE modelling are also presented in these graphs.



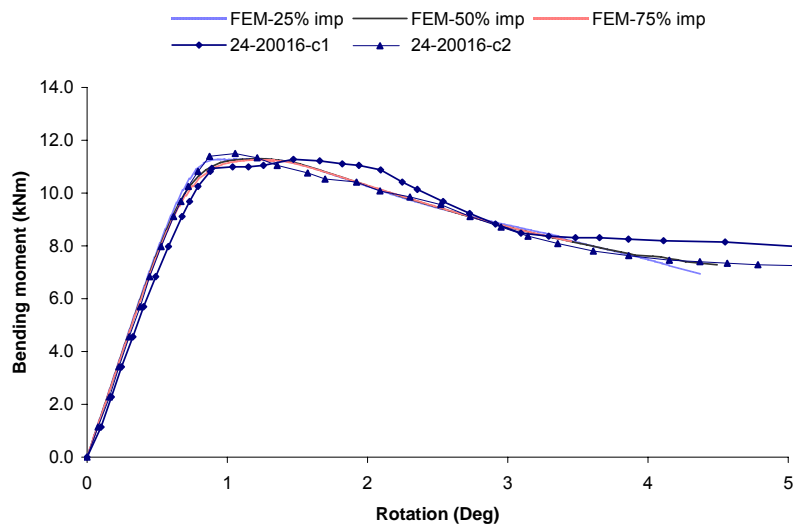
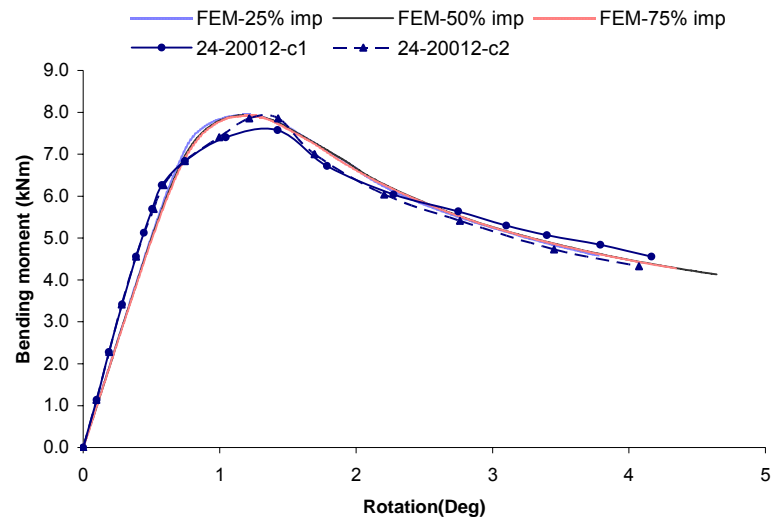


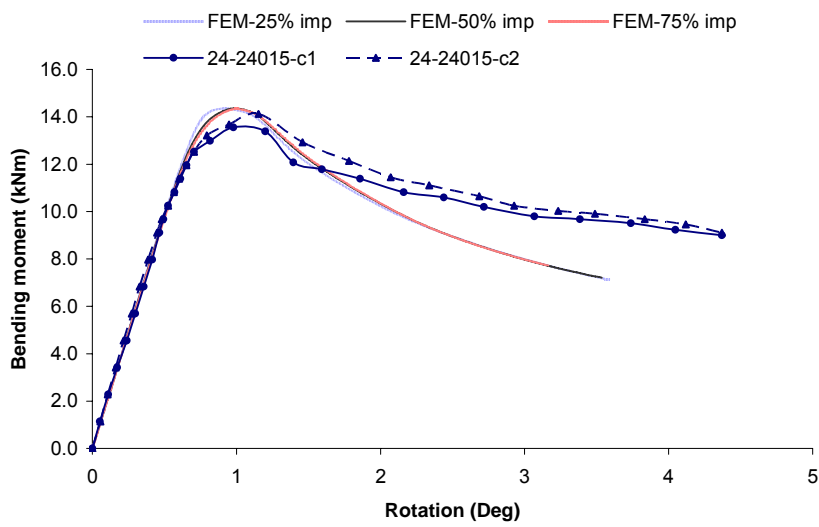
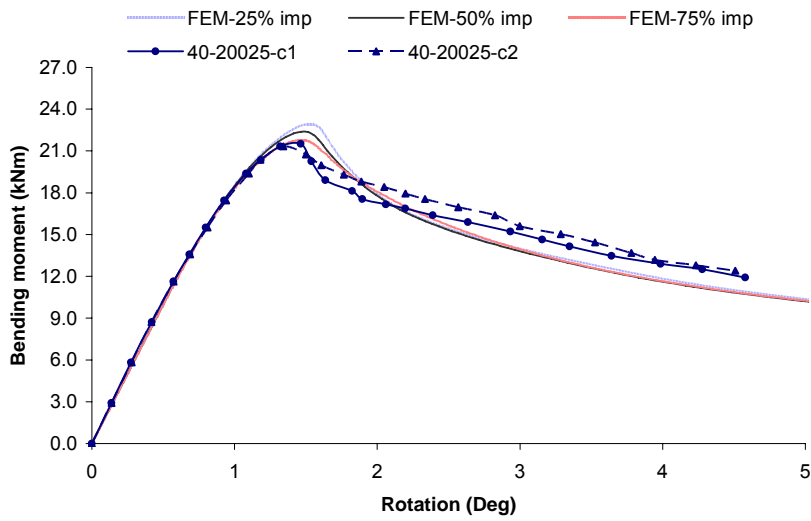
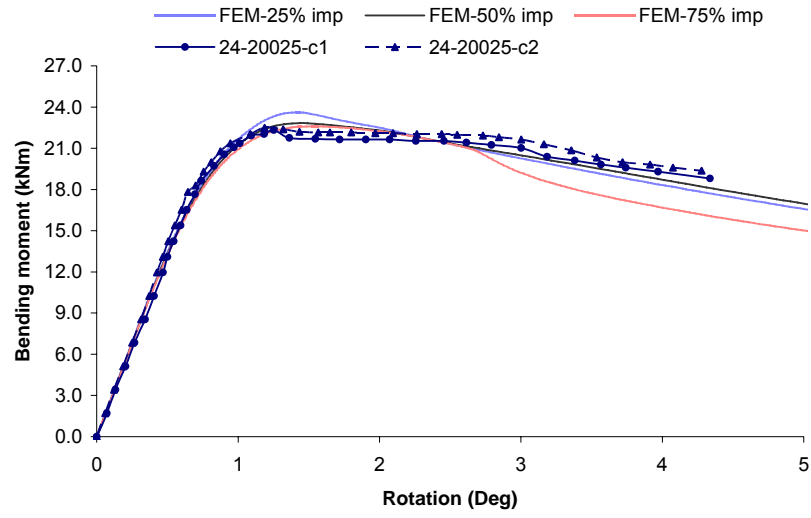


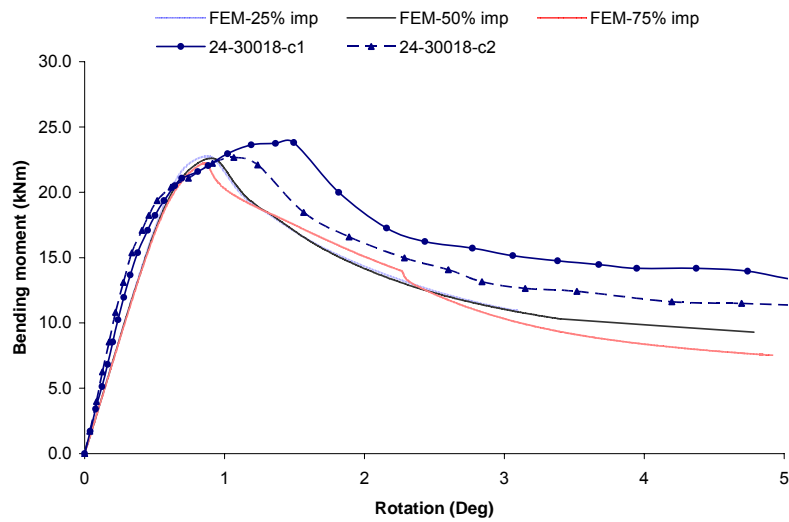
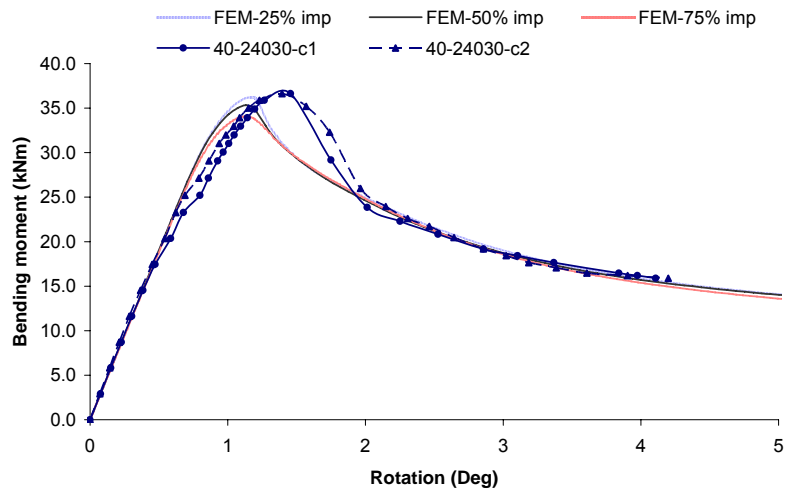
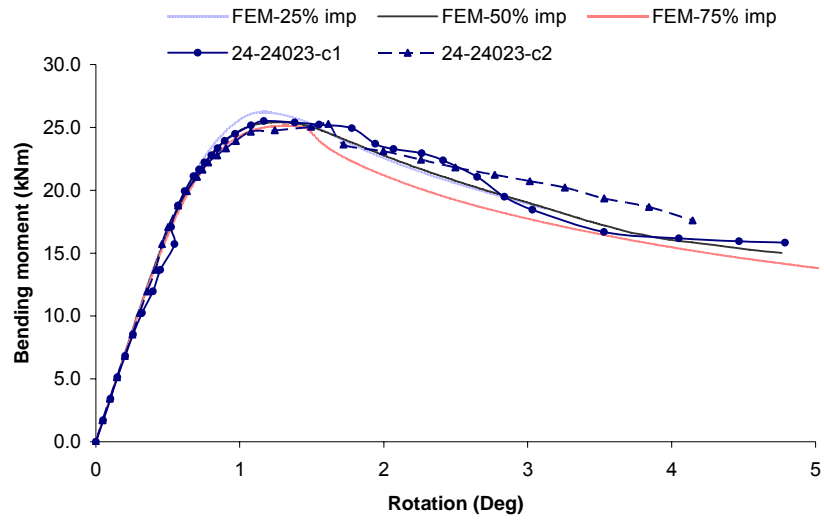


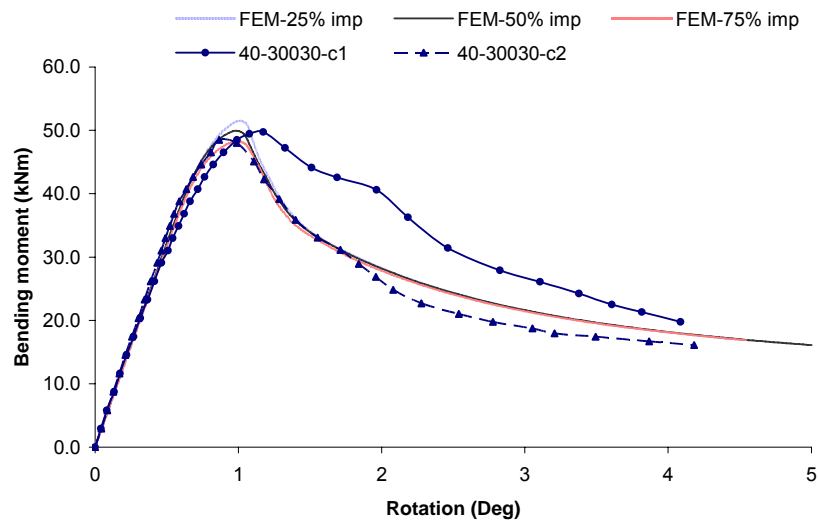
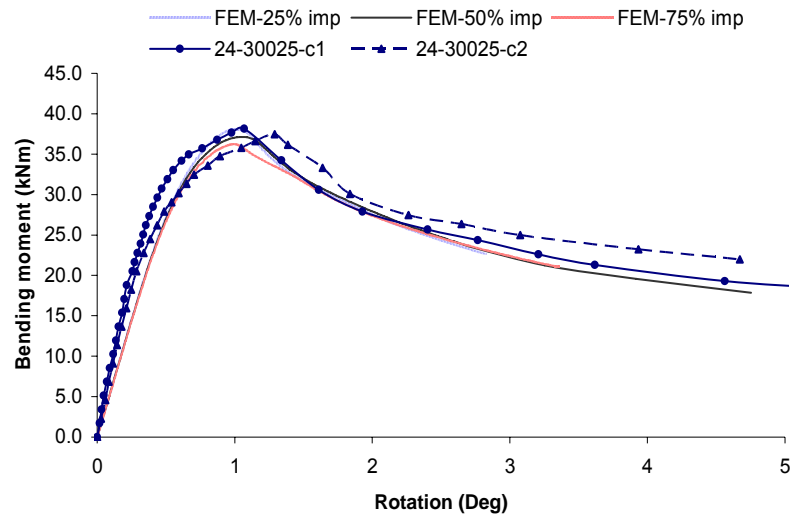


## Appendix V: Comparison of FE predictions using different imperfection magnitudes

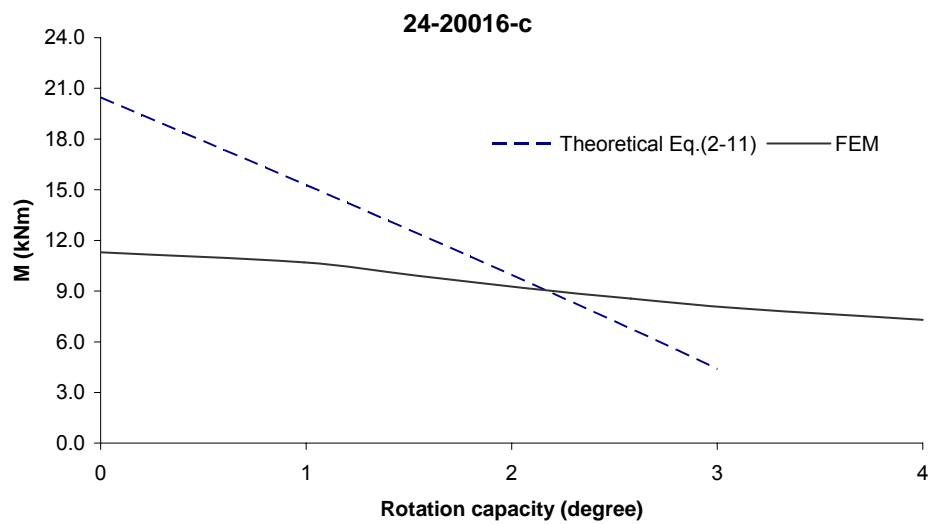
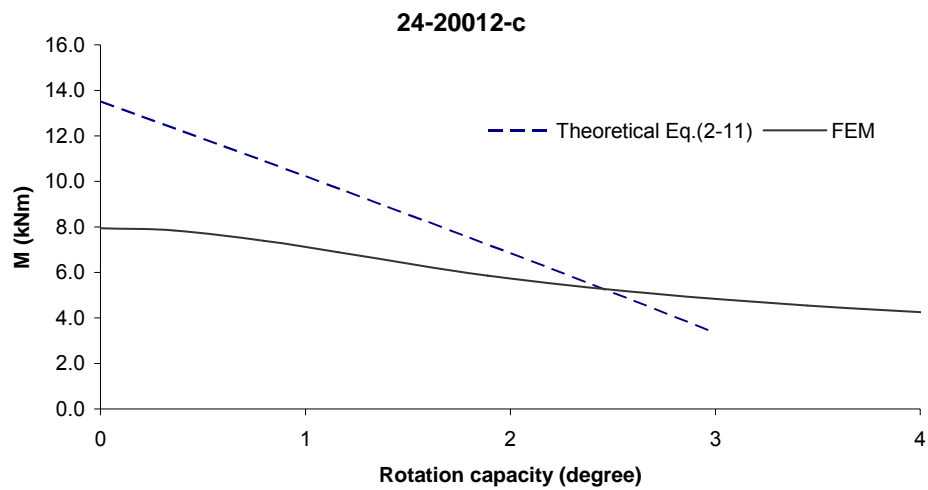


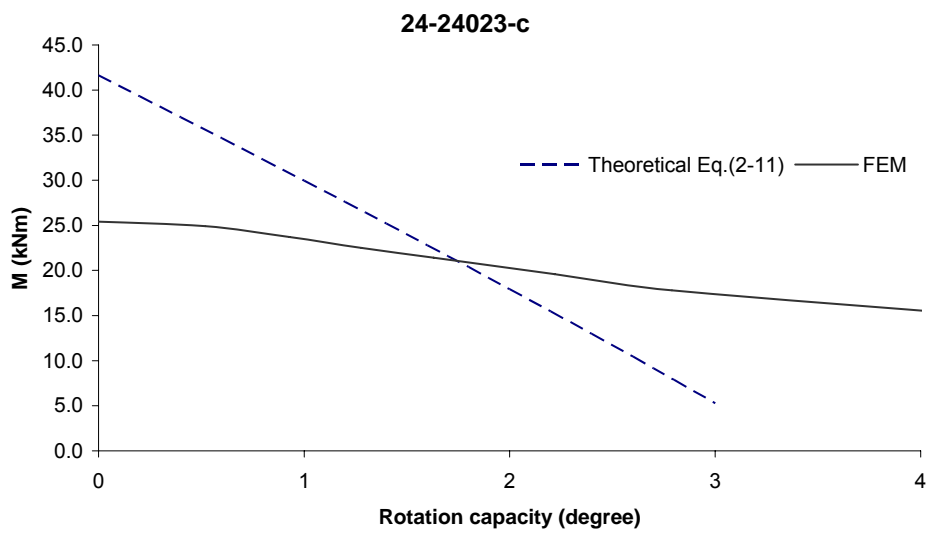
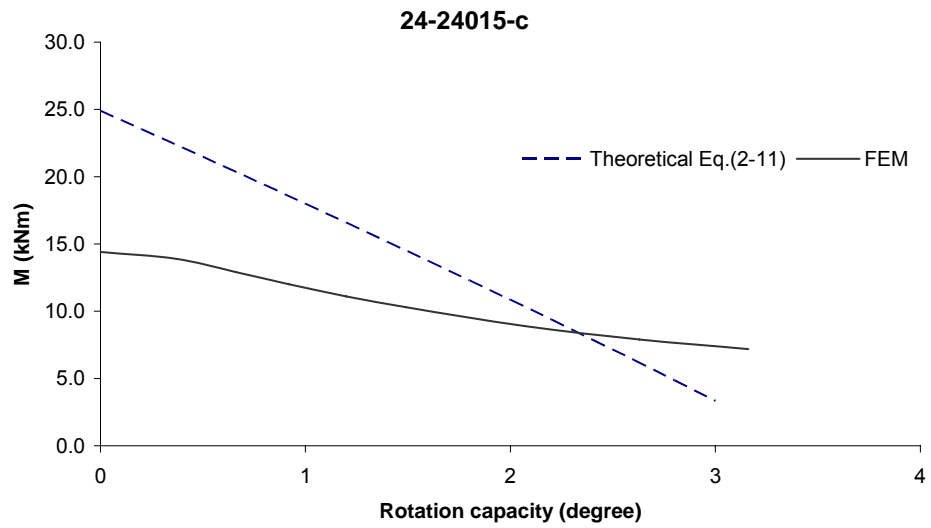
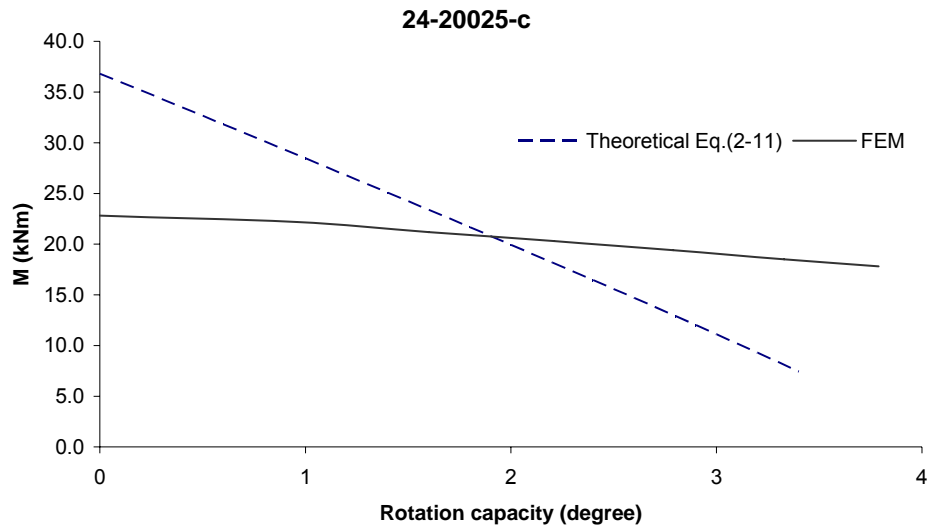




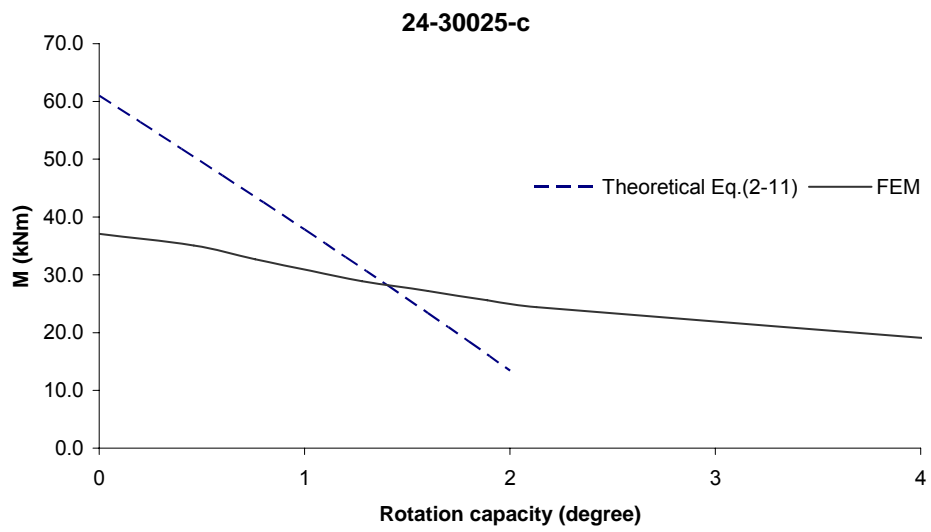
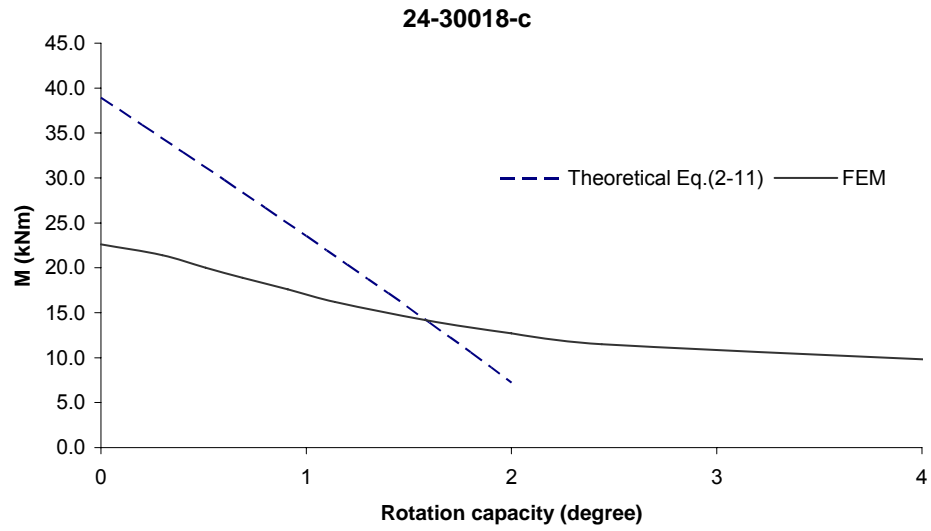
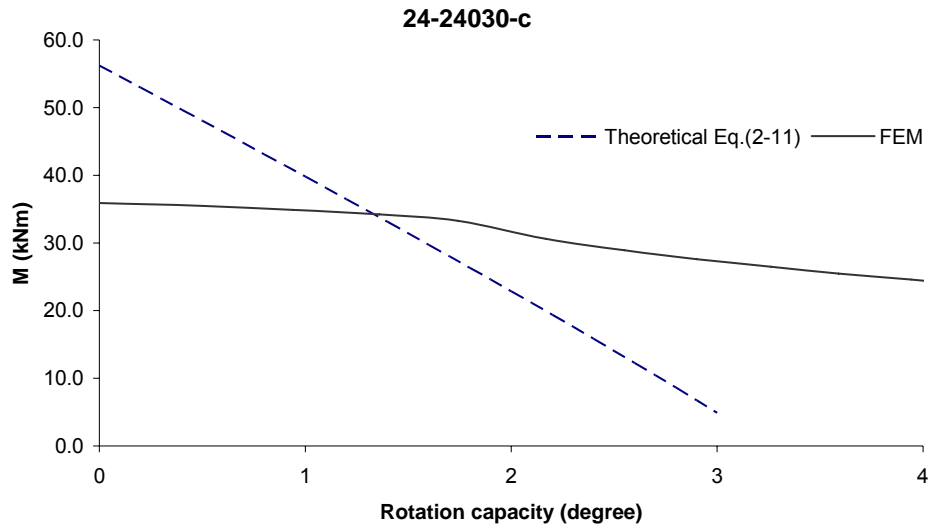


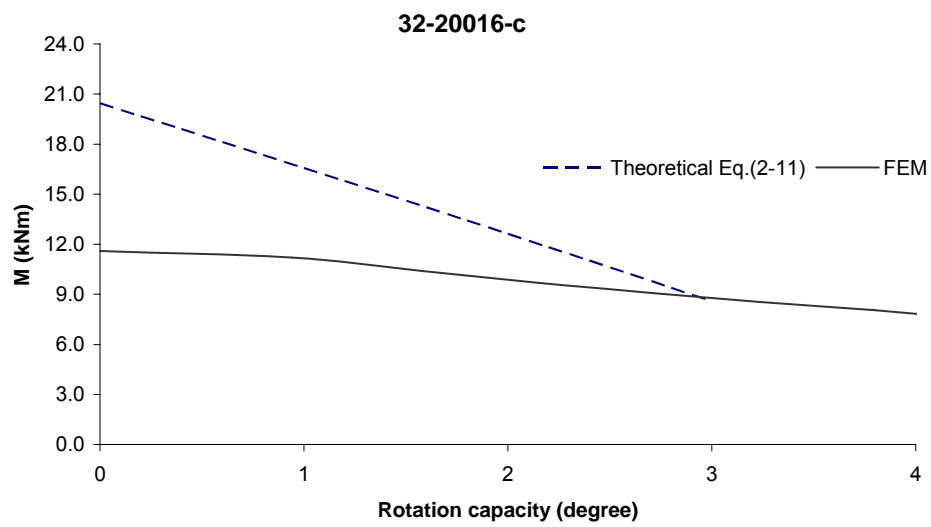
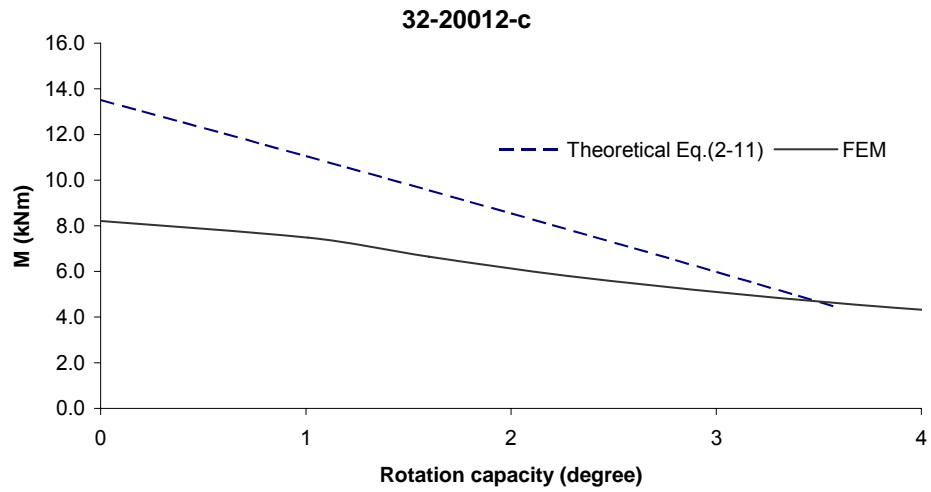
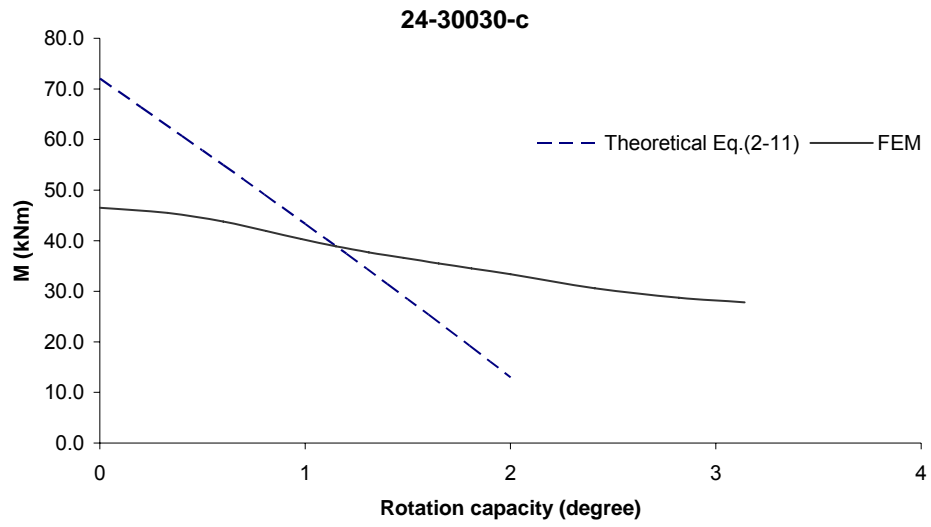
## Appendix VI: Determination of the PPMR and PPR for each specimen

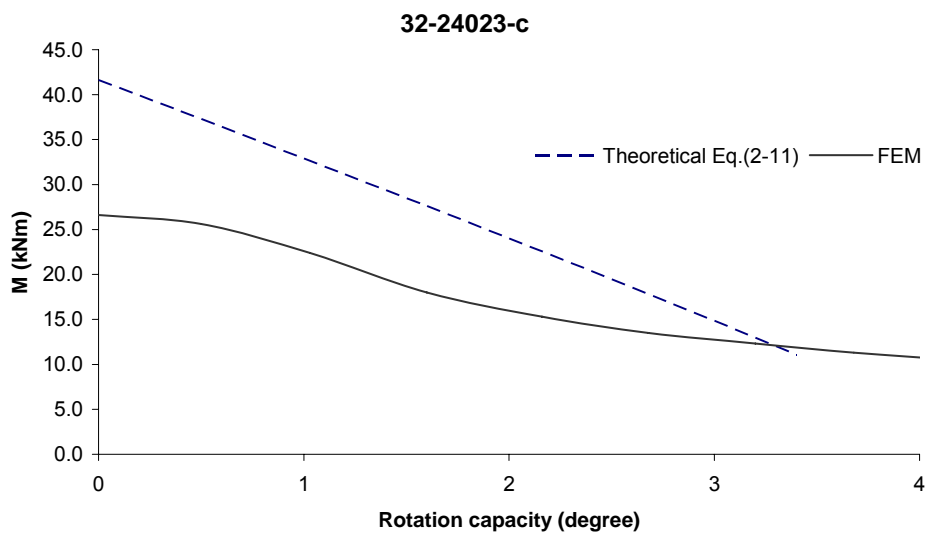
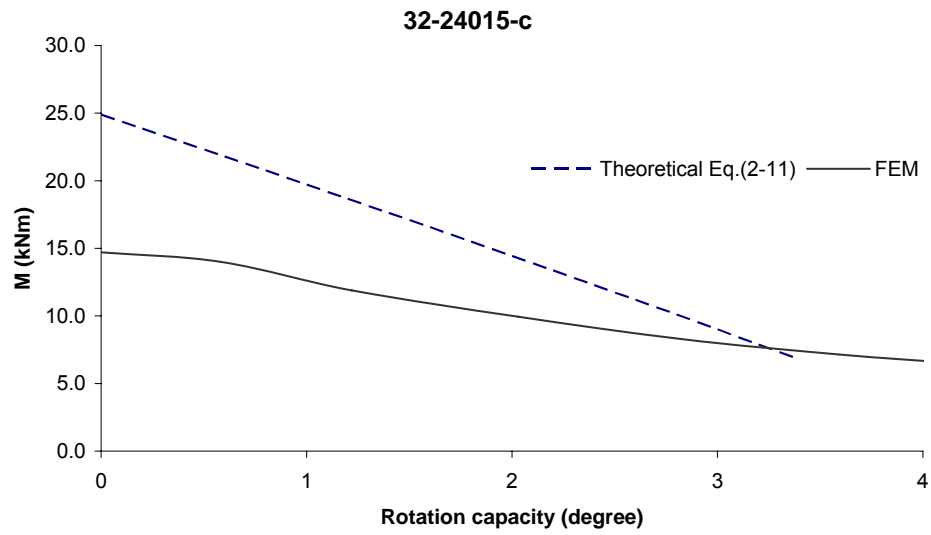
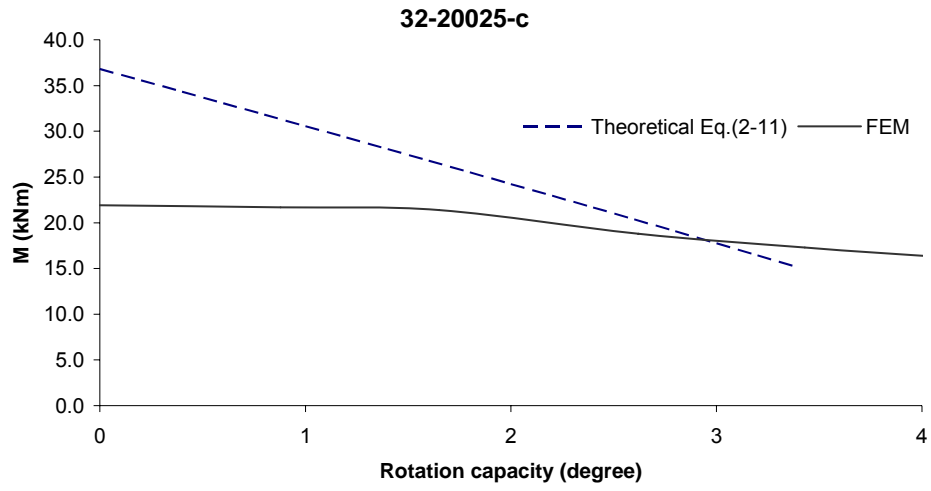


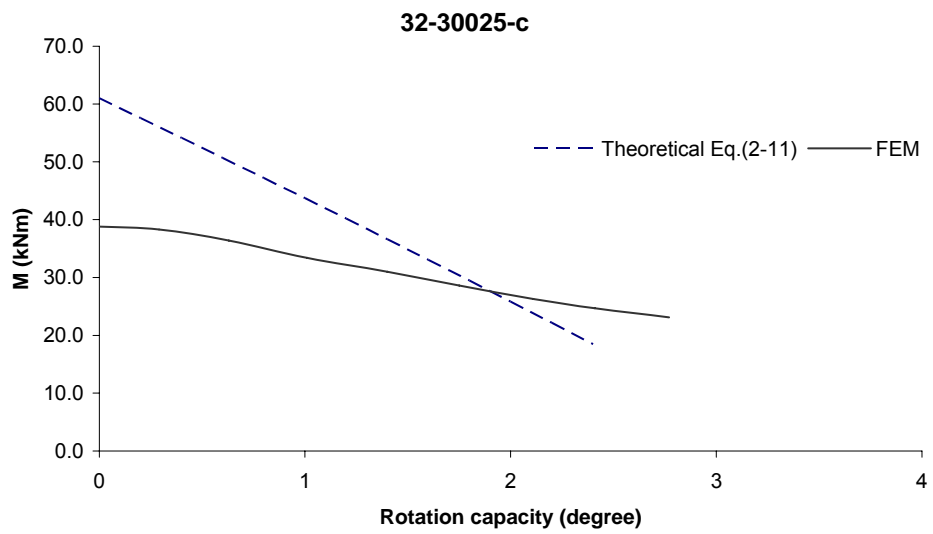
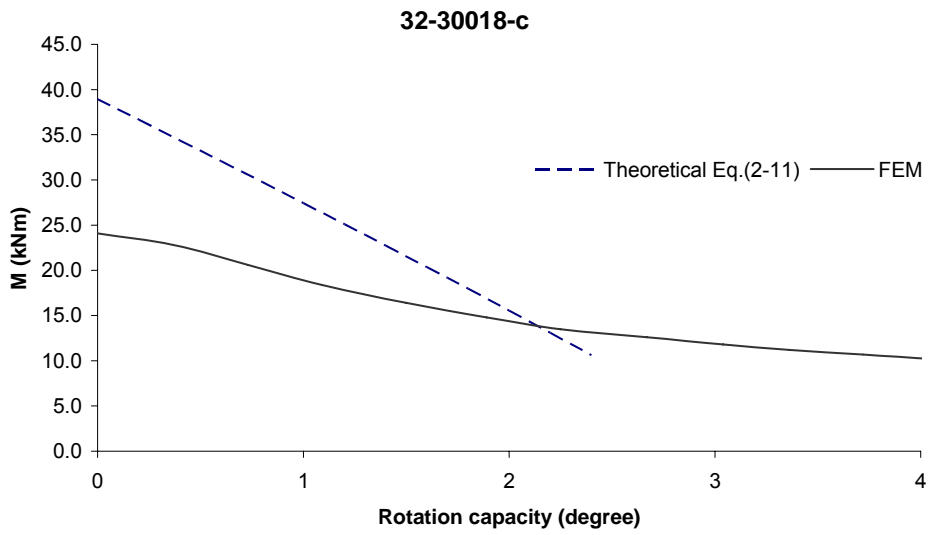
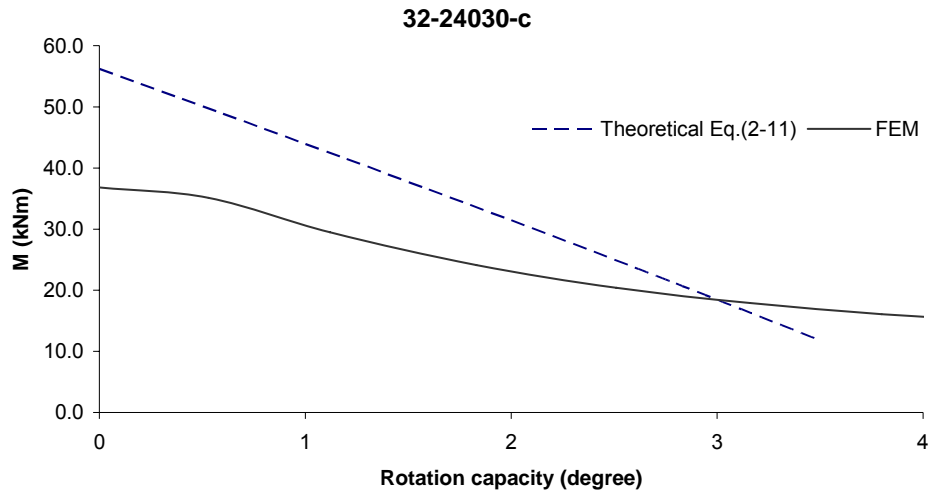


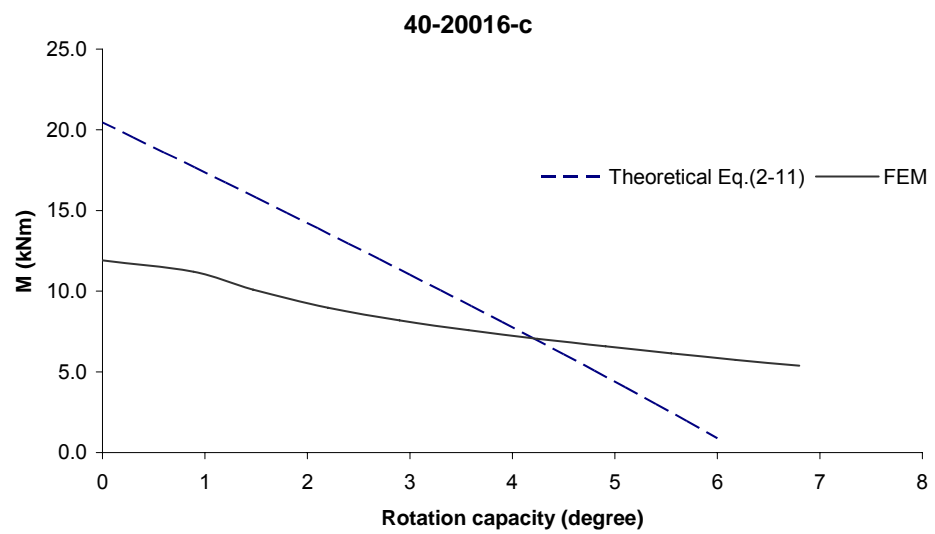
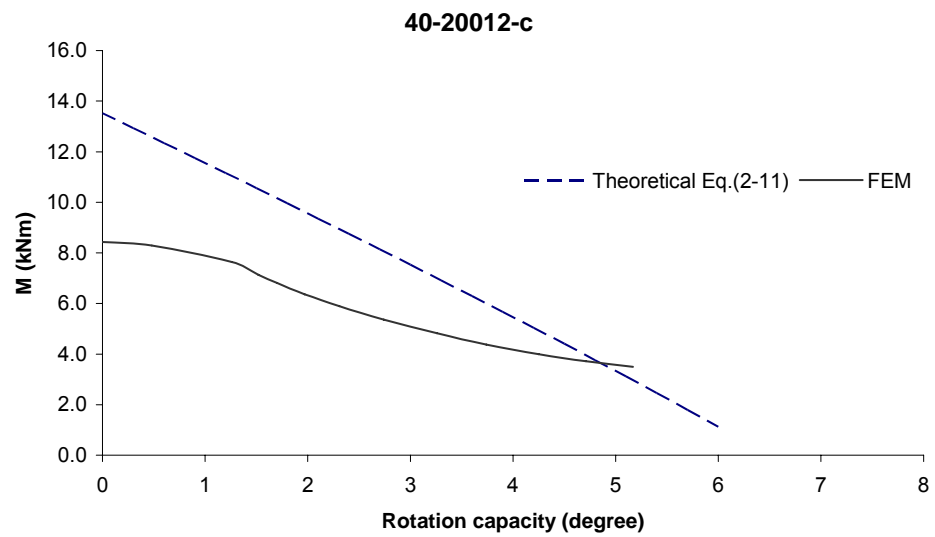
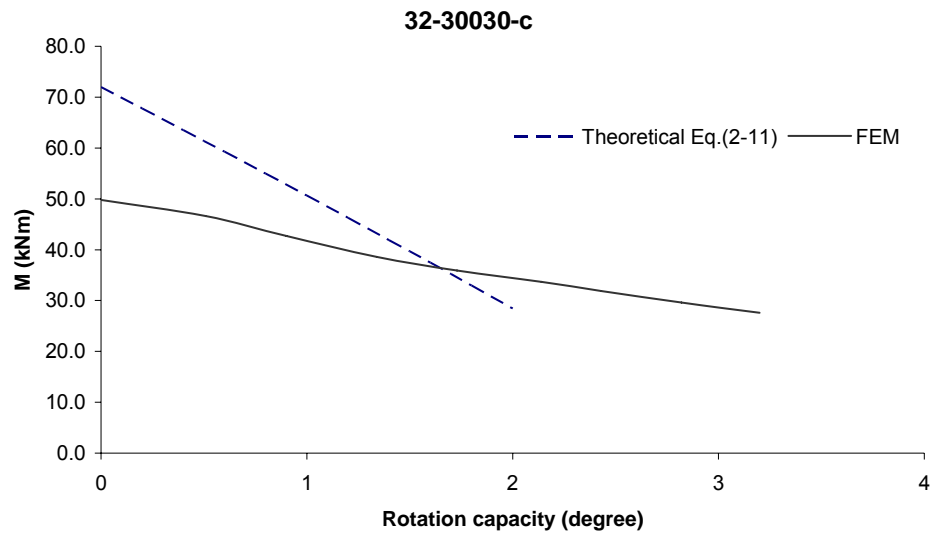


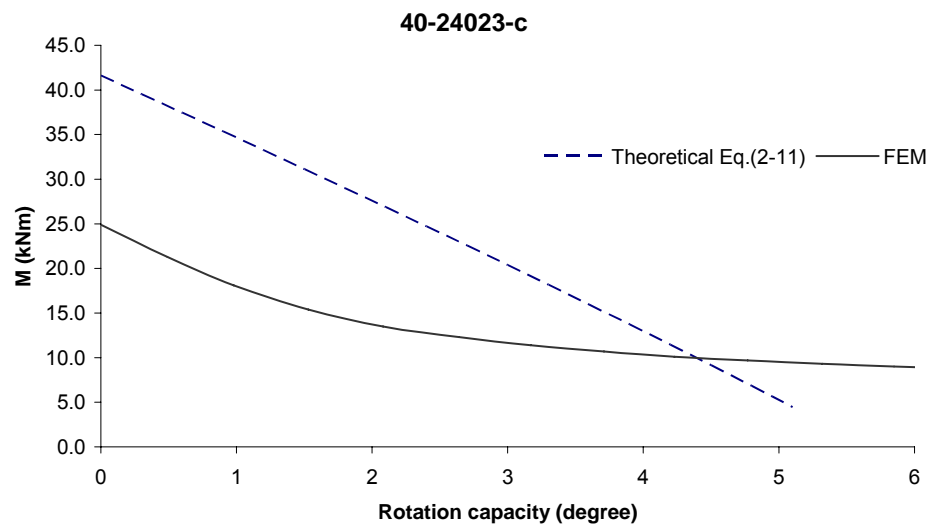
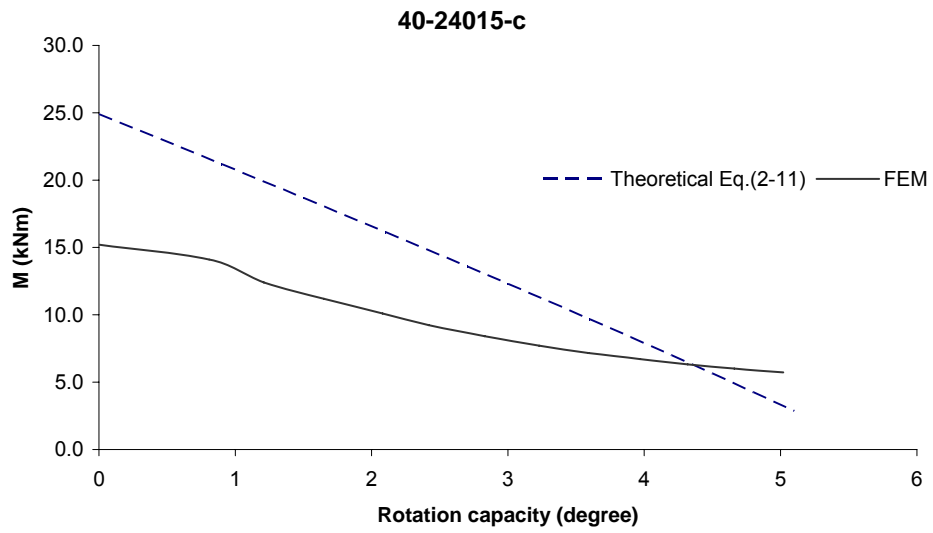
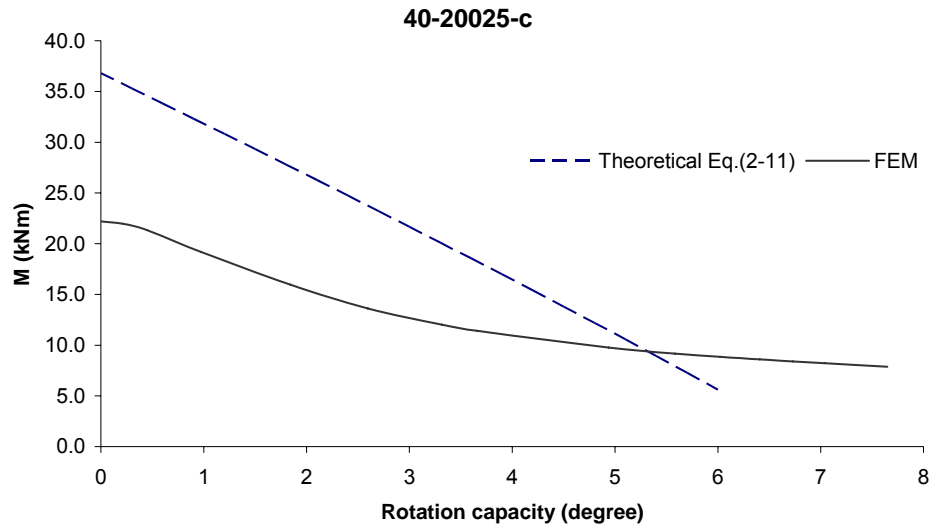


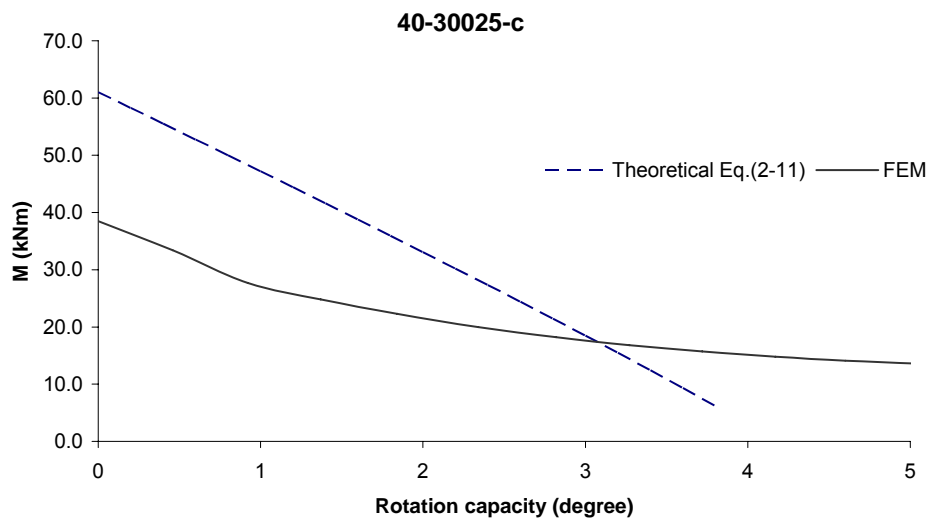
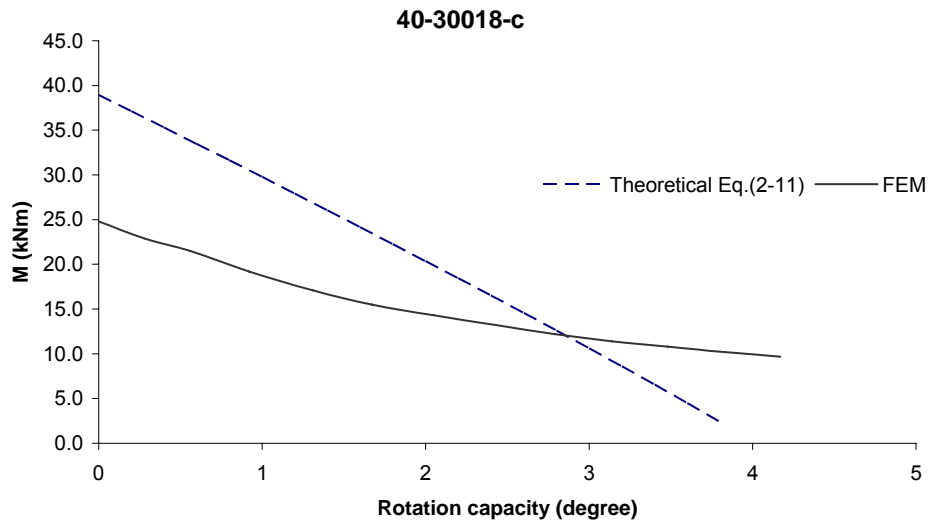
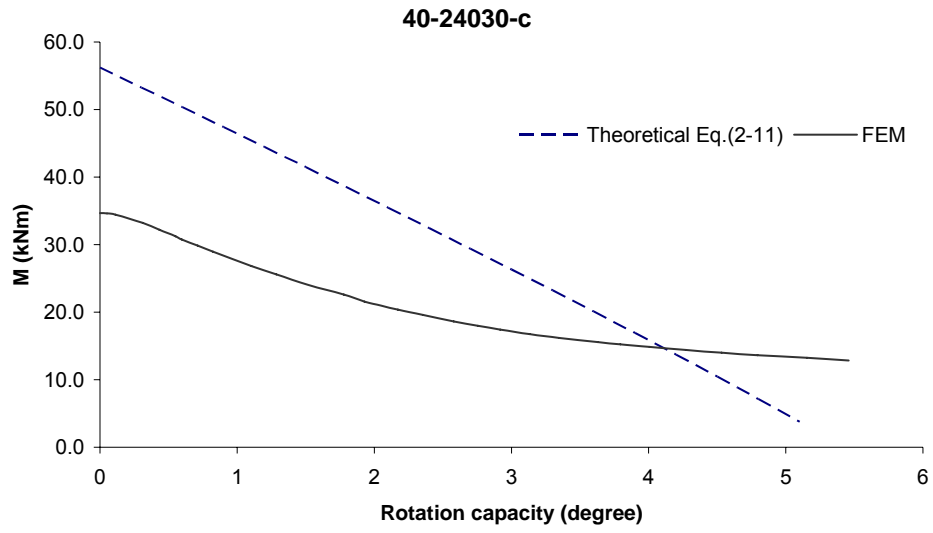


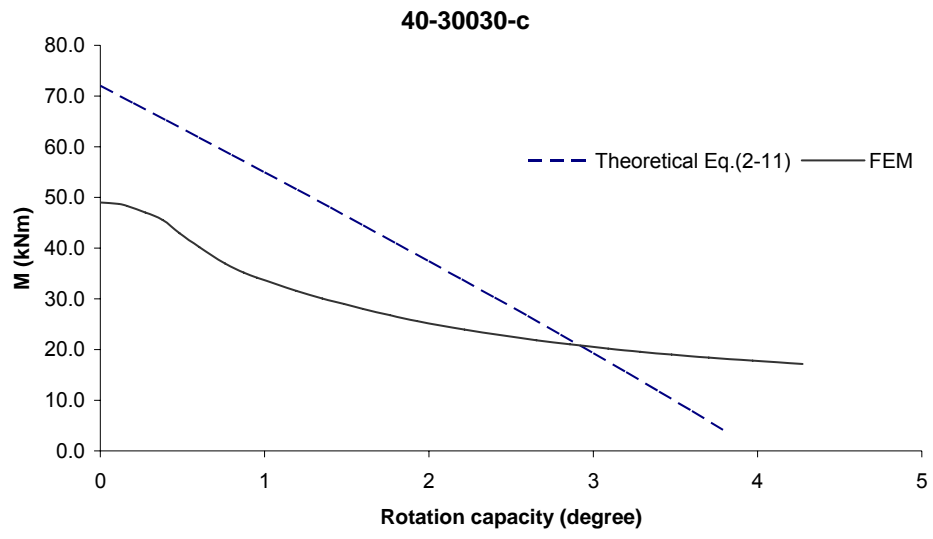














## Appendix VII: Derivation of the relationship between rotation angle at support end and rotational stiffness provided by the sleeve connection

Considering Fig. VII-1, a fictitious rotational spring is utilized to model the sleeve connection of the purlin system. The rotational stiffness of the spring  $k$  can be calculated by the measured rotation angle  $\theta$  at support ends.

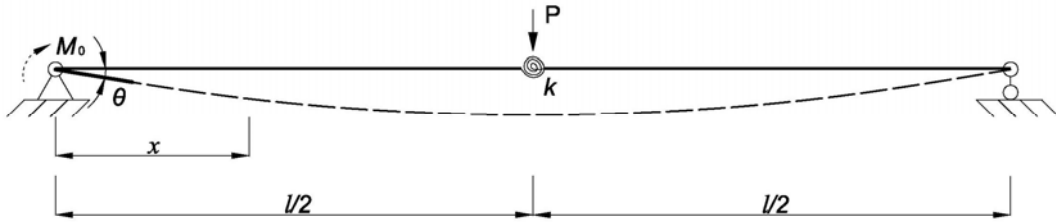


Figure VII-1

By using Castigliano's theorem, a virtual couple  $M_0$  is applied at the support end of the beam. The internal moment  $M$  is computed as follows:

$$\text{At the left half span: } M_L = M_0 (1-x/l) + Px/2 \quad (\text{VII-1a})$$

$$\text{At the right half span: } M_R = M_0 (1-x/l) + Pl(1-x/l)/2 \quad (\text{VII-1b})$$

The spring with a rotation stiffness  $k$  will produce a rotation angle  $\alpha$ , and by using the moment-stiffness relationship, one has:

$$M_0/2 + Pl/4 = k\alpha \quad (\text{VII-2a})$$

$$\text{So, } \alpha = (M_0/2 + Pl/4) / k \quad (\text{VII-2b})$$

The internal strain energy  $U_i$  of the sleeve beam can be calculated as follows:

$$U_i = \int_0^{l/2} \frac{M_L^2}{2EI} dx + \int_{l/2}^l \frac{M_R^2}{2EI} dx + k\alpha^2 / 2 \quad (\text{VII-3})$$

in which  $I$  is the second moment of area of the sigma purlin section.

The partial derivative of  $U_i$  with respect to  $M_0$  is:

$$\frac{\partial U_i}{\partial M_0} = \frac{1}{2EI} \left( 2M_0 l / 3 + \frac{Pl^2}{8} \right) + \frac{1}{2k} \left( M_0 / 2 + \frac{Pl}{4} \right) \quad (\text{VII-4})$$

By letting  $M_0 = 0$ , the end rotation  $\theta$  is therefore obtained as

$$\theta = \frac{Pl^2}{16EI} + \frac{Pl}{8k} \quad \text{or} \quad \theta = \frac{M_{(l/2)} l}{4EI} + \frac{M_{(l/2)}}{2k} \quad (\text{VII-5})$$

where  $M$  is the mid-span moment. By rearranging Eq. VII-5, one has

$$k = \frac{1}{\frac{2\theta}{M} - \frac{l}{2EI}} \quad (\text{VII-6})$$

## **Appendix VIII: Derivation of the end rotation attributed to mid-span point loading for the sleeved beams in the sleeved internal support tests**

Conjugate-Beam Method is employed to determine the end rotation  $\theta_1$  of the sleeved beam shown in Fig. VIII-1.

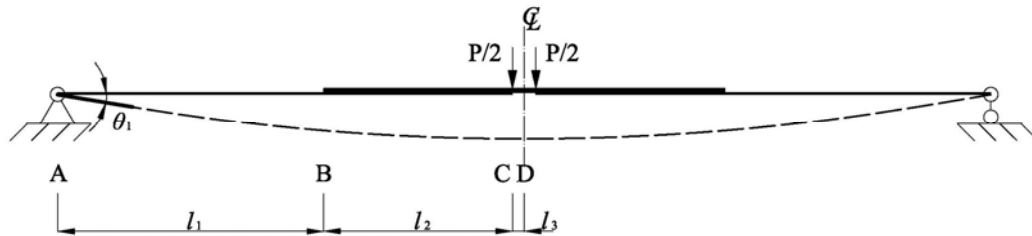


Figure VIII-1 Real beam

From static equilibrium condition, it is known that:

$$M_A=0; \quad M_B=P \times l_1/2; \quad M_C=M_D=P \times (l_1+l_2)/2 \quad (\text{VIII-1})$$

Thus the conjugate beam and the  $M/EI$  values at point B, C and D are:

$$\text{-B: } P \times l_1 / 2EI_p; \text{ +B: } P \times l_1 / 2E(I_p + I_s); \text{ -C: } P \times (l_1 + l_2) / 2E(I_p + I_s); \text{ +C=D: } P \times (l_1 + l_2) / 2EI_s \quad (\text{VIII-2})$$

as shown in Fig. VIII-2, where  $I_p$  and  $I_s$  are the second moment of area of the sigma section and the sleeve respectively.

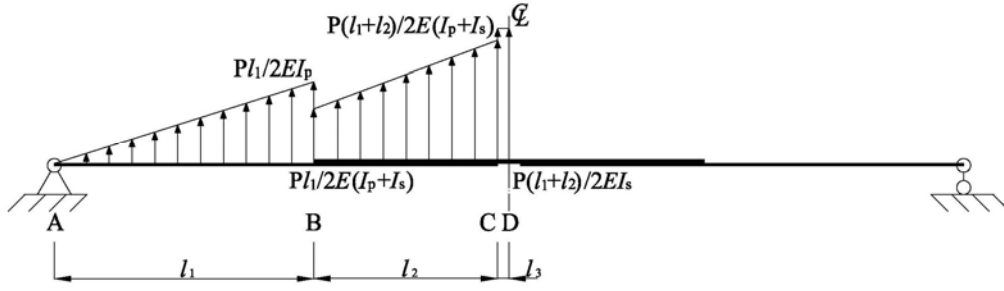


Figure VIII-2 Conjugate beam

The reactions on the conjugate beam are as shown in Fig. VIII-3, in which:

$$F_1 = Pl_1/2EI_p \times l_1/2; F_2 = Pl_1/2E(I_p + I_s) \times l_2; F_3 = [P(l_1 + l_2)/2E(I_p + I_s) - Pl_1/2E(I_p + I_s)] \times l_2/2;$$

$$F_4 = P(l_1 + l_2)/2EI_s \times l_3 \quad (\text{VIII-3})$$

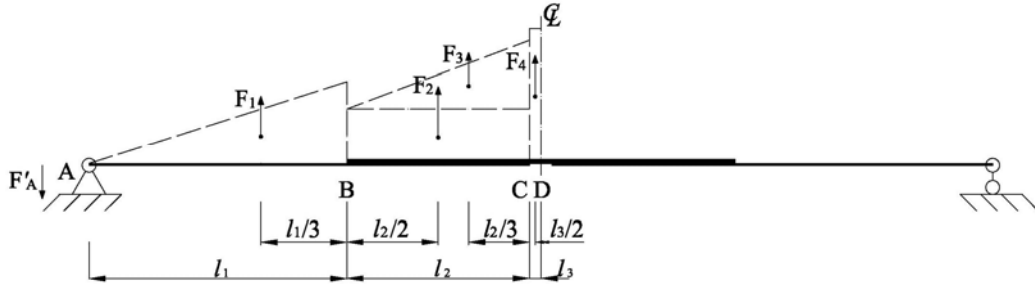


Figure VIII-3 Reactions on the conjugate beam

Hence, the reaction at point A on the conjugate beam, that is the end rotation  $\theta_1$  on the real beam, can be calculated as:

$$\theta_1 = F'_A = F_1 + F_2 + F_3 + F_4 = Pl_1^2/4EI_p + Pl_1l_2/2E(I_p + I_s) + P(l_1 + l_2)l_3/2EI_s + Pl_2^2/4E(I_p + I_s) \quad (\text{VIII-4})$$

Replace  $P$  in Eq.(VIII-4) with  $2M_D/(l_1 + l_2)$ , where  $M_D$  is the moment at the mid-span. The end rotation vs. mid-span moment relationship can therefore be obtained, which is:

$$\theta_1 = M_D l_1^2/2EI_p(l_1 + l_2) + M_D l_1 l_2/E(I_p + I_s)(l_1 + l_2) + M_D l_2^2/2E(I_p + I_s)(l_1 + l_2) + M_D l_3/EI_s \quad (\text{VIII-5})$$

## Appendix IX: Derivation of the joint rotation due to bolt hole elongation in a four-bolt moment connection, after Bryan (1993)

With reference to Fig. IX-1:

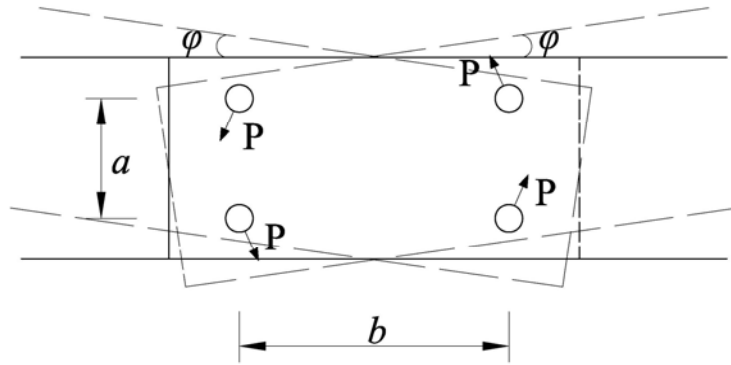


Figure IX-1 Four-bolt moment connection

$$M = 2P\sqrt{a^2 + b^2} \quad (\text{IX-1})$$

$$\theta = 2\phi = 2\left(\frac{P \times c}{\sqrt{(a/2)^2 + (b/2)^2}}\right) = \frac{4P \times c}{\sqrt{a^2 + b^2}} \quad (\text{IX-2})$$

therefore,

$$\theta = \frac{2Mc}{a^2 + b^2} \quad (\text{IX-3})$$

in which  $P$  is the bearing force;  $M$  is the moment generated in the connection;  $\theta$  is the joint rotation.  $c$  (mm/kN) is the joint flexibility and is calculated by:

$$c = 5n\left(\frac{10}{t_1} + \frac{10}{t_2} - 2\right) \times 10^{-3} \quad (\text{IX-4})$$

in which  $t_1$  and  $t_2$  are the sheet thicknesses;  $n$  is an empirical factor dependent on the type of bolt and joint and values of  $n$  are listed in Table IX-1:

Bolted joints in tension	One-bolt connection	Two or more bolt connection
Shear plane on plain shank	3.0	1.8
Shear plane on thread	5.0	3.0

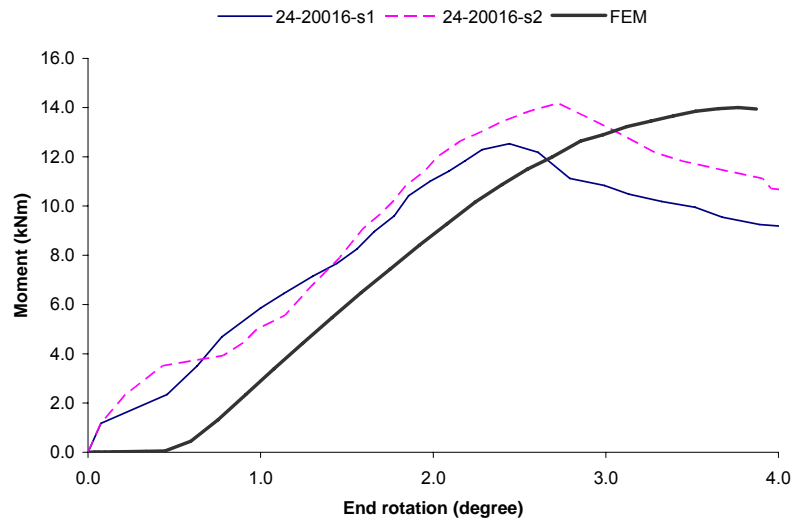
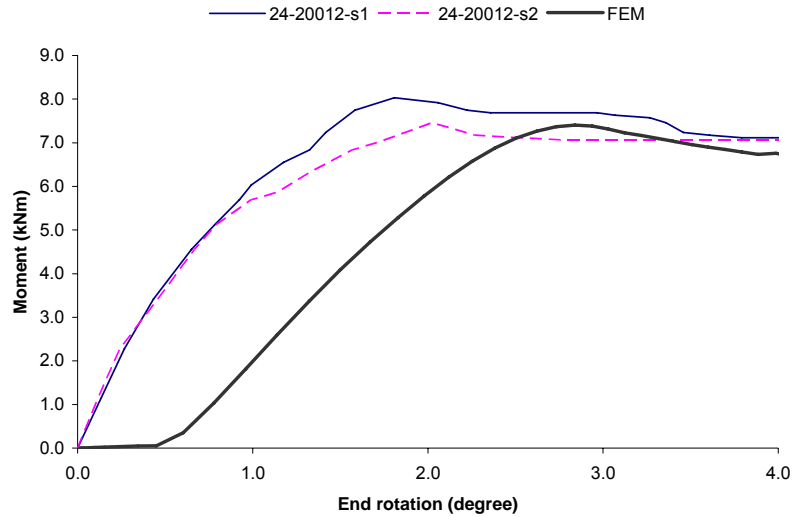
(a)

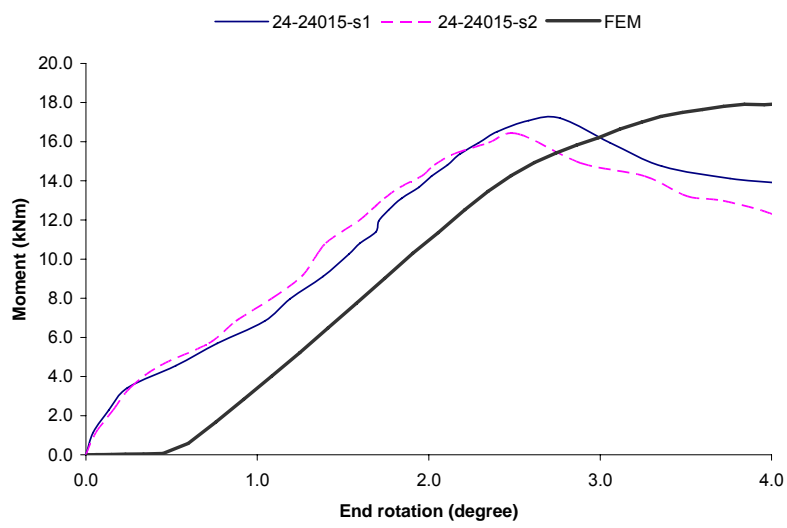
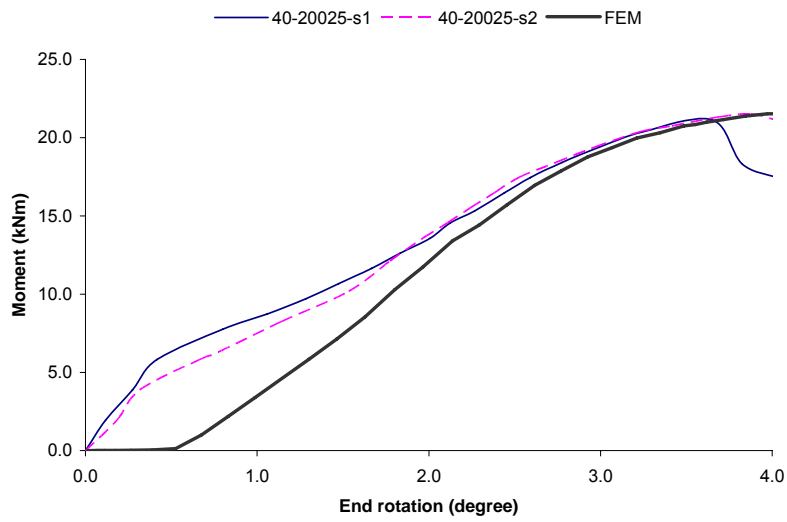
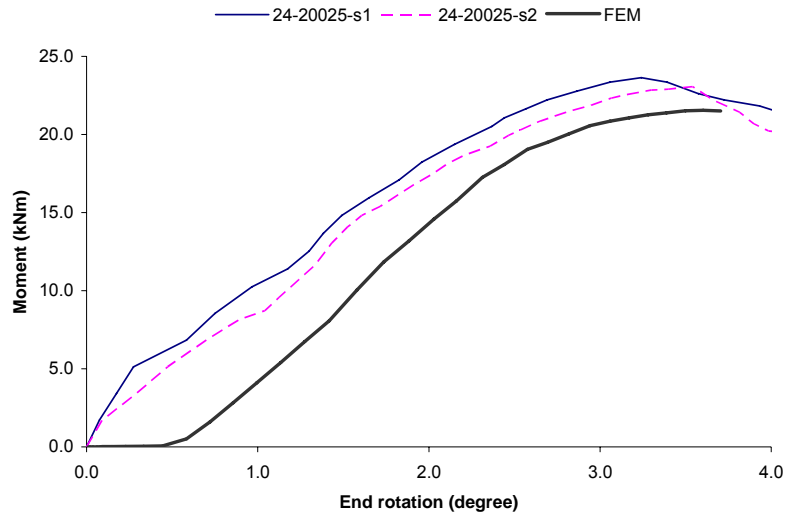
Bolted joints under moment	Simple bolted joints	Joint which nest or interlock	Joints which nest or interlock
Shear plane on plain shank	1.8	1.4	1.2
Shear plane on thread	3.0	2.4	2.0

(b)

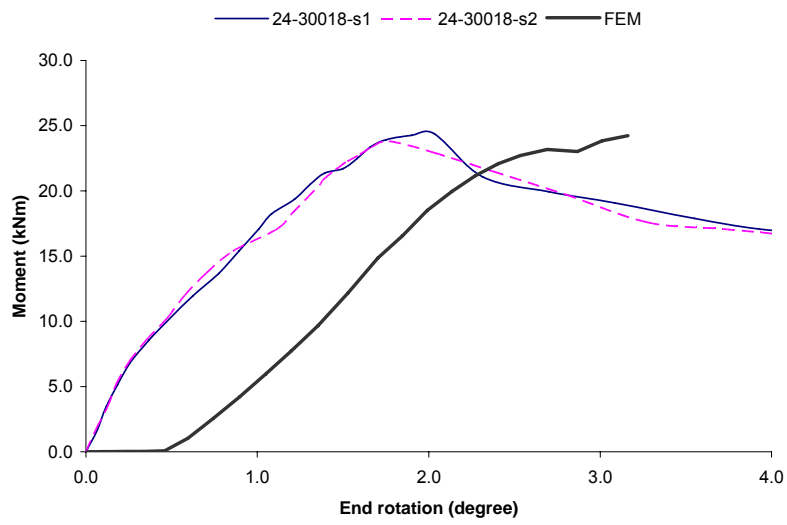
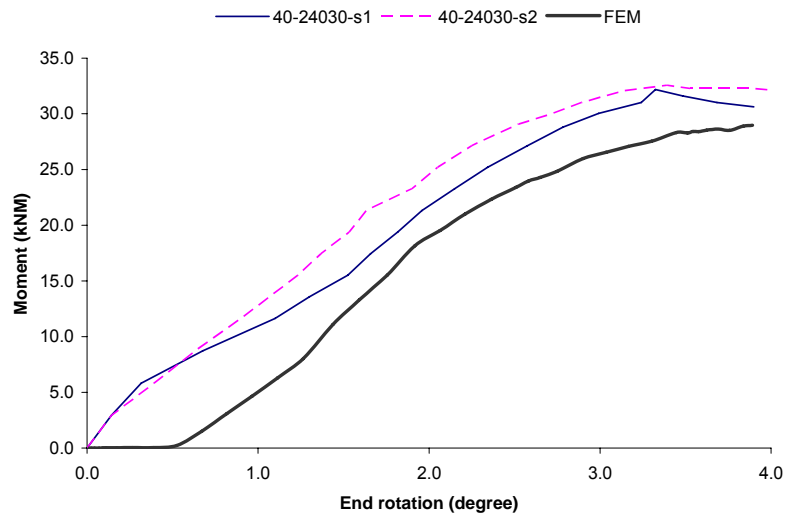
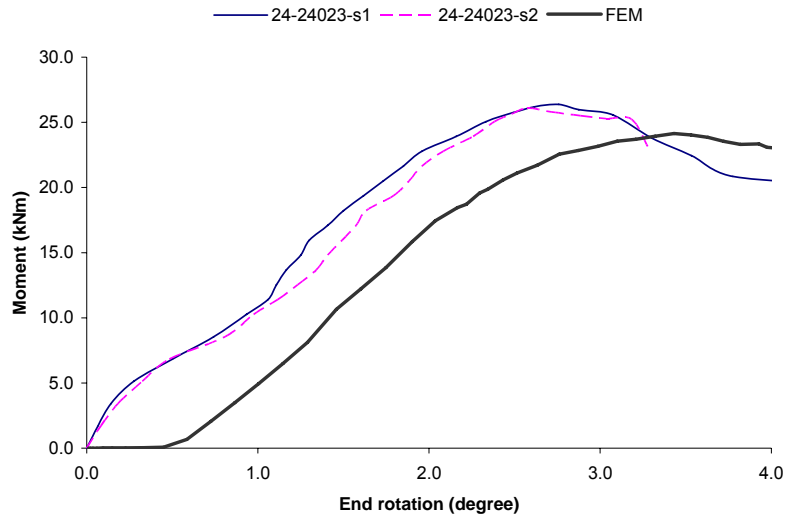
Table IX-1 *n* values of bolted joints

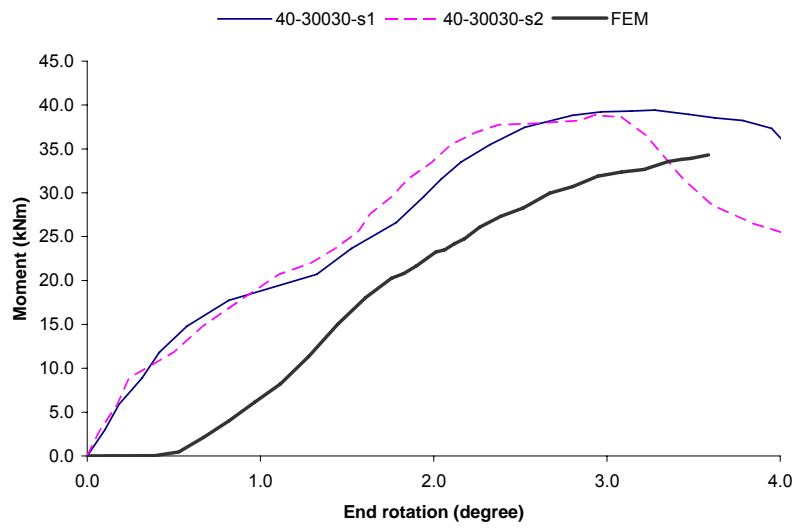
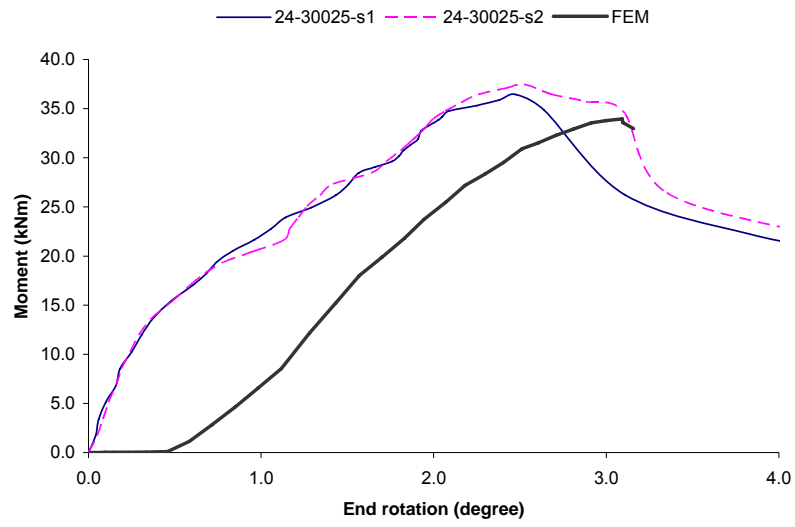
# Appendix X: Comparison of moment vs. rotation graphs between the tests and the FE analysis











## Appendix XI: Derivation of the theoretical moment vs. deflection curve

The Conjugate-Beam Method is employed to determine the deflection at mid-span (point D) of the beam shown in Fig. XI-1.

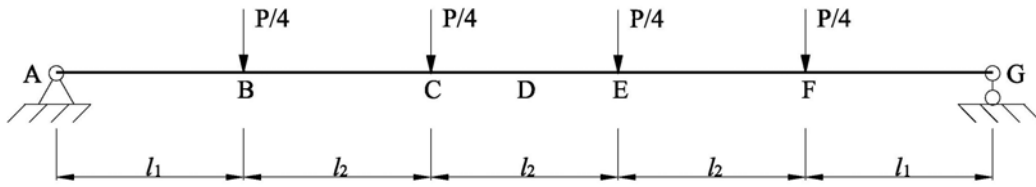


Figure XI-1 Real beam

From static equilibrium condition, it is known that:

$$M_A = M_G = 0; \quad M_B = M_F = P \times l_1 / 2; \quad M_C = M_D = M_E = P \times l_1 / 2 + P \times l_2 / 4 \quad (\text{XI-1})$$

Thus the conjugate beam and the  $M/EI$  diagram are as shown in Fig. XI-2.

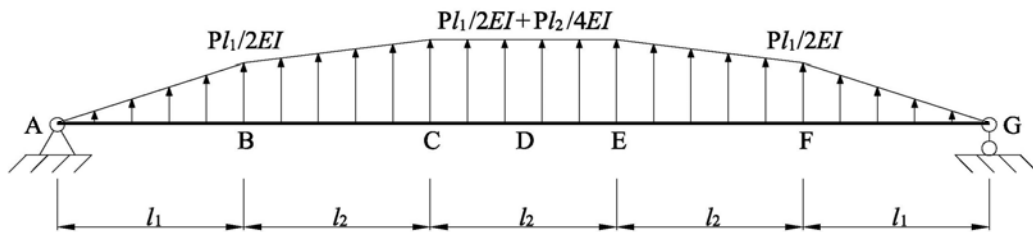


Figure XI-2 Conjugate beam

The reactions on the conjugate beam are as shown in Fig. XI-3, in which:

$$F_1 = Pl_1/2EI \times l_1/2; \quad F_2 = Pl_1/2EI \times l_2; \quad F_3 = Pl_2/4EI \times l_2/2; \quad F_4 = (Pl_1/2EI + Pl_2/4EI) \times l_2 \quad (\text{XI-2})$$

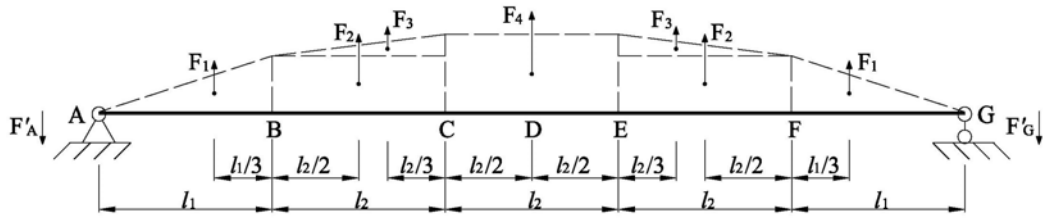


Figure XI-3 Reactions on the conjugate beam

Static equilibrium equation for the conjugate beam,  $\Sigma F=0$ :

$$F'_A = F'_G = F_1 + F_2 + F_3 + F_4 / 2 = Pl_1^2 / 4EI + 3Pl_1l_2 / 4EI + Pl_2^2 / 4EI \quad (XI-3)$$

Hence, the moment at point D on the conjugate beam, that is the deflection at point D on the real beam, can be calculated as:

$$\begin{aligned} \Delta = M'_D &= F'_A \times (l_1 + l_2 + l_2/2) - F_1 \times (l_1/3 + l_2 + l_2/2) - F_2 \times (l_2/2 + l_2/2) - F_3 \times (l_2/3 + l_2/2) - F_4/2 \times l_2/4 \\ \Rightarrow \Delta = M'_D &= Pl_1^3 / 6EI + 3Pl_1^2l_2 / 4EI + 13Pl_1l_2^2 / 16EI + 23Pl_2^3 / 96EI \end{aligned} \quad (XI-4)$$

## **Appendix XII: Calculation of the lateral spring stiffness $K$ by following BSI (2006a)**

The lateral spring stiffness  $K$  is determined from:

$$1 / K = 1 / K_A + 1 / K_B + 1 / K_C \quad (\text{XII-1})$$

in which  $K_A$  is the lateral stiffness representing the rotational stiffness of the joint between the sheeting and the purlin;  $K_B$  is the lateral stiffness considering distortion of the cross section of the purlin;  $K_C$  is the lateral stiffness allowing for the flexural stiffness of the sheeting. As  $K_C$  is usually much larger than  $K_A$  and  $K_B$  in practice, BSI (2006a) indicates that the total lateral spring stiffness  $K$  should then be determined from the following equation:

$$1 / K = 1 / K_A + 1 / K_B \quad (\text{XII-2})$$

BSI (2006a) suggests using the following equation to calculate the total lateral spring stiffness  $K$ :

$$1 / K = 4(1 - \nu^2)h^2(h_d + b_{\text{mod}}) / Et^3 + h^2 / C_D \quad (\text{XII-3})$$

in which  $t$  is the thickness of the beam;  $h$  is the height of the beam;  $h_d$  is the developed height of the purlin;  $b_{\text{mod}}$  is a dimension determined as follows:

- for cases that the equivalent lateral force  $q_{h,Ed}$  making the beam and the sheeting contacting at the purlin web:  $b_{\text{mod}} = a$
- for cases that the equivalent lateral force  $q_{h,Ed}$  making the purlin and the sheeting contacting at the purlin lip:  $b_{\text{mod}} = 2a + b$

in which  $b$  is the width of the purlin flange fastened to the sheeting;  $a$  is the distance from the fastener to the purlin web (In this test programme, the fasteners were all applied along the central line of the purlin flange therefore  $b = 2a$ ), see Fig. XII-1.

and  $C_D$  is the rotational spring stiffness provided by the joint between the sheeting and the purlin.

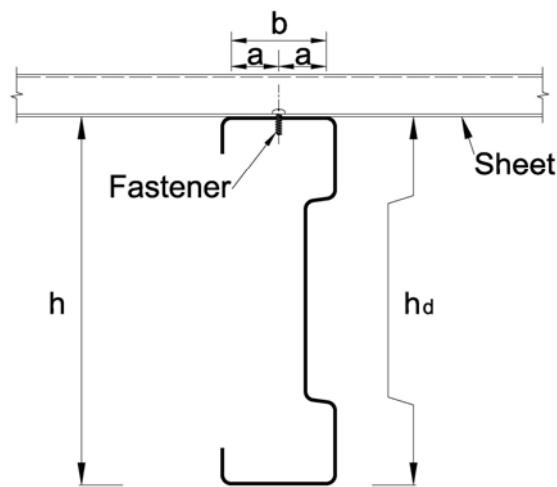


Figure XII-1 Sheeted purlin

The determination of  $C_D$  thus becomes crucial in order to calculate  $K$ . BSI (2006a) indicates that the total rotational spring stiffness  $C_D$  should be determined from the following equation:

$$C_D = \frac{1}{1/C_{D,A} + 1/C_{D,C}} \quad (\text{XII-4})$$

in which  $C_{D,A}$  is the rotational stiffness provided by the connection between the sheeting and the purlin;  $C_{D,C}$  is the rotational stiffness due to the flexural stiffness of the sheeting.

The calculation of  $C_{D,C}$  is suggested by BSI (2006a) as following:

$$C_{D,C} = kEI_{\text{eff}} / s \quad (\text{XII-5})$$

in which  $I_{\text{eff}}$  is the effective second moment of area per unit width of the sheeting;  $s$  is the spacing between two purlins;  $k$  is a coefficient dependent on bending shape of the sheeting and equal to 2 for cases in this test programme.

The calculation of  $C_{D,A}$  is given in BSI (2006a) as follows:

$$C_{D,A} = C_{100}k_{ba}k_tk_{bR}k_Ak_{bT} \quad (\text{XII-6})$$

in which

$k_{ba} = (b_a / 100)^2$ , for  $b_a < 125\text{mm}$  ( $b_a$  is the width of the purlin flange);

$k_t = (t_{\text{nom}} / 0.75)^{1.5}$ , for  $t_{\text{nom}} < 0.75\text{mm}$  ( $t_{\text{nom}}$  is the nominal thickness of the sheeting);

$k_{bR} = 185 / b_R$ , for  $b_R > 185\text{mm}$  ( $b_R$  is the corrugation width of the sheeting);

$k_{bT} = \sqrt{b_{T,\text{max}} / b_T}$ , for  $b_T > b_{T,\text{max}}$  ( $b_T$  is the width of the sheeting flange fastened to the purlin, and  $b_{T,\text{max}}$  is given in Table XIII-1);

for uplift load,  $k_A = 1$ ;




for downward load and the sheeting is connected to the purlin in negative position:

$k_A = 1 + (A - 1.0) \times 0.16$ , if  $t_{\text{nom}} = 0.75\text{mm}$

$k_A = 1 + (A - 1.0) \times 0.095$ , if  $t_{\text{nom}} = 1.00\text{mm}$

where  $A$  [kN/m] is load introduced from sheeting to purlin;

$C_{100}$  is a reference rotational stiffness, given in Table XII-1.

Positioning of sheeting		Sheet fastened through		Pitch of fasteners		Washer diameter [mm]	$C_{100}$	$b_{T,max}$
Positive 1)	Negative 1)	Trough	Crest	$e = b_R$	$e = 2b_R$		[kNm/m]	[mm]
For gravity loading:								
×		×		×		22	5,2	40
×		×			×	22	3,1	40
	×		×	×		$K_s$	10,0	40
	×		×		×	$K_s$	5,2	40
	×	×		×		22	3,1	120
	×	×			×	22	2,0	120
For uplift loading:								
×		×		×		16	2,6	40
×		×			×	16	1,7	40
Key: $b_R$ is the corrugation width; $b_T$ is the width of the sheeting flange through which it is fastened to the purlin. $K_s$ indicates a steel saddle washer as shown below with $t \geq 0,75$ mm								
						Sheet fastened: - through the trough:  - through the crest: 		
The values in this table are valid for: - sheet fastener screws of diameter: $\phi = 6,3$ mm; - steel washers of thickness: $t_w \geq 1,0$ mm.								

1) The position of sheeting is positive when the narrow flange is on the purlin and negative when the wide flange is on the purlin.

Table XII-1 Rotational coefficient  $C_{100}$  for trapezoidal sheeting, after BSI (2006a)

Work example: Calculate the lateral spring stiffness  $K$  provided by the sheeting to the sigma purlin in the test SU60-20016-1.

### Geometry

$b_a = 62.5\text{mm}$ ;  $t_{nom} = 0.70\text{mm}$ ;  $b_R = 200\text{mm}$ ;  $b_T = 129\text{mm}$ ;  $b_{T,max} = 40\text{mm}$ ;  $s = 660\text{mm}$ ;  
 effective second moment of area of the sheeting  $I_{eff} = 10^5\text{mm}^4$ ;  $h = 200\text{mm}$ ;  $h_d = 232\text{mm}$ ;  
 $b_{mod} = 109\text{mm}$ ,  $t = 1.60\text{mm}$ .

Step 1: Determine  $C_{D,A}$  from Eq. (XII-6)



$$C_{100} = 1700 \text{ Nm/m/rad}; k_{ba} = 0.391; k_t = 0.902; k_{bR} = 0.925; k_A = 1; k_{bT} = 0.557$$

therefore  $C_{D,A} = 308 \text{ (Nm/m/rad)}$

Step 2: Determine  $C_{D,C}$  from Eq. (XII-5)

$$C_{D,C} = 6.4 \times 10^7 \text{ (Nm/m/rad)}$$

Step 3: Determine  $C_D$  from Eq. (XII-4)

$$C_D = 308 \text{ (Nm/m/rad)}$$

Step 4: Determine  $K$  from Eq. (XII-3)

$$K = 0.00536 \text{ (N/mm}^2\text{)}$$

**Appendix XIII: Calculation of the equivalent lateral load,  $q_{h,Ed}$ , the lateral bending moment,  $M_{fz,Ed}$ , and the buckling reduction factor,  $\chi_{LT}$ , for purlins attached to sheeting by following BSI (2006a)**

BSI (2006a) indicates that the equivalent lateral load  $q_{h,Ed}$  allowing for the effect of torsion and lateral bending should be obtained as following:

$$q_{h,Ed} = k_h q_{Ed} \quad (\text{XIII-1})$$

in which  $k_h$  is the equivalent lateral load factor and  $q_{Ed}$  is the design vertical load. The determination of the  $k_h$  factor for sigma sections is shown in Fig. XIII-1.

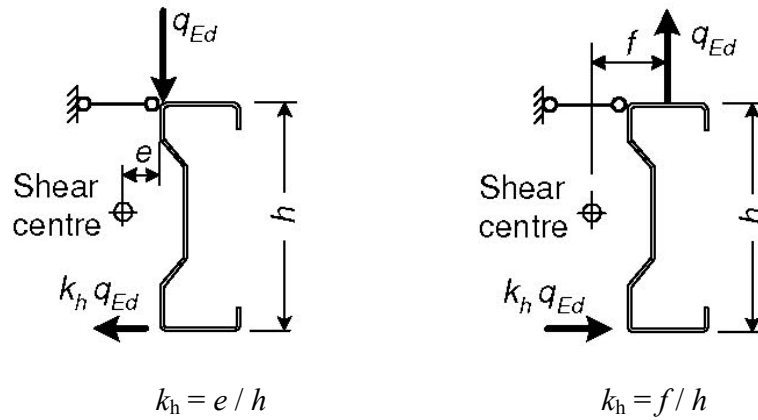


Figure XIII-1 Conversion of torsion and lateral bending into the equivalent lateral load

$$q_{h,Ed}, \text{ after BSI (2006a)}$$

The lateral bending moment  $M_{fz,Ed}$  is obtained from:

$$M_{fz,Ed} = \kappa_R M_{0,fz,Ed} \quad (\text{XIII-2})$$

in which  $M_{0,fz,Ed}$  is the initial lateral bending moment in the free flange without accounting for the effect of the lateral spring stiffness  $K$ ;  $\kappa_R$  is a correction factor allowing for the effect of  $K$ . The determination of  $M_{0,fz,Ed}$  and  $\kappa_R$  for different design cases is given in Table XIII-1. The coefficient  $R$  of the lateral spring for  $\kappa_R$  in Table XIII-1 is calculated from:

$$R = (KL_a^4) / (\pi^4 EI_{fz}) \quad (\text{XIII-3})$$

in which  $L_a$  is the span  $L$  of the purlin, or the distance between intermediate bridges if present;  $I_{fz}$  is the second moment of area of the gross cross-section of the free flange plus the contributing part of the web.

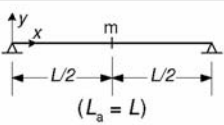
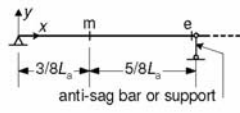
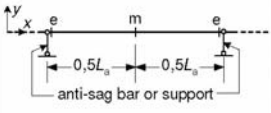
System	Location	$M_{0,fz,Ed}$	$\kappa_R$
	m	$\frac{1}{8} q_{h,Ed} L_a^2$	$\kappa_R = \frac{1 - 0,0225R}{1 + 1,013R}$
	m	$\frac{9}{128} q_{h,Ed} L_a^2$	$\kappa_R = \frac{1 - 0,0141R}{1 + 0,416R}$
	e	$-\frac{1}{8} q_{h,Ed} L_a^2$	$\kappa_R = \frac{1 + 0,0314R}{1 + 0,396R}$
	m	$\frac{1}{24} q_{h,Ed} L_a^2$	$\kappa_R = \frac{1 - 0,0125R}{1 + 0,198R}$
	e	$-\frac{1}{12} q_{h,Ed} L_a^2$	$\kappa_R = \frac{1 + 0,0178R}{1 + 0,191R}$

Table XIII-1 Values of initial moment  $M_{0,fz,Ed}$  and correction factor  $\kappa_R$ , after BSI (2006a)

BSI (2006a) recommends to using buckling curve  $b$  in BSI (2005a) to determine the reduction factor  $\chi_{LT}$  for lateral torsional buckling of the free compression flange, that is:

$$\chi_{LT} = 1 / (\phi_{LT} + \sqrt{\phi_{LT}^2 - \beta \bar{\lambda}_{fz}^2}) \quad (\text{XIII-4})$$

in which  $\phi_{LT} = 0.5[1 + \alpha_{LT}(\bar{\lambda}_{fz} - \bar{\lambda}_{LT,0}) + \beta \bar{\lambda}_{fz}^2]$ ;

$$\alpha_{LT} = 0.34; \bar{\lambda}_{LT,0} = 0.4; \beta = 0.75;$$

$\bar{\lambda}_{fz}$  is the relative slenderness for flexural buckling of the free flange and is calculated by:  $\bar{\lambda}_{fz} = l_{fz} / (i_{fz} \lambda_1)$  with  $\lambda_1 = \pi(E / f_y)^{0.5}$ , in which  $l_{fz}$  is the buckling length for the free flange, and  $i_{fz}$  is the radius of gyration of the gross cross-section of the free flange plus the contributing part of the web.

For purlins in uplift loading, BSI (2006a) suggests to using the following two empirical expressions to calculate the buckling length  $l_{fz}$ :

$$\text{If intermediate bridges are not used: } l_{fz} = 0.7L_0(1 + 13.1R_0^{1.6})^{-0.125} \quad (\text{XIII-5})$$

$$\text{with } R_0 = KL_0^4 / \pi^4 EI_{fz}$$

in which  $L_0$  is the distance between two moment inflections points defining tension zone (For simple span beams,  $L_0$  is equal to the span length of the beam);

$$\text{otherwise: } l_{fz} = \eta_1 L_a (1 + \eta_2 R^{\eta_3})^{\eta_4} \quad (\text{XIII-6})$$

in which  $L_a$  and  $R$  are given in Eq. (XIII-3);

Empirical coefficients  $\eta_1$ ,  $\eta_2$ ,  $\eta_3$  and  $\eta_4$  are dependent on the number of intermediate bridges used. In the case of No. 4, the values of  $\eta_1$ ,  $\eta_2$ ,  $\eta_3$  and  $\eta_4$  are 0.902, 8.55, 2.18 and -0.111, respectively.

Example: Calculate the lateral bending moment  $M_{fz,Ed}$ , the buckling reduction factor  $\chi_{LT}$ , the section moment resistance  $M_{RF,BSI}$ , and the member moment resistance  $M_{LTB,BSI}$  for the sigma purlin in the test SU60-20016-1.

#### Geometry

$h = 200\text{mm}$ ;  $f = 39.8\text{mm}$ ;  $L_a = L_0 = 5942\text{mm}$ ;  $I_{fz} = 105068\text{mm}^4$ ;  $Z_{fz} = 3742\text{mm}^3$ ; effective section modulus of the sigma purlin  $Z_e = 26587\text{mm}^3$ .

Yield stress  $f_y$  of the purlin:  $433\text{N/mm}^2$ .

Step 1: Determine the equivalent lateral load factor  $k_h$  from Fig. XIII-1

$$k_h = f / h = 0.199$$

Step 2: Determine the initial lateral bending moment  $M_{0,fz,Ed}$  based on the approach shown in Table XIII-1:

$$M_{0,fz,Ed} = k_h M_{y,Ed} = 0.199 M_{y,Ed}$$

Step 3: Determine the coefficient  $R$  from Eq. (XIII-3):

$$R = 3.058$$

Step 4: Determine the correction factor  $\kappa_R$  from Table XIII-1:

$$\kappa_R = 0.227$$

Step 5: Determine the lateral bending moment  $M_{fz,Ed}$  from Eq. (XIII-2):

$$M_{fz,Ed} = 0.0452 M_{y,Ed}$$

Step 6: Determine the  $M_{RF,BSI}$ :

$$\begin{aligned} M_{y,Ed(\max)} + M_{fz,Ed(\max)} Z_e / Z_{fz} &= Z_e f_y \\ \Rightarrow M_{y,Ed(\max)} \times (1 + 0.0452 \times Z_e / Z_{fz}) &= Z_e f_y \end{aligned}$$

Therefore  $M_{RF,BSI} = M_{y,Ed(max)} = 8.7\text{kNm}$

Step 7: Determine the buckling length  $l_{fz}$  from Eq. (XIII-5)

$$l_{fz} = 2408\text{mm}$$

Step 8: Determine the relative slenderness  $\bar{\lambda}_{fz}$ :

$$\bar{\lambda}_{fz} = l_{fz} / (i_{fz} \lambda_1) \text{ with } \lambda_1 = \pi(E / f_y)^{0.5}$$

$$\bar{\lambda}_{fz} = 1.43$$

Step 9: Determine the reduction factor  $\chi_{LT}$  from Eq. (XIII-4)

$$\chi_{LT} = 0.459$$

Step 10: Determine the  $M_{LTB,BSI}$ :

$$M_{y,Ed(max)} / \chi_{LT} + M_{fz,Ed(max)} Z_e / Z_{fz} = Z_e f_y$$

$$\Rightarrow M_{y,Ed(max)} / 0.459 + 0.0452 \times M_{y,Ed(max)} \times Z_e / Z_{fz} = Z_e f_y,$$

$$\text{Therefore } M_{RF,BSI} = M_{y,Ed(max)} = 4.6\text{kNm}$$

## REFERENCES

AISI. (2007) **North American Specification for the Design of Cold-Formed Steel Structural Members**. AISI S100-2007.

Alinia, M.M. (2005) **A study into optimization of stiffeners in plates subjected to shear loading**. Thin-Walled Structures, 43, 845-860.

Alinia, M.M. and Moosavi, S.H. (2008) **A parametric study on the longitudinal stiffeners of web panels**. Thin-Walled Structures, 46, 1213-1223.

ANSYS (2007) **Commands Reference, Elements Reference, Operations Guide, Basic Analysis Guide**. Theory Reference for ANSYS.

Bakker, M.C.M. and Peköz, T. (2003) **The finite element method for thin-walled members-basic principles**. Thin-Walled Structures. 41, 179-189.

Bambach, M.R. (2006) **Local buckling and post-local buckling redistribution of stress in slender plates and sections**. Thin-Walled Structures, 44, 1118-1128.

Bambach, M.R. and Rasmussen, K.J.R. (2004a) **Tests of unstiffened plate elements under combined compression and bending**. Journal of Structural Engineering, 130(10), 1602–1610.

Bambach, M.R. and Rasmussen, K.J.R. (2004b) **Design provisions for sections containing unstiffened elements with stress gradient.** Journal of Structural Engineering, 130(10), 1620–1628.

Batista, E.D.M. (2010) **Effective section method: A general direct method for the design of steel cold-formed members under local–global buckling interaction.** Thin-Walled Structures, 48, 345-356.

Bryan, E.R. (1993) **The design of bolted joints in cold-formed steel sections.** Thin Walled Structures, 16, 239-262.

Bryan, G.H. (1891) **On the stability of a plane plate under thrusts in its own plane with applications to the buckling of the sides of a ship.** In: Proceedings of London Mathematics Society, 22, 54–67.

BSI. (2001) **Metallic materials-Tensile testing-Part 1: Method of test at ambient temperature.** BS EN 10002-1:2001.

BSI. (2005a) **Design of Steel Structures—General rules and rules for buildings.** BS EN 1993-1-1: 2005.

BSI. (2005b) **Design of Steel Structures – Design of Joints.** BS EN 1993-1-8: 2005.



BSI. (2006a) **Design of Steel Structures – Cold Formed Structures**. BS EN 1993-1-3:2006.

BSI. (2006b) **Design of Steel Structures – Plated Structural Elements**. BS EN 1993-1-5:2006.

Bulson, P.S. (1970) **Stability of Flat Plates**. London: Chatto and Windus.

Camotim, D. Silvestre, N. and Dinis, P.B. (2005) **Numerical analysis of cold-formed steel members**. International Journal of Steel Structures, 5, 63-78.

Casafont, M. Arnedo, A. Roure, F. and Rodriguez-Ferran, A. (2006) **Experimental testing of joints for seismic design of lightweight structures. Part 2: Bolted joints in straps**. Thin-Walled Structures, 44, 677-691.

Cheung, M.S. (1976) **Finite strip method in structural analysis**. Oxford: Pergamon Press.

Chu, X.T. Kettle, R. and Li, L.Y. (2004) **Lateral-torsion buckling analysis of partial-laterally restrained thin-walled channel-section beams**. Journal of Constructional Steel Research, 60, 1159-1175.

Chu, X.T. Ye, Z.M. Kettle, R. and Li, L.Y. (2005) **Buckling behaviour of cold-formed channel sections under uniformly distributed loads.** Thin-Walled Structures, 43, 531-542.

Chu, X.T. Ye, Z.M. Li, L.Y. and Kettle, R. (2006) **Local and distortional buckling of cold-formed zed-section beams under uniformly distributed transverse loads.** International Journal of Mechanical Sciences, 48, 378-388.

Chung, K.F. and Ho, H.C. (2005). **Analysis and design of lapped connections between cold-formed steel Z sections.** Thin-Walled Structures, 43, 1071-1090.

Chung, K.F. and Ip, K.H. (2000) **Finite element modelling of bolted connections between cold-formed steel strips and hot rolled steel plates under static shear loading.** Engineering Structures, 22, 1271-1284.

Chung, K.F. and Ip, K.H. (2001) **Finite element investigation on the structural behaviour of cold-formed steel bolted connections.** Engineering Structures, 23, 1115-1125.

Chung, K.F. and Lau, L. (1999) **Experimental investigation on bolted moment connections among cold-formed steel members.** Engineering Structures, 21, 898-911.

Chung, K.F. and Lawson, R.M. (2000) **Structural performance of shear resisting connections between cold-formed steel sections using web cleats of cold-formed steel strip.** Engineering Structures, 22, 1350-1366.

Chung, K.F. and St Quinton, D. (1996) **Structural performance of modern roofs with thick over-purlin insulation-Experimental investigation.** Journal of Constructional Steel Research, 40(1), 17-38.

Clough, R.W. (1960) **The finite element method in plane stress analysis.** In: Proceedings of the 2<sup>nd</sup> ASME Conference on Electronic Computation. Pittsburgh, Pa, 345-378.

Davies, J.M. and Brown, B.A. (1996) **Plastic design to BS5950.** Oxford: Blackwell Science.

Davies, J.M. and Leach, P. (1994) **First-order generalised beam theory.** Journal of Constructional Steel Research, 31(2-3), 187-220.

Davies, J.M. Leach, P. and Heinz, D. (1994) **Second-order generalised beam theory.** Journal of Constructional Steel Research, 31(2-3), 221-241.

Davis, J.M. and Raven, G.K. (1986) **Design of cold formed steel purlins.** IABSE Thin Walled Metal Structures in Buildings Colloquium, Stockholm, 151-160.

Desmond, T.P. Peköz, T. and Winter, G. (1981a) **Edge stiffeners for thin-walled members.** Journal of Structural Engineering, 107(2), 329-353.

Desmond, T.P. Pekoz, T. and Winter, G. (1981b) **Intermediate stiffeners for thin-walled members.** Journal of Structural Engineering, 107(4), 627-648.

Dinis, P.B. and Camotim, D. (2010) **Local/distortional mode interaction in cold-formed steel lipped channel beams.** Thin-Walled Structures, 48, 771-785.

Dinis, P.B. Camotim, D. and Silvestre, N. (2007) **FEM-based analysis of the local-plate/distortional mode interaction in cold-formed steel lipped channel columns.** Computers and Structures, 85, 1461-1474.

Djugash, A.C.R. and Kalyanaraman, V. (1990) **Experimental study on the lateral buckling behaviour of cold-formed beams.** In: Proceedings of the 10th International Specialty Conference on Cold-formed Steel Structures. St. Louis, MO, USA, 363-380.

Dubina, D. and Ungureanu, V. (2002) **Effect of imperfections on numerical simulation of instability behaviour of cold-formed steel members.** Thin-Walled Structures, 40, 239-262.

Dubina, D. and Ungureanu, V. (2010) **Behaviour of multi-span cold-formed Z purlins with bolted lapped connections**. Thin-Walled Structures, 48, 866-871.

Ellifritt, D.S. Sposito, T. and Haynes, J.R. (1992) **Flexural strengths and deflections of discretely braced cold-formed steel channel and Zee sections**. In: Proceedings of the 11<sup>th</sup> International Specialty Conference on Cold-formed Steel Structures. St. Louis, MO, USA, 109-129.

Fan, S.C. and Cheung, Y.K. (1983) **Analysis of shallow shells by spline finite strip method**. Engineering Structures, 5(4), 255-262.

Gao, T. and Moen, C. (2011). **A prediction model for girt-panel interaction in metal building wall systems**. In: Proceedings the 6<sup>th</sup> International Conference on Thin Walled Structures. Timisoara, Romania, 579-586.

Gerard G. and Becker, H. (1957) **Handbook of Structural Stability Part I: Buckling of Flat Plates**. NACA TN 3781.

Ghosn, A. and Sinno, R. (1995). **Governing stresses in Z-purlin lap joints**. Journal of Structural Engineering, 121(12), 1735–1741.

Graciano, C. and Edlund, B. (2003) **Failure mechanism of slender girder webs with a longitudinal stiffener under patch loading.** Journal of Constructional Steel Research, 59, 27-45.

Grundy, P. (1990). **Effect of pre- and post-buckling behaviour on load capacity of continuous beams.** Thin-Walled Structures, 9, 407-415.

Gutierrez, R. Loureiro, A. Lopez, M. and Moreno, A. (2011) **Analysis of cold-formed purlins with slotted sleeve connections.** Thin-Walled Structures, 49, 833-841.

Hancock, G.J. (1985). **Distortional buckling of steel storage rack columns.** Journal of Structural Engineering, 111(12), 2770-2783.

Hancock, G.J. (1997) **Design for distortional buckling of flexural members.** Thin-Walled Structures, 27(1), 3-12.

Hancock, G.J. (2003). **Cold-formed steel structures.** Journal of Constructional Steel Research, 59, 473-487.

Hancock, G.J. Murray, T.M. and Ellifritt, D.S. (2001) **Design of cold-formed steel structures to the AISI specification.** New York: Marcel Dekker Inc.

Hancock, G.J. Roger, C.A. and Schuster, R.M. (1996) **Comparison of the distortional buckling method for flexural members with tests**. In: Proceedings of the 13th International Specialty Conference on Cold-formed Steel Structures. St. Louis, MO, USA, 125-140.

Heinz, D. A. (1994) **Application of Generalized Beam Theory to the Design of Thin-Walled Purlins**. Thin-Walled Structures, 19, 311-335.

Hetrakul, N. and Yu, W.W. (1978) **Webs for cold-formed steel flexural members: Structural behaviour of beam webs subjected to web crippling and a combination of web crippling and bending**. Final Report, Civil Engineering Study 78-4, University of Missouri-Rolla, Rolla, MO.

Hibbeler, R.C. (2006). **Structural analysis, 6<sup>th</sup> Ed**. Singapore: Pearson Prentice Hall.

Hiriyur, B.K.J. and Schafer, B.W. (2005) **Yield-line analysis of cold-formed steel members**. International Journal of Steel Structures, 5(1), 43-54.

Ho, H.C. and Chung, K.F. (2004) **Experimental investigation into the structural behaviour of lapped connections between cold-formed steel Z sections**. Thin-Walled Structures, 42, 1013-1033.

Ho, H.C. and Chung, K.F. (2006a) **Structural behaviour of lapped cold-formed steel Z sections with generic bolted configurations.** Thin-Walled Structures, 44, 466–480.

Ho, H.C. and Chung, K.F. (2006b) **Analytical prediction on deformation characteristics of lapped connections between cold-formed steel Z sections.** Thin-Walled Structures, 44, 115–130.

Ings, N.L. and Trahair, N.S. (1984) **Lateral buckling of restrained roof purlins.** Thin-Walled Structures, 2, 285-306.

Jiang, C. and Davies, J.M. (1997) **Design of thin-walled purlins for distortional buckling.** Thin-Walled Structures, 29, 189-202.

Johansen, K.W. (1962) **Yield Line Theory.** London: Cement and Concrete Association.

Johnston, N. and Hancock, G. (1994) **Calibration of the AISI R-factor design approach for purlins using Australian test data.** Engineering Structures, 16(5), 342-347.

Kalyanaraman, V. Peköz, T. and Winter, G. (1977) **Unstiffened compression elements.** Journal of the Structural Division, ASCE, 103, 1833-1848.



Katnam, K.B. Van Impe, R. Lagae, G. and De Strycker, M. (2007a) **A theoretical numerical study of the rotational restraint in cold-formed steel single skin purlin-sheet systems.** Computers and Structures. 85, 1185-1193.

Katnam, K.B. Van Impe, R. Lagae, G. and De Strycker, M. (2007b) **Modelling of cold-formed steel sandwich purlin-sheeting systems to estimate the rotational restraint.** Thin-Walled Structures, 45, 584-590.

Kim, J. Yoon, J. and Kang, B. (2007) **Finite element analysis and modelling of structure with bolted joints.** Applied Mathematical Modelling, 31, 895–911.

Kitipornchai, S. Al-Bermani, F.G.A. and Peyrot, A.H. (1994) **Effects of bolt slippage on ultimate behaviour of lattice structures.** Journal of Structural Engineering, 120(8), 2281-2287.

Kotelko, M. (2004) **Load-capacity estimation and collapse analysis of thin-walled beams and columns-recent advances.** Thin-Walled Structures, 42, 153-175.

Kurniawan, C.W. and Mahendran, M. (2009) **Lateral buckling strength of simply supported LiteSteel beams subject to moment gradient effects.** Journal of Structural Engineering, 135(9), 1058-1067.

LaBoube, R.A. and Yu, W.W. (1978a) **Webs for cold-formed steel flexural members: Structural behaviour of beam webs subjected primarily to shear stress.** Final Report, Civil Engineering Study 78-2, University of Missouri-Rolla, Rolla, MO.

LaBoube, R.A. and Yu, W.W. (1978b) **Webs for cold-formed steel flexural members: Structural behaviour of beam webs subjected a combination of bending and shear.** Final Report, Civil Engineering Study 78-3, University of Missouri-Rolla, Rolla, MO.

Laine, M. and Tuomala, M. (1999). **Testing and design of gravity-loaded steel purlins restrained by sheeting.** Journal of Constructional Steel Research, 49, 129-138.

Lau, S.C.W. and Hancock, G.J. (1987) **Distortional buckling formulas for channel columns.** Journal of Structural Engineering, 113(5), 1063-1078.

Lee, S.C. Davidson, J.S. and Yoo, C.H. (1996) **Shear buckling coefficients of plate girder web panels.** Computer and Structures, 59(5), 789-795.

Li, L.Y. (2004) **Lateral-torsional buckling of cold-formed zed-purlins partial-laterally restrained by metal sheeting.** Thin-Walled Structures, 42, 995-1011.

Li, L.Y. (2011) **Calculation of moment capacity of cold-formed steel members.** International Journal of Structural Engineering, 2(2), 101-115.

Li, L.Y. and Chen, J.K. (2008) **An analytical model for analyzing distortional buckling of cold-formed steel sections.** Thin-Walled Structures, 46, 1430-1436.

Lim, J.B.P. and Nethercot, D.A. (2003) **Ultimate strength of bolted moment-connections between cold-formed steel members.** Thin-Walled Structures, 41, 1019-1039.

Lim, J.B.P. and Nethercot, D.A. (2004a) **Finite element idealization of a cold-formed steel portal frame.** Journal of Structural Engineering, 130(1), 78-94.

Lim, J.B.P. and Nethercot, D.A. (2004b) **Stiffness prediction for bolted moment-connections between cold-formed steel members.** Journal of Constructional Steel Research, 60, 85-107.

Lindner, J. and Aschinger, R. (1994) **Load-carrying capacity of cold-formed beams subjected to overall lateral-torsional buckling and local plate buckling.** Journal of Constructional Steel Research, 31, 267-287.

Liu, Q. Yang, J. and Li, L.Y. (2011) **Pseudo-plastic moment resistance of continuous beams with cold-formed Sigma sections at internal supports: Experimental study.** Engineering Structures, 33, 947-957.

Liu, Q. Yang, J. Chan, A.H.C. and Li, L.Y. (2011) **Pseudo-plastic moment resistance of continuous beams with cold-formed Sigma sections at internal supports: A numerical Study.** Thin-Walled Structures, 49, 1592-1604.

Lucas, R.M. Al-Bermani, F.G.A. and Kitipornchai, S. (1997a) **Modeling of cold-formed purlin-sheeting systems-Part 1: Full model.** Thin-Walled Structures, 27(3), 223-243.

Lucas, R.M. Al-Bermani, F.G.A. and Kitipornchai, S. (1997b) **Modeling of cold-formed purlin-sheeting systems-Part 2: Simplified model.** Thin-Walled Structures, 27(4), 263-286.

Macdonald, M. Heiyantuduwa, M.A. and Rhodes, J. (2008) **Recent developments in the design of cold-formed steel members.** Thin-Walled Structures, 46(7-9), 1047-1053.

Mäkeläinen, P. and Kesti, J. (1999) **Advanced method for lightweight steel joining.** Journal of Constructional Steel Research, 49, 107-116.

Moen, C.D. Igusa, T. and Schafer, B.W. (2008) **Prediction of residual stresses and strains in cold-formed steel members.** Thin-Walled Structures, 46, 1274-1289.

Moore, D.B. (1990) **Moment-Rotation Characteristics of Purlin Connections.** In: Proceedings of the 10th International Specialty Conference on Cold-formed Steel Structures. St. Louis, MO, USA, 525-544.

Moore, D.B. and Sims, P.A.C. (1988) **Load tests on full-scale cold formed steel roofs. Part 1: Sigma purlin system (BRE Report BR122), Part 2: Zed purlin system (BRE Report BR123) and Part 3: Zeta purlin system (BRE Report BR124).** Building Research Establishment.

Moreyra, M.E. and Peköz, T. (1993) **Behaviour of cold-formed steel lipped channels under bending and design of edge stiffened elements.** Research Report 93-4, School of Civil and Environmental Engineering, Cornell University, Ithaca.

Murray, N.W. (1986) **Introduction to the theory of thin-walled structures.** Oxford: Clarendon Press.

Murray, N.W. and Khoo, P.S. (1981) **Some basic plastic mechanisms in the local buckling of thin-walled steel structures.** International Journal of Mechanical Sciences, 23(12), 703-713.

Papazian, R. P. Schuster, R. M. and Sommerstein, M. (1994) **Multiple stiffened deck profiles.** In: Proceedings of the 12th International Specialty Conference on Cold-formed Steel Structures. St. Louis, MO, USA, 217 -228.

Pastor, M.M. and Roure, F. (2008) **Open cross-section beams under pure bending I. Experimental investigations.** Thin-Walled Structures, 46, 476-483.

Pastor, M.M. and Roure, F. (2009) **Open cross-section beams under pure bending II. Finite element simulation.** Thin-Walled Structures, 47, 514-521.

Pedreschi, R.F. Sinha, B.P. and Davies, R. (1997) **Advanced connection techniques for cold-formed steel structures.** Journal of Structural Engineering, 123(2), 138-144.

Peköz, T. (1987) **Development of a unified approach to the design of cold-formed steel members.** American Iron and Steel Institute, Research Report CF87-1.

Peköz, T. and Soroushian, P. (1982) **Behaviour of C- and Z-purlins under wind uplift.** In: Proceedings of the 6<sup>th</sup> International Specialty Conference on Cold-formed Steel Structures. St. Louis, MO, USA, 409-429.

Pham, C.H. and Hancock, G.J. (2009a) **Shear buckling of thin-walled channel sections.** Journal of Constructional Steel Research, 65, 578-585.

Pham, C.H. and Hancock, G.J. (2009b) **Direct strength design of cold-formed purlins.** Journal of Structural Engineering, 135(3), 229-238.

Pham, C.H. and Hancock, G.J. (2010a) **Experimental investigation of high strength cold-formed C-sections in combined bending and shear.** Journal of Structural Engineering, 136(7), 866-878.

Pham, C.H. and Hancock, G.J. (2010b) **Numerical simulation of high strength cold-formed purlins in combined bending and shear.** Journal of Constructional Steel Research, 66, 1205-1217.

Pi, Y.L. Put, B.M. and Trahair, N.S. (1998) **Lateral buckling strengths of cold-formed channel section beams.** Journal of Structural Engineering, 124, 1182-1191.

Pi, Y.L. Put, B.M. and Trahair, N.S. (1999) **Lateral buckling strengths of cold-formed Z-section beams.** Thin-Walled Structures, 34, 65-93.

Prola, L.C. and Camotim, D. (2002) **On distortional post-buckling behaviour of cold-formed lipped channel steel beams.** In: Proceedings of the Third International Conference on Advances in Steel Structures, Hong Kong, China, 331-339.

Put, B.M. Pi, Y.L. and Trahair, N.S. (1999a) **Lateral buckling tests on cold-formed channel beams.** Journal of Structural Engineering, 125, 532-539.

Put, B.M. Pi, Y.L. and Trahair, N.S. (1999b) **Lateral buckling tests on cold-formed Z-beams.** Journal of Structural Engineering, 125, 1277-1283.

Quach, W.M. Teng, J.G. and Chung, K.F. (2006) **Finite element predictions of residual stresses in press-braked thin-walled steel sections.** Engineering Structures, 28, 1609-1619.

Reck, H.P. Peköz, T. and Winter, G. (1975) **Inelastic strength of cold-formed steel beams.** Journal of the Structural Division, 101, 2193-2203.

Ren, W.X. Fang, S.E. and Young, B. (2006) **Analysis and design of cold-formed steel channels subjected to combined bending and web crippling.** Thin-Walled Structures, 44, 314-320.

Rhodes, J. and Nash, D. (1998) **An investigation of web crushing behaviour in thin-walled beams.** Thin-Walled Structures, 32, 207-230.

Rockey, K.C. and Bagchi, D.K. (1970) **Buckling of plate girder webs under partial edge loadings.** International Journal of Mechanics Science, 12, 61-76.

Roger, C.A. (1995) **Local and distortional buckling of cold formed steel channel and zed sections in bending.** M.A.Sc. thesis presented to the department of Civil Engineering, University of Waterloo, Waterloo Ontario.

Rogers, C.A. and Hancock, G.J. (2000) **Failure modes of bolted-sheet-steel connections loaded in shear.** Journal of Structural Engineering, 126(3), 288-296.



Rousch, C.J. and Hancock, G.J. (1997) **Comparison of tests of bridged and unbridged purlins with a non-linear analysis model.** Journal of Constructional Steel Research, 44, 197-220.

Sarawit, A.T. Kim, Y. Bakker, M.C.M. Pekoz, T. (2003) **The finite element method for thin-walled members-applications.** Thin-Walled Structures, 41, 191-206.

Schafer, B.W. (2002) **Local, Distortional, and Euler Buckling of Thin-Walled Columns.** Journal of Structural Engineering, 128(3), 289–299.

Schafer, B.W. (2006) **CUFSM 3.12: Elastic buckling analysis of thin-walled members by finite strip analysis.** (<http://www.ce.jhu.edu/bschafer/cufsm>)

Schafer, B.W. (2008) **Review: The Direct Strength Method of cold-formed steel member design.** Journal of Constructional Steel Research, 64, 766-778.

Schafer, B.W. Li, Z. and Moen, C.D. (2010) **Computational modelling of cold-formed steel.** Thin-Walled Structures, 48, 752-762.

Schafer, B.W. and Peköz, T. (1998a) **Direct strength prediction of cold-formed steel members using numerical elastic buckling solutions.** In: Shanmugam NE, et al., editors. Thin-walled structures. Amsterdam: Elsevier.

Schafer, B.W. and Peköz, T. (1998b) **Computational modelling of cold-formed steel: Characterizing geometric imperfections and residual stresses.** Journal of Constructional Steel Research, 47(3), 193–210.

Schafer, B.W. Sarawit, A.T. and Peköz, T. (2006) **Complex edge stiffeners for thin-walled members.** Journal of Structural Engineering, 132 (2), 212–226.

Schardt, R. (1983) **The generalised beam theory.** In: Proceedings of the M.R. Horne Conference, University of Manchester, Granada, London, 469-475.

Shifferaw, Y. and Schafer, B.W. (2008) **Inelastic bending capacity in cold-formed steel members.** Report to AISI. Thin-Walled Structures Research Group, Department of Civil Engineering, Johns Hopkins University.

Silvestre, N. and Camotim, D. (2004a) **Distortional buckling formulae for cold-formed steel C and Z-section members Part I-derivation.** Thin-Walled Structures, 42(11), 1567-1597.

Silvestre, N. and Camotim, D. (2004b) **Distortional buckling formulae for cold-formed steel C and Z-section members Part II-Validation and application.** Thin-Walled Structures, 42(11), 1599-1629.

Sokol, L. (1996) **Stability of cold-formed purlins braced by steel sheeting**. Thin-Walled Structures, 25(4), 247-268.

Standards Australia. (2006) **Cold-Formed Steel Structures, AS/NZS 4600:2005**. Standards Australia/Standards New Zealand.

Stein, M. (1985) **Analytical results for post-buckling behaviour of plates in compression and shear**. In: Aspects of the Analysis of Plate Structures (Dawe, D.J. Horsington, R.W. Kamtekar, A.G. and Little, G.H., eds.), Oxford University Press, 205-223.

Teng, J.G. Yao, J. and Zhao, Y. (2003) **Distortional buckling of channel beam-columns**. Thin-Walled Structures, 41, 595-617.

Timoshenko, S. (1956) **Strength of materials, Part II, 3<sup>rd</sup> ed.** New York: Van Nostrand Reinhold Company.

Timoshenko, S. and Gere, J.M. (1961) **Theory of elastic stability, 2<sup>nd</sup> ed.** New York: McGraw-Hill Book Co. Inc.

Tomà, A. Sedlacek, G. and Weynand, K. (1993) **Connections in cold-formed steel**. Thin-Walled Structures, 16, 219-237.

Tomà, T. and Wittemann, K. (1994) **Design of cold-formed purlins and rails restrained by sheeting**. Journal of Constructional Steel Research, 31, 149-168.

Trahair, N.S. (1993) **Flexural-torsional buckling of structures**. London: E & FN Spon.

Trahair, N.S. (1994) **Lateral buckling strengths of unsheeted cold-formed beams**. Engineering Structures, 16(5), 324-331.

Ungureanu, V. and Dubina, D. (2004) **Recent research advances on ECBL approach. Part I: Plastic-elastic interactive buckling of cold-formed steel sections**. Thin-Walled Structures, 42, 177-194.

Ungureanu, V. Kotelko, M. Mania, R.J. and Dubina, D. (2010) **Plastic mechanisms database for thin-walled cold-formed steel members in compression and bending**. Thin-Walled Structures, 48, 818-826.

Von Kármán, T. Sechler, E.E. and Donnell, L.H. (1932) **The strength of thin plates in compression**. ASME Transactions, APM-54, 553–57.

Vieira, L.C.M. Malite, M. and Schafer, B.W. (2010) **Simplified models for cross-section stress demands on C-section purlins in uplift**. Thin-Walled Structures, 48, 33-41.

Vrany, T. (2006) **Effect of loading on the rotational restraint of cold-formed purlins.** Thin-Walled Structures. 44, 1287-1292.

White, R.M. and Cottingham, W. (1962) **Stability of plates under partial edge loadings.** Proceedings, ASCE, 88, 67-86.

Willis, C.T. and Wallace, B. (1990) **Behaviour of cold-formed steel purlins under gravity loading.** Journal of Structural Engineering, 116 (8), 2061–2069.

Winter, G. (1947) **Strength of thin steel compression flanges.** Transactions, ASCE, 112, 527-576.

Wong, M.B. (2009) **Plastic analysis and design of steel structures.** Oxford: Elsevier Ltd.

Wong, M.F. and Chung, K.F. (2002) **Structural behaviour of bolted moment connections in cold-formed steel beam-column sub-frames.** Journal of Constructional Steel Research, 58, 253-274.

Yang, D. and Hancock, G.J. (2004) **Compression tests of high strength steel channel columns with interaction between local and distortional buckling.** Journal of Structural Engineering, 130(12), 1954-1963.

Yang, D. and Hancock, G.J. (2006) **Numerical simulation of high-strength steel box-shaped columns failing in local and overall buckling modes.** Journal of Structural Engineering, 132 (4), 541–549.

Ye, Z.M. Kettle, R.J. Li, L.Y. and Schafer, B.W. (2002) **Buckling behaviour of cold-formed zed-purlins partially restrained by steel sheeting.** Thin-Walled Structures, 40, 853-864.

Ye, Z.M. Kettle, R.J. and Li, L.Y. (2004) **Analysis of cold-formed zed-purlins partially restrained by steel sheeting.** Computers and Structures, 82, 731-739.

Yener, M. and Peköz, T. (1983) **Limit design in cold-formed steel.** Journal of Structural Engineering, 109 (9), 2033-2047.

Yener, M. and Peköz, T. (1985a) **Partial Stress Redistribution in Cold-Formed Steel.** Journal of Structural Engineering, 111 (6), 1169-1185.

Yener, M. and Peköz, T. (1985b) **Partial Moment Redistribution in Cold-Formed Steel.** Journal of Structural Engineering, 111(6), 1187-1203.

Yoo, C.H. and Lee, S.C. (2006) **Mechanics of web panel postbuckling Behavior in Shear.** Journal of Structural Engineering, 132(10), 1580–1589.

Yorgun, C. Dalci, S. and Altay, G.A. (2004) **Finite element modelling of bolted steel connections designed by double channel**. Computers and Structures, 82, 2563-2571.

Young, W.C. and Budynas, R.G. (2002) **Roark's formulas for stress and strain**, 7<sup>th</sup> ed. New York: McGraw-Hill Professional.

Young, B. and Hancock, G.J. (2001) **Design of cold-formed channels subjected to web crippling**. Journal of Structural Engineering, 127 (10), 1137-1144.

Young, B. and Hancock, G.J. (2002) **Tests of channels subjected to combined bending and web crippling**. Journal of Structural Engineering, 128 (3), 300-308.

Yu, W.W. (2000) **Cold-formed steel design**, 3<sup>rd</sup> ed. New York: John Wiley and Sons Inc.

Yu, W. K. Chung, K.F. and Wong, M.F. (2005) **Analysis of bolted moment connections in cold-formed steel beam-column sub-frames**. Journal of Constructional Steel Research, 61, 1332-1352.

Yu, C. and Schafer, B.W. (2003) **Local buckling tests on cold formed steel beams**. Journal of Structural Engineering, 129, 1596-1606.

Yu, C. and Schafer, B.W. (2006a) **Effect of longitudinal stress gradient on the ultimate strength of thin plates.** Thin-Walled Structures, 44, 787-799.

Yu, C. and Schafer, B.W. (2006b) **Distortional buckling tests on cold-formed steel beams.** Journal of Structural Engineering, 132, 515-528.

Yu, C. and Schafer, B.W. (2007) **Simulation of cold-formed steel beams in local and distortional buckling with applications to the direct strength method.** Journal of Constructional Steel Research, 63, 581-590.

Zaharia, R. and Dubina, D. (2006) **Stiffness of joints in bolted connected cold-formed steel trusses.** Journal of Constructional Steel Research, 62, 240-249.

Zetlin, L. and Winter, G. (1955) **Unsymmetrical bending of beams with and without lateral bracing.** In: Proceedings of the American Society of Civil Engineering, Vol. 81.

Zhang, L. and Tong, G.S. (2008) **Moment resistance and flexural rigidity of lapped connections in multi-span cold-formed Z purlin systems.** Thin-Walled Structures, 46, 551-560.

Zhao, X.L. and Hancock, G.J. (1993) **A theoretical analysis of the plastic-moment capacity of an inclined yield line under axial force.** Thin-Walled Structures, 15, 185-207.



Zienkiewicz, O.C. and Taylor, R.L. (2000) **The finite element method, 5th ed.** Oxford:  
Butterworth-Heinemann.